ISBN 978-82-326-3140-7 (printed ver.)
ISBN 978-82-326-3141-4 (electronic ver.)
ISSN 1503-8181

NTNU
Norwegian University of
Science and Technology

Lucas Cantinelli Sevillano

Doctoral theses at NTNU, 2018:175

NTNU

Doctoral thesis

NTNU
Norwegian University of Science and Technology
Thesis for the Degree of
Philosophiae Doctor
Faculty of Engineering
Department of Geoscience and Petroleum

Doctoral theses at NTNU, 2018:175

Lucas Cantinelli Sevillano

Effects of Well Temperature on Wellhead Fatigue Assessment

NTNU
Norwegian University of
Science and Technology

Lucas Cantinelli Sevillano

Effects of Well Temperature on Wellhead Fatigue Assessment

Thesis for the Degree of Philosophiae Doctor

Trondheim, June 2018

Norwegian University of Science and Technology
Faculty of Engineering
Department of Geoscience and Petroleum

NTNU
Norwegian University of
Science and Technology

NTNU
Norwegian University of Science and Technology

Thesis for the Degree of Philosophiae Doctor

Faculty of Engineering
Department of Geoscience and Petroleum

ISBN 978-82-326-3140-7 (printed ver.)
ISBN 978-82-326-3141-4 (electronic ver.)
ISSN 1503-8181

Doctoral theses at NTNU, 2018:175

Printed by NTNU Grafisk senter

Summary

Construction and later re-entering of subsea wells require the use of a tubular component called riser to connect the rig to the wellhead. The motions of the rig and of the riser itself, which are created by the sea state excitement, are transferred all the way down to the wellhead, thus subjecting the latter for wear and in worst cases fatigue failure.

Fatigue failure of the wellhead has been deemed as a major concern for oil companies. Operators in the Norwegian continental shelf and Det Norske Veritas (DNVGL) have cooperated in a Joint Industry Project (JIP) to improve the methodology used for modelling and estimating wellhead fatigue damage during the life cycle of a well. The ongoing work has resulted in several research papers, as well as a Recommended Practice (RP) issued by DNVGL.

This doctoral thesis contributes to the available research work by investigating how temperature will impact on wellhead fatigue. This has not been investigated in the past.

The circulation of fluids in the well during drilling and other operations influences how temperature develops on casings strings, cement sheaths and surrounding rock formations. Because the surface casing and the conductor strings are integral components of the wellhead, their temperature distributions can influence the mechanical response of the wellhead system, not only by induced thermal expansion and contraction but also by altering how the mechanical load is shared within the wellhead.

The fatigue assessment methodology presented by the JIP employs 3D models to simulate the mechanical response of the wellhead when subject to loading and from that it estimates the stress at the points of the equipment most at risk for failing by fatigue, so called fatigue hot spots.

The JIP’s methodology assumes that the relation between applied load and resulting stresses remains constant for as long as the structural configuration of the wellhead is not altered. However, this doctoral research makes a case for that when the temperature profiles of the well are added to the 3D mechanical simulations, the relation between load and stress at the fatigue hot spots can be considerably changed. Furthermore, the load-stress relation could continue to change during operations as a result of the induced changes of temperature in the well.

Therefore, the current wellhead fatigue assessment methodology is at risk for miscalculating the damage undergone by the equipment and it could benefit from a more-accurate representation of the mechanical response of the wellhead. For the most susceptible hot spots, the transient temperature of the typical drilling scenario modelled in the study

resulted in fatigue estimates 10 to 20% lower than what a conventional analysis would indicate.

The thermal strain of tubular components has been investigated in an attempt to expand and generalize results for a wider range of temperature profiles in the well, thus enabling to identify under which thermal conditions the different wellhead fatigue hot spots would be more at risk for failing.

As a complementary effort for assessing wellhead fatigue, the research work has also addressed possible solutions for reducing fatigue. Therefore, the merits of anchoring the Blowout Preventer, and thus reducing the loading transferred to the wellhead, was investigated and discussed as a feasible solution. This alternative would require planning and costly marine operations, but the results of the analyses indicate that this approach has the potential to more than double the service life of a well.

Sammendrag

Konstruksjon og senere tilgang til brønnhodet i undervannbrønner krever bruk av et såkalt stigerør for å forbinde riggen til brønnhodet. Riggen og stigerørets bevegelser, som skapes av bølger og strømning, overføres ned til brønnhodet, slik at dette utsettes for slitasje og i verst fall utmattingsbrudd.

Utmattingsbrudd i brønnhodet er kritisk og bekymring for oljeselskapene. Operatører på den norske kontinentalsokkelen og Det Norske Veritas (DNVGL) har samarbeidet om et Joint Industry Project (JIP) for å forbedre metoden som brukes for å modellere og anslå utmattingsskader i brønnhodet over brønnens levetid. Arbeidet har ført til flere forskningsartikler, i tillegg til en anbefalt framgangsmåte - Recommended Practice (RP) utarbeidet av DNVGL.

Denne doktorgradsoppgaven bidrar ved å undersøke hvordan temperatur påvirker utmatting av brønnhodet. Dette har ikke vært undersøkt tidligere.

Sirkulasjonen av væsker i brønnen under boring og andre operasjoner påvirker temperatur på fôringsrør, sement og omkringliggende formasjoner. Siden lederøret og forankringsrøret er vesentlige komponenter i brønnhodet, kan temperaturdistribusjonen på fôringsrørene påvirke den mekaniske responsen på brønnhodet, ikke bare ved å føre til termisk ekspansjon og sammentrekning, men også ved å endre hvordan den mekaniske belastningen fordeles i brønnhodet.

Metoden for å vurdere utmatting av brønnhodet, som ble presenterte av JIP prosjektet, bruker 3D modeller for å simulere den mekaniske responsen i brønnhodet utfra påført belastning. Deretter beregnes spenningen i punkter i brønnhodet som er mest utsatt for utmattingsbrudd, såkalte «hot-spots».

Metoden antar forholdet mellom påført belastning og resulterende spenning forblir konstant så lenge den strukturelle konfigurasjonen til brønnhodet ikke endres. Mitt doktorgradsarbeid argumenterer derimot at når brønnens temperatureprofil tas med i de mekaniske 3D simuleringene, kan forholdet mellom belastning og spenning ved «hot-spots» endres betraktelig. Dessuten kan spenningsrelasjonen fortsette å endres i løpet av operasjonene som et resultat av temperaturendring i brønnen. Den nye metoden, som tar temperatur i betraktning, beregner utmatting i brønnhodet på en mer nøyaktig måte. For «hot-spots» som blir mest påvirket av temperatur, utmatting resultatene til simulasjonene var 10 til 20 % lavere enn det den konvensjonelle metoden ville forutsi.

Den termiske deformasjonen av fôringsrør ble undersøkt i et forsøk på å utvide og generalisere resultater for et bredere spekter av temperatureprofiler i brønnen for å

identifisere under hvilke termisk betingelser brønnhodet vil være mer utsatt for utmattingsbrudd i «hot-spots».

Som et komplementært bidrag for å vurdere utmattingsskade i brønnhodet, har doktorgradsarbeidet også adressert mulige tiltak for å øke utmattingskapasiteten. Ved hjelp av forankringslinjer mellom utblåsningssikringen (BOP) og havbunnen kan utmattingskapasiteten øke betraktelig. Dette krever planleggingsarbeid og til dels kostbare marine operasjoner, men resultatene av analysene indikerer at tiltaket har potensialet til å doble brønnens levetid.

Acknowledgements

Completion of this thesis has been possible by the support of many.

Having finished my masters back at Unicamp in Brazil, I had the desire to seek a PhD abroad. Therefore, I would like to first show my gratitude to my friend Marte for letting me know about NTNU.

I am grateful to Professor Paulo Ribeiro from Unicamp, for introducing me as a potential PhD candidate to his contacts in Statoil and Norway.

I would like to thank my supervisor, Professor Sigbjørn Sangesland, for giving me the opportunity to carry out this doctoral work. His guidance, motivation, generosity, and patience turned a challenging task into a fulfilling achievement.

I would like to thank my co-supervisor Dr. Jesus de Andrade, for all the ideas, comments, and discussions we had, which greatly improved the research carried out during the doctoral work.

I am thankful to Dr. Guttorm Grytøyr, at Statoil, for the opportunity given to discuss my research, and for all the insightful comments. I am also thankful to Dr. Lorents Reinås for the valuable comments at the OMAE conference held in Trondheim. I would like to acknowledge Bjørn Brechan, at both Statoil and the Department of Geoscience and Petroleum, for the help initiating the contact with Drs. Reinås and Grytøyr.

I wish to thank all the lecturers I had during the doctorate, for all they have taught me. In special, professors Tor Berge Gjersvik and Milan Stanko from the Department of Geoscience and Petroleum, and professors Stein Sævik and Carl M. Larsen, at the Department of Marine Technology.

I thank PhD candidate Dag Vavik, whose interest in my wellbore temperature model resulted in a joint publication. I also thank master student Rikke Mohn for her help at correcting mistakes on the model's documentation.

I would like to thank my office mates, Nur, Babak and Xiaoqian, for their camaraderie and companionship. I would like to thank Filipe, Vegard, Hamid, Tore and all my friends and colleagues in the department.

Great thanks to my family, for all the love, support, and encouragement throughout my life, and especially during the years we have been apart, while I conducted this PhD.

This doctoral work has been funded by the Science without Borders program. Therefore, I would like to acknowledge the Brazilian Ministry of Education, the Ministry of Science and Technology, and their respective funding agencies, CAPES and CNPq.

List of publications

This thesis presents and expands on the research published in the technical publications I to III below. Paper IV presents the computational tool developed for calculating the temperature in the well. Publications I, II, II and IV are included in the Annexes.

Paper I
"Thermal Effects on Subsea Wellhead Fatigue during Workover Operations"
Lucas Cantinelli Sevillano, Jesus De Andrade, Milan Stanko, Sigbjørn Sangesland
Published in the SPE Bergen One Day Seminar, Bergen, Norway, 20 April, 2016
Presented by: Lucas Cantinelli Sevillano

Paper II
"Subsea Wellhead Fatigue Analysis with Focus on Thermal Conditions"
Lucas Cantinelli Sevillano, Jesus De Andrade, Milan Stanko, Sigbjørn Sangesland
Published in the ASME 35th International Conference on Ocean Offshore and Arctic Engineering, Busan, South Korea, 19-24 June, 2016
Presented by: Lucas Cantinelli Sevillano

Paper III
"Subsea Wellhead Life Cycle Fatigue Analysis and the Role of Well Temperature"
Lucas Cantinelli Sevillano, Jesus De Andrade, Sigbjørn Sangesland
SPE Drilling & Completion Journal (peer approved 26 February, 2018)

Paper IV
"Estimation of Undisturbed Geothermal Gradient in Wells from Measured Drilling Data – A Numerical Approach"
Lucas Cantinelli Sevillano, Jesus De Andrade, Sigbjørn Sangesland
Published in the ASME 36th International Conference on Ocean, Offshore and Artic Engineering, Trondheim, Norway, 25-30 June, 2017
Presented by: Lucas Cantinelli Sevillano

Additional Publications

Paper V
"Gas in Riser – The Elephant in the Room"
Dag Vavik, Lucas Cantinelli Sevillano, Sigbjørn Sangesland, Bjarte Knappen Røed
Published in the IADC/SPE Managed Pressure Drilling & Underbalanced Operations Conference & Exhibition, Rio de Janeiro, Brazil, 28–29 March, 2017
Presented by: Dag Vavik

Nomenclature

Greek Letters

α	Coefficient of thermal expansion; angle
γ	Peakedness factor
δ	Misalignment
ε	Strain; sea wave component phase angle; roughness of pipe
ζ	Wave elevation
θ	Angle
κ	Curvature
μ	Friction Coefficient
ρ	Density
σ	Stress
ω	Sea wave angular frequency; drillstring angular velocity
$\bar{\sigma}_{range}$	Stress range corrected according to meant stress level

Roman Letters

a	Coefficients in the temperature calculation matrix equation
b	Coefficients in the temperature calculation matrix equation
g	Acceleration of gravity
h	Water depth; coefficient of convective heat exchange
j	Horizontal position in the temperature calculation mesh grid
k	Stiffness; sea wave number; thickness exponent; thermal conductivity; vertical position in the temperature calculation mesh grid
n	Stress cycles; power-law fluid behavior index
q	Flow rate
r	Radius
s	Standard deviation
t	Time; thickness
u	Horizontal component of water particle velocity
v	Horizontal component of riser velocity
w	Mass flow rate; weight
z	Depth
z_{bot}	Bottom depth of a well

A	Area
C_D	Drag Coefficient
C_M	Mass Coefficient
D	Diameter
E	Young modulus
E_{mec}	Mechanical Energy
E_{the}	Thermal Energy
F	Force
H	Height; enthalpy
H_S	Significant wave height of a sea state
H_{st}	Stick-up height of the wellhead beam-proxy model
I	Moment of inertia
L	Length
N	Cycles to fail; Normal Force
P	Pressure; Power
Q	Heat exchanged
R	Bending radius
S	Stress; sea wave spectral density
T	Temperature; Torque
T_P	Spectral peak period of a sea state
V	Flow velocity
f_{ds}	Fanning’s friction factor
f_x	Mean stress influence factor used for determining $\bar{\sigma}_{range}$
f_y	Notch radius influence factor used for determining $\bar{\sigma}_{range}$
r_n	Notch radius
C_p	Heat capacity
D_f	Failure criterion
I_{MAX}	Number of columns of the finite-element-mesh grid for temperature calculation
J_{MAX}	Number of rows of the finite-element-mesh grid for temperature calculation
R_{exp}	Thermal strain ratio
Re	Reynold’s number

Abbreviations

3D	Three Dimensions

ASV	Annulus Safety Valve
BOP	Blowout Preventer
DFF	Design Fatigue Factor
DHSV	Downhole Safety Valve
DNVGL	Det Norske Veritas
EDP	Emergency Disconnect Package
FE	Finite Element
FEA	Finite-Element Analysis
GLV	Gas Lift Valve
JIP	Joint Industry Project
JONSWAP	Joint North Sea Wave Observation Project
LRP	Lower Riser Package
MD	Measured Depth
ML	Mudline
NCS	Norwegian Continental Shelf
PSA	Petroleum Safety Authority
RAO	Response Amplitude Operator
ROP	Rate of Penetration
SCF	Stress Concentration Factor
SCSSV	Surface Controlled Subsurface Safety Valve
SRA	Structural Reliability Analysis
TOB	Torque on Bit
TOC	Top of Cement
TRSV	Tubing-Retrievable Safety Valve
TVD	True Vertical Depth
WH	Wellhead
WO	Workover
WOB	Weight on Bit
XT	Xmas Tree
Subscripts	
a	Amplitude
e	Endurance limit
f	Friction

i	Inner
m	Mean
n	Nozzle
o	Outer
A	Annulus
ca	Casing annulus
cw	Casing wall
db	Drill bit
df	Drilling fluid
ds	Drillstring
fs	Formation surface
max	Maximum
pl	Pressure losses
rw	Riser wall
ut	Ultimate
yt	Yield
Superscript	
n	Step in time of the temperature calculation routine

“Ah, but a man's reach should exceed his grasp,
Or what's a heaven for?”
Robert Browning

Table of Contents

List of Figures

List of Tables

Chapter 1

Introduction

1.1 Background and Motivation

1.1.1 Well Integrity

Properly equipping the well and maintaining it to prevent leakages is at the core of the well integrity concept. This concept is defined in the NORSOK Standard D-010 (2011) as the "*Application of technical, operational and organizational solutions to reduce risk of uncontrolled release of formation fluids throughout the life cycle of a well."*

The main objective of any well integrity plan is to prevent formation fluids from flowing from one zone of the well to another or to the surface. This objective is pursued through redundancy: it is required that at least two well barriers are present in the well at any given moment. Well barriers are composed of one or more elements that when working together will prevent formation fluids from exiting the well and reaching the outside environment. As the construction of a well progresses and it assumes different roles during its life cycle, Figure 1.1 shows that the well barriers and well-barrier elements in place will change.

During drilling, the drilling fluid is the sole well-barrier element of the primary well barrier. The hydrostatic pressure exerted on the formation by the fluid column should be high enough to prevent the flow of formation fluids into the wellbore during drilling operations. In case of a kick because of insufficient pressure from the drilling fluid column, the secondary well-barrier envelope formed by casing cement, casing, wellhead (WH) and Blowout Preventer (BOP) should be able to hold the formation fluid inside the well, while actions are taken to remediate the kick.

During production, the primary and secondary barriers are changed when compared to drilling operations, because a different set of equipment is in place: tubing, production packer and the Surface Controlled Subsurface Safety Valve (SCSSV) comprise the primary well barrier, as the secondary well barrier is comprised by casing cement, casing, wellhead, tubing hanger, valves, and the production (Xmas) tree.

Well barriers need to be defined with specific criteria prior to initiation of an operation and there should be a method for testing and verifying them periodically. If a well barrier has failed, the only action that can take place in the well is to restore the failed well barrier. Alternatively, the well can be plugged and made secure or, in some cases, the well barrier can be redefined, and production continued until the failure can be corrected.

Breach of barriers and thereby loss of well integrity may lead to hazardous incidents. If not stopped in time, the situation may evolve to an accidental catastrophe. Severe examples of lost integrity in wells include the Phillips Petroleum’s Bravo blowout in 1977, the Saga Petroleum’s underground blowout in 1989, the blowout on Statoil’s Snorre platform in 2004, and British Petroleum’s Macondo blowout in the Gulf of Mexico in 2010.

Many different types of failures can lead to loss of well integrity, with varying severity. Each of the accidents previously mentioned was only possible because of a long chain of events took place. Figure 1.2 shows a Swiss cheese accident-causation model for the Macondo blowout, presented in the report on the investigation of the accident (BP Incident Investigation Team 2010).

According to the report, eight barriers were breached before the hydrocarbon influx could reach the surface and ultimately cause the destruction of the Deepwater Horizon platform. This displays the importance of continuously investigating the several different instances on which something can go wrong during or after operations in a well, to improve the knowledge available to the petroleum industry and propose safer solutions.

Failure to ensure well integrity can be very costly, and it can also threaten the environment. The Petroleum Safety Authority (PSA) initiated in 2006 a pilot study on the state of well integrity in the Norwegian Continental Shelf (NCS). The study was based on supervisory audits and input from seven operating companies, including 12 offshore facilities and 406 wells, from a total number of 2862 developments wells in the NCS. It presented a summary of the well integrity status of the selected wells at the time.

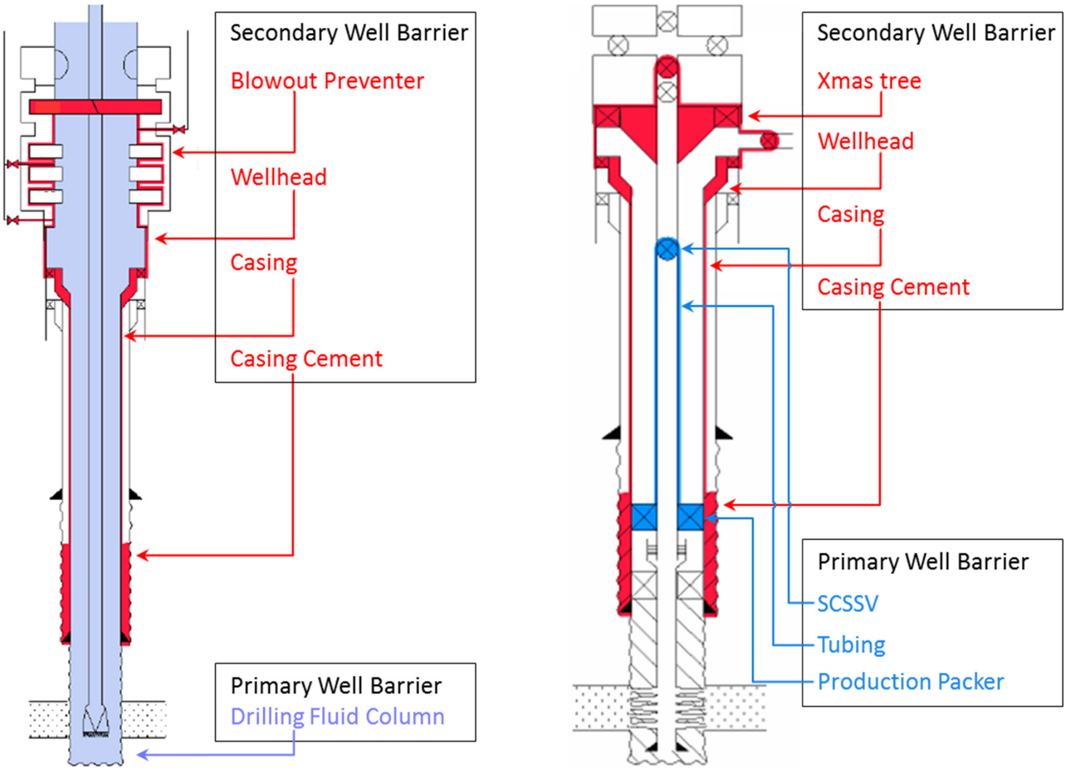

Figure 1.1 – Well-barrier schematics during different operational phases of a well’s life cycle. Left: Drilling. Right: Production. NORSOK Standard D-010 (2011). ©Norwegian Oil and Gas Association.

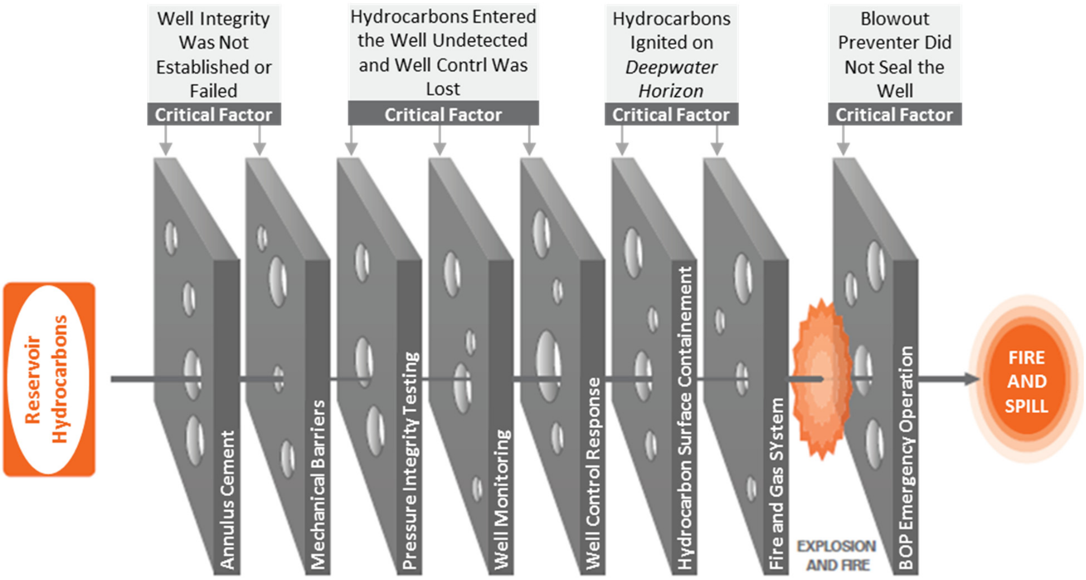

Figure 1.2 – Swiss cheese accident-causation model for the Macondo accident (BP Incident Investigation Team 2010).

Results indicated that 18% of the wells in the survey had integrity failures, issues or uncertainties. Of these, 7% were shut in because of well integrity issues. Approximately one out of seven production wells and one out of three injection wells had integrity issues (Vignes et al. 2006). Other results from the study presented by Vignes and Aadnøy (2010) showed that the tubing was to account for most of the well integrity issues (Figure 1.3).

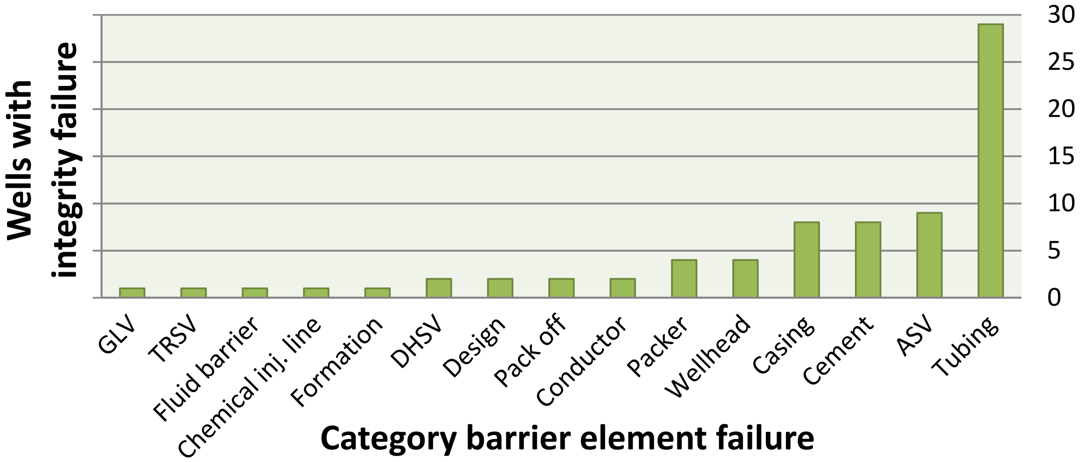

Figure 1.3 – Number of wells with integrity failure, issues, or uncertainty and category of barrier-element failure (Vignes and Aadnøy 2010). ©Society of Petroleum Engineers.

The planned life span of a typical subsea well is between 20 to 25 years. However, re-completion of a well may take place after 5 to 8 years, or even later. The need to convert production wells to injections wells, or the opposite, along with modifying wells for artificial lift have created challenges regarding well integrity. These modifications normally involve replacing the production tubing and part of the casing strings, while the main supporting structures of the well, the conductor casing and the surface casing, remain in place.

According to Figure 1.3, issues with the wellhead were responsible for four of the wells with well integrity problems. Though these are significantly fewer instances than those identified for the tubing, they still put the wellhead ahead of several of the other well-barrier elements as the leading cause for well integrity problem. As such, within the context of maintaining well integrity and extending the service lifetime of wells, Hokstad et al. (2010), in their report for the PSA, have identified the need for keeping comprehensible documentation on subsea wellhead fatigue damage.

1.1.2 Subsea Wellhead Systems

The subsea wellhead system (Figure 1.4) is a pressure-containing vessel located on the ocean floor and a permanent structural component of the well. It is installed remotely with running tools and drill pipe in stages: first the low-pressure housing, welded to the conductor, and then the high-pressure housing, welded to the surface casing.

The wellhead will then provide profiles for the subsequent casing strings to be suspended from and the means to seal them off during drilling of the well. In this way, access to the wellbore is secure in a pressure-controlled environment.

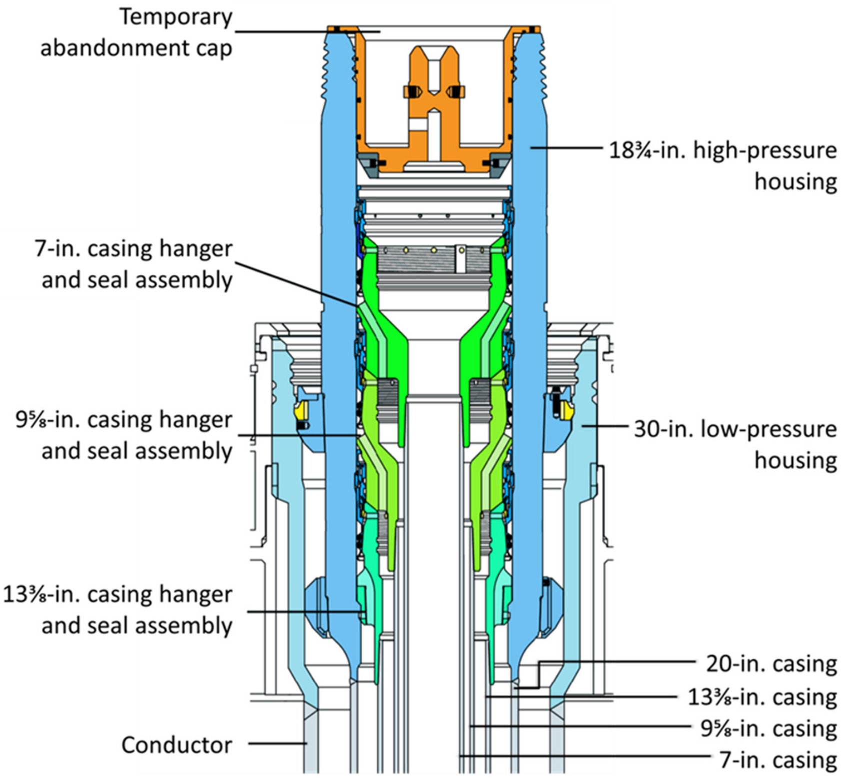

Figure 1.4 – Typical subsea wellhead system and casing program (Petrowiki 2015). ©Society of Petroleum Engineers.

As the interface between well and outside environment, the wellhead provides during drilling a profile to latch the BOP stack and drilling riser, thus acting as a foundation for the riser. During subsequent phases of the well's life cycle the BOP may be substituted by the Xmas tree.

Different mechanisms can lead to wellhead failure and critical among them is high-cycle fatigue. During drilling, completion, interventions, workovers, and plugging operations, a riser is used to connect the well to a floating rig. The rig's wave-induced motions are thus transferred to the wellhead through the riser, and the resulting time-varying loads on the wellhead lead to fatigue damage while the connection takes place.

Fatigue damage on a wellhead component was first identified as the cause of a failure in 1981, when the welded connection between the surface casing and the high-pressure housing of a well located west of the Shetland Islands failed (Hopper 1983). This incident led to the development of the modern lock-down wellhead systems (Thorogood et al. 1998). Further failures of wellheads during service were reported in the literature by Singeetham (1989), King (1990), and Milberger et al. (1991). Singeetham (1989) claimed that "The industry has experienced multiple field failures in the last 10 years, primarily at the bottom of the high-pressure housing."

Focus on the subject was renewed in 2005, when Statoil observed significant lateral movements of the BOP during drilling operations in the North Sea, which were explained by a parted conductor-casing-extension weld, caused by fatigue loading driven by drilling riser dynamic loads (Reinås et al. 2011). The reported incident showed that subsea wellheads can still fail structurally from fatigue loading by a connected drilling riser.

In that regard, Grytøyr et al. (2016) presented that current typical loading scenarios for subsea wellhead systems in the NCS can be of significantly greater magnitude than those presented as design load cases in the past (Dykes et al. 1989). Meanwhile, as Reinås et al. (2011) stated, the features of modern wellheads systems have remained similar to the universal system proposed by Dykes et al. (1989). Pertaining to wellhead design, it can also be said that while floating rigs and BOPs, and the corresponding fatigue inducing loads, increased in size (Figure 1.5), the wellhead design did not match this development (Jaiswal and Healy 2016).

Taller and heavier BOP stacks increase the rate of fatigue damage accumulation. The increased distance between the top of the BOP and the top of the wellhead creates a larger lever arm for the shear force applied by the riser at the BOP, which increases the magnitude of the time-varying bending moment transferred to the wellhead. Moreover, horizontal Xmas trees, while better-suited for operations when multiple interventions are planned during the life of the well, also incur in the same problem of larger bending moment during reentry operations, since horizontal trees must be taller than vertical ones to accommodate the tubing.

Howell et al. (2015) stated that the present awareness of the importance of fatigue loading means that newer wells are designed to achieve satisfactory fatigue lives. But, because fatigue was often not properly considered in the case of older wells, the latter have features in the wellhead system that result in locally low fatigue resistance, such as: short housing extension joints, the absence of a lockdown device, cement top-up systems, casing connectors located near the seabed and centralization and torsion resistance fins.

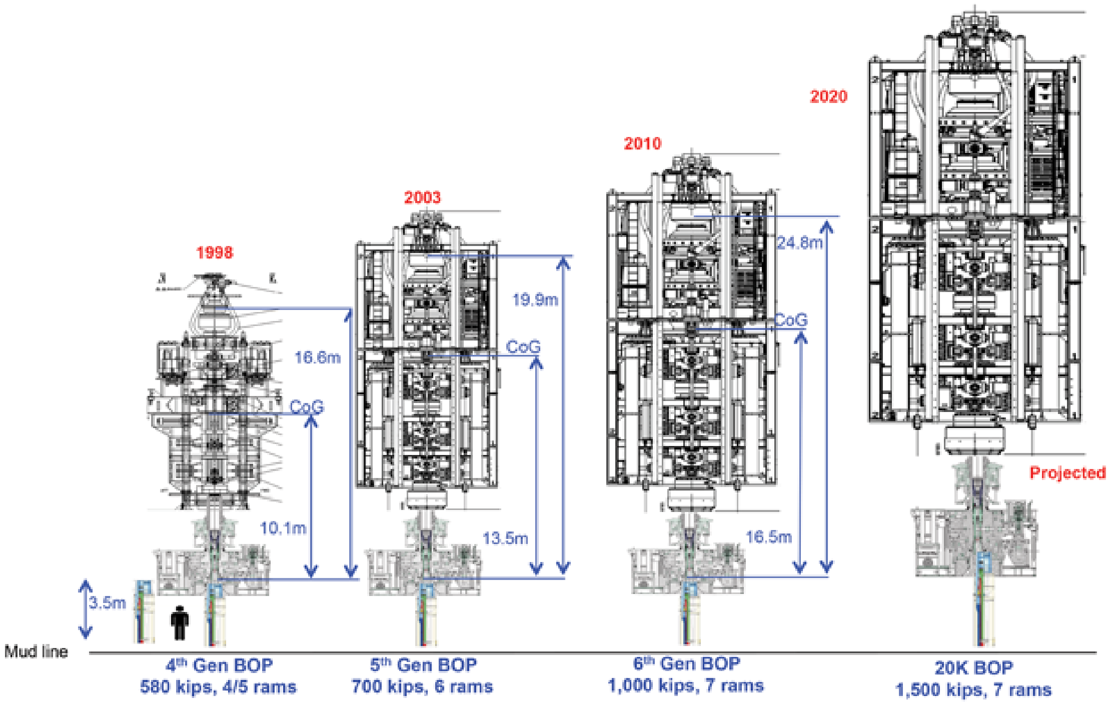

Figure 1.5 – Outline of fourth, fifth and sixth generation BOP's and the projected development (Read and Shilling 2016). ©Offshore.

1.1.3 Temperature in Wells

Among the several variables involved in planning and executing the drilling operation of an offshore well, temperature is one of the most critical ones. The cause for the change of temperature is the circulation of fluid inside the well. On its way from the drill rig into the drillstring, passing through the drill bit and returning upwards through the annulus space between drillstring and the wellbore or the riser, the fluid both cools down and heats up the well, as it transports the thermal energy from one section of the well to another. Drilling ahead ensures the fluid to be continuously exposed to new, warmer rock surfaces, thus enabling the overall heating up of the well to continue.

Most noticeably affected by the temperature distribution along the well and the riser is the drilling fluid. The fluid's rheology, density, and its ability to transport rock cuttings and ensuring bottomhole pressure will be impacted. While at the mudline level the drilling fluid may thicken excessively due to the surround cold water, the high downhole temperatures can make it too thin, leading to barite sag, well control issues and stuck pipe (Lake 2006).

Wellbore temperature distribution is also critical in the design of cementing jobs, as it affects the slurry's rheology, stability and thickening time. For instance, when cementing large casing intervals, it might be necessary to design two slurries to accommodate for the temperature difference between the bottom and the top locations (Lake 2006).

Moreover, the wellbore temperature distribution has an impact on the overall response of casing and tubing, as thermal stresses and strains develop due to temperature variance (Bourgoyne et al. 1986). This concerns the wellhead system directly since the wellhead is connected to the installed casing strings.

Previous studies on the impact of temperature on the wellhead focused on the wellhead movement caused by the thermal length variation of casing: Aasen and Aadnøy (2004) and Liang (2012) both investigated wellhead failures on which casing thermal growth and stress were suspected to be the cause, and presented analytical models used to estimate the wellhead growth and the variation in axial load. These models account for the different total lengths of the casing strings, their non-cemented lengths, the different temperature profiles of each string, and their self-weight.

However, though these developed models could be useful for verifying numerical results obtained using computer software, they could not substitute computer simulations, especially within a wellhead fatigue assessment, which requires a thoroughly detailed 3D modelling of the wellhead, which is subjected to complex geometric features and variable loading scenarios.

1.2 Thesis Objective

The main objective of the research has been the mitigation of wellhead fatigue, by studying and proposing improvements to the state of the art in subsea wellhead fatigue, and thus further developing the understanding of well integrity issues of offshore oil and gas wells.

A major part of the research work within this PhD has focused on the methodology itself, which is used when assessing the structural integrity of a subsea wellhead and the fatigue damage it is subject to throughout the well's life cycle. A minor part of the research work has also been dedicated to evaluating alternatives for mitigating wellhead fatigue.

Trends have been identified that point to the wellhead systems being exposed to longer fatigue loading: subsea wells have been drilled in continuously deeper water, to reach deeper targets, and requiring more-complex activities (Reinås 2012). In addition, subsea wells have shown an average oil recovery factor up to 15% lower when compared to wells with platform well access (Ministry of Petroleum and Energy 2010), thus creating the demand for future intervention work to extend the life of the well and exploit the production potential.

To prevent such scenarios of wellhead-fatigue failure, eleven operators in the NCS, along with Det Norske Veritas (DNVGL), took part in a joint industry project (JIP) with focus on structural well integrity. This JIP led to the publication of a report[1] on a wellhead fatigue assessment method (Reinås et al. 2011), designed to serve as a standardized analysis procedure based on the best-established practices in the industry, and later to the publication of a wellhead analysis recommended practice document DNVGL-RP-0142 (2015).

As previously stated, the released documents were based on the best-established practices in the industry. However, the temperature of the components of the well was not included in the methodology since it was deemed necessary to acquire more experience and input from the JIP

---

[1] Grytøyr, G., Hørte, T., Lem, A. I. 2011, Wellhead Fatigue Analysis Method, Technical Report. Report no.: 2011-0063, JIP Structural Well Integrity, Det Norske Veritas, Høvik, Norway. Since its publication by DNV the Wellhead Fatigue Analysis Method report has been referred to by several research studies on wellhead fatigue but is no longer made available to the general public.

partners on the matter. DNVGL-RP-0142 (2015) briefly mentions that effects of temperature for all operations and corresponding system configurations should be considered, but no specific modelling recommendations are given.

Mitigation of wellhead fatigue damage can result from a more-accurate modelling of the problem, and the scope for the JIP in structural well integrity has been the riser and the uppermost section of the well (Buchmiller et al. 2012b).

The approaches pursued have focused mostly on the measurement and modelling of the environmental loads transferred from the riser to the wellhead. While some works (Kebadze et al. 2017; Nilsen et al. 2017) have presented instrumentation and monitoring campaigns over riser and subsea stack to accurately measure the environmental loads, other works (Russo et al. 2016; Walker et al. 2017) have shown how field data can be used to validate and calibrate models used for predicting wellhead fatigue.

Jaiswal et al. (2016) and Healy et al. (2017) have investigated the structural response of the wellhead itself under different numeric-modelling approaches, for non-rigid and rigid locked models respectively, providing guidelines for simplifying the analysis while maintaining acceptable accuracy. Kuzmichev et al. (2017) also present comparisons between simplified and detailed models of the wellhead taking into consideration how stresses develop at different spots.

The industry's efforts for a better modeling of wellhead fatigue and ensuing awareness of the challenges represented by lower available fatigue capacity have been complemented by the research and development of technical solutions to decrease the fatigue damage inducing loading on the wellhead. On that front, TechnipFMC has developed a reactive flex-joint (Rørgård et al. 2017) that can reduce dynamic bending moments transferred from the riser to the wellhead during drilling and workover operations.

An alternative solution is to use anchors and ropes to tether the BOP, restraining the motion and decreasing the resulting dynamic loading at the subsea stack level (2H Offshore 2017). Because of its novelty and lack of published technical works at the time of the writing of this thesis, the merits of the latter technical solutions were also made part of the investigation presented in this thesis.

Thus, the doctoral research has contributed to the body of work in wellhead fatigue assessment methodology by tackling an important aspect of well's operations not previously considered.

More specifically, the thesis has investigated the effects on wellhead fatigue that might arise from the temperature variations that occur during the different operations that are carried out in a well, either during drilling or any other operation that requires a connection to a floating rig through a riser. In addition to that, the research conducted has also investigated one of the technical solutions proposed for mitigating wellhead fatigue.

1.3 Thesis Content

Chapter 1 gives an overview of the motivation and goals pursued with this thesis.

Chapter 2 briefly presents topics on the fatigue failure mechanism that are pertinent to the study conducted in this thesis.

Chapter 3 summarizes a conventional methodology employed for estimating the fatigue damage on the wellhead. It briefly presents how the method is structured, what considerations must be made regarding creating the models that will represent the wellhead and the riser, how to link the intermediary results of different analyses, and how to present the final fatigue results.

Chapter 4 describes how the thesis proposes for the temperature distribution of the well to be incorporated into a wellhead fatigue assessment methodology, and it presents the considerations made for each part of the methodology.

Chapter 5 presents the initial study conducted to assess the impact of the well-temperature distribution on the analyses performed within a wellhead fatigue damage assessment, and how the effect of temperature can be influenced by the non-cemented length of the surface casing.

Chapter 6 applies the findings from previous chapters and expands the scope of the fatigue assessment. A broader picture of the impact of temperature in the wellhead fatigue assessment during the life cycle of a well is presented, along with considerations on how the allowable riser connection time of future well operations may be affected.

Chapter 7 takes a closer look into how the temperature distributions of casing strings and cement columns are affecting the mechanical response of the wellhead components. A relation between the thermal strain of the tubular components and the fatigue-damage rates estimated for the wellhead fatigue hot spots is proposed to make it possible to expand the results obtained by a limited number of simulations to a wider range of temperature scenarios.

Chapter 8 presents an initial investigation of a technical solution proposed for mitigating wellhead fatigue by restraining the motions of the subsea stack using a BOP tethering system. The modelling of the system is presented, along with the results in fatigue capacity spent for different tethering systems.

Chapter 9 presents the conclusions of the thesis, along with recommendations made for future work.

Annex A presents in greater details how the properties of the wellhead beam-proxy model, which couples the riser global response analysis to the wellhead local response analysis, are obtained.

Annex B presents the well thermal model developed and used in this thesis for calculating the temperature distribution of the well during the simulated operations.

Annex C presents additional graphs created for Chapters 5, 6 and 7 of this thesis.

Annexes D, E, F, and G present Papers I II, III and IV, respectively.

Chapter 2

Topics on High-Cycle Fatigue

2.1 Introduction

One of the tests available to determine a material's ultimate strength (S_{ut}) and if it can withstand the maximum stress it will be subject to during operation involves the application of a gradually increasing force until failure occurs. Figure 2.1 shows the typical results of such tests for metals: yield stress (S_{yt}) refers to the maximum applicable stress for which the test body has suffered a reversible deformation, while S_{ut} is the maximum observed stress as the body is continuously deformed before failure occurs.

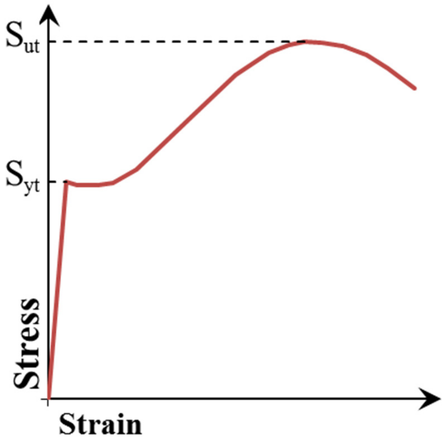

Figure 2.1 – Typical tension strain curve for metal.

The static nature of this test approximates actual operating conditions, but it is often the case that failure occurs under fluctuating stresses that can be very far below the ultimate strength. Because this failure happens after a very large repetition of these fluctuating stresses, this mechanism has been denominated fatigue.

The process starts with a small crack, usually at a point of discontinuity in the material, such as a change in cross section. Once initiated, the crack increases progressively faster, as the stress-concentration effect increases. The area bearing the load becomes smaller, until the stresses on the affected area become too big and the material suddenly fails.

Static failures occur at stress levels greater than the yield strength of the material, and therefore large deflections are developed. These deflections give visible warning and allow for the fracture of the material to be avoided. However, since they develop under relatively lower stress levels, the cracks initiated because of fatigue loading are much harder to be detected.

2.2 S-N Curves

Determining the strength of materials under fatigue loading involves subjecting test specimens to repeated stress cycles of specified amplitudes until failures occurs. The number of required cycles, *N*, for fatigue failure to occur under a given stress amplitude, *S*, obtained from experiments is recorded on an S-N diagram.

Because of the spread in the test results, the design S-N curve is given as the mean curve subtracted by the standard deviation, *s*, multiplied by a factor based on the number of tests performed (Figure 2.2); the value of this factor approaches 2 as the total number of tests performed increases beyond 100 (DNVGL-RP-C203 2016).

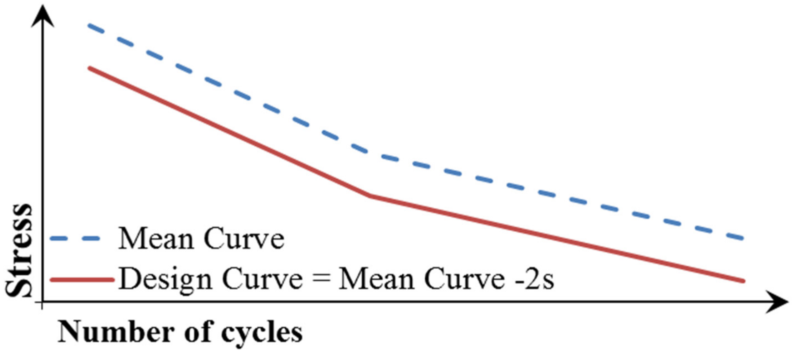

Figure 2.2 – Schematic illustration of a bi-linear S-N curve (DNVGL-RP-C203 2016).

Typical S-N curves have the form presented in Equation 2.1, where *N* is the number of cycles for failure to occur under the stress range ΔS, and *C* and *m* are constants. On a log-log scale (Figure 2.2) S-N curves become linear and assume the form shown in Equation 2.2.

$$\mathrm{N}(\Delta S)^m = \mathrm{C}$$ **Equation 2.1**

$$\log N = \log C - m \log \Delta S$$ **Equation 2.2**

Figure 2.3 presents a typical S-N diagram for steels. Steels, in particular, present an endurance limit, or fatigue limit, S_e. Stress amplitudes below S_e do not lead to fatigue failure, independent of the number of cycles.

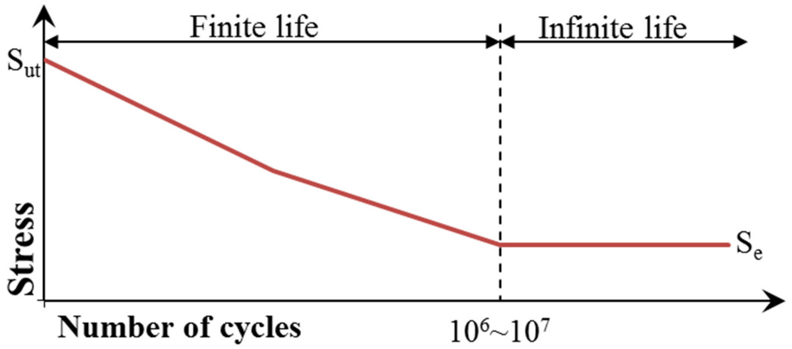

Figure 2.3 – Typical S-N diagram for steels.

S-N curves are specific to each component of the wellhead system. Recommended practices such as DNVGL-RP-C203 (2016) make available a wide array of S-N curves for different hot spots, presenting the conditions for which each curve can be applied to. A welded joint hot spot, for instance, can be classified according to its location on the weld and the weld's geometry. Examples of classification and the corresponding curves are presented in Table 2.1.

For welded joints strength towards fatigue is to some extent dependent on wall thickness. When the thickness of the component is larger than the reference thickness, a correction must be made to the S-N curves, as presented by Equation 2.3, where t is the plate thickness, t_{ref} is the reference thickness, and k is the thickness exponent for the curve.

$$\log N = \log C - m \log\left(\Delta S \left(\frac{t}{t_{ref}}\right)^{k}\right)$$ **Equation 2.3**

Table 2.1 also indicates that it might be necessary to correct the stress ranges using a stress concentration factor (SCF), due to the local geometry of a component. For welds, the SCF may account for stress magnification due to misalignment of two adjacent joints (*e.g.* due to fabrication tolerances at the weld). Equation 2.4 presents the formulation of the SCF. D_o is the outer diameter of the joint, t_{joint} is the thickness of the joint, and δ_{max} is the maximum allowable misalignment.

$$SCF = 1 + \frac{3 \cdot \delta_{max}}{t_{pipe}} \cdot e^{-\sqrt{\frac{t_{pipe}}{D_o}}}$$ **Equation 2.4**

Table 2.1 – Classification of welds (DNVGL-RP-C203 2016).

Welding	Geometry and hot spot	Misalignment, δ	S-N curve	Thickness exponent, k	SCF
Single side	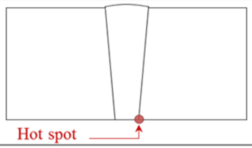	$\delta \leq min(0{,}15t; 3\ mm)$	F1	0.00	1.0
		$\delta > min(0{,}15t; 3\ mm)$	F3	0.00	1.0
Single side on backing	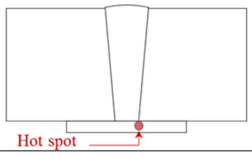	$\delta \leq min(0{,}1t; 2\ mm)$	F	0.00	1.0
		$\delta > min(0{,}1t; 2\ mm)$	F1	0.00	1.0
Single side	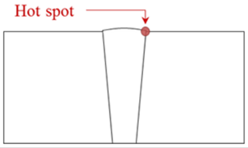		D	0.15	Equation 2.4
Double side	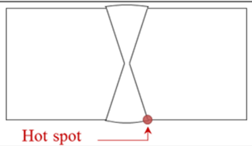		D	0.15	Equation 2.4

2.3 Cumulative Fatigue Damage

A specimen subject to an alternating stress S_1 for n_1 cycles and an alternating stress S_2 for n_2 cycles can still fail because of fatigue, even though n_1 and n_2 are lower than the corresponding N_1 and N_2 cycles determined from an S-N diagram. It becomes clear that each reversed stress cycle damages the specimen, and the damage adds up leading to fatigue failure.

This problem has not been solved completely (Shigley and Mischke 1989). But the most common method for calculating cumulative fatigue damage, despite it not consistently agreeing with experiments, is the Miner-Palmgren summation procedure, or Miner's rule.

Miner's rule states that under a complex loading, in which the stress range ΔS_i contributes with n_i cycles, fatigue failure occurs when:

$$\sum_{i=1}^{k} \frac{n_i}{N_i} = D_f$$

Equation 2.5

where N_i is the number of cycles to failure corresponding to ΔS_i, and D_f is the failure criterion.

The parameter D_f is experimentally found between 0.7 and 2.2, but usually assumed to be 1 for design purposes (Shigley and Mischke 1989). A design fatigue factor (DFF) is often applied to reduce the probability of failure (DNVGL-RP-C203 2016). The DFF is dependent on the consequences of failure and the availability for inspection. The failure criterion then becomes:

$$\sum_{i=1}^{k} \frac{n_i}{N_i} = \frac{1}{DFF}$$

Equation 2.6

2.4 Mean Stress

Figure 2.4 presents a stress-time history with typically used notations. The figure defines the maximum stress, σ_{max}, minimum stress, σ_{min}, mean stress, σ_{mean}, stress amplitude, σ_a, and stress range, σ_{range}. Moving from point A to B, and then to C the time-varying stress has completed two reversals, or one cycle. The identified stress range is used together with an S-N curve to determine the number of cycles to failure, and it may also be referred to as cyclic stress.

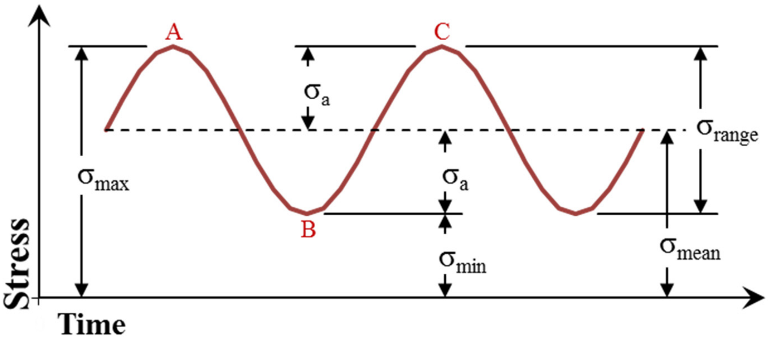

Figure 2.4 – Stress-time diagram and notation used.

Often, stress-time histories will present situations on which the mean stress level is different than zero. The mean stress, however, is not the same as the steady, or static, stress. The steady stress is caused by a fixed load or preload and is generally independent of the time-varying load.

The value of the mean stress can heavily influence fatigue behavior, and it has been usually observed that tensile mean stresses are detrimental to fatigue life, while compressive mean stresses are beneficial (Stephens et al. 2001), as presented in Figure 2.5.

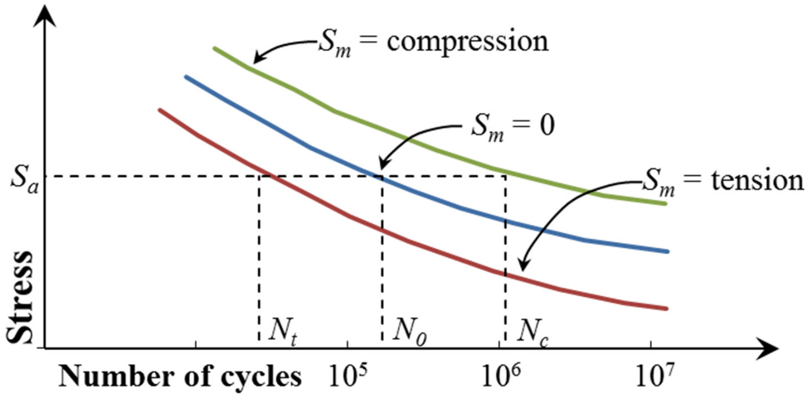

Figure 2.5 – Effect of mean stress in fatigue life (Stephens et al. 2001).

In Figure 2.5 the compressive mean stress moved the design curve up, while the tensile stress moved it down, respectively increasing and decreasing the allowable cycles, *N*, for a given alternating stress, S_a. This effect of the mean stress can be quantified according to the criteria of failure used (Shigley and Mischke 1989).

Figure 2.6 presents the modified Goodman, the Soderberg, and the Gerber criteria, along with yielding. Any point on or above the lines indicate failure, according to the corresponding criteria. For zero mean stress, fatigue failure occurs above S_e. If the mean stress increases, the threshold for alternating stress decreases. The equation forms for these criteria can be found in Equation 2.7, Equation 2.8 and Equation 2.9.

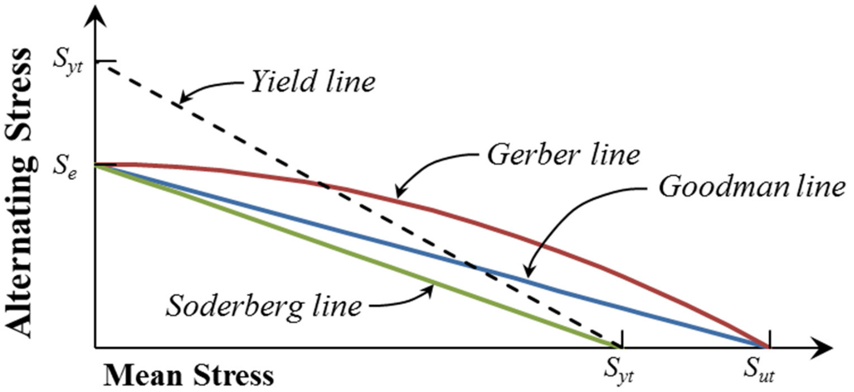

Figure 2.6 – Fatigue diagram showing various criteria of failure (Shigley and Mischke 1989).

Goodman line:

$$\frac{S_a}{S_e} + \frac{S_m}{S_{ut}} = 1 \qquad \textbf{Equation 2.7}$$

Soderberg line:

$$\frac{S_a}{S_e} + \frac{S_m}{S_{yt}} = 1 \qquad \textbf{Equation 2.8}$$

Gerber line:

$$\frac{S_a}{S_e} + \left(\frac{S_m}{S_{ut}}\right)^2 = 1 \qquad \textbf{Equation 2.9}$$

Neither the fatigue diagram nor the equations explicitly state the effects of compressive mean stresses. But since compressive mean stresses can increase the fatigue strength (Sines 1955, Stephens et al. 2001), the Goodman and Soderberg relations can be extrapolated to the compressive mean stress region, while the Gerber relation will erroneously predict a detrimental effect.

A possible problem faced when employing the previous equations is the unavailability of the mean stress developed on the tests specimens used to create the S-N curve. An alternative method to account for the effect of mean stress is provided by DNVGL-RP-C203 (2016). It employs the ratio between the developed mean stresses and the stress ranges.

The stress range to be entered to the S-N curves provided by the DNVGL-RP-C203 (2016) can be derived as:

$$\Delta\bar{\sigma}_{range} = \Delta\sigma_{range}\frac{f_m}{f_x} \qquad \textbf{Equation 2.10}$$

where $\Delta\sigma_{range}$ is the local stress range at the considered hot spot, f_m is a factor considering the mean stress influence and f_x is a factor considering the notch radius.

The design S-N curves provided for base material by DNVGL-RP-C203 (2016) are developed for a mean stress/stress range ratio equal to 0.5. Whenever a component is subjected to higher mean stresses, this is accounted for by calculating the factor f_m from the following equation:

$$f_m = \frac{1 + 0.5\dfrac{\sigma_m}{\Delta\sigma_{range}}}{1.25} \qquad \textbf{Equation 2.11}$$

The notch factor f_x can be obtained as a function of the notch radius r_n (Equation 2.12) for steels with tensile strength of 724 MPa and below, otherwise it should be set equal to 1.

$$f_x = \begin{cases} 1.37 & if\ r_n \le 1mm \\ 10^{0.136[1-\log(r_n)]} & if\ 1mm < r_n \le 10mm \\ 1.0 & if\ r_n > 10mm \end{cases} \qquad \textbf{Equation 2.12}$$

2.4.1 Mean Stress in Welds

In the welding process of steel structures, metal is heated up, melted, and then cooled down. During the cooling phase, the shrinkage of the weld metal is restricted by the surrounding base metal, thus developing tensile residual stress, which increases in magnitude until room temperature is reached.

This residual stress in welds has a detrimental effect on their fatigue capacity. It reduces the fatigue strength and eliminates almost completely the effect of mean stresses (Fricke 2005). For practical applications, is often assumed that the magnitude of the maximum tensile residual stress in a weld in the as-welded condition is equal to the yield strength of the weld or parent material (Leggatt 2007).

The assessment of fatigue damage in a welded component becomes simpler, as no corrections for the mean stress are necessary, and the analyst must only account for the range of cyclic stresses. In that regard, API RP 2RD (2006) states: “Unlike parent material S-N curves, S-N curves for welded joints are in general, not influenced by mean stress, because the bulk of the fatigue life is spent in the crack propagation phase.”

Moreover, in DNVGL-RP-C203 (2016) it reads: “The procedure for the fatigue analysis is based on the assumption that it is only necessary to consider the ranges of cyclic stresses in determining the fatigue endurance (*i.e.* mean stresses are neglected for fatigue assessment of welded connections due to presence of residual stresses).”

2.5 Effect of Temperature

The temperature of the operating environment could potentially influence fatigue failure by altering the properties of the materials. Shigley and Mischke (1989), when discussing temperature effects, used data from tables made available by Gale and Totemeir (1983) to show that the tensile ultimate strength and the yield strength of steels are not a strong function of temperature, unless temperatures become significantly high, beyond 300°C.

Conversely, the induced thermal length variation if restrained creates either tensile or compressive stresses, thus altering the value of the mean stress at a given location, as seen in Figure 2.7. Assuming the figure presents the stress levels on a single member, fixed at both ends, and subject to a constant variation of temperature, ΔT, along its length, then the variation in stress due to temperature could be calculated by the equation in place, where α is the coefficient of linear thermal expansion and E is the Young’s module.

This thermal stress when superimposed into the mean stress shifts the parental S-N curve and potentially leads to either a longer fatigue life, in the case of a compressive stress, or to a shorter life, in the case of a tensioning stress (Stephens et al. 2001). In that sense, even small temperature deviations could influence the estimated fatigue damage of equipment.

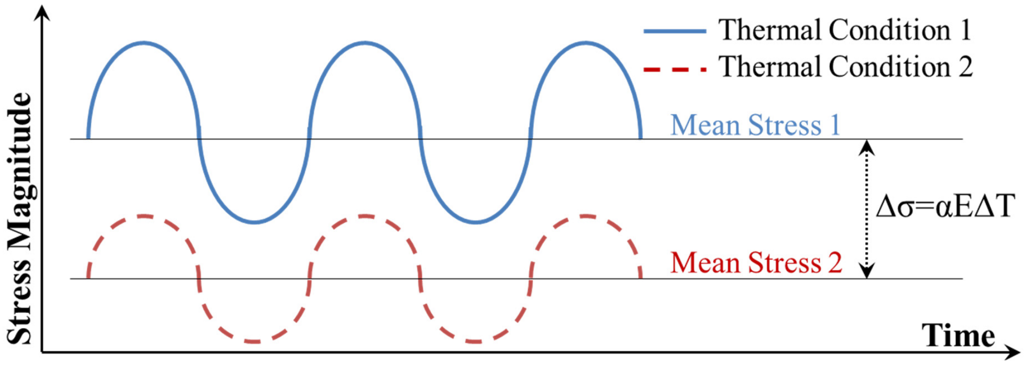

Figure 2.7 – Effect of temperature on mean stress magnitude.

However, the subsea wellhead is a structural member composed of multiple components, and the interactions of said components may not enable a straightforward relation between variation of temperature and variation of stress. Especially when considering that estimating fatigue damage also requires to calculate the stress ranges, or cyclic stresses.

The cyclic stresses on the wellhead are created by the load applied at the top of the wellhead system by the riser connection. This load is shared among the high- and low-pressure housings. Consequently, a structural analysis of the whole system is necessary to determine how much of the applied load is transferred to the surface casing and to the conductor.

The thermally-induced interactions among the wellhead's interdependent components could alter the way the load is shared between said components, and the resulting stresses. Figure 2.8 presents the cyclic stresses of the two cases previously shown in Figure 2.7. In the figure, the emphasized variation of cyclic stress cannot be solely explained by the variation of temperature.

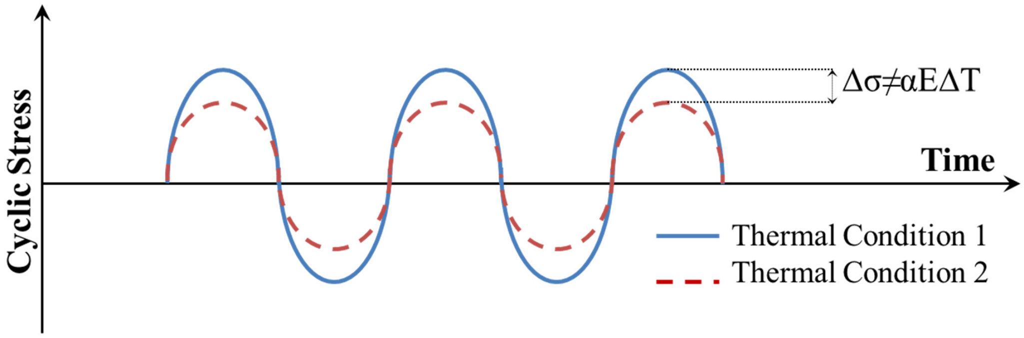

Figure 2.8 – Effect of temperature on cyclic stress magnitude.

Chapter 3

The Conventional Wellhead Fatigue Assessment

3.1 Modelling Philosophy

The wellhead fatigue assessment is a complex and multidisciplinary endeavor, which requires structural, hydrodynamic, geotechnical, metocean and operational knowledge to be carried out. Heat transfer, as well, could be included in this list, as this thesis will make a case for.

The structure of the wellhead is a complex one, with several interacting components, going through changes as components are either added or removed during the process of drilling a well. The material processes responsible for the formation of the crack that leads to failure are dependent on the design of the structure and how it internally distributes the loading it is subjected to, controlling the local stress levels within itself. The damage will inevitably be concentrated to certain structural features of the wellhead, often referred to as fatigue hot spots.

Given that the wellhead system interacts with the surrounding soil it has been cemented into, a wellhead-soil interface must be included in the analysis. Eventual template structure and the corresponding additional boundary conditions further increase the complexity of the analysis of the system.

In a subsea wellhead system, the fatigue loading takes place during the processes of drilling, completion, interventions, workovers, plugging, and other activities conducted from a floating rig with a riser being used as a temporal conduit to the well. The motions of vessel and riser are transmitted to the wellhead, and the dynamic loading will cause fatigue damage, as the riser connection lasts.

It is not possible to inspect a subsea wellhead for fatigue fractures given the lack of access to the fatigue hot spots while the wellhead is operational. Determining if, or when, those hot spots will fail depends on properly estimating the accumulated loading cycle history and the corresponding fatigue damage. Other technical systems in offshore applications also face the same challenges. In the assessment of fatigue of offshore structures, a DFF of 10 is recommended for safety critical components that cannot be inspected (NORSOK Standard N-004 2004, API RP 2RD 2006).

As a result of the efforts of JIP on Structural Well Integrity, the then published methodology[2] was designed to serve as a standardized procedure based on the best-established practices in the industry and offer a consistent modelling approach to wellhead-fatigue analysis, thus ensuring comparability of results. The main focus of the calculations presented then was on establishing the relations between environmental loading at the wellhead and the resulting stresses

---

[2] See Footnote 1. Section 1.2 - Thesis Objective, page 7.

at the hot spots located within the upper part of the well, by way of a hybrid decoupled beam and 3D analysis (Buchmiller et al. 2012).

The aforementioned approach is similar to the decoupled approach described in ISO 13628-2 (2009). However, in the hybrid approach there is a link between the riser beam model and the wellhead 3D model, since the boundary conditions applied to the riser model at the wellhead datum are created based on results obtained when using the wellhead 3D model.

Figure 3.1, presents the workflow for this hybrid decoupled approach and the following sections outline this approach. DNVGL-RP-0142 (2015) provides examples of flowcharts for different modelling approaches, including that of the coupled analysis with a fully integrated riser and wellhead model.

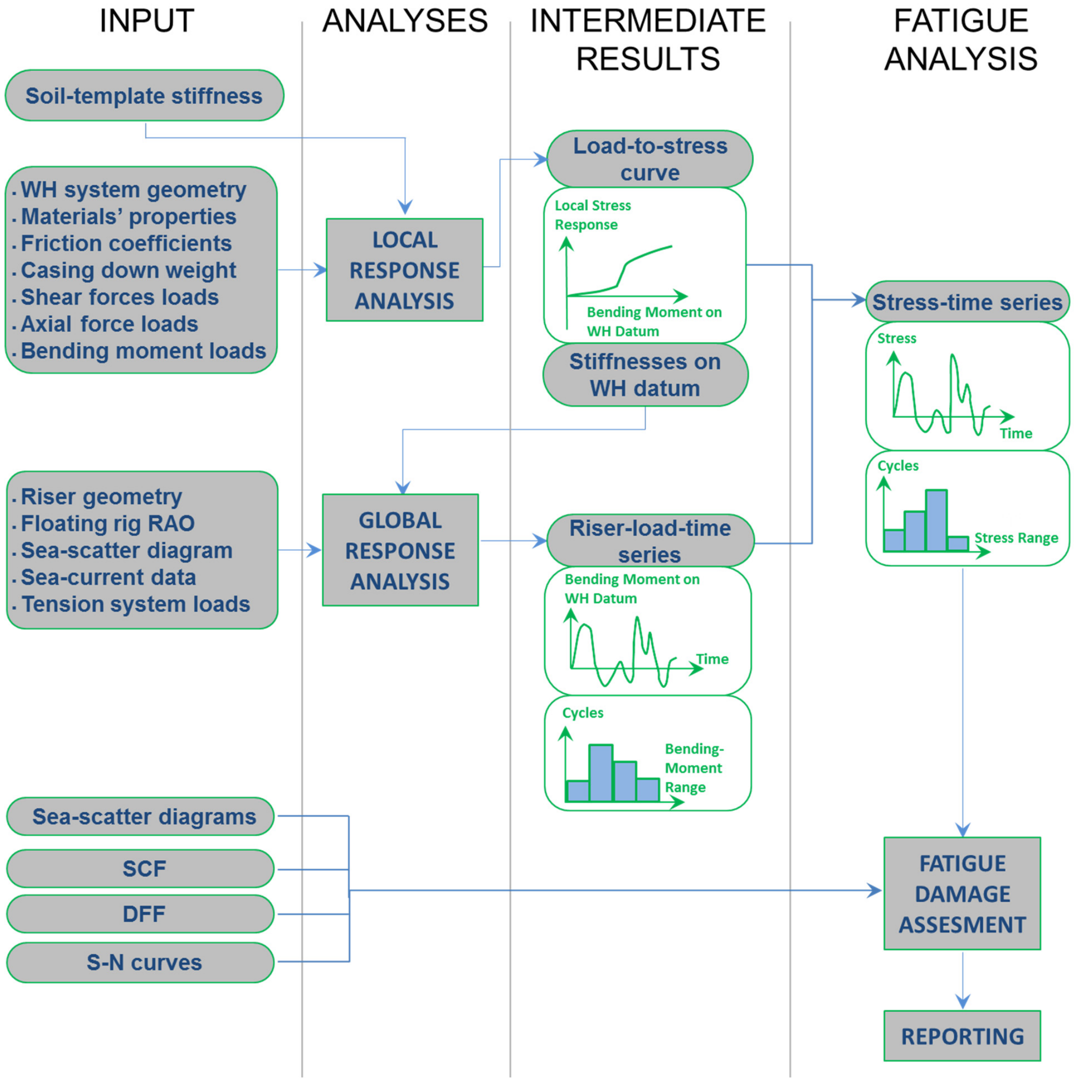

Figure 3.1 – Wellhead fatigue assessment methodology flowchart (Reinås et al. 2011). ©American Society of Mechanical Engineers.

3.2 Local Response Analysis

The wellhead system is the foundation of the riser. As such, it is subject to external loading created by the response of the riser and the drilling rig to waves and current forces. These external loads can be static and cyclic combinations of bending and tension/compression. The local response analysis consists of calculating the structural response of the wellhead system to the range of loading it is expected to be subject to during drilling and other well activities.

As discussed by Valka and Fowler (1985) on the behavior of a conventional wellhead system, the shear force, tension force and bending moment applied to the top of the wellhead by the riser are reacted through the wellhead body and into the conductor and surface casing; the reactions by the other casing strings can be neglected. The load transfer mechanism in the system is complex and dependent on different factors:

- Presence of a template. A rigid template will exert a significant reactive shear on the subsea wellhead system, thus reducing the effective bending moments on the wellhead.
- Soil's shear strength. The shear strength of the soil will shift the location of the effective reactions of the conductor. For a relatively strong soil, the location of the reaction will be near the mudline, while for a weak soil the reaction point will be at a lower location and, consequently, the maximum internal loads in the wellhead/casing string assemblies will be higher at the lowered reaction point.
- Relative rigidity of the high-pressure housing and low-pressure housing load paths, as the load is transmitted from the top of the high-pressure housing to the other components of the wellhead assembly and shared between the surface casing and the conductor below it.

The top of cement (TOC) between the conductor and the surface casing heavily influences the load path at the wellhead and the resulting estimated fatigue life (Britton and Henderson 1988, Reinås 2012). A full cement return locks the high-pressure housing to the low-pressure housing and is the best possible load path for the wellhead assembly.

However, cement slurry losses to the formation or failure of bonding between cement and steel can lower the "effective" TOC. This cement shortfall may be problematic when the TOC is found just below the high-pressure housing and low-pressure housing region (Britton and Henderson 1988), as it does not allow for proper load sharing between the housings, and the loads at the wellhead datum go directly to the surface casing.

Conversely, a deep TOC level enables the high-pressure housing to pivot about the suspension shoulder until loads become great enough that the high-pressure housing touches the low-pressure housing at a lower contact point. This two-point contact lockdown mechanism enables improved load sharing between the housings and lowers the loads in the surface casing.

In any event, the bending moment transfer within the high-pressure housing can be idealized as a cantilever beam (Valka and Fowler 1985). Figure 3.2 presents a beam with opposing lateral supports at different depths along the low-pressure housing. The increasing moment causes the beam to bend and its boundary conditions to change, as the beam first contacts the upper lateral supports and then the lower lateral support.

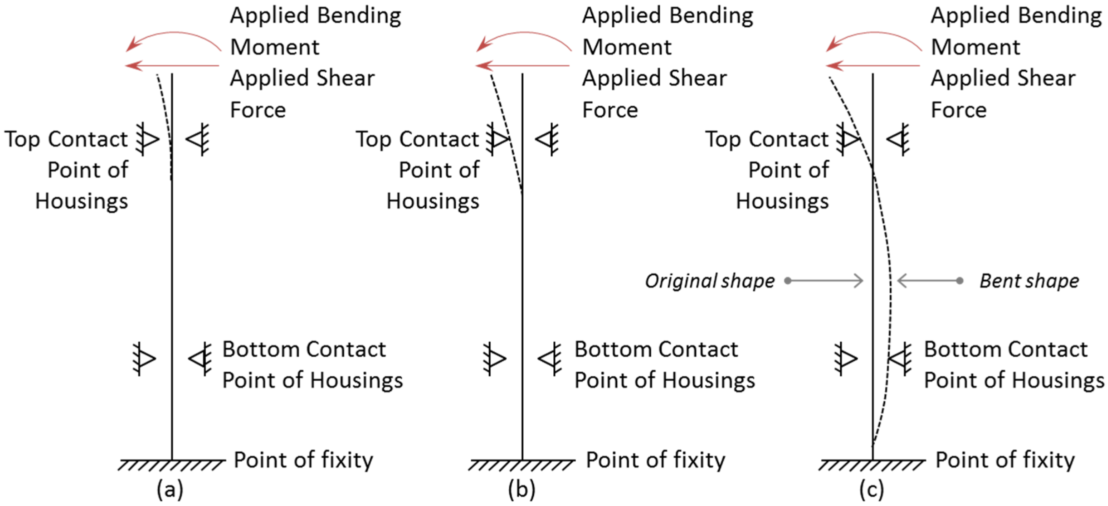

Figure 3.2 – Interactions of housings of the wellhead as a cantilever beam and contact points during bending. A: No contact established. B: Contact at top support. C: Contact at both supports. Valka and Fowler (1985). ©Offshore Technology Conference.

The bending moment carried by the high-pressure housing and the surface casing is dependent on several factors, such as:

- The thickness of the casing strings.
- The magnitude of the load applied.
- The vertical distance between the supports.
- The clearance between supports and the wellhead body.
- The structurally effective TOC (point of fixity).

Taking the radial gaps between the supports and the beam as an example, smaller clearances enable contact and load sharing among the housings to be established under a smaller bending moment load, thus decreasing the stresses developed when the wellhead is subject to larger loads.

Closely examining a section of surface casing, Reinås (2012) presented the linear relation between the stress on the pipe due to bending and the curvature, κ, reproduced here by Figure 3.3.

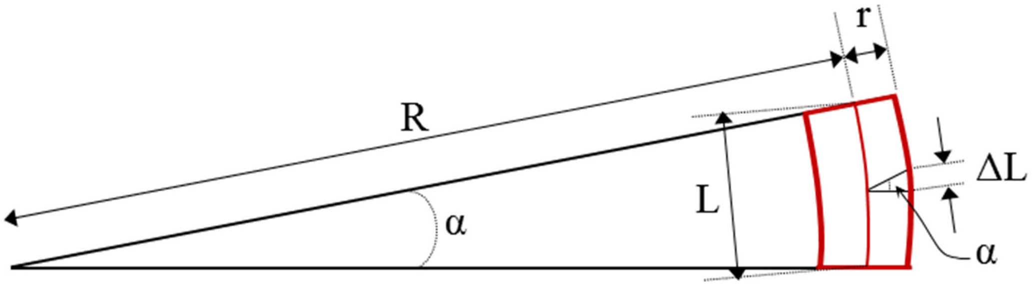

Figure 3.3 – Pipe section in bending and notation used (Reinås 2012).

During the application of the bending moment the pipe section will assume a configuration similar to the one demonstrated in Figure 3.3, where α is the angle associated with the casing section, L is the casing section original length, R is the bending radius of the neutral axis, ΔL is the elongation of the outer wall, and r is the pipe section radius. Based on the geometry, and assuming that α is small, the following equations are obtained:

$$\alpha = \frac{\mathrm{L}}{R}$$ **Equation 3.1**

$$\alpha = \frac{\Delta \mathrm{L}}{r}$$ **Equation 3.2**

The strain, ε, in the outer fiber, and consequently the stress, σ, thus can be written as:

$$\varepsilon = \frac{\Delta \mathrm{L}}{L} = \frac{\alpha \cdot r}{\alpha \cdot R} \rightarrow \varepsilon = \frac{r}{R}$$ **Equation 3.3**

$$\sigma = \mathrm{E} \cdot \varepsilon = \mathrm{E}\frac{r}{R} = E \cdot r \cdot \frac{1}{R} = E \cdot r \cdot \kappa \rightarrow \sigma = E \cdot r \cdot \kappa$$ **Equation 3.4**

Based on this link between bending stresses and curvature, Valka and Fowler (1985) draw their conclusions regarding the impact of the vertical distance between supports and the elevation of the point of fixity on the stresses at the wellhead.

It can be observed in Figure 3.4 that a larger non-cemented length brings the point of fixity further down the well, decreasing the radius of curvature of the beam and consequently the stresses on the beam. Likewise, increasing the vertical distance between the contact points reduces the angle of rotation at both the contact points and, consequently, the curvature of the beam decreases.

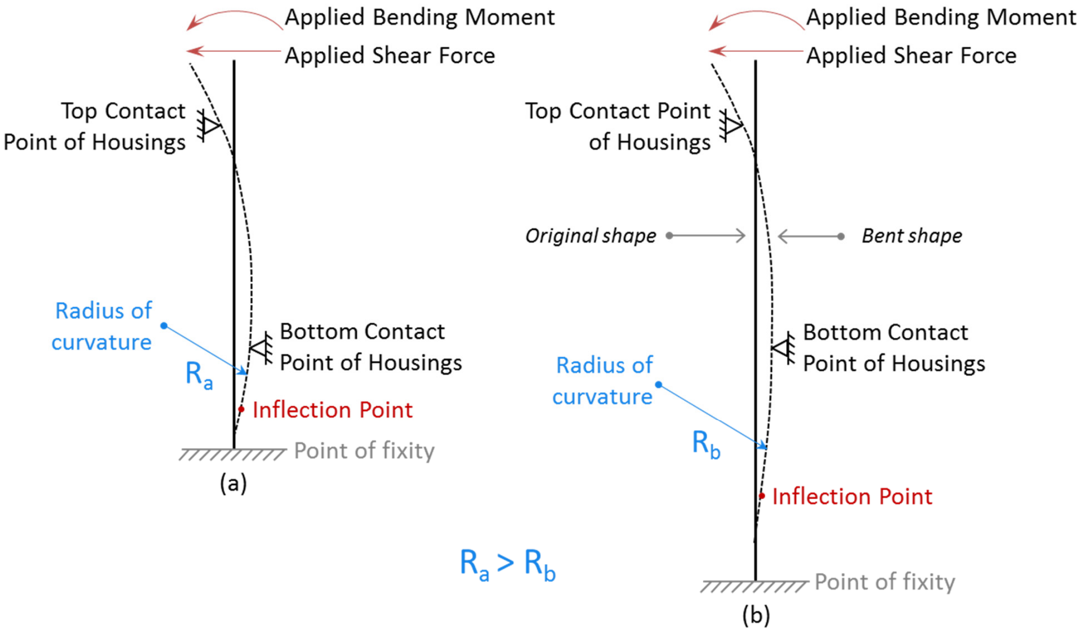

Figure 3.4 – Point of fixity and corresponding radius of curvature in beam (Valka and Fowler 1985). ©Offshore Technology Conference.

3.2.1 Wellhead 3D Model

A detailed 3D model of the wellhead is required for properly investigating the stresses at fatigue hot spots, and the quasi-static solution is obtained with a stepwise increasing unit load. The subsea wellhead model (Figure 3.5) used for the local response analysis is a fully parametric 3D, 180 degrees symmetric finite-element (FE) model and is meant only for fatigue calculation using the S-N approach.

Because the 3D model is not intended for any other structural evaluations than fatigue, it enables simplifications. The fatigue hot spots and the components important for the load transfer through the system must be modelled and meshed accurately, but the remaining of the wellhead components only are intended to behave structurally correct (Reinås 2012). In that regard, the wellhead components and casing sections with stress point of interest are modelled using solid type of elements[3], while the lower part of the model is used beam type of elements[4].

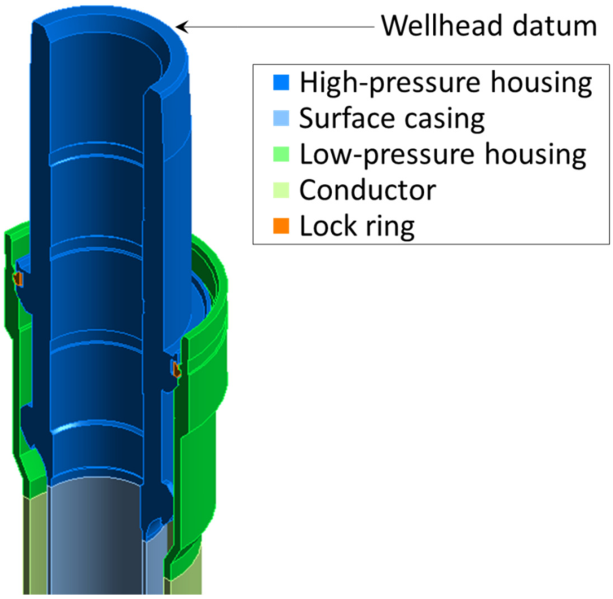

Figure 3.5 – Wellhead model used in the local response analysis.

The casing strings connected to the wellhead can surpass hundreds of meters of length. However, common practice dictates these tubular components need only to extend to a certain depth in the FE model, so the stresses on the wellhead fatigue hot spots are not influenced by the model termination. This approach decreases the computational time of the analysis without deteriorating the quality of the end results. A rule of the thumb suggested in the JIP report is that the model be terminated about 50 m below the mudline (ML), or 20 m below the lowest relevant hot spot.

---

[3] Solid elements are 3D elements made up of up to 20 nodes. Each node has three degrees of freedoms: translations in the nodal x, y, and z directions. Displacements for details between nodes usually follow a quadratic behavior.

[4] Beam elements are linear elements with 2 nodes and six degrees of freedom at each node: translation in x, y and z directions and rotation in x, y and z. A cross section must be defined for them.

Terminating the length of the tubular components of model at certain depth makes necessary to include the effects of the weight of its abbreviated section by way of an additional load at the lower boundary of the model. Together with the external loading and casing down weight, the wellhead system model must consider the force reaction of the soil surrounding it. Non-linear springs connected to the nodes of the elements facing the soil are used for that purpose.

During well construction, the wellhead can assume different configurations, as deeper sections of the well are reached, and additional casing strings are suspended on the wellhead. The wellhead fatigue assessment begins with the conductor and the surface casing in place, after the BOP and riser have been connected to the wellhead. This is one of the configurations that must be modelled for fatigue damage.

Following a typical casing program, when the 13⅜-in. and 9⅝-in. casing strings are installed, additional wellhead FE models must be created with the corresponding casing hangers, tubulars and terminated length down weight. An additional model with the corresponding down weight of the 7-in. liner is also necessary. In case that a vertical Xmas tree will be used later, then another wellhead model is needed in which the production tubing has been installed.

For completion and workover operations, the wellhead models must account for the different subsea stack present, as there could be either a BOP or a lower riser package (LRP) landed on top of the Xmas tree (XT). Reinås et al. (2011) differentiates between modes of operation and assigns to the drilling operation the denomination operational phase 1, while completion and workover (WO) are respectively phases 2 and 3. Table 3.1 presents details on some of the different configurations, pertinent to fatigue damage, assumed by the wellhead throughout the life cycle of the well.

Table 3.1 – Possible mechanical and loading configurations of the wellhead system.

Phase	Stack up/installed casing description	Xmas Tree Type	Riser Model
1.1	BOP on WH, surface casing installed.	Horizontal and vertical	Drilling
1.2	BOP on WH, intermediate casing installed	Horizontal and vertical	Drilling
1.3	BOP on WH, all casings installed	Horizontal and vertical	Drilling
1.4	Phase 1.3 + production tubing installed	Vertical	Drilling
2.1	BOP on XT, all casings installed	Horizontal	Completion
2.2	Phase 2.1 + production tubing installed	Horizontal and vertical	Completion
2.3	Phase 2.2 + WO landing string inside riser	Horizontal and vertical	Completion
3.1	LRP on XT, all casings & production tubing installed	Horizontal and vertical	Workover

3.2.2 Applied Quasi-Static Loading

The bending moment and shear force acting on the wellhead are simulated in the local response analysis by applying a horizontal force at the top of the subsea stack, which corresponds to the elevation of the rotation point of the flex joint connected to the subsea stack. This force is applied in incremental steps, so that the bending moment generated at the wellhead datum is ramped from zero to the maximum value expected. This loading is referred to as cyclic loading.

Prior to the application of the cyclic loading, the FE model is subject to riser tension, down weight, and other forces or prescribed motions that mimic the loading gone through the assembly and installation phases, on what is referred to as the preload step. Only the cyclic stress components are used for the fatigue calculation. Thus, the static stresses resulting from the preload step are simply subtracted from the stress results in each of the steps in the cyclic loading.

3.2.3 Analysis of Results

The main results of the local response analysis are the load-to-stress curves for each of the fatigue hot spots. Those curves present the non-linear relation between the loads at the wellhead datum and the stress at a selected hot spot (Buchmiller et al. 2012a).

The two diametrical points corresponding to the highest compression and tension stress on the surface of interest of the fatigue hot spot are the basis for the load-to-stress curve. Figure 3.6 presents a typical load-to-stress curve for the surface casing weld. It shows the relation between cyclic stresses in the hot spot and the bending moment applied on the wellhead datum.

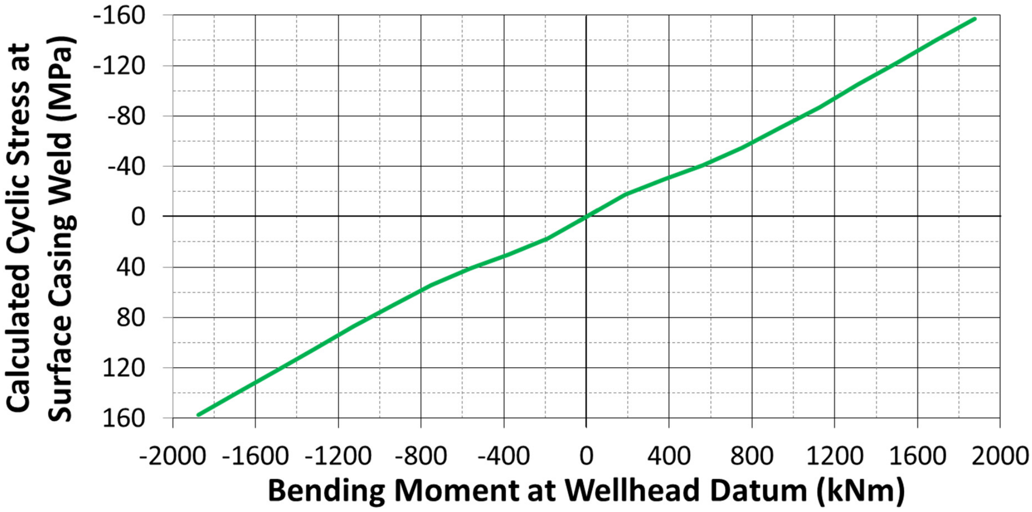

Figure 3.6 – Typical load-to-stress curve for the surface casing weld-fatigue hot spot.

The stress component which mainly influences fatigue damage is dependent on the hot spot. Most of the fatigue life of non-welded components is spent during the initiation of the crack, and for this stage the most important stress component is the one governing yield (*i.e.* the von Mises stress). Most of the fatigue life of welded components is spent during the crack growth process, and for that the maximum principal stress is the most important component (DNVGL-RP-C203 2016). Table 3.2 summarizes these specifications:

Table 3.2 – Relevant stress used for fatigue calculation.

Material Characteristics of Fatigue Hot Spot	Relevant Stress
Welded connection	Maximum Principal
Non-welded base metal	Equivalent Stress
Bolts	Axial

A secondary result of the local response analysis is the wellhead beam-proxy model (Figure 3.7). Following the hybrid decoupled approach, and thus linking the local and global analyses by way of the non-linear rotational and lateral stiffness's of the well (Reinås et al. 2012a), this beam-proxy model is the lower boundary of the riser model in the global response analysis.

The displacements and rotations of the wellhead 3D model at the wellhead datum, under different loading levels, are used to determine the properties of the beam-proxy model (see Figure 3.7). Further details on this simplified modelling of wellhead stiffness for global dynamic analyses are given in Annex A.

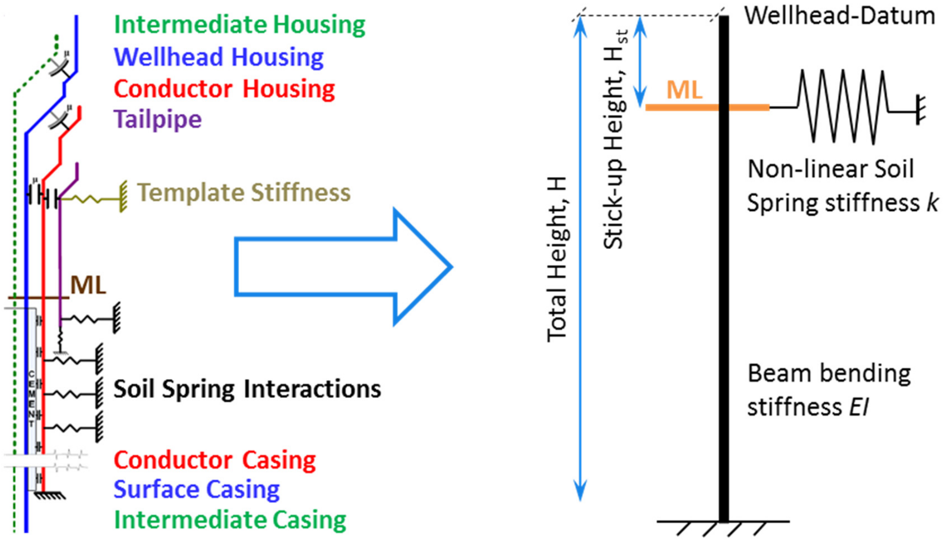

a) Wellhead system modelled in the structural local analysis

b) Wellhead beam proxy model used in the riser global analysis

Figure 3.7 – Wellhead beam-proxy model created from local analysis (Reinås et al. 2011). ©American Society of Mechanical Engineers.

3.3 Global Response Analysis

The global response analysis is carried out to establish the loads acting on the wellhead, which are caused by the wave induced motions of both the riser and the floating rig. Throughout this study the program Riflex version 4.6 (SINTEF, 2016) was used to calculate the riser's dynamic response. As it can be noticed from Table 3.1, there is the need for at least three riser models (Figure 3.8) to cover the different loading scenarios faced during the life cycle of a well.

The riser, the subsea stack and the floating rig can all change depending on the well operation being executed. Drilling and completion operations are both performed using a marine-drilling riser, but during completion the BOP is landed on top of the Xmas tree, which is landed on the wellhead. Workover operations, on their turn, may adopt two different riser configurations. A high-pressure workover riser connected to a lower workover riser package may be run in the open sea and connected to the Xmas tree, or a specialized riser can be run inside the marine riser.

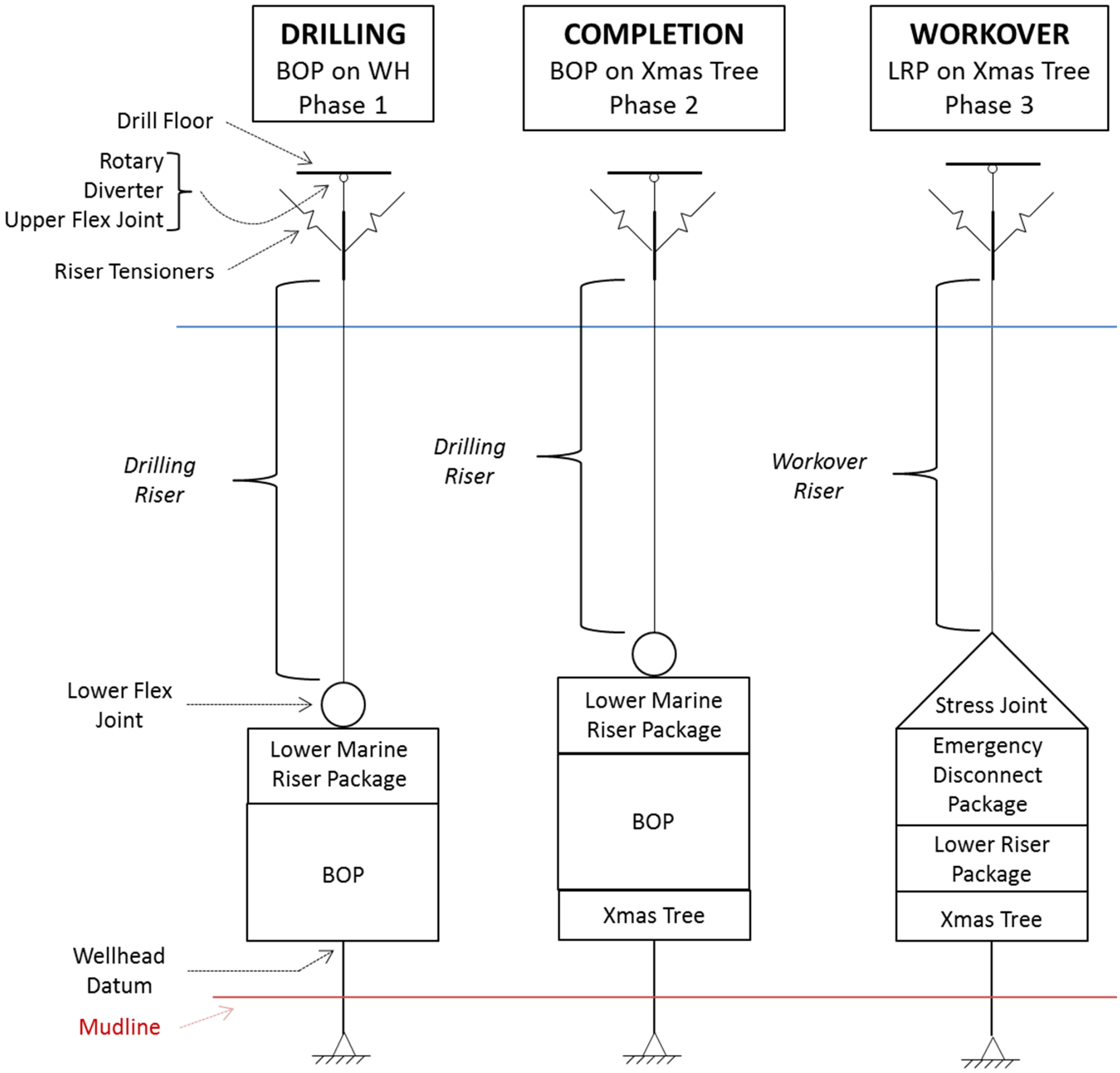

Figure 3.8 – Riser models used for different operational modes (Reinås et al. 2011). ©American Society of Mechanical Engineers.

Each analytical riser model must adequately describe the mechanical and physical effects derived from buoyancy, weight, effective tension and geometric stiffness, hydrodynamic loads from waves and current, floating rig wave-induced motions, the non-linear characteristics of flex joints, and the characteristic response of the riser-tensioner system.

3.3.1 Environmental Loading

The environmental conditions the riser and the floating rig are subject to may be described by the combined effect of current, wind, and sea states (or waves) that may occur simultaneously for a specific site. The stochastic nature of the loading applied to the wellhead, and its impact on fatigue damage estimates, is briefly described in the following sections.

3.3.1.1 *Wave height and spectrum*

Wave forces are dependent on the instantaneous velocities of the water particles, which are dependent on instantaneous height of the wave. The instantaneous height of real, irregular, waves is described as the sum of several regular waves of different periods (or frequencies) and heights (Journée and Massie 2001), as presented by Equation 3.5. Where:

- $\zeta(t,x)$ is the wave elevation at instant t and location x.
- ζ_{an} is the wave amplitude of the component n.
- k_n is the wave number of component n.
- ω_n is the circular wave frequency of component n.
- ε_n is the random phase angle of component n.

$$\zeta(\mathrm{t},\mathrm{x}) = \sum_{n=1}^{N} \zeta_{\mathrm{a_n}} \cos(k_n x - \omega_n t + \varepsilon_n)$$ **Equation 3.5**

The distribution of amplitudes and frequencies of the wave components are constant only for short durations of time, referred to as short term sea states. The energy distribution, or wave spectral density $S(\omega)$, along the frequency range of the waves during a sea state is modelled by a wave spectrum. As an example, take the spectrum shown in Figure 3.9. The amplitude of the wave component of frequency between ω_n and $\omega_n+\Delta\omega$ can be obtained by Equation 3.6:

$$\frac{1}{2}\zeta_{a_n}^2(\omega_n) = S(\omega_n)\Delta\omega$$ **Equation 3.6**

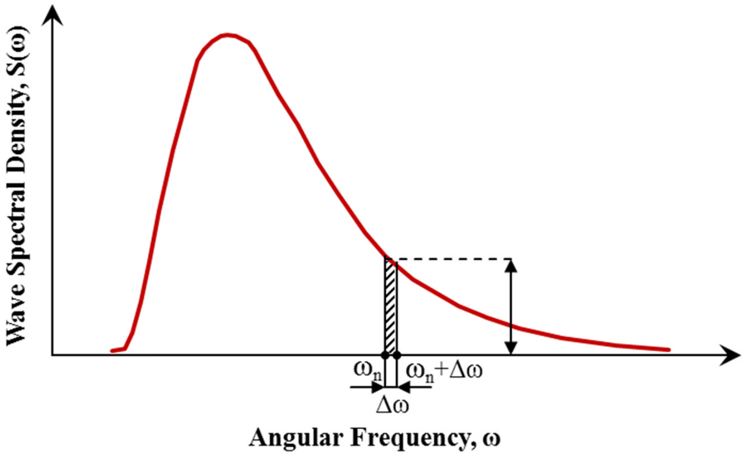

Figure 3.9 – Wave spectrum.

Sea spectra use two main parameters to describe a sea state, the spectral peak period, T_P, which is the period at which the energy density is highest, and the significant wave height, H_S, which is the average height of the largest one third of the waves observed in that sea state.

There are several spectrum formulas applicable to different locations in the world (Chakrabarti 2005) and depending on the model used to describe the wave spectrum additional parameters can be used. The most commonly used sea spectrum in the North Sea was developed from measurements made by the Joint North Sea Wave Observation Project (JONSWAP). A JONSWAP spectrum definition is presented by Equation 3.7, which employs a third factor called the peakedness factor, γ.

$$S(\omega) = \gamma^{A} \frac{320 \cdot H_s^2}{T_p^4} \cdot \omega^{-5} \cdot e^{\frac{-1950}{T_p^4} \cdot \omega^{-4}} \qquad \textbf{Equation 3.7}$$

where:

$$A = e^{-\left(\frac{\frac{\omega}{\omega_p}-1}{\sigma\sqrt{2}}\right)^2}, \quad \omega_p = \frac{2\pi}{T_p} \quad \text{and} \quad \sigma = 0.07 \; if \; \omega < \omega_p \; or \; \sigma = 0.09 \; if \; \omega > \omega_p$$

3.3.1.2 *Water kinematics*

The total water depth, h, of the offshore location influences how the wave energy is distributed, along the measured depth, z. Equation 3.8 presents the horizontal component, u, of a water particle velocity in a shallow water wave, while Equation 3.9 presents the horizontal velocity in a deep water wave.

$$u = \zeta_{\mathrm{a}} \cdot \omega \cdot \frac{\cosh k(h+z)}{\sinh kh} \cdot \cos(kx - \omega t) \qquad \textbf{Equation 3.8}$$

$$u = \zeta_{\mathrm{a}} \cdot \omega \cdot e^{kz} \cdot \cos(kx - \omega t) \qquad \textbf{Equation 3.9}$$

Accelerations are found directly from a differentiation of the velocities. This yields for shallow water and deep water, respectively:

$$\dot{u} = \zeta_{\mathrm{a}} \cdot \omega^2 \cdot \frac{\cosh[k(h+z)]}{\sinh(kh)} \cdot \sin(kx - \omega t) \qquad \textbf{Equation 3.10}$$

$$\dot{u} = \zeta_{\mathrm{a}} \cdot \omega^2 \cdot e^{kz} \cdot \sin(kx - \omega t) \qquad \textbf{Equation 3.11}$$

3.3.1.3 *Hydrodynamics forces*

The hydrodynamic load on a slender structure with circular cross-section such as a marine-drilling riser is found using the Morison's equation. The force given by this equation is the resultant of dynamic and static pressure fields acting on the riser, thus it is built up from two contributions, a drag force, F_D, and an inertia force, F_I, (Sparks 2007). The drag force is a result of the velocity of the flow that passes the riser, while the inertia force is a result of the acceleration of the flow.

Considering that a riser, with outer diameter D_o, moves with a velocity v in the direction of the flow, then the drag force, per unit length of the riser, will be:

$$F_D = \frac{1}{2} \rho C_D D_o (u - v)|u - v| \qquad \textbf{Equation 3.12}$$

where C_D is the drag coefficient, and ρ is the fluid density.

The inertia force, per unit length, is given by Equation 3.13, where C_M is the inertia coefficient, and A_o is the outer cross-sectional area of the riser.

$$F_I = \rho A_o \dot{u} + (C_M - 1)\rho A_o(\dot{u} - \dot{v}) \qquad \textbf{Equation 3.13}$$

Both coefficients, C_D and C_M, are determined empirically for each specific case.

3.3.1.4 Sea scatter diagram

As previously stated the sea state on a given location changes with time. All relevant sea states must be covered in the global response analysis. Charts, as the example presented in Table 3.3, are built based on observations, and are used to list the long-term probability of occurrence of each H_S and T_P pair. This probability of occurrence is later used as a weight when assessing the contribution of each sea state to the estimated wellhead fatigue damage.

Table 3.3 – Example of scatter diagram. Observed occurrences of sea states modelled by the specified H_S and T_P pair (Grytøyr and Steinkjer 2012). ©American Society of Mechanical Engineers.

	T_p (s)																		
H_s (m)	**2.5**	**3.5**	**4.5**	**5.5**	**6.5**	**7.5**	**8.5**	**9.5**	**10.5**	**11.5**	**12.5**	**13.5**	**14.5**	**15.5**	**16.5**	**17.5**	**18.5**	**19.5**	**20.5**
0.5	42	429	1172	1662	1634	1291	888	558	331	189	105	57	31	17	9				
1.5	2	109	964	3034	5260	6292	5902	4689	3317	2160	1325	778	443	246	135	73	39	21	11
2.5		71	76	578	1837	3373	4297	4248	3504	2532	1659	1009	581	320	171	89	46	23	11
3.5			2	47	320	1006	1881	2442	2436	2000	1419	900	523	285	147	73	35	16	7
4.5				2	33	206	635	1181	1519	1485	1179	797	475	257	128	60	27	12	5
5.5					1	22	133	395	715	888	829	619	388	212	103	46	19	7	3
6.5						1	16	85	242	414	485	420	287	163	79	34	13	5	2
7.5							1	11	55	144	228	244	191	117	58	25	9	3	1
8.5								1	8	35	83	117	112	77	41	18	6	2	1
9.5									1	6	22	45	55	45	27	12	4	1	
10.5										1	4	13	22	23	18	8	3	1	
11.5											1	3	7	10	9	5	2	1	
12.5													2	4	4	3	1		
13.5														1	2	1	1		
14.5																1			

The necessary simulation length for each sea state to reach the required certainty level on the fatigue assessment is dependent on the degree of non-linearity at the system's investigated locations (Steinkjer et al. 2010). Grytøyr and Steinkjer (2012) presented a statistical uncertainty measure used to evaluate the robustness in the estimated fatigue life and have shown for a particular hot spot that a minimum simulation time of 600 s may be sufficient to obtain reliable estimates, but more-pronounced non-linearities in the system may demand significantly longer simulation lengths.

3.3.1.5 Current loading

During the global response analysis, the sea current is a static load, applied before the wave loading. The riser assumes an initial static geometric configuration, from which it oscillates as wave forces vary with time. Sea current profiles are obtained from measurements and presented according to their probability of occurrence: the P10 percentile current is, then, a profile that is exceeded 90% of the time.

The increase in drag loads due to the use of sea current can have different effects along the riser. Below the wave influence zone current forces produce damping that may decrease the dynamic response, while within the wave zone current forces may increase the system's dynamic response (DNVGL-RP-0142 2015). Conservatism can be added to the analysis depending on the profile chosen, therefore, the use of current must be carefully considered.

3.3.2 Typical Results

For each individual short-term sea state is generated a time series of the global bending moment at the wellhead datum (Figure 3.10). The time series are to be later combined with the load-to-stress curves from the local response analysis (Section 3.2) for the fatigue assessment.

If current loading is applied to the riser model, the load time series gets a mean value different from zero. In this case, the mean value of the time series must be subtracted before it is combined with the load-to-stress curves.

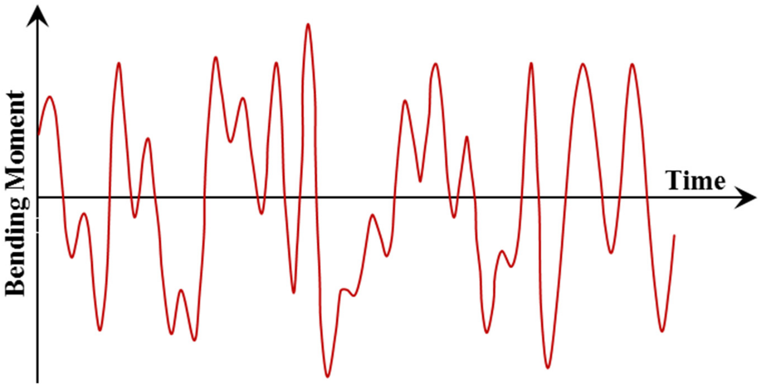

Figure 3.10 – Example of bending moment time history.

It is convenient, and a compact way of storing the load histories, to combine the several short-term loading time histories into a long-term loading-time history, by means of a weighted sum corresponding to their probability of occurrence presented in the scatter diagram. This enables quick comparison of loading histories for different wells.

3.4 Fatigue Damage Assessment

The random nature of waves subject marine structures to complex load histories. To be able to calculate the fatigue damage is first necessary to identify and group the load cycles. The load history is divided into blocks or bins, and each bin contains all load cycles within a stress range. For calculation purposes the identified cycles assume the mean value of the stress range of the bin.

3.4.1 Cycle Counting

Stress-time histories are obtained by combination of the loading time histories with the load-to-stress curves. Then, it is necessary to identify the individual stress cycles contained in the stress-time history. Given the irregular nature of the source of the fatigue damage, the definition of a cycle is not obvious, and the resulting cycle count will be dependent on the counting method.

There are different methods available for counting stress cycles in a variable load history. Of those, the most widely used is the Rainflow Method (Stephens et al. 2001). In this method, a cycle is counted each time a hysteresis loop is closed in the stress/strain curve (Anzai and Endo 1979).

Rainflow counting has obtained its name from an analogy of rain flowing off a pagoda roof. Its application can be described thusly:

- Reduce the stress-time history to a sequence of peaks and troughs.
- Display the load history in a way that the time axis is in the vertical direction, increasing downwards (Figure 3.11).

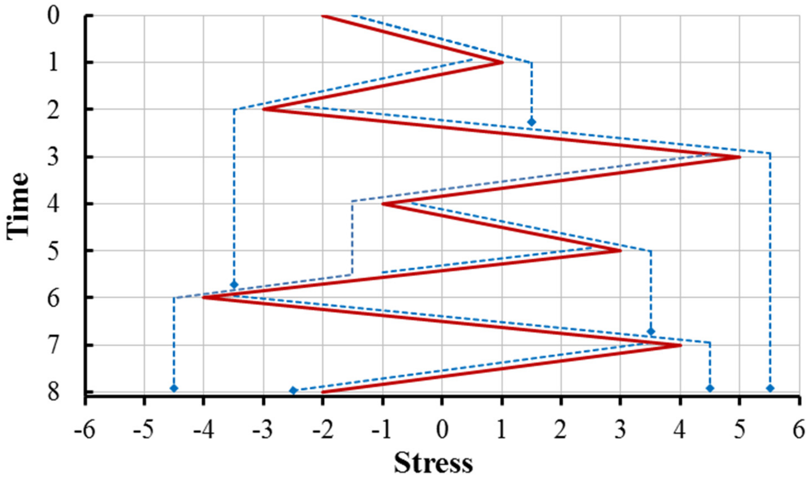

Figure 3.11 – Load history turned 90° clockwise (in red) and the "streams" of water (in blue).

- Consider each tensile peak as a source of water that "drips" down the pagoda.
- Count the number of half-cycles by looking for flow interruptions that occur when:
  - A flow reaches the end of the time history; or
  - It merges with another flow that started at an earlier tensile peak; or
  - It encounters a trough of greater magnitude.
- Repeat the previous step for the compressive troughs.
- Assign a magnitude to each half-cycle equal to the stress difference between its start and termination.
- Pair up half-cycles of identical magnitude (but opposite sense) to count the number of complete cycles.
- Create a table listing for each stress range the number of cycles counted, as shown as an example in Table 3.4.

The identified stress ranges and corresponding number of cycles can then be used to estimate the cumulative fatigue damage incurred using the Miner-Palmgren summation procedure.

Table 3.4 – Rainflow counting results from Figure 3.11.

Stress range	1	2	3	4	5	6	7	8	9
Cycles Counted	0	0	0.5	1	0	0.5	0	1	0.5

3.4.2 Reporting

Fatigue damage should be reported as function of the duration of riser connected time, where the operational phases that contributed to the incurred fatigue damage are consecutively put after each other in chronological order. If at the design stage the duration of different operations is not known, then damage rates (*e.g.* damage/year) should be calculated for each operational phase. (DNVGL-RP-0142 2015).

Due to uncertainties on the TOC level in the annular space between the surface casing and the conductor, the fatigue-damage rate or remaining capacity should be reported for the most unfavorable cement level, which will not necessarily be the same for all fatigue hot spots.

Figure 3.12 presents an example of results, using fictitious numbers for two different hot spots. The beginning of a new operational phase is indicated by vertical dashed lines. Each operational phase contributes to the total accumulated fatigue damage at a different rate. The figure shows for which fatigue hot spot the design criteria is reached or not for the specified operations.

In this example, the fatigue capacity of hot spot 2 is completely consumed after 150 days of operation, which would demand a reevaluation of the selected design criterion. The new value selected for the DFF should be balanced against the associated consequences of failure in risk evaluations.

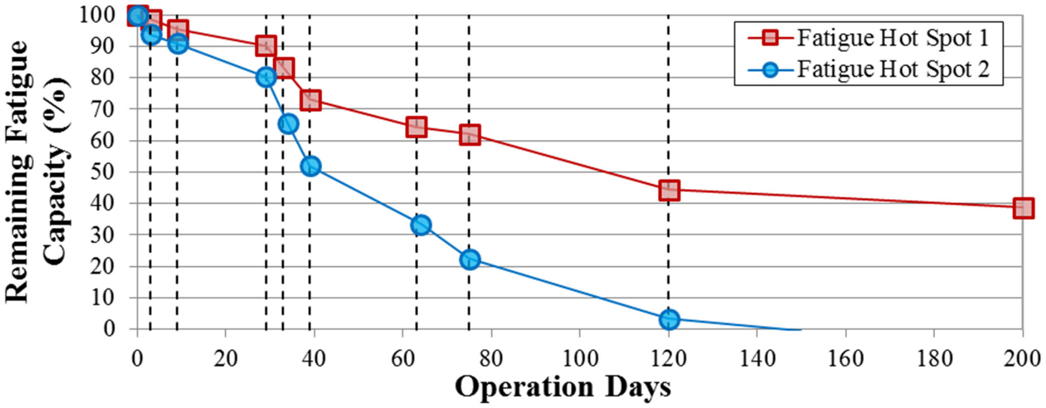

Figure 3.12 – Fatigue damage throughout consecutive operational phases. Remaining capacity of 0 implies that the selected fatigue design criterion has been reached.

3.5 Structural Reliability Analysis in Wellhead Fatigue Assessment

The method described in the previous sections of this chapter is deterministic, though the analyses within each of its three parts may be associated with high sensitivity to variations in input parameters. Sensitivity analyses of specified parameters may determine the worst case, which is typically used as the basis of the fatigue assessment.

The inherent problem of this approach is that the level of conservatism associated to the worst cases is not quantified and, therefore, not entirely justified. Consequently, over-conservative fatigue estimates may unnecessarily reduce the service life of a well.

Hørte et al. (2012) argue that Structural Reliability Analysis (SRA) may be applied to wellhead fatigue assessment, so the assessment can account for the uncertainty associated to input parameters, as given by probability distributions. The level of conservatism of the analysis is evaluated versus the acceptable probability of failure, and this information can support the decision-making process to extend service life.

The challenges associated to SRA include defining the probability distribution of each parameter, and performing the necessary analyses (local, global, fatigue) for the possible sets of input parameters. Hørte et al. (2012) present that the results of SRA enable importance factors to be assigned for each of the input parameters.

Thus, parameters of low importance can be dismissed from the probabilistic analyses, and focus can be shifted to reducing the uncertainty of the parameters of greater importance. The uncertainties associated to TOC, the global response analysis, the S-N curve and the SCF due to misalignments in welded connections have been deemed to affect the end results the most.

Chapter 4

Adapting the Fatigue Assessment Methodology to Account for Temperature

The necessary measures for adapting the wellhead fatigue methodology to well temperature are presented in this chapter. The incorporation of well temperature has been described in sections of Papers I, II and III. Figure 4.1 indicates how well temperature becomes a new input parameter in the local response analysis. The in-house well thermal model developed for the temperature-distribution analysis (Paper IV) is briefly described in this chapter, and at greater depth in Annex B.

The following sections will present how the local response analysis is directly affected by temperature, and how the other parts of the methodology are indirectly affected by it.

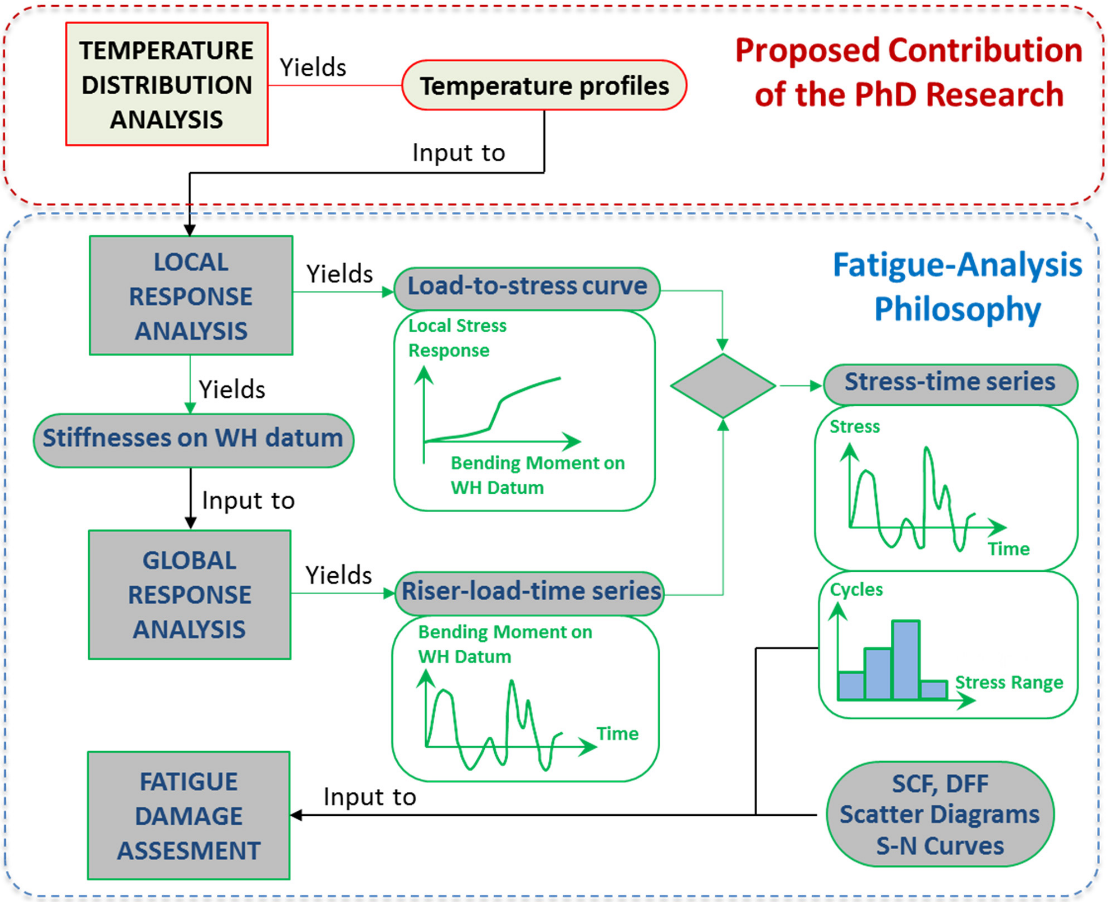

Figure 4.1 – Incorporation of temperature to the DNVGL's wellhead-fatigue method.

4.1 Obtaining the Temperature Distribution

The early stages of drilling operations in a subsea well are executed without a riser, and the heat exchange processes taking place inside the well are quite challenging to model because the interior of the well is exposed to the sea environment. However, fatigue damage on the wellhead becomes an issue after the deployment of the BOP, and the connection to the riser and drilling rig is made. This is a much simpler scenario to model for the heat exchanges taking place inside the well.

The first published work for estimating downhole temperatures (Farris 1941) used measurements of bottomhole circulation temperatures in several wells in the Gulf of Mexico to create charts that predicted the bottomhole temperature during cementing periods. Ramey (1962) and Edwardson et al. (1962) were the first to present a theoretical model for estimating fluid temperature as a function of well depth and producing time. Both works, however, neglected the effect of kinetic energy and friction and were applicable only to single-phase fluids.

Later, Holmes and Swift (1970) published an analytical model for temperature profile of moving fluids that has been often referred to. Following that, several authors (Keller et al. 1973; Wooley 1980; Marshal and Bentsen 1982; Oster and Scheffler 1982) published works that described improved numerical methods for calculating the temperature profile, generally introducing improvements in the mathematical method.

The axisymmetric wellbore transient thermal model developed for the calculation of the temperature distribution in the wellbore was based on the FE solution methods presented by Keller et al. (1973) and Marshal and Bentsen (1982), which were adapted to offshore wells. The following sections will briefly describe the model. A more-detailed description is presented in Annex B and in the works referred to.

The temperature calculations may take place at any time after deployment of the BOP and marine riser, so that the return of the drilling fluid to the surface through the riser can be modelled. The following assumptions were made in the model:

- When the well circulation takes place, the heat transfer within the drilling fluid is by axial convection. Conduction heat transfer is neglected, except when the fluid is not circulating.
- Heat generation by viscous dissipation within the fluid is neglected.
- Density and thermal properties of fluids were considered constant and independent of temperature and pressure.
- Surrounding seawater acts as a thermal reservoir, and surfaces exposed to seawater, such as the riser and BOP stack, exchange heat by the natural and forced convection mechanisms.

4.1.1 System’s Energy Balances

The heat exchange process taking place inside the well can be described applying the conservation of energy to different control volumes. Depending on the vertical coordinate of the points being investigated, there will be different components and corresponding control volumes to be accounted for, as presented by Figure 4.2.

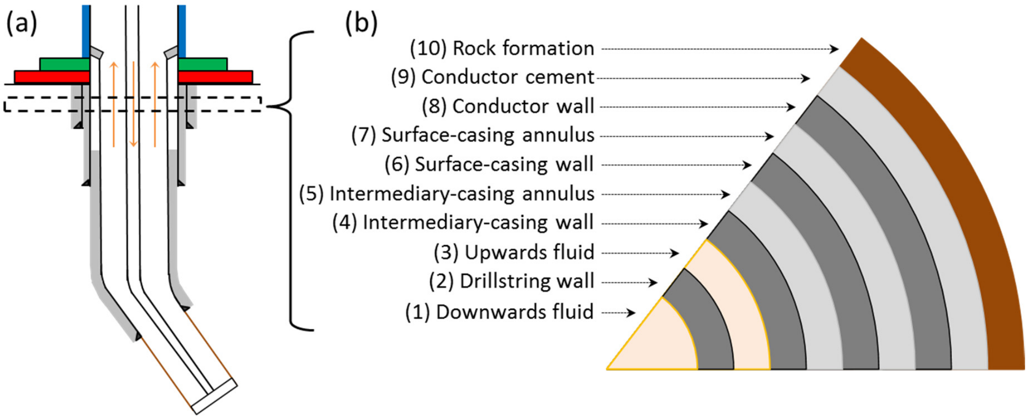

Figure 4.2 – Well schematics (a) and components of the well system at a given depth (b).

For each of the different components in the rectangular area, starting with the drilling fluid inside the drillstring and moving outwards until the rock face is met, the energy balance of the corresponding control volumes leads to a set of differential equations. Those equations are briefly described below.

Equation 4.1 presents the final form of the energy balance for the fluid inside the drillstring, based on the total energy of a flowing fluid (Çengel and Boles 1989) and the energy crossing the control volume. The first term on the left side accounts for the fluid's variation of enthalpy as it crosses the control volume, the third term describes the radial convective heat transfer, while the second term accounts for the changes in the fluid's potential energy, in which α is the wellbore inclination angle with the horizontal.

The first and second terms on the right side account for the energy accumulated by the fluid and the heat generated by pressure losses inside the drillstring, respectively. Annex B discusses with more detail modelling of the generation and exchange of heat within the well system.

$$\rho_{df} q C_{p\_df} \frac{\partial T}{\partial z} + wgsin\alpha + h_{ds\_i} 2\pi r_{ds\_i}\left(T_{df\_ds} - T_{ds}\right) = Q_{pl\_ds} - \rho_{df} \pi r_{ds\_i}^{2} C_{p\_df} \frac{\partial T}{\partial t}$$

Equation 4.1

Equation 4.2 represents the energy balance in the drillstring wall. The first term on the left side accounts for the vertical heat conduction in the drillstring. The two remaining terms account for the heat exchanged by convection with the fluid flowing in its interior and on the surrounding annulus, respectively. The term on the right side accounts for the accumulation of energy along the drillstring.

$$k_{ds} \frac{\partial^2 T}{\partial z^2} + \frac{h_{ds\_i} 2 r_{ds\_i}}{\left(r_{ds\_o}^2 - r_{ds\_i}^2\right)}\left(T_{df\_ds} - T_{ds}\right) + \frac{h_{ds\_o} 2 r_{ds\_o}}{\left(r_{ds\_o}^2 - r_{ds\_i}^2\right)}\left(T_{ds} - T_{df\_A}\right) = \rho_{ds} C_{p\_ds} \frac{\partial T}{\partial t}$$

Equation 4.2

Equation 4.3 describes the energy balance of the fluid flowing upwards in the annulus. It is similar to equation 1, with a fourth term on the left side accounting for the radial convective heat transfer between the drilling fluid and either the riser, the casing, or the formation.

$$\begin{aligned}&\rho_{df} q C_{p\_df} \frac{\partial T}{\partial z} + wgsin\alpha + h_{ds\_o} 2\pi r_{ds\_o}\left(T_{ds} - T_{df\_A}\right) + \\ &h_{cw\_i} 2\pi r_{cw\_i}\left(T_{df\_A} - T_{cw}\right) = \rho_{df}\pi\left(r_{cw\_i}^2 - r_{ds\_o}^2\right) C_{p\_df}\frac{\partial T}{\partial t} - Q_{pl\_A}\end{aligned}$$

Equation 4.3

Solving Equation 4.1 through Equation 4.3 requires evaluating the convective heat transfer coefficients for laminar or turbulent flow inside and around the drillstring. Keller et al. (1973) provides empirical relations for this purpose.

The energy balance in the casing string wall is shown by Equation 4.4. The first term on the left side accounts for the radial heat transfer by conduction between the casing and the cement annulus, while the second term represent the axial heat conduction in the casing, and the third term accounts for the radial heat transfer by convection between casing and fluid.

$$\begin{aligned}&\frac{2(T_{cw}-T_{ca})}{\left(r_{cw\_o}^2-r_{cw\_i}^2\right)}\frac{k_{cw}k_{ca}}{k_{ca}ln\left(r_{cw\_o}/r_{cw\_m}\right)+k_{cw}ln\left(r_{ca\_m}/r_{cw\_o}\right)} + k_{cw}\frac{\partial^2 T}{\partial z^2} + \\ &\frac{h_{cw\_i}2r_{cw\_i}}{\left(r_{cw\_o}^2-r_{cw\_i}^2\right)}\left(T_{df\_A} - T_{cw}\right) = \rho_{cw}C_{p\_cw}\frac{\partial T}{\partial t}\end{aligned}$$

Equation 4.4

The energy balance in the casing annulus, and the subsequent layers, is shown by Equation 4.5. Here, the subscript *j* refers to the layer's radial position, starting from the center and increasing outwards. On the left side of the equation there can be seen the two terms accounting for the radial heat transfer by conduction, besides other terms previously addressed.

$$\begin{aligned}&\frac{\left(T_j-T_{j+1}\right)}{r_j\Delta r_j}\frac{k_jk_{j+1}}{k_{j+1}ln\left(r_{j\_o}/r_{j\_m}\right)+k_jln\left(r_{(j+1)\_m}/r_{j\_o}\right)} + k_j\frac{\partial^2 T}{\partial z^2} + \\ &\frac{\left(T_{j-1}-T_j\right)}{r_j\Delta r_j}\frac{k_{j-1}k_j}{k_jln\left(r_{(j-1)\_o}/r_{(j-1)\_m}\right)+k_{j-1}ln\left(r_{j\_m}/r_{(j-1)\_o}\right)} = \rho_i C_{p\_i}\frac{\partial T}{\partial t}\end{aligned}$$

Equation 4.5

The energy balance in the riser wall is shown in Equation 4.6 and it is similar to Equation 4.4. The riser wall exposed to the seawater exchanges heat by natural convection and forced convection; the corresponding heat transfer coefficients for those mechanisms can be summed up and calculated according to the formulations provided by Bergman et al. (2011).

$$\begin{aligned}&k_{rw}\frac{\partial^2 T}{\partial z^2} + \frac{h_{rw\_i}2r_{rw\_i}}{\left(r_{rw\_i}^2-r_{ds\_o}^2\right)}\left(T_{rw} - T_{df\_A}\right) + \frac{h_{rw\_o}2r_{rw\_o}}{\left(r_{rw\_o}^2-r_{rw\_i}^2\right)}\left(T_{rw} - T_{sea}\right) = \\ &\rho_{rw}C_{p\_rw}\frac{\partial T}{\partial t}\end{aligned}$$

Equation 4.6

The first order partial derivatives on the previous equations can be represented by two-point forward and backward difference approximations, while the second order derivatives can be represented by three-point centered difference approximations (Marshal and Bentsen 1982).

Applying the finite-difference method is made possible by discretizing the well/riser system and representing it as an axisymmetric two-dimensional grid, shown in Figure 4.3, where a generic node exchanges heat with the four adjacent nodes.

As an example, Equation 4.1 for the drillstring, results into the form below, in which subscript *k* refers to an element's vertical position, and the superscript *n* refers to the simulation's time step for which the temperature calculation is done.

$$\rho_{df} q C_{p\_df} \frac{\left(T^{n}_{1,k-1}-T^{n}_{1,k}\right)}{\Delta z_k} + h_{ds\_i} 2\pi r_{ds\_i}\left(T^{n}_{2,k} - T^{n}_{1,k}\right) = -wgsin\alpha - \rho_{df}\pi r^{2}_{ds\_i} C_{p\_df} \frac{\left(T^{n}_{1,k}-T^{n-1}_{1,k}\right)}{\Delta t}$$

Equation 4.7

The term Δz_k corresponds to the vertical length of all the elements at the vertical position *k*. It is calculated based on the measured depth of the elements' ends, and it can be adjusted to better suit the needs of the calculation, for example, large values to decrease computational time, or small values to pinpoint equipment installed in the drillstring or to capture the cement/mud interfaces on the casing annuli.

The time step, Δt, of the calculation is based on the provided description of the history of well operations. It can assume different values, to cover and better simulate the well operations performed during drilling.

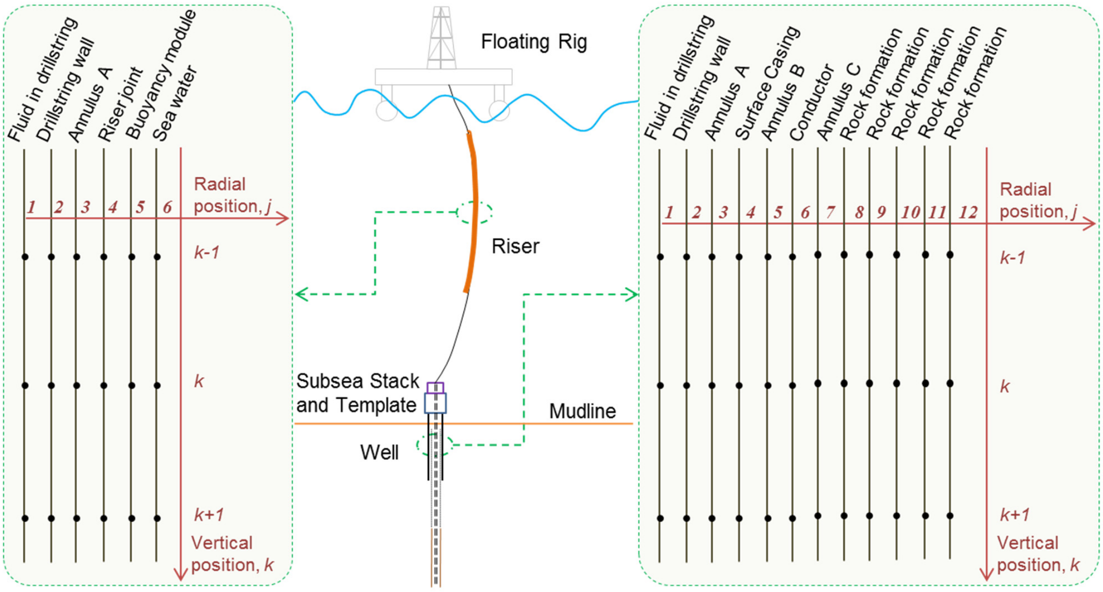

Figure 4.3 – Schematic representation of well system's mesh.

4.1.2 Initial State and Boundary Conditions

The initial and boundary conditions of the model, assumed to perform the well-temperature calculations, are described in the following bullet points and in Figure 4.4.

- Initial temperatures are either obtained from environmental data (sea temperature, geothermal gradient) or read from results of previously performed calculations.
- Because of the symmetry of the model, no heat exchange takes place across the innermost (r=0) surface of the fluid inside the drillstring.
- The rock formation surface immediately after the outermost (r=r_{fs}) rock element in the mesh grid is considered sufficiently distant from the well as to retain its original undisturbed, *in situ* temperature.
- Surfaces exposed to the sea/air exchange heat by convection mechanisms, including the rock formation elements at the seabed level.
- No heat exchange takes place across the uppermost (z=0) surfaces of the system.
- Heat exchange does take place across the lowermost (z=z_{bot}) surfaces of the system. However, temperature variations of formation elements outside the delimited well system are not computed.
- The inlet temperature of the drilling fluid is known at all time steps and is also a boundary condition.
- When circulation takes place, the temperature of the flowing fluids and drillstring are equalized at the drill bit.

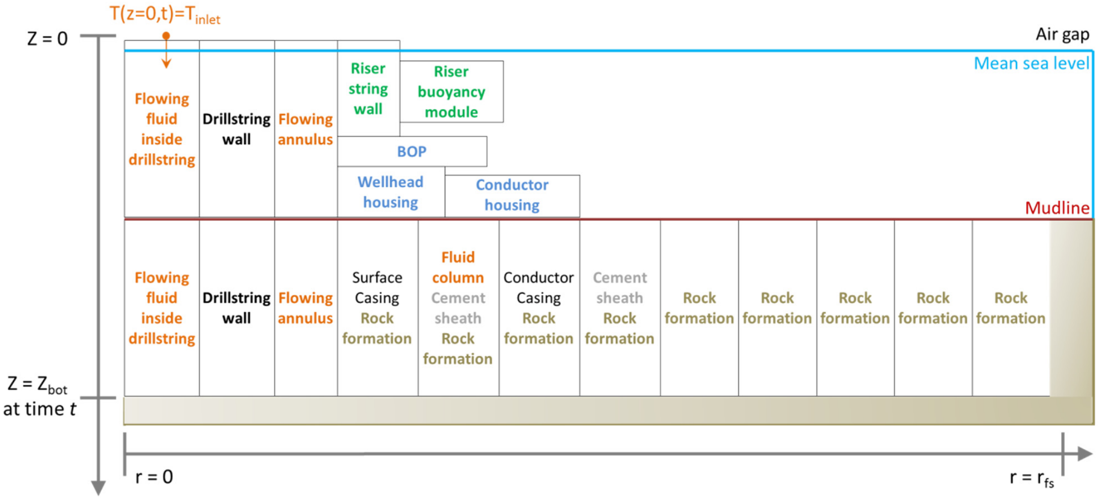

Figure 4.4 – Auxiliary sketch of the discretized heat transfer problem and boundary conditions. Sketch shows the components present on the well and riser during the operational phase 1.1.

4.2 Local Response Analysis

In the local response analysis, as described by Reinås et al. (2011), a 3D finite-element model of the wellhead and the upper part of the well is built in a structural calculation program to estimate the relevant stresses at the wellhead fatigue hot spots when exposed to different operational loads. The model is subjected to the self-weight of the well components, the loads transferred by the riser into the wellhead system, and the well-soil mechanical interaction, represented by non-linear springs connected to the components facing the soil.

The proposed incorporation of temperature into the wellhead fatigue methodology leads to additional load cases in the local response analysis, as the impact of the sequential variations on the temperature distribution along the well is included.

Before the local response analysis, the operations performed inside the well are simulated, using either a commercial or an in-house (Sevillano et al. 2017) thermal model of the well and the corresponding temperature distributions are calculated at appropriate time intervals. Of all the temperature profiles generated, those from selected points in time become an input in the local response calculation, resulting in several analyses performed.

To account for the thermal-related stresses, first it has been assumed that the stresses resulting from the temperature distribution in a casing string become significant to the response of the well once the casing string has been cemented in place. Prior to that, the casing is suspended from the wellhead and it can expand in a scenario of changing temperature. However, when the cement slurry sets and bonds to the casing and surrounding formation, the casing's thermally-induced length variation becomes constrained by the cement and formation.

The thermally-induced stresses are related to the temperature distribution that the casing strings attains by the time the cement sets. The temperature distribution of casing string when cement sets is, for simplicity, called T_{set}. Any thermal stress and strain from that point forward will be calculated based on the temperature variations computed from T_{set}, which is represented by the temperature differential ΔT.

In Figure 4.5, temperature profiles of the conductor, the surface casing, and annular cement sheaths are presented at a certain time during drilling. The temperature values of interest for the structural analysis are expressed in terms of ΔT, calculated from the well's components initial temperature along depth.

The commercial software Ansys Workbench v16.2 (Ansys 2016) was used to carry out the finite-element analysis (FEA). It is recommended that the 3D structural wellhead model built for the local response analysis should include the upper part of well to such an extent that wellhead stresses are not influenced by the model termination (Buchmiller et al. 2012a).

However, a model representative of the entire well is necessary to compute the thermally induced interaction between well components, along the entirety of their respective lengths. Thus, the different casing strings and annular cement sheaths are modelled from the wellhead datum to their complete extent, along the well trajectory followed to reach the drilling target.

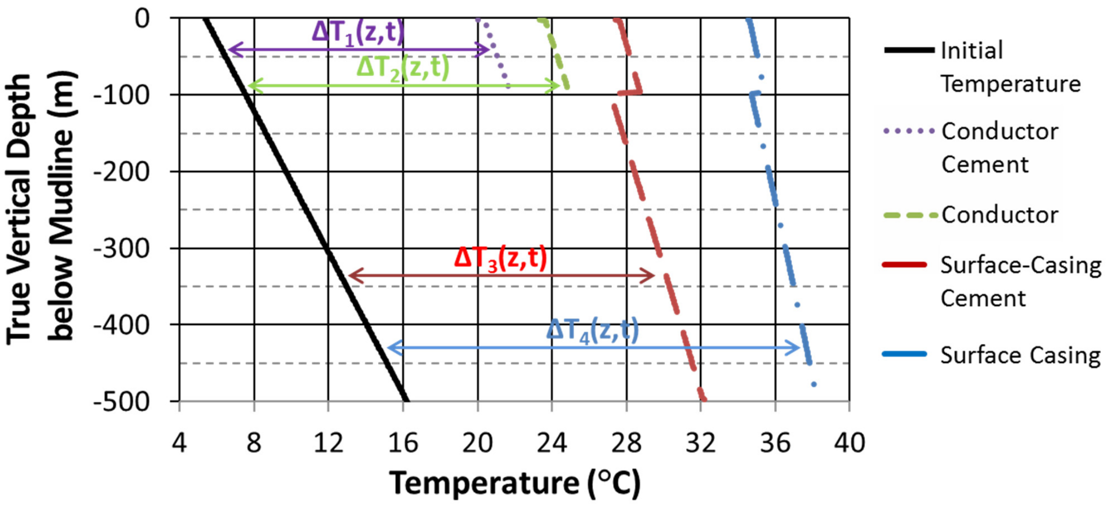

Figure 4.5 – Example of temperature distributions calculated for well components at a given time of the drilling operation.

Yet, detailed thermal-structural simulations of the entire wellhead and well system, which would require a fine mesh of the well components to calculate the stresses at wellhead hot spots, may be costly in terms of computational resources and time. To overcome this challenge the local response analysis is divided in two computing stages of local response calculations, the schematics of which are presented in Figure 4.6.

In the first stage, thermal-mechanical simulations of the entire well are performed with a "coarsely" discretized model. The calculations in this stage do not focus on stresses at fatigue hot spots. The aim is to determine the loads generated on the upper section of the well model by the thermal expansion induced on its lower section. Therefore, it is possible to perform these calculations using a coarse model to save on computational resources and time. The operational loads considered at this stage are riser tension, self-weight, and the temperature distribution.

DNVGL-RP-0142 (2015) states that the 3D model can be created using a combination of solid and beam type of elements. In the coarse model, the wellhead and well components up to 50 m below the mudline level were modelled using solid type of elements. The remaining lengths of the components were modelled using shell type of elements instead of beam type of elements, because of the former's satisfactory results while being computationally inexpensive, and the need to properly establish the contact boundary conditions between different shell components. This is especially relevant when simulating the response of bonded components at different temperatures.

The mechanical response of the first-stage wellhead model, at a certain depth (*e.g.* 100 m below the mudline), is used as the bottom-end boundary condition of the more-finely discretized sub-model of the second stage of the local response calculations. The sub-model is subjected, in addition to the forces acting upon the first-stage coarse model, to a gradually increasing shear force transferred by the marine riser at its connection point to the BOP, which generates the bending moment load at the wellhead datum.

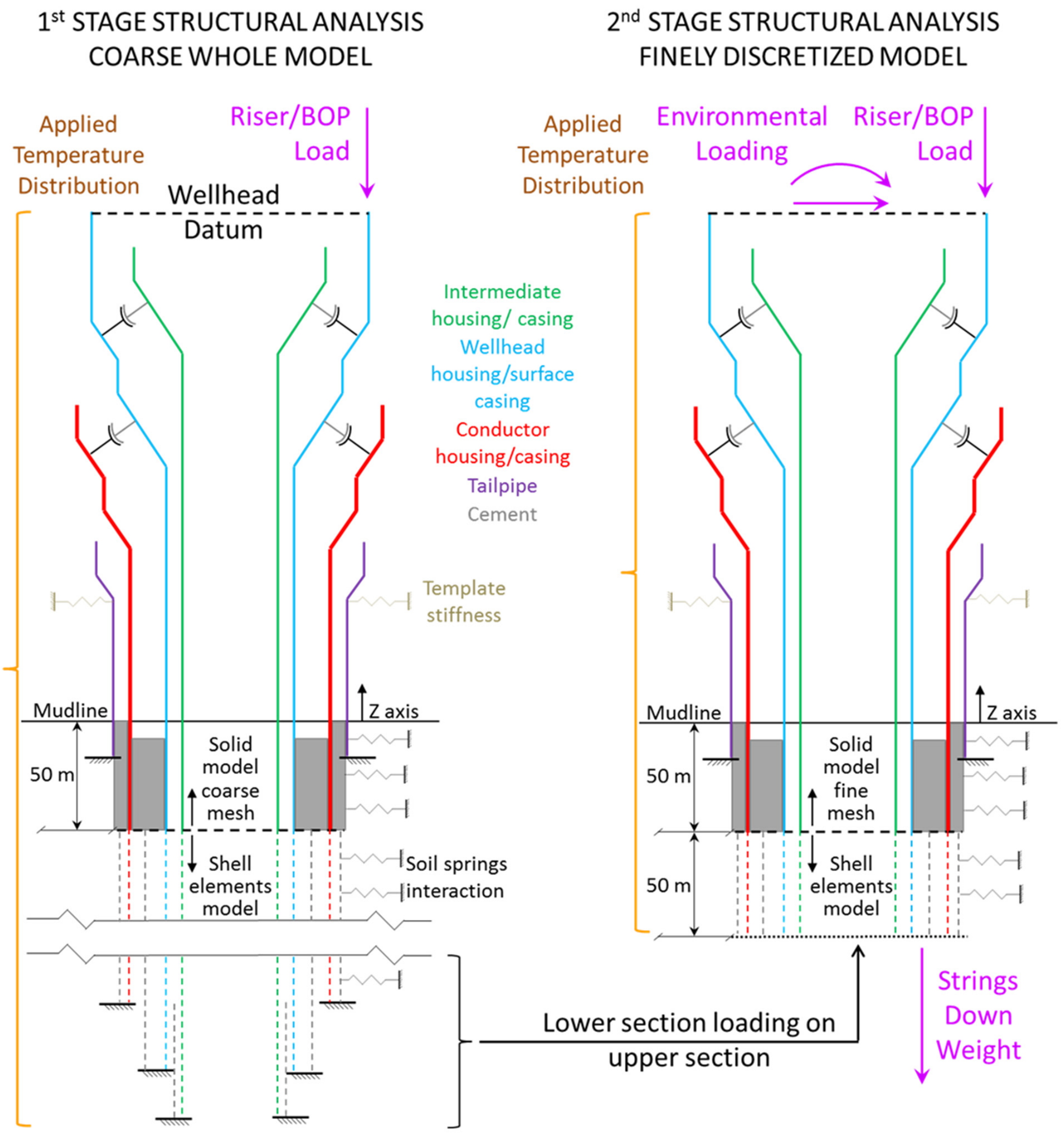

Figure 4.6 – Schematics of models used for local response analyses. Adapted from Reinås et al. (2011).

Finally, the local stresses calculated at the wellhead hot spots during the succeeding loading steps of the sub-model are used to create the load-to-stress curves. Only the cyclic stress components are to be used for the fatigue calculation. Hence, the static stresses resulting from the first loading step (when bending moment loading is zero) are not considered.

The models used in the wellhead fatigue assessment must differentiate between the several operational phases that the well goes through as it is being drilled and prepared to operate (Table 3.1). Each phase has a different load combination, either because a new casing has been suspended or cemented in place, which alters the configuration of the wellhead, or the equipment landed on the wellhead has changed. During drilling, for example, the riser and subsea stack remain the same, but each configuration assumed by the wellhead requires a set of structural simulations.

However, if it is assumed that the temperature distribution in the well can alter the loading distribution on the wellhead, different loading scenarios may then be found for the same wellhead configuration. Thus, several sets of structural simulations might be needed to properly describe the response of the wellhead as the temperature distribution in the well changes with time.

The history of operations commonly performed inside the well can include circulating the fluid inside it, running the drillstring, or a casing string, or another tool into or out of the well, cementing jobs, drilling ahead, as well as non-productive time.

Rigorously speaking, the temperature-distribution analysis should thoroughly simulate all the operations performed inside the well, but it would be unfeasible to run structural analyses for all the instantaneous temperature profiles generated.

Therefore, sufficient specific moments during well operations must be chosen so that the wellhead response to the temperature distribution, corresponding to the operations performed inside of the well, is properly investigated.

The moments selected for structural analyses should cover the start and end of all operations (drilling ahead, circulating, cementing, retrieving the drillstring, etc.) carried out. Long operations, *e.g.* 20 hours or more, during which the well goes through substantial temperature changes, might require to be subdivided, so additional structural calculations may be carried out to better describe the response of the wellhead during the allocated period.

Special attention must be given when circulation in the well starts, since the outermost casing string will, at first, suffer a change in temperature significantly larger than that of the other casing strings, thus requiring more structural analyses to describe the response of the wellhead, until the temperature of the rest of the casing strings properly develop.

4.3 Global Response Analysis

The global response analysis involves structural modelling of the dynamic response of the riser towards the expected environmental loads. However, even though the temperature of the riser is computed by the temperature-distribution analysis, it has not been included as one of loads acting on the riser when calculating its dynamic response. There are two reasons for this.

The first reason is that most of the riser length can be directly exposed to the sea water, and because the sea acts as a heat sinking hole, this often results in the calculated temperature variations on the riser wall to be small, thus allowing for them to be neglected.

The second reason relates to the riser system telescopic joint and tensioners system. The telescopic joint system works as a motion compensator in the vertical direction, developed to compensate the heave motions of the drilling rig. Therefore, the temperature variations of the riser are not expected to influence the riser and wellhead axial tension.

Nonetheless, the riser global response is still indirectly affected by the temperature distribution in the well because of the bottom-end wellhead beam-proxy model. The wellhead beam-proxy model is created by the local response analysis to link the local and global analyses. Consequently, it makes the global response analysis subjected to the temperature distribution of the well. Because every loading configuration creates a different wellhead beam-proxy model, it may be initially expected that the fatigue assessment would need as many riser dynamic response analyses as wellhead structural analyses.

4.4 Fatigue Assessment

The curves in DNVGL-RP-C203 (2016) are assumed to be valid for material temperatures of up to 100° C; for higher temperature, a correction factor would be required. However, the temperature at the wellhead is not expected to achieve such a high value during operations.

Conversely, it might be needed to adapt the adopted parental S-N curve to the developed mean stresses on a hot spot, according to the Goodman or Soderberg relations, or the method provided by DNVGL-RP-C203 (2016), as presented in section 2.4. Therefore, the third part of the wellhead fatigue assessment may have to include a step for correcting the S-N curves, based on the thermally induced mean stresses calculated throughout the operational phases.

4.5 Structural Reliability Analysis

Considering the inherent uncertainty of measuring or predicting the temperature distribution in a well, either due to incomplete operational data or the disparity between results yielded by different thermal models (section B.3), a certain level of uncertainty would be inevitable when incorporating temperature as a new parameter in the wellhead fatigue assessment. Therefore, an SRA of the wellhead would have to account for the uncertainty associated to the multiple parameters used to predict the temperature in the well.

Depending on the input parameters, the temperature differentials, ΔT, of the members of the well, calculated at the selected moments during an operation, may be either larger or smaller; altering the stress response of wellhead accordingly.

Section 4.1 has shown that the thermal modelling of a well requires several input parameters to be accounted for. It is reasonable to assume that the physical properties of the manufactured components (steel members, drilling fluid, cement, etc.) are fairly known, while there might be large uncertainties regarding the properties of the rock formations surrounding the well.

The temperature distribution of the well is influenced by the operations performed in it. Detailed records of past operations will reduce the uncertainty of the thermal calculations, regarding the operational parameters. The temperature calculations for future operations might need to consider multiple input values for the operational parameters to obtain a comprehensible picture of the temperature scenarios likely to happen.

Paper IV presents a method for determining the thermal properties of rock formations during the drilling operation, based on a thermal model of the well and on in-situ temperature measurements of the drilling fluid. If temperature measurements data is available, the method proposed in paper IV could be used together with SRA to decrease the uncertainty regarding the calculated temperatures.

Chapter 5

Initial Findings on the Impact of Temperature

The proposed approach for incorporating temperature to the wellhead fatigue assessment methodology is presented as a two-part case study based on analytical models, and which combines Papers I, II and III. The results of the first part of the study are included in this chapter, which covers and expands on the results presented in Papers I and II.

Both papers investigated the effect temperature would have on the local and global analyses of the wellhead fatigue assessment, but at different stages in the life cycle of a well. Paper I looked at the wellhead during reentry operations, while Paper II focused on the early stages of the drilling process. Their results enabled to later improve the implementation of the proposed approach.

Chapter 5 is not a direct translation of Papers I and II, but a study that complements the findings of these papers. It focuses on the drilling operation, when only the conductor and surface casing have been installed. This chapter compares the fatigue damage estimates according to the conventional procedure (Chapter 3) and to the proposed approach (Chapter 4).

The combined effect that temperature distribution and cement levels might have on the stress response of the wellhead analytical models was investigated. The main motivation being that it has been shown that the TOC on the surface casing annulus has a significant impact on the stresses calculated at the wellhead (Valka and Fowler 1985, Britton and Henderson 1986, Boehm 1986, Hørte et al. 2013, Reinås et al. 2012b). But also, the "effective" TOC level, relevant for wellhead fatigue modeling, may be unknown and influenced by different factors:

- The cement slurry hydrostatic pressure can break down weak formations and lower the unsettled cement level, as well as cement near the top of the well may not properly bond to the casing strings (Britton and Henderson 1988).
- The riser induced lateral movements of the high-pressure housing and the surface casing, relative to the conductor, towards the cement sheath can cause micro annuli and cement-sheath failures (Nelson and Guillot 2006).
- The prolonged curing time of cement at the top of the well because of low temperatures close to the sea bed can exceed the wait on cement time, thus making the well more susceptible to annulus cement gap due to relative casing movements (Reinås 2012).

5.1 System Description

5.1.1 Wellhead Analytical Model and Fatigue Hot Spots

Figure 5.1 presents the upper part of the 3D wellhead model created on the commercial software Ansys Workbench v16.2 (Ansys 2016) for the structural calculations in the local response analysis. The color code on the top right identifies the components that make up the 3D model: surface casing, conductor, cement sheaths, low-pressure housing, high-pressure housing, and the lock ring that locks the two housings. Seabed level is located at the level of the top of the conductor cement. The red arrows in Figure 5.1 indicate the fatigue hot spots considered:

- Lock ring between the high-pressure housing and the low-pressure housing.
- Welded joint between surface casing and high-pressure housing.
- Welded joint between conductor and low-pressure housing.

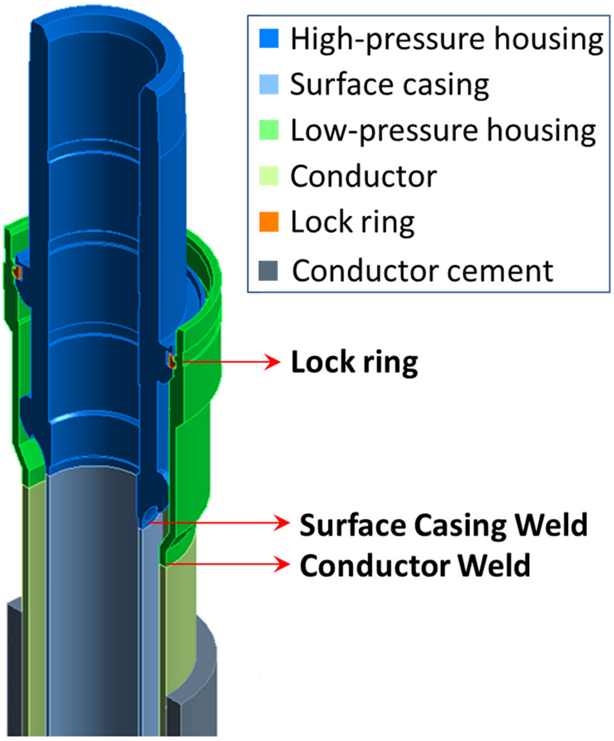

Figure 5.1 – Location of fatigue hot spots on 3D wellhead model of case study.

5.1.2 Cement Shortfall

The effects of cement shortfall of the surface-casing cement were investigated by establishing four wellhead configurations with different TOC levels: 2, 5, 10 and 25 meters below the mudline.

5.1.3 Soil Springs, Guide Bases and Templates

Conductor and soil interaction was modelled using non-linear soil springs acting on the XZ plane (Figure 5.2) and distributed along the depth of the conductor corresponding to the identified soil layers. One spring is modelled for each soil layer; each spring is connected to a master node at the center line at the corresponding soil layer's mean Y-level, which in turn is connected to the outer nodes (blue dots in Figure 5.2) of the elements facing the soil.

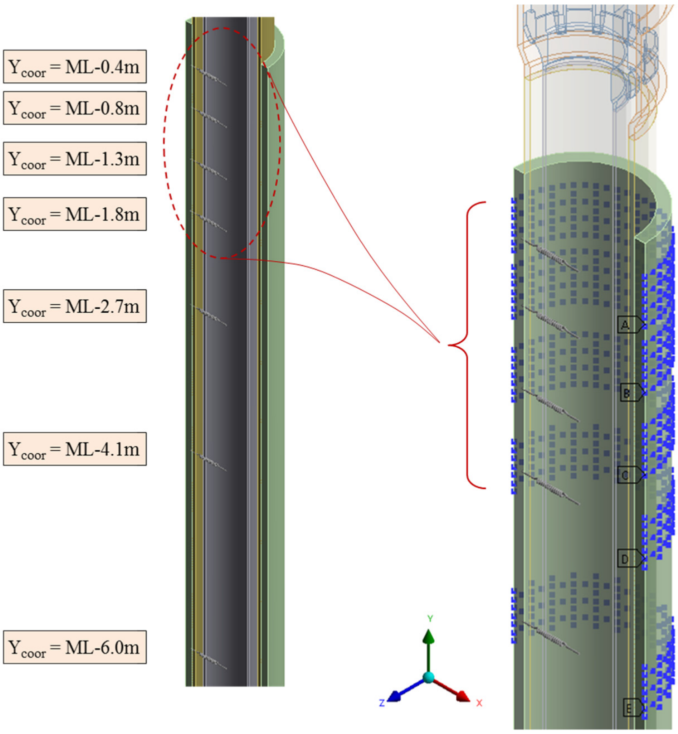

Figure 5.2 – Vertical distribution of soil springs and connection to conductor.

The transversal and rotational stiffness of the guide bases (Figure 5.3, left side) were included in the wellhead model by connecting a rotational spring to the outer nodes of the low-pressure housing (Figure 5.3, right side), so that the displacement behavior of the wellhead model is accurate enough while allowing for shorter computational times. A similar technique may be employed to model the interactions with a template.

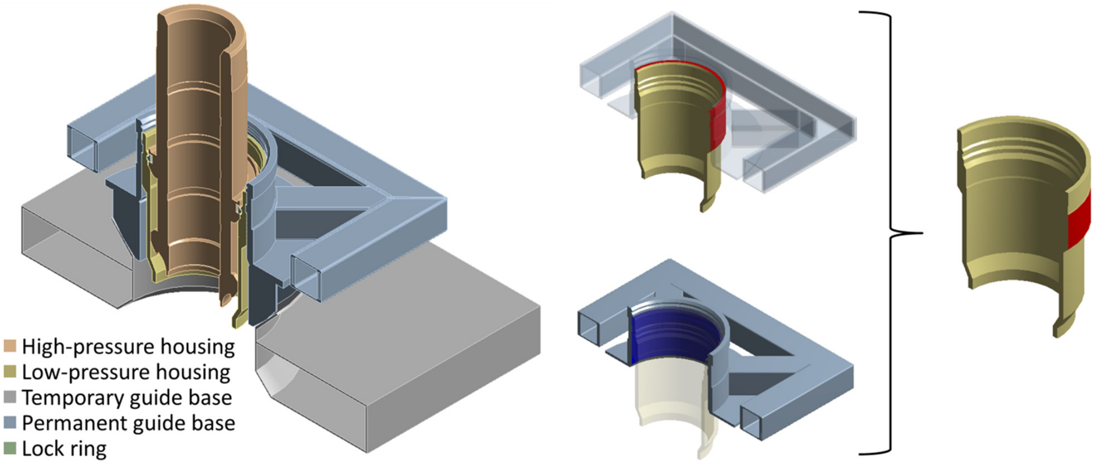

Figure 5.3 – Left: Wellhead and guide base contact surfaces. Right: Surface to which spring was connected to simulate guide base/wellhead interaction.

5.1.4 BOP Modelling

A simplified representation of the BOP and its connection to the wellhead was used. The BOP was modelled as a beam connected to the top surface of the high-pressure housing. The beam was modeled with a height of 13.1 m and linear weight corresponding to the total weight of the equivalent BOP equipment.

5.1.5 Well Tubular Components

The modelled well is vertical. The total length of the surface casing is 500 m, and the total length of the conductor is 100 m, the same for the conductor cement. Total length of the surface-casing cement is dependent on the modelled TOC level. The uppermost 50 m long sections of the tubular components were modelled using solid elements, while the remainder was modelled using shell elements. This approach was used for both analyses, with and without temperature, to ensure the comparability of results.

5.1.6 Well-Temperature Distribution

The in-house wellbore-thermal model was used to carry out the temperature calculations. The simulated operation was the drilling of the 17½-in. wellbore section, right after the BOP has been landed and the marine-drilling riser has been connected to the wellhead. Total duration of simulated operation was 70 hours. Initial temperature condition of the well was assumed to be the undisturbed formation temperature.

5.2 System Loads

5.2.1 Static Loads

At the first calculating step of the FEA the wellhead model is subject to the riser tension at the top of the BOP and the self-weight of the model's components, in addition to the effects induced by the temperature distribution. These forces and the temperature distribution are kept constant throughout the subsequent steps of the FEA.

The riser tension applied at the top of the BOP was 50 kN. Total mass of the BOP was 160 tons. Since the BOP is represented by a geometrically simplified component in the wellhead model, the specific mass of the simulated component was adjusted to comply with the weight of the equipment. For the remaining components, the average specific mass of steel or cement was used.

5.2.2 Quasi-static Loads

The environmental loads are simulated by imposing a shear force at the top of the BOP in incremental steps, to produce a bending moment at the wellhead datum that corresponds to the expected load transferred by the riser to the wellhead during real operations.

Based on previously published studies on wellhead fatigue, it can be expected of the sea states found on the NCS to produce maximum bending moment loads in the wellhead around the 1000 kNm mark order of magnitude. In this case study, the applied bending moment was ramped up to the maximum value of 1300 kNm.

5.3 Results

5.3.1 Local Response Analysis – Stress Levels and Load-to-Stress Curves

Table 5.1 presents some of the results yielded by the structural analyses carried out for each of the wellhead models with different TOC levels. The table compares the calculated maximum stresses for three fatigue hot spots, with and without temperature incorporated into the calculations. The stresses shown correspond to the step in the calculations before the application of bending moment, and therefore the stress distribution is symmetrical. Overall, the stress levels for the considered fatigue hot spots were significantly affected by the imposed temperature distribution.

Looking at the stresses in the tubular components, the surface casing weld was subject to a larger compression stress because of the restrained thermal expansion of the surface casing, while the conductor weld was subject to a smaller compression stress because of the induced thermal expansion.

Moreover, the impact of the temperature distribution in the stress levels of these two components is influenced by the length of the cement column between them. The largest differences in stress levels were obtained for the wellhead model with TOC=ML-2m, and this difference decreased as the TOC became deeper and the section of casing free to thermally expand increased.

Table 5.1 – Largest stress levels relevant* for fatigue calculations (MPa). Calculated with the local response analysis before bending moment load is applied at the wellhead datum.

	Surface Casing Weld		**Conductor Weld**		**Lock Ring**	
TOC level	**With temperature**	**Without temperature**	**With temperature**	**Without temperature**	**With temperature**	**Without temperature**
ML-2m	-37.2	-20.1	-11.2	-20.3	57.5	71.9
ML-5m	-32.9	-19.9	-11.2	-18.8	58.5	72.1
ML-10m	-28.8	-19.7	-13.5	-18.7	58.1	72.1
ML-25m	-25.0	-18.7	-15.7	-18.2	57.8	72.2

***Relevant stress for the lock ring is the equivalent von Mises stress. Relevant stress for the welded connections is the algebraically largest principal stress (negative sign means compression).**

Regarding the stress levels in the lock ring, the results of the 3D structural analyses indicate that the thermal expansion of the tubular components led to lower von Mises stress levels on the lock ring. Moreover, the resulting stress levels seem to not be significantly affected by the TOC level, as the values obtained for the four wellhead models remained approximately the same. A possible explanation for this is that, for each of the different wellheads, though the individual contributions of the principal stresses do change according to the TOC level, the summed effect of these stresses approach the same value.

Table 5.2 expands on the results of Table 5.1 by presenting the calculated principal stresses acting on the lock ring for the different wellhead models and comparing the results for the analyses with and without temperature. The principal stresses on the lock ring are affected by both the induced temperature and the TOC, however the equivalent stress (Table 5.1) remains approximately the same.

Table 5.2 – Principal stresses acting on the lock ring calculated by the local response analysis before the application of bending moment load at the wellhead datum.

	MINIMUM		MIDDLE		MAXIMUM	
TOC level	**With temperature**	**Without temperature**	**With temperature**	**Without temperature**	**With temperature**	**Without temperature**
ML-2m	-52.8	-70.3	-15.9	-4.5	12.2	6.9
ML-5m	-54.7	-70.2	-18.7	-5.2	11.7	7.3
ML-10m	-52.7	-70.2	-20.6	-5.0	15.7	7.4
ML-25m	-58.1	-65.8	-16.3	-2.6	18.7	5.1

During the structural calculations, with the application of bending moment, the stress levels presented in Table 5.1 may either increase or decrease, depending on whether the material location being inspected is originally under compression or tension. Nonetheless, the trends shown in Table 5.1 are kept throughout the steps of the calculations; for the surface casing weld, for example, the compression stress levels obtained by the simulations with temperature are always larger than the corresponding stresses yielded by the simulation without temperature.

However, for fatigue calculations purposes it is necessary to look at the cyclic stresses, or how much stress levels on fatigue hot spots are changing by the incremental bending moment load. Thus, Figure 5.4, Figure 5.5 and Figure 5.6 present the load-to-stress curves generated by the local response model, for the three different fatigue hots spots, under four different TOC configurations, with and without temperature effects.

Figure 5.4 and Figure 5.5 present the results for the surface casing weld and the conductor weld, respectively. The curves show the correlation between the value of the algebraically largest principal stress at the welded connection and the bending moment at the wellhead datum. Figure 5.6 shows the value of the equivalent (von Mises) stress calculated at the lock ring according to the bending moment loading at the wellhead datum.

It can be seen in Figure 5.4 that the largest cyclic stresses were found for the wellhead configurations with the TOC closer to the mudline. When comparing the results obtained for wellheads with the same TOC depth it can be seen that the thermal effects incorporated to the analyses led to lower cyclic stresses at the surface-casing-weld-fatigue hot spot.

For the wellhead configuration with TOC=ML-2m the cyclic stress levels corresponding to a bending moment of 1300 kNm decreased from approximately 105 to 90 MPa. The corresponding reduction in stress calculated for the wellhead configuration with TOC=ML-5m was from 70 to 60 MPa. The stress levels obtained for the two remaining wellhead configurations were similar in value; the corresponding stress reduction was, approximately, from 61 MPa to 50 MPa.

In Figure 5.5 it is shown that the stress levels calculated for the conductor weld are significantly smaller than that the stress levels obtained for the surface casing weld. The trend detected in Figure 5.4 is now reversed, with the largest stresses found for the wellhead configurations with the TOC farther away from the mudline. In absolute values, the reduction on stress levels ranged between 7.5 and 10 MPa. The largest reduction was calculated by the analysis for the wellhead configuration with TOC=ML-25m.

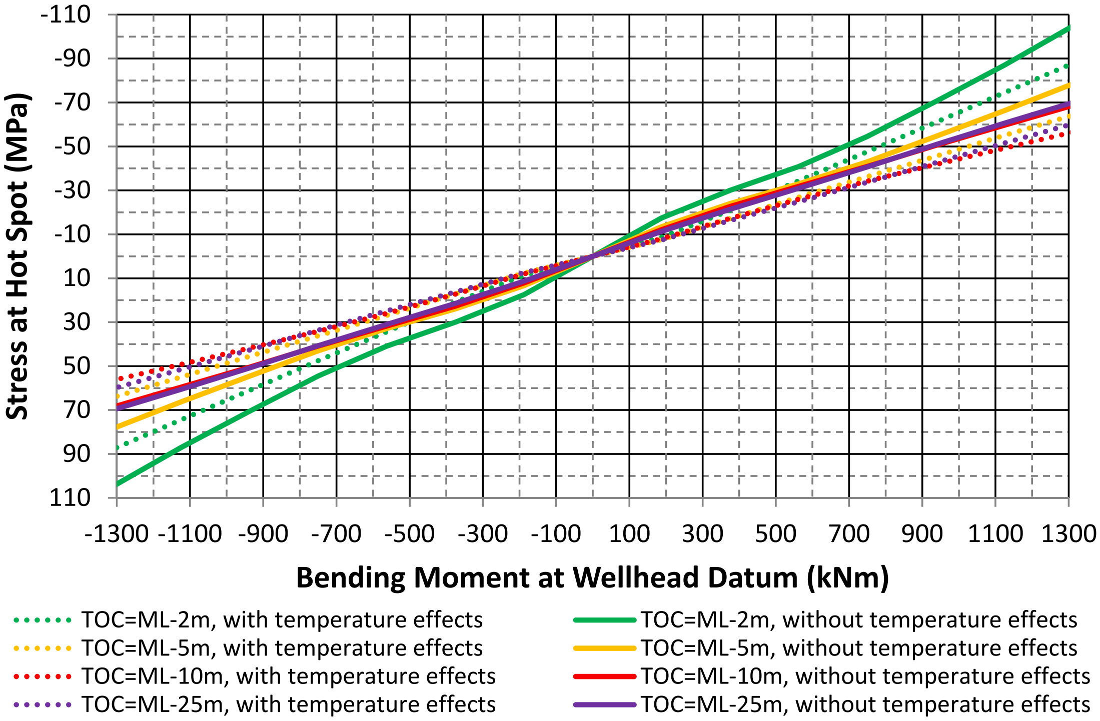

Figure 5.4 – Load-to-stress curves generated for the surface-casing-weld-fatigue hot spot.

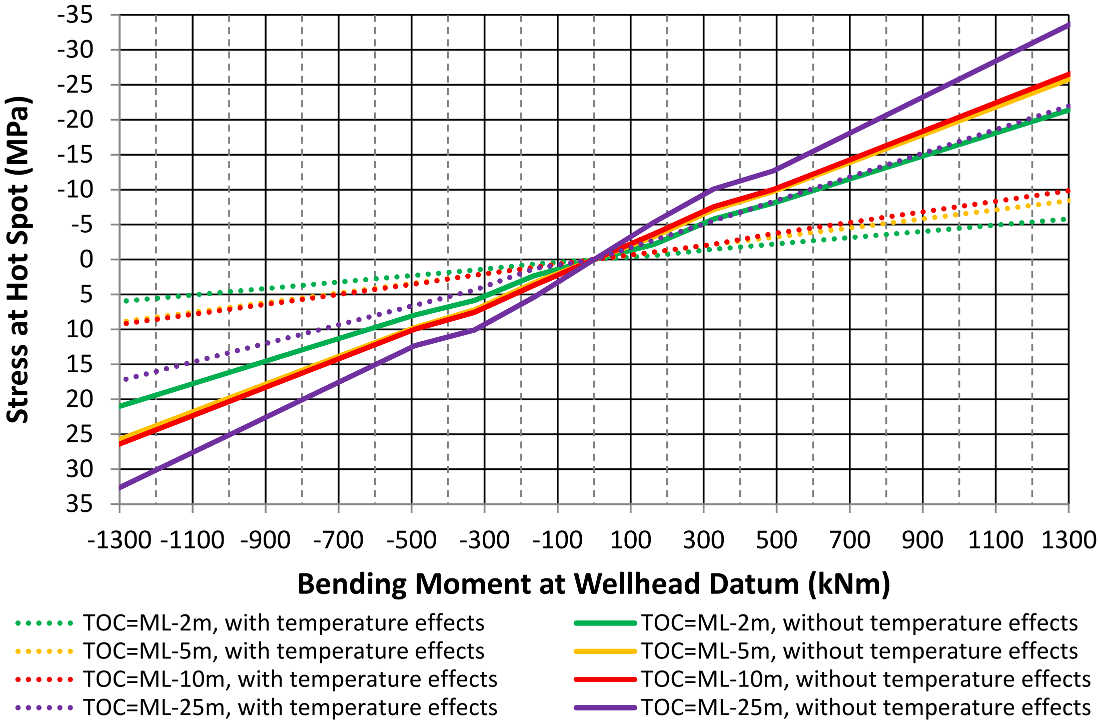

Figure 5.5 – Load-to-stress curves generated for the conductor-casing-weld-fatigue hot spot.

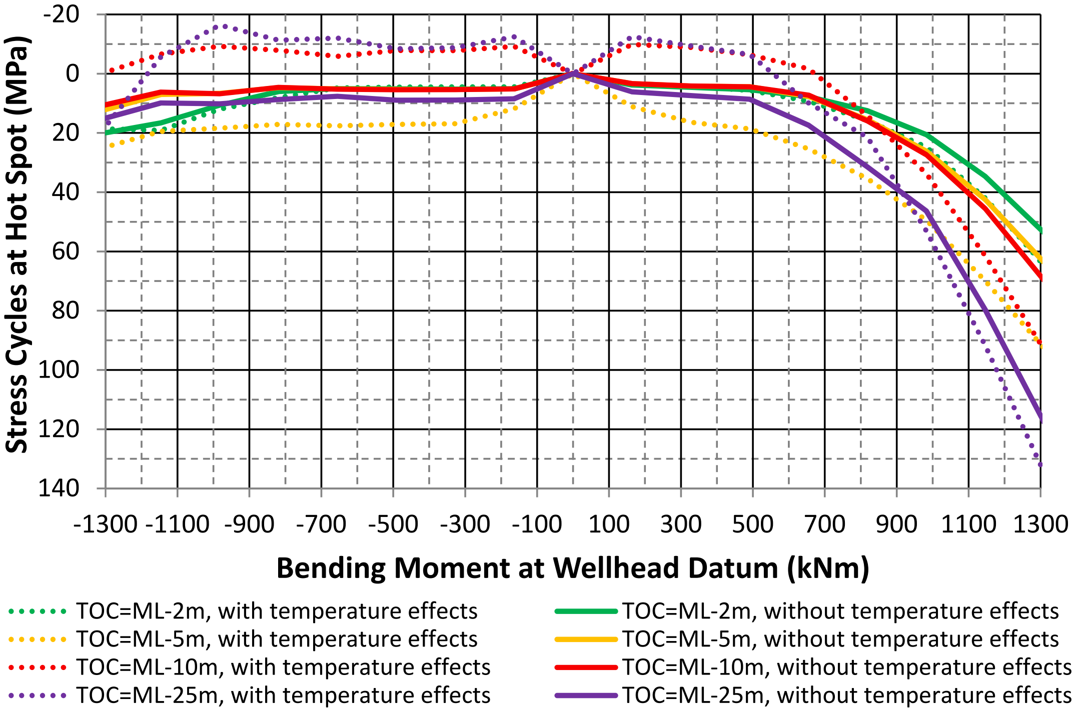

Figure 5.6 – Load-to-stress curves generated for the lock ring fatigue hot spot.

Figure 5.6 presents the stress levels calculated on the lock ring. Figure 5.7 shows where the stresses were extracted from, the red circle at the top contact surface between the lock ring and the high-pressure housing. It also shows three snapshots of the geometric configuration assumed by the lock ring, the high-pressure housing, and the low-pressure housing during different loading scenarios, which explain the shapes of the curves in Figure 5.6.

In snapshot *A* there is no bending moment load applied to the model, and the wellhead rests straight. In snapshot *B* it can be seen the configuration assumed when maximum bending moment is applied to the counterclockwise direction of the axis exiting the paper. The model is "bending" to the left, and the lock ring is in contact with both wellhead housings.

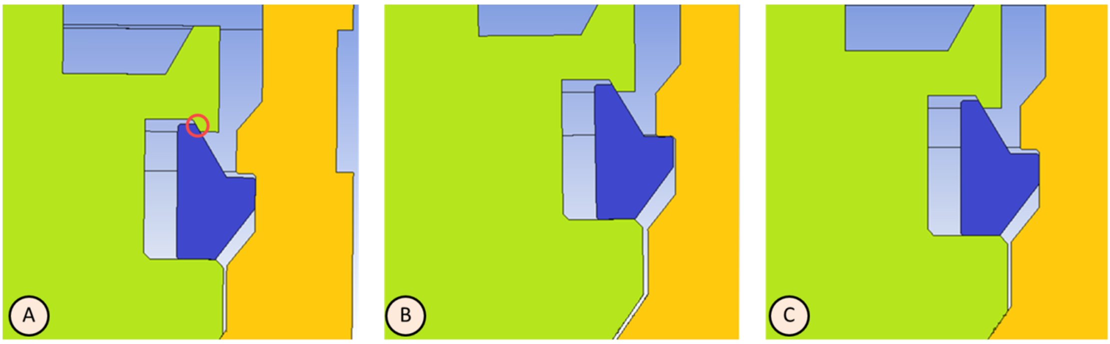

Figure 5.7 – Contact configuration of lock ring (blue), high-pressure housing (green) and low-pressure housing (orange) under different bending moment loads. A: No bending. B: -1300 kNm. C: 1300 kNm.

The stress distribution on this configuration is such that the stress levels on the fatigue hot spot considered vary only slightly. In snapshot C the bending moment is being applied to the clockwise direction, the model is “bending” to the right, and the stress levels increase significantly.

Contrary to the previous set figures, Figure 5.6 shows that the cyclic stress levels on the lock ring fatigue hot spots increase when temperature has been incorporated to the analysis. The largest increase in cyclic stress levels was computed for the wellhead configuration with TOC=ML-5m, approximately 30 MPa corresponding to an applied bending moment of 1300 kNm. However, for the wellhead configuration with TOC=ML-25m the increase was approximately 17 MPa.

A common trend for the three fatigue hot spots extracted from the structural analyses, presented in Table 5.3, is that the contribution of temperature to the stress levels seems to decrease significantly for the wellhead model with TOC level located 25 m below the mudline. For an applied bending moment of 1300 kNm, the stress calculated on the surface casing weld of the wellhead model with TOC=ML-2m by the analysis without temperature was 16.8 MPa higher than the results by the analysis with temperature, while the same comparison for the wellhead model with TOC=ML-25m yielded a stress level only 9.7 MPa higher.

For the lock ring, the effect of the TOC level becomes more prominent. The calculated differences between the analyses with and without temperature are 52.0 MPa and 15.8 MPa, respectively, for the wellheads with TOC=ML-2m and TOC=ML-25m. However, the stress levels calculated for the three fatigue hot spots of the wellhead models with the intermediary TOC levels do not follow all the same trend, with the surface casing weld being the only one that shows an apparent linear trend between TOC level, stresses and temperature.

Table 5.3 – Maximum stress level calculated by the analyses with temperature for different TOC levels, subtracted by the corresponding stress level calculated without temperature.

	Stress level difference between analyses with and without temperature			
Fatigue Hot Spot	**TOC=ML-2m**	**TOC=ML-5m**	**TOC=ML-10m**	**TOC=ML-25m**
Surface Casing Weld	17.0	14.2	12.1	9.7
Conductor Weld	15.7	17.5	16.8	11.7
Lock ring	52.0	49.6	61.7	15.8

5.3.2 Local Response Analysis – Wellhead Beam-Proxy Models

The wellhead used in the structural analyses is modeled in the riser analyses as a vertical beam, with its lowermost extremity fixed underground and connected to a non-linear spring at the mudline level, as described in section 3.2.3 and shown in Figure 3.7.

The beam models corresponding to all the wellhead configurations in this study had the same elevation above the mudline. The variation from one proxy model to another was the total length, bending stiffness, and soil spring stiffness. Figure 5.8 and Table 5.4 describe the wellhead beam-proxy models created.

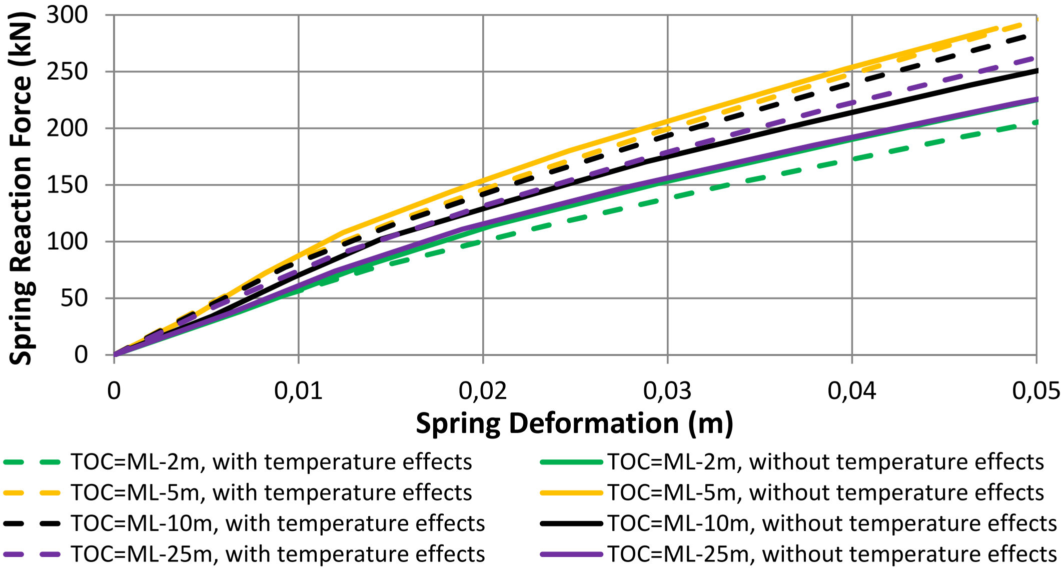

Figure 5.8 – Wellhead beam-proxy models non-linear springs.

It can be seen in Figure 5.8, for the two configurations with the TOC level closer to the mudline, TOC=ML-2m and TOC=ML-5m, that the wellhead model with temperature effects is represented by a spring with a higher stiffness value than the spring of the wellhead model without temperature effects.

This trend is reversed for the two remaining wellhead configurations, TOC=ML-10m and TOC=ML-25m, as less stiff springs are generated. Moreover, the impact of the temperature distribution on the spring characteristics seems to become larger the farther away from the mudline the TOC level is.

Table 5.4 shows that all the wellhead configurations subjected to temperature effects are represented by beam-proxy models with higher bending stiffness, and smaller total length. Recalling the discussion in section 3.2, the smaller length of the beam-proxy model, and therefore a point of fixity closer to the mudline, seems to be in accordance with the higher stress levels calculated in the surface casing weld by the analyses with temperature, as so do the higher bending stiffness values obtained for the model.

Table 5.4 – Wellhead beam-proxy models characteristics.

	Beam total height, H (m)		**Beam bending Stiffness, EI (GPa)**	
TOC level	***Analysis with temperature***	***Analysis without temperature***	***Analysis with temperature***	***Analysis without temperature***
ML-2m	13.0	13.0	2.10	1.86
ML-5m	11.0	12.3	1.98	1.60
ML-10m	11.3	13.4	1.97	1.76
ML-25m	11.0	13.5	2.05	1.69

5.3.3 Global Response Analysis – Wellhead Loading History

The riser dynamic response analysis is indirectly affected by the temperature distribution in the well because of the wellhead beam-proxy model that couples the local and the global analyses. The global response analysis comprised eight different riser models, one for each of the beam-proxy models created due to TOC level and temperature scenario, to determine the influence temperature might have on the calculation of the loading time histories.

A dynamic response analysis of the riser models was carried out for each of the sea states presented in Table 3.3. The simulated time in the analyses was 7200 s, with 0.1 s time steps. The sea states' short-term loading time histories obtained were fed into a cycle counting routine and the resulting cycles per bending moment range for each sea state were extrapolated to correspond to a one-year period.

The short-term bending moment cycles count were summed up using each sea state's probability of occurrence as the weighting factor to obtain the long-term bending moment cycles count. In the fatigue assessment, the long-term bending moment cycles count is at a later stage combined with the load-to-stress curves generated by the local response analysis to estimate the fatigue damage in each fatigue hot spot.

Figure 5.9 and Figure 5.10 present a representative comparison made between the long-term bending moment cycles count obtained for the wellhead models with the TOC level 2 m below the mudline, with and without temperature. The results obtained for the remainder TOC levels are presented in Annex C. The bending moment interval used for cycle counting was 10 kNm.

For ease of visualization, the graph in Figure 5.9 was divided into two parts. The horizontal axis indicates the bending moment range in which cycles were detected, while the vertical axis indicates the corresponding number of cycles during a one-year period.

In Figure 5.9 (A), the cycle counts obtained for the models with and without temperature are similar for the high cycle/low load area and up until around the 700 kNm bending moment value. Past the 700 kNm mark, Figure 5.9 (B), it is possible to observe significant differences in the cycle count, with the higher cycle count obtained for the no temperature condition.

Figure 5.10 presents the cumulative bending moment cycles density. The comparison in Figure 5.10 shows that, for both temperature conditions, more than 90% of the identified bending moment cycles are lower than 800 kNm. The two cumulative cycles densities are practically identical.

The analyses for the riser models with different bottom boundary conditions comprised by the calculations with and without temperature showed that most of the identified bending moment cycles are below 700 kNm. For that value and below, the results have shown a good agreement between the loading time histories obtained for wellhead models with the same TOC, but under different temperature conditions.

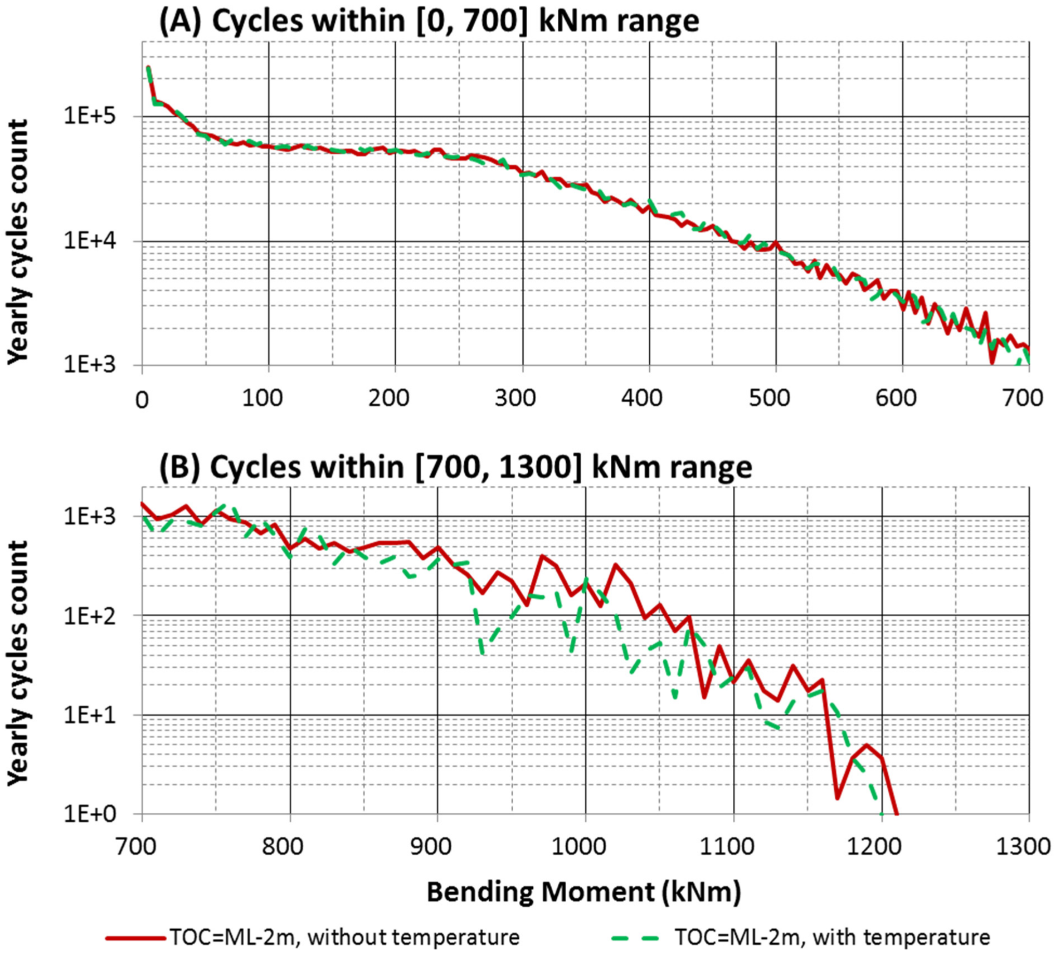

Figure 5.9 – Comparison of long-term bending moment histograms. Global riser dynamic analyses with and without temperature. TOC=ML-2m.

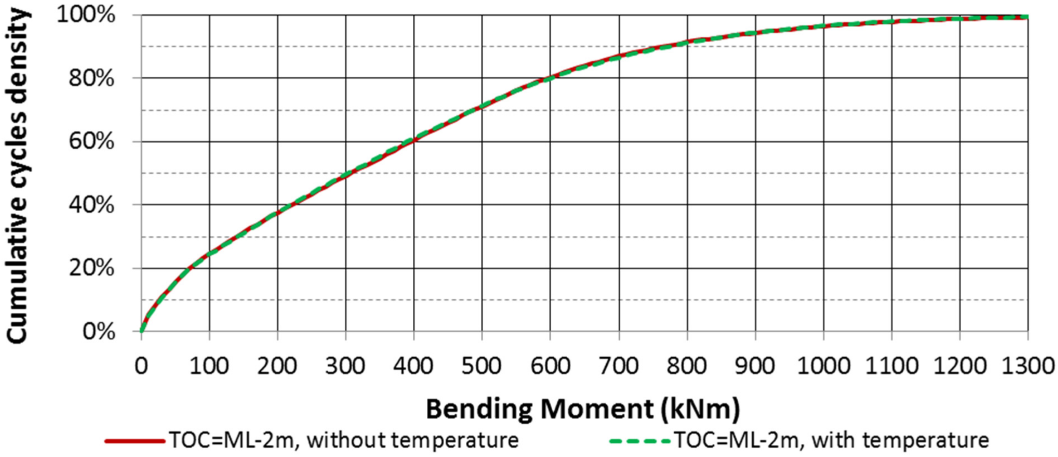

Figure 5.10 – Cumulative cycle density comparison of long-term histograms presenting the indirect impact of the temperature distribution of the well. TOC=ML-2m.

5.4 Fatigue Damage Assessment Results

The fatigue damage on a hot spot is calculated based on the estimated stress cycles it is subject to. For fatigue hot spots with a linear and symmetrical load-to-stress curve, such as the welds on the low- and high-pressure housings, it is possible to combine the load-to-stress curves with either the bending moment loading-time history or the bending moment cycles count. However, for the non-linear load-to-stress curve obtained for the lock ring fatigue hot spot it is necessary to first obtain the stress-time history, and then perform the cycle counting.

The identified stress cycles of each fatigue hot spot were paired with the corresponding S-N curve. Miner's law was used to estimate the fatigue damage incurred. The S-N curves selected to describe the behavior of the welded-connection-fatigue hot spots at the high-pressure housing and the low-pressure housing were the DNV F curve and DNV F3 curve, respectively. Both curves are used for seawater cathodic protection (DNVGL-RP-C203 2016).

The S-N curve for high strength steel for subsea applications identified as BM4 was selected for the lock ring fatigue hot spot. Curve BM4 is recommended for base material of high strength steel with tensile strength above 655 and up to 724 MPa in seawater with cathodic protection. Figure 5.11 presents the curves mentioned, as well as other curves provided by DNVGL.

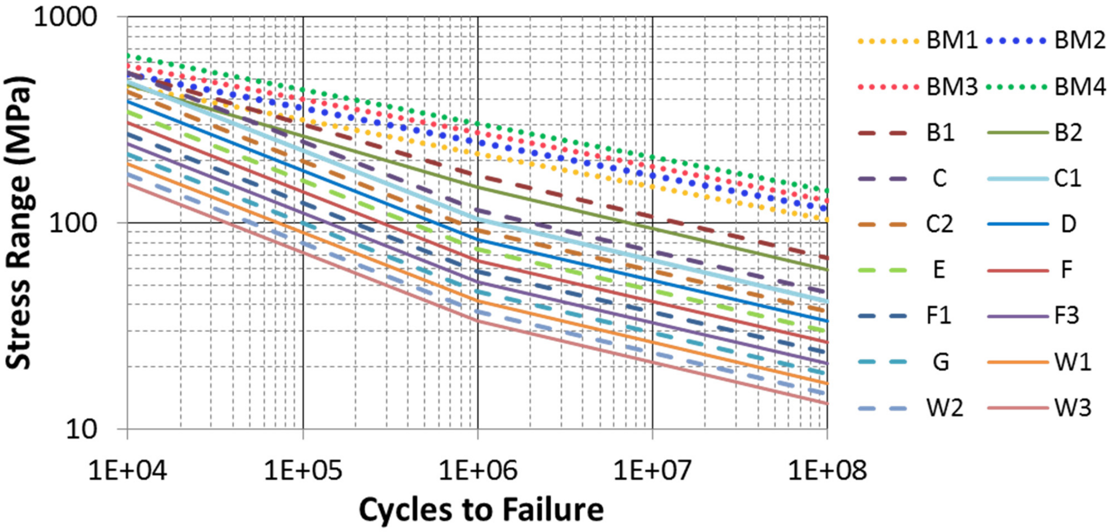

Figure 5.11 – S-N curves for seawater cathodic protection (DNVGL-RP-C203 2016).

The results of the fatigue damage assessment of the three fatigue hot spots for each of the four wellhead TOC configurations are illustrated in Figure 5.12, Figure 5.13 and Figure 5.14. The figures compare the accumulated fatigue damage after a 70 hours long drilling operation, as estimated by the analyses with and without thermal effects.

The generated load-to-stress curves revealed that, of the three fatigue hot spots, the surface casing weld is subjected to the highest stress cycles throughout the simulated sea states. However, the surface casing weld may not necessarily be the critical fatigue hot spot, because each hot spot was assigned a different S-N curve. Therefore, the fatigue damage of the conductor weld and the lock ring were also calculated to verify the trends extracted from the load-to-stress curves.

In Figure 5.12, the dark green columns present the damage estimated by the analyses without temperature as an input to the wellhead structural calculations, whereas the light green columns present the damage estimated based on the structural calculations with temperature.

An accumulated damage value of 100% would indicate that the DFF was reached. The figure reveals that the inclusion of thermal effects into the analysis led to lower fatigue damage on the surface casing weld hot spot for the four wellheads with different TOC levels.

In percentage points, the largest reduction in accumulated fatigue damage was computed for the wellhead configuration with TOC=ML-2m: from 22.4% to 11.7%. In relative values, overall, the estimates for accumulated fatigue damage for all wellheads were around 50% smaller.

The results shown in Figure 5.12 are based on temperature profiles which correspond to a moment in time 70 hours after continuous drilling operation. That is an instantaneous snapshot of the conditions that can be found in the well and could only be considered valid for a brief period. It is expected that the temperature distribution of the components inside the well will greatly vary during the different operations performed during well construction.

While approximating the expected reduction in accumulated fatigue damage, the results in Figure 5.12 show that the reduction, or in more general terms the difference, obtained when comparing estimates generated by analyses with and without temperature could be significant.

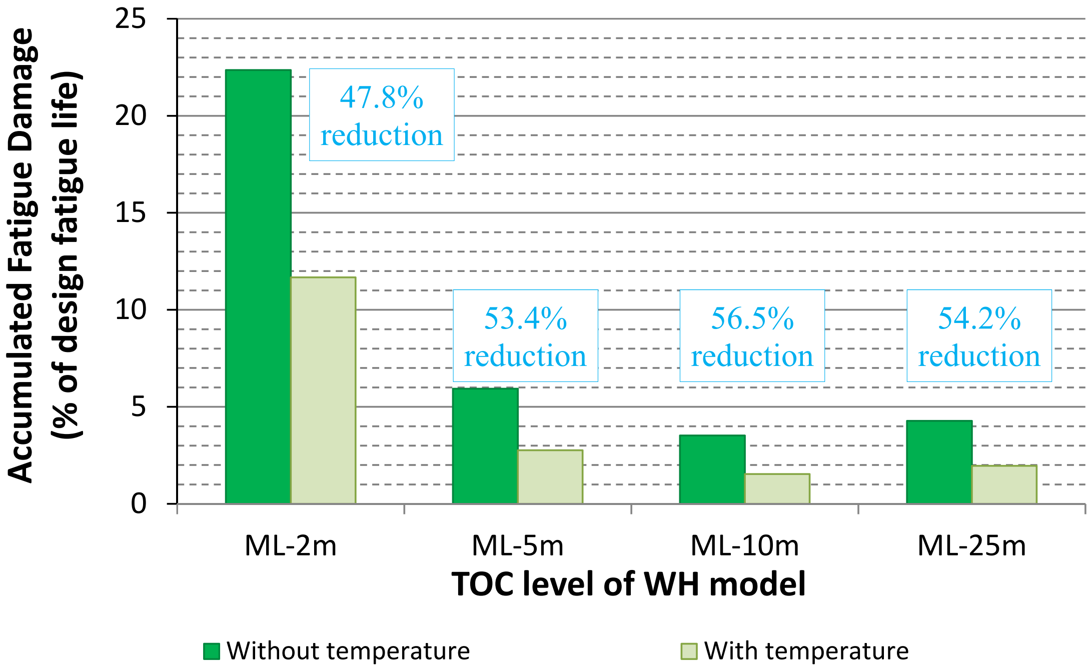

Figure 5.12 – Comparison of accumulated fatigue damage on the surface casing weld after 70 hr of drilling operation. DFF=10. S-N curve F for seawater cathodic protection.

Figure 5.13 presents the estimated fatigue damage on the welded connection between the conductor and the low-pressure housing. Results for the four considered TOC levels are displayed.

It may be established that the inclusion of temperature in the calculations resulted in considerable reduction of the estimated fatigue damage: in relative terms, more than 90% for the four TOC levels. The largest reduction in percentage points was computed for the wellhead with TOC=ML-25m; the estimated accumulated fatigue damage went from 19.1% to 1.7%.

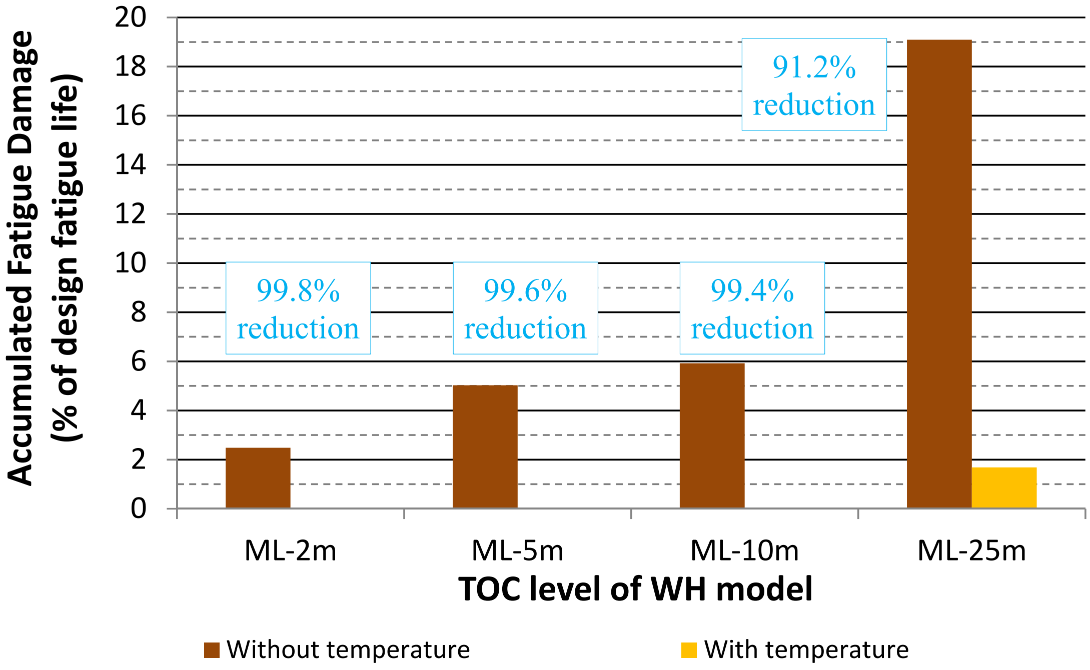

Figure 5.13 – Comparison of accumulated fatigue damage on the conductor weld after 70 hr of drilling operation. DFF=10. S-N curve F3 for seawater cathodic protection.

Figure 5.14 presents the accumulated fatigue damage estimated for the lock ring. For this hot spot, the inclusion of temperature into the structural analyses resulted into higher estimated fatigue damage. This effect was more significant for the wellhead models with TOC closest to the mudline; nonetheless, the estimated accumulated fatigue damage for the four wellheads remained below 4.4%.

Considering the analyses without temperature from the three previous figures, it can be established that one of the welded connections is the critical component for fatigue damage on the wellhead. For the two wellheads with the shallowest TOC, the high-pressure housing weld is the critical fatigue hot spot. For wellheads with the TOC level equal to and below 10 m, it is the low-pressure housing weld that becomes the critical fatigue hot spot.

Considering the analyses with temperature, the high-pressure housing weld remains the critical fatigue hotpots for two wellheads with the shallowest TOC. However, the lock ring becomes the critical fatigue hot spot for the other two wellheads. Table 5.5 summarizes the results presented in Figure 5.12, Figure 5.13 and Figure 5.14.

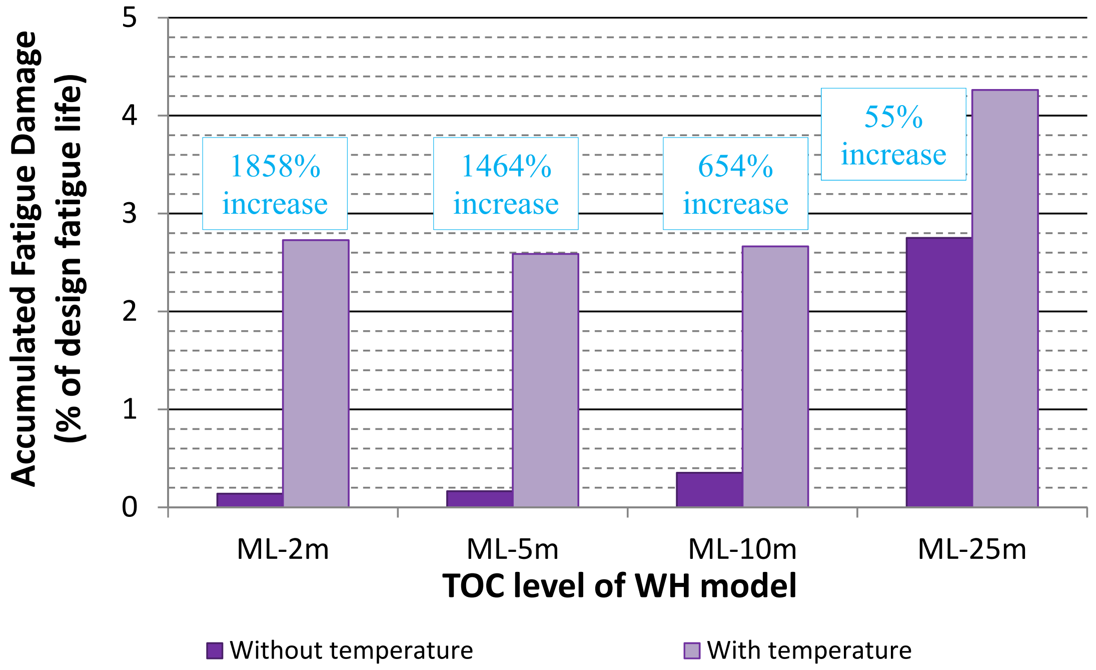

Figure 5.14 – Comparison of accumulated fatigue damage on the lock ring after 70 hr of drilling operation. DFF=10. S-N curve BM4 for seawater cathodic protection.

Table 5.5 – Estimated accumulated fatigue damage on the wellhead.

	Critical Hot Spot		**Accumulated Fatigue Damage (% of design-fatigue life)**	
TOC level	***Analysis without temperature***	***Analysis with temperature***	***Analysis without temperature***	***Analysis with temperature***
ML-2m	Surface casing weld	Surface casing weld	22.4	11.7
ML-5m	Surface casing weld	Surface casing weld	5.90	2.80
ML-10m	Conductor weld	Lock ring	5.92	2.70
ML-25m	Conductor weld	Lock ring	19.1	4.30

5.5 Discussion

The case study presented in chapter 5 intended to investigate how each part of the wellhead fatigue assessment methodology would respond to the implemented temperature input. Some general conclusions can be drawn from the results obtained, but these are not meant to categorically answer whether well temperature would reduce or decrease the estimated wellhead fatigue damage, and to what extent.

For that purpose, extensive analyses would be necessary, representing the different mechanical configurations of the wellhead, and the diverse thermal conditions found in the well. The results found from this case study, however, enabled the remarks presented in the following sections.

5.5.1 Local Response Analysis

The results of the local response analyses performed in this case study have shown that the induced temperature distribution of the well can have diverse effects over the different wellhead fatigue hot spots. Whereas the cyclic stresses at the two welded-connection fatigue hot spots decreased when comparing the cyclic stress levels obtained for analyses with and without temperature, the temperature input led to higher cyclic stress levels on the lock ring.

Because of material characteristics (*i.e.* the S-N curve) the welds hot spots may be the critical hot spots in the wellhead. The TOC may determine whether the surface casing weld or the conductor weld will fail first. But the results of the analyses indicate that the temperature distribution of the well may redefine the cyclic stress and significantly reducing the fatigue damage at the hot spots. At the same time, the cyclic stress calculated for the lock ring increased, indicating that because of the temperature loading in the well, the focus of the wellhead fatigue assessment might need to be directed to other hot spots.

The welded connections are distant from the contact points of the two housings, but the lock ring is located between the housings and thus is more dependent on the load path and interactions between low and high-pressure housings, which can be highly non-linear (Kuzmichev et al. 2017). Contrary to the welds hot spots, the lock ring's position may shift because of the forces applied by the low- and high-pressure housings and the bending moment load, thus significantly altering the stress distribution (Figure 5.6).

Hence, the location of the hot spots dictates whether the loading generated by temperature leads to lower or higher cyclic stresses. Depending on the most critical load-to-stress curves created, this can lead to either lower or higher estimated fatigue damage.

5.5.2 Global Response Analysis

The loading time series generated for each wellhead configuration are converted to a stress-time series by its respective load-to-stress curve. The results of the analyses performed have enabled to establish that the temperature has a small effect on the loading-time history, whereas the effect of temperature on the load-to-stress curves can be significant.

Figure 5.15 presents the overall impact that the wellhead proxy models, created with and without the effect of temperature, have on fatigue capacity and the estimated allowable riser connection period. The estimates were based on the fatigue damage computed for surface casing weld.

In general, by taking the temperature into account, the allowable riser connection days has approximately doubled for all the TOC cases investigated. The scenarios depicted in Figure 5.15 indicate that the indirect contribution of temperature to the loading history generated by the riser dynamic analysis has a small impact on the estimated fatigue capacity, when compared to the impact of the thermal load-to-stress curves created by the wellhead structural analysis.

The deviation in the total allowable riser connection days, induced by using the bending moment loading-time history generated without the effects of temperature loading together with the load-to-stress curves generated by the analyses with the effects of temperature loading, is:

- TOC=ML-2m → 4 fewer days, or 1.5% difference.
- TOC=ML-5m → 54 additional days, or 5.1% difference.
- TOC=ML-10m → 6 fewer days, or 0.3% difference.
- TOC=ML-25m → 186 additional days, or 12.5% difference.

For the wellhead model used in the case study, it may be generalized from the results in Figure 5.15 that large cement shortfalls (25 m) require performing both local and global response analyses with the corresponding temperature loading.

However, for wellheads with TOC level down to 10 m it might be possible to observe the full effect of temperature in the estimated fatigue damage just with the load-to-stress curves created for the predicted temperature scenarios, thus saving computational power and time without compromising the quality of the analysis.

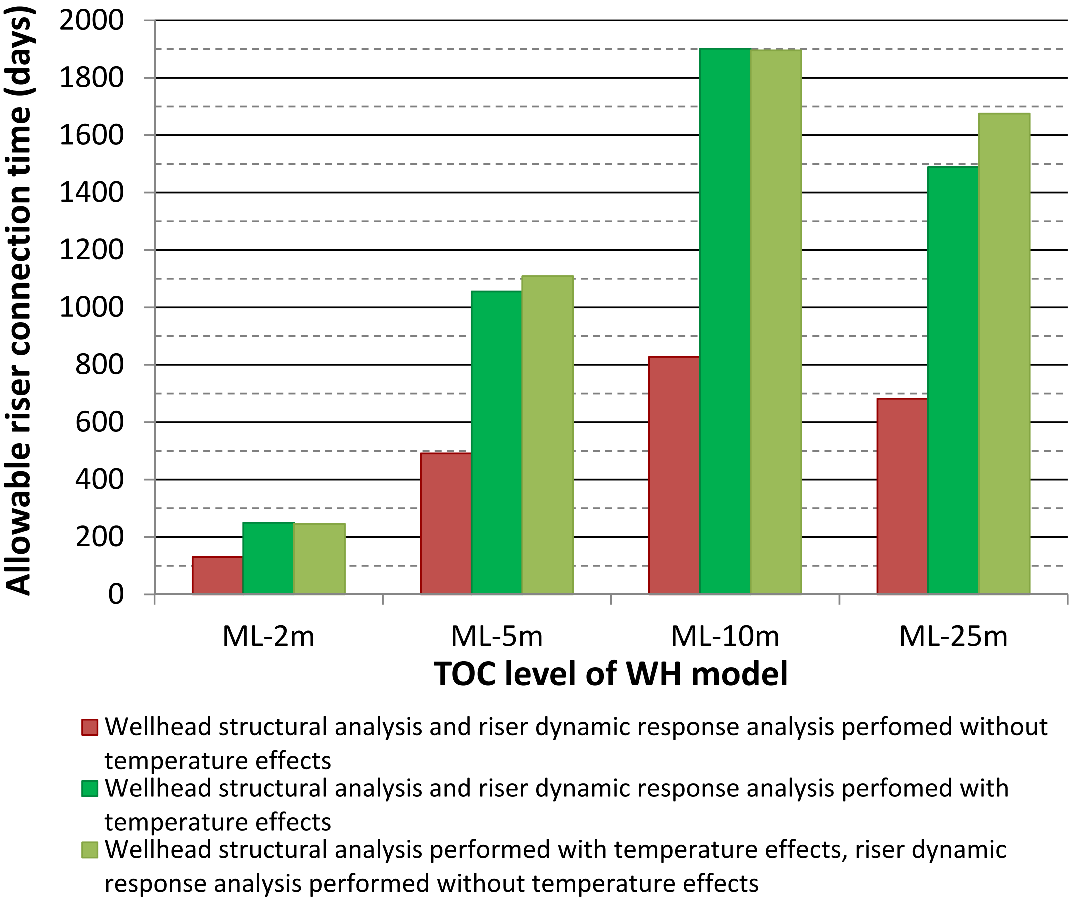

Figure 5.15 – Comparison of allowable riser-connection days before DFF is reached.

Chapter 6

Well Temperature as a Time-Varying Driver of Wellhead Fatigue

This chapter presents and expands on the results presented by Paper III. It continues the analytical investigation of the impact that the time-varying temperature distribution in a well might have on the wellhead fatigue assessment of a typical satellite subsea well in the North Sea.

Paper III comprised operations from when the BOP has been deployed and a connection has been established through the riser, to the point in time when the well is temporarily abandoned before the completion phase. It showed that temperature may alter the cyclic stresses on a fatigue hot spot and how much the corresponding fatigue estimate may be influenced.

Moreover, Chapter 6 expands the investigation made on Paper III by presenting the impact temperature has on the stress levels and the fatigue-damage rates of multiple fatigue hot spots, welds and base metal, first throughout the drilling operation and later during a workover operation. The damage estimates for the workover, together with the estimated fatigue damage accumulated during drilling, were translated into remaining operational days to fatigue failure, providing a more-readily comparison between estimates for reentry operations.

6.1 System Description

6.1.1 Cement Shortfall

Cement shortfall on the annular space between the 20-in. surface casing and the 30-in. conductor remains a relevant variable of the study. However, the investigation has now been limited to two scenarios:

- Wellhead with TOC level 2 m below the mudline; designated as Wellhead A.
- Wellhead with TOC level 10 m below the mudline; designated as Wellhead B.

6.1.2 Fatigue Hot Spots

In Figure 6.1, the red arrows indicate the wellhead fatigue hot spots added to the analysis:

- Lower outer edge of the conductor low-pressure housing.
- Welded connection between the conductor’s first and second joints.
- Lower outer edge of the surface casing high-pressure housing.
- Upper outer edge of the surface casing high-pressure housing.
- Welded connection between the surface casing’s first and second joints.
- Welded connection between the surface casing’s second and third joints.
- Surface of the low-pressure housing on which the high-pressure housing is landed.

6.1.3 Well Geometry

The casing program of the wellhead system used in the case study is presented in Figure 6.2. It consists of four casing strings and one liner. True vertical depths (TVD) of the bottom of the strings are shown in the figure, maximum TVD of the well is 2000 meters below the mudline. The water depth of the location is 330 meters.

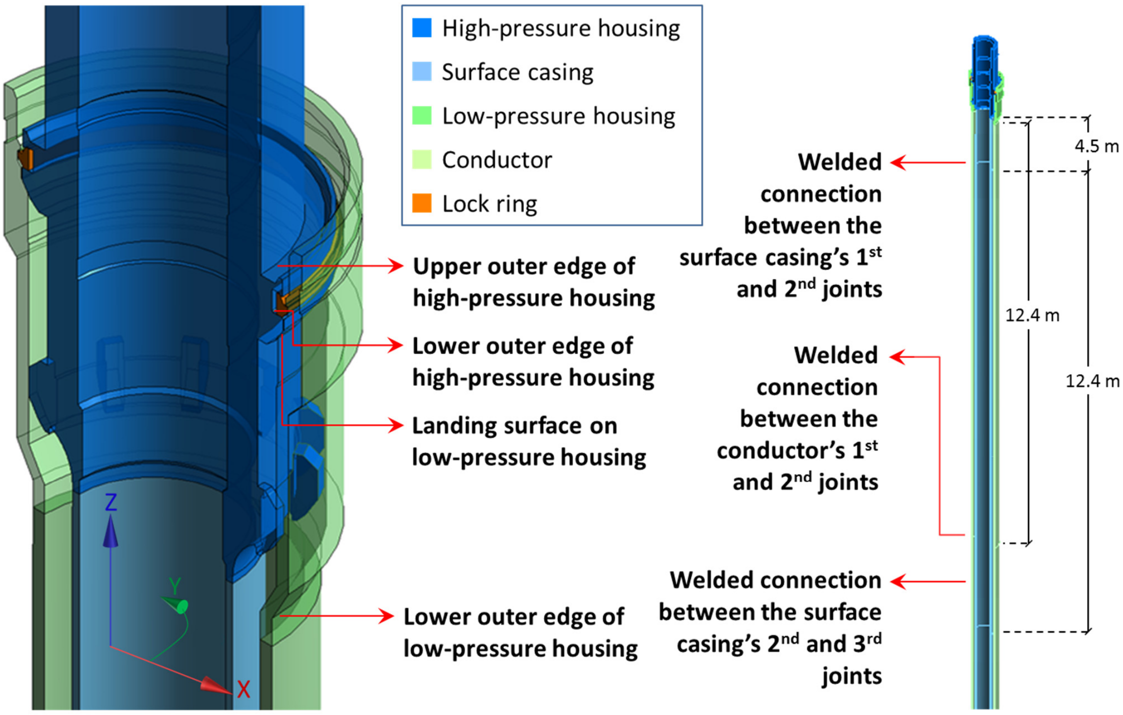

Figure 6.1 – Fatigue hot spots included in the case study.

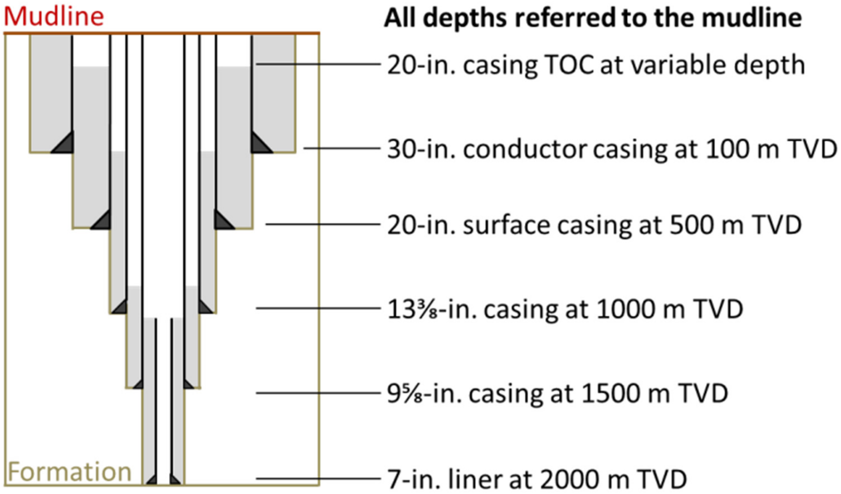

Figure 6.2 – Casing program of well modelled in the case study.

6.1.4 Simulated Well Operations

The simulated drilling covered different well operations performed when drilling a subsea well. Table 6.1 lists those well operations that were simulated in the study, along with their start and finish points. These actions are grouped according to the operational phase in the well, and the third column in the table indicates what prompted the change in operational phase.

Table 6.1 – Well operations being carried throughout time.

Start-end (hour)	Description of operation	Wellhead geometry change
0-2	Circulating well	BOP/Riser connection
2-50	Drilling ahead	
50-60	Circulating well	
60-70	Retrieving drillstring	
70-90	Running 13⅜-in. casing	
90-103	Retrieving/deploying drillstring	13⅜-in. casing suspended from WH
103-105	Circulating well	
105-108	Cementing the 13⅜-in. casing	
108-131	Retrieving/deploying drillstring	
131-181	Drilling ahead	13⅜-in. casing cemented
181-191	Circulating well	
191-201	Wait on weather	
201-215	Retrieving drillstring	
215-234	Running 9⅝-in. casing	
234-240	Retrieving/deploying drillstring	9⅝-in. casing suspended from WH
240-242	Cementing 9⅝-in. casing	
242-260	Retrieving/deploying drillstring	
260-354	Drilling ahead	9⅝-in. casing cemented
355-375	Circulating well	
375-395	Retrieving the drillstring	
395-420	Running the 7-in. liner	
420-444	Retrieving/deploying drillstring	7-in. liner suspended from 9⅝-in. casing
444-450	Cementing 7-in. liner	
450-461	Retrieving the drillstring	

To simplify the overall fatigue analysis, the simulated drilling operation was an ideal one, meaning that operational parameters were kept constant and non-productive time was almost non-existent. Table 6.2 lists typical values used for operation parameters such as tripping speed, rate of penetration, and drilling fluid flow rate.

Table 6.2 – Operational parameters and typical values adopted.

Parameter	Value	Unit
Tripping speed	60-100	m/h
Rate of penetration	10	m/h
Drilling fluid flow rate	800	l/min

The mechanical response of the wellhead during operational phases other than drilling, along with how the temperature on the well might affect the fatigue damage incurred, was also investigated. However, there are several different well operations that can be carried out during completion, intervention, or workover. It would be impracticable for the sake of this investigation to analyze all of them. Because of that, it was opted to create a single simplified workover procedure that would serve as a substitute for the procedures performed after drilling is completed.

The drilling and workover operations simulated comprise each a different riser and subsea stack, as seen in Figure 6.3. In both scenarios, the riser models were subjected to the environmental loads generated by the expected sea states and current at a North Sea location. The same heave-compensation and tensioners system was used as the upper boundary condition for both models.

In accordance with the previous case studies (section 5.3.3), it was deemed that the temperature distribution in the well did not significantly affect the dynamic response of the riser. Therefore, the global response analyses for the drilling case study were executed according to the different mechanical configurations the wellhead assumes during the drilling operation or the workover operation. These mechanical configurations are numbered below, by referring to the last major change on well and wellhead geometry. The notation in Table 6.3 will be used when differentiating between mechanical configurations.

Table 6.3 – Notation used for the mechanical configurations of the wellhead.

Mechanical configuration	Operational phase	Previous change in the system	Tubulars in the well
1	Drilling	Surface casing cemented in place	30-in., 20-in.
2	Drilling	13⅜-in. casing suspended from the wellhead	30-in., 20-in., 13⅜-in.
3	Drilling	13⅜-in. casing cemented in place	30-in., 20-in., 13⅜-in.
4	Drilling	9⅝-in. casing suspended from the wellhead	30-in., 20-in., 13⅜-in., 9⅝-in.
5	Drilling	9⅝-in. casing cemented in place	30-in., 20-in., 13⅜-in., 9⅝-in.
6	Drilling	7-in. liner suspended from the 9⅝-in. casing	30-in., 20-in., 13⅜-in., 9⅝-in., 7-in.
Workover	Workover	-	30-in., 20-in., 13⅜-in., 9⅝-in., 7-in.

For the drilling case study, the difference between riser models was the wellhead beam-proxy-model used as the bottom boundary, which is representative of the different load configurations. On the other hand, the workover operation case study required just one riser model, and consequently just one wellhead beam-proxy-model.

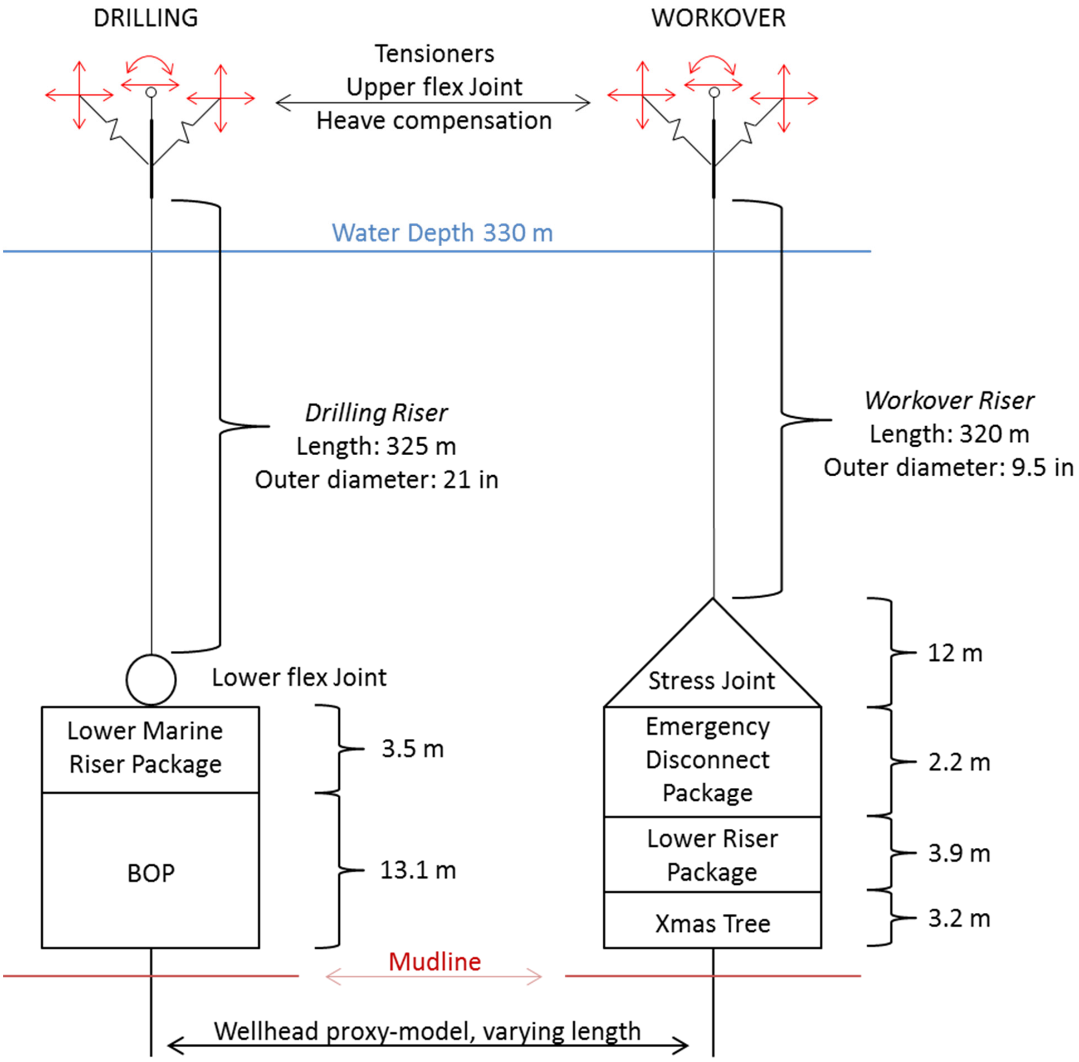

Figure 6.3 – Simplified schematic representation of the drilling and workover riser models.

6.2 System Loads

6.2.1 Well-Temperature Distributions

Figure 6.4 shows the temperature-deviation envelopes obtained for each casing string as the drilling process was simulated. Temperature deviations for each casing string were calculated from the corresponding T_{set}. It can be seen along the intermediary section of the well that the 13⅜-in. and 9⅝-in. casing strings were subjected to a large temperature deviation range throughout drilling. In comparison, the temperature deviations calculated for the workover operation were much smaller and can be found in Paper I.

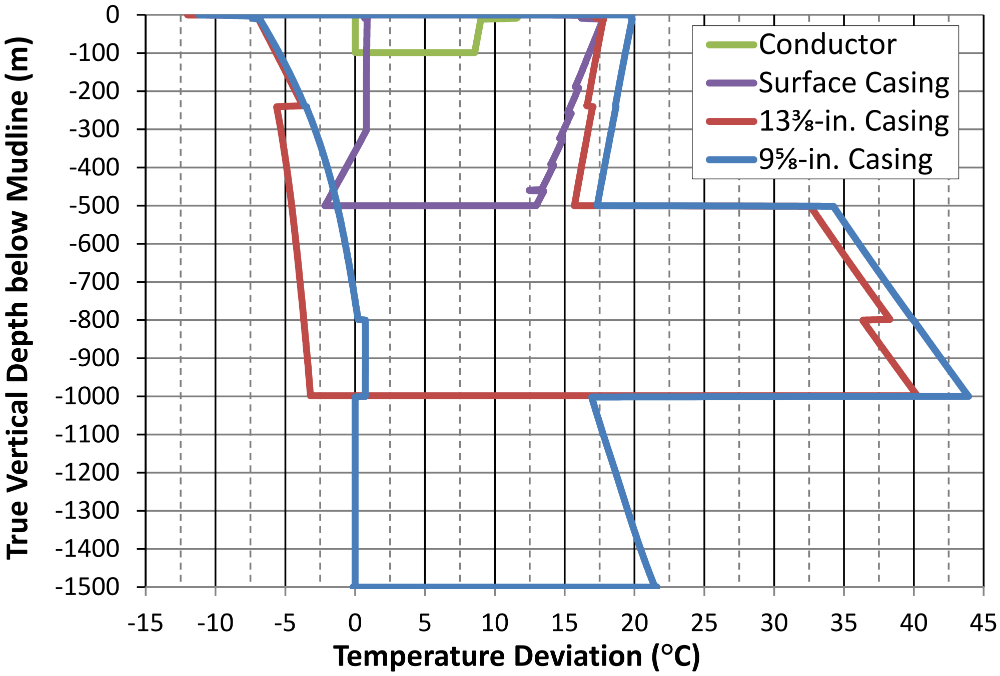

Figure 6.4 – Temperature-deviation envelopes of the casing strings.

6.2.2 Static and Quasi-static Loads

6.2.2.1 Drilling

The drilling operation simulated in the second part of the case study is similar to the operation simulated in section 5.2. The same wellhead model, BOP and marine-drilling-riser system (represented by the applied riser tension) were employed. The riser tension applied at the top of the BOP was 500 kN, and the total mass of the BOP was 160 tons.

For simulations corresponding to moments during the first operational phase (right after the surface casing has been cemented in place), the difference between the structural simulations of the first and second parts of the case study was the induced temperature distribution of the well components. For the succeeding operational phases of the drilling operation, the FEA model had to be updated because of the components added to the wellhead system: casing hangers, casing strings, and cement sheaths.

The quasi-static loads, meant to represent environmental loading, were modelled by a bending moment load applied in incremental steps at the wellhead datum, and ramped up to the maximum value of 1300 kNm.

6.2.2.2 Workover Operation

The subsea stack and the workover riser used in the simulated workover operation are schematically represented in Figure 6.3. Due to the different arrangement of the subsea stack, the static loads in the numerical simulations were significantly different. The submerged weights of the

EDP, LRP and Xmas tree were, respectively, 11.7 tons, 31 tons, and 40 tons. The applied riser tension at the top of the EDP was 250 kN. The stress joint shown in Figure 6.3 is modelled in the riser global response analysis, but not in the wellhead's local response analysis.

The quasi-static loads were simulated in the same fashion of the previous cases described: bending moment load applied at the wellhead datum at progressively larger increments and ramped up to the maximum value of 1300 kNm.

6.3 Analytical Results

The following sections present the results of the analyses of fatigue assessment conducted for the hot spots selected in the wellhead. Comparisons are made between the fatigue estimates obtained for the different wellheads models and between the results obtained by the analyses with and without temperature.

A more-in-depth investigation is performed for the wellhead fatigue hot spot located at the welded connection between the high-pressure housing and the surface casing, by presenting the load-to-stress curves obtained from the local response analyses performed for the different temperature scenarios found during the simulated drilling and workover operations.

6.3.1 Preload-stress levels

Prior to be subjected to the bending moment load, the analytical model of the wellhead is subjected to the temperature distribution of the well. The well temperature affects the stress response of the model already at the preload step.

Figure 6.5 and Figure 6.6 present the preload-stress levels calculated for the fatigue hot spots selected during the simulated drilling operation. The short dashed, vertical, black lines delimit the operations carried out inside the well, which are presented in Table 6.1. The thicker dashed vertical lines delimit the mechanical configurations assumed by the wellhead model. Because bending has not been introduced, the TOC has little influence on the calculated stress levels. Therefore, the trends presented by Figure 6.5 and Figure 6.6 may be interpreted as for both wellhead A and wellhead B.

Section 2.4 states that the static or preload-stress levels are not necessarily the same as mean stress levels. Nonetheless, the results displayed by Figure 6.5 and Figure 6.6 provide an insight on the influence of temperature on mean stresses at the wellhead. As it can be read in section 3.3.2, sea current loading shifts the mean value of the bending moment time series away from zero. Therefore, if the modelled sea current loading is zero, the preload-stress levels calculated at the fatigue hot spots may be interpreted as the mean stresses.

Figure 6.5 presents the preload-stress levels calculated for the welded-connection-fatigue hot spots. The welded connections are in compression. The welds in the surface casing were predicted to experience a sharp increase in compression levels at the start of the drilling operations when temperature variations along the tubular components of the well start to develop. At the five hours mark, stress levels at these hot spots more than double, but later achieve lower levels.

As it might be expected, the compression levels calculated on the welds located on the conductor display the reverse response of the welds in the surface casing. But, at the moments when the mechanical configuration of the wellhead changes and a new casing string is suspended, the added weight may exceed the effects of the induced temperature.

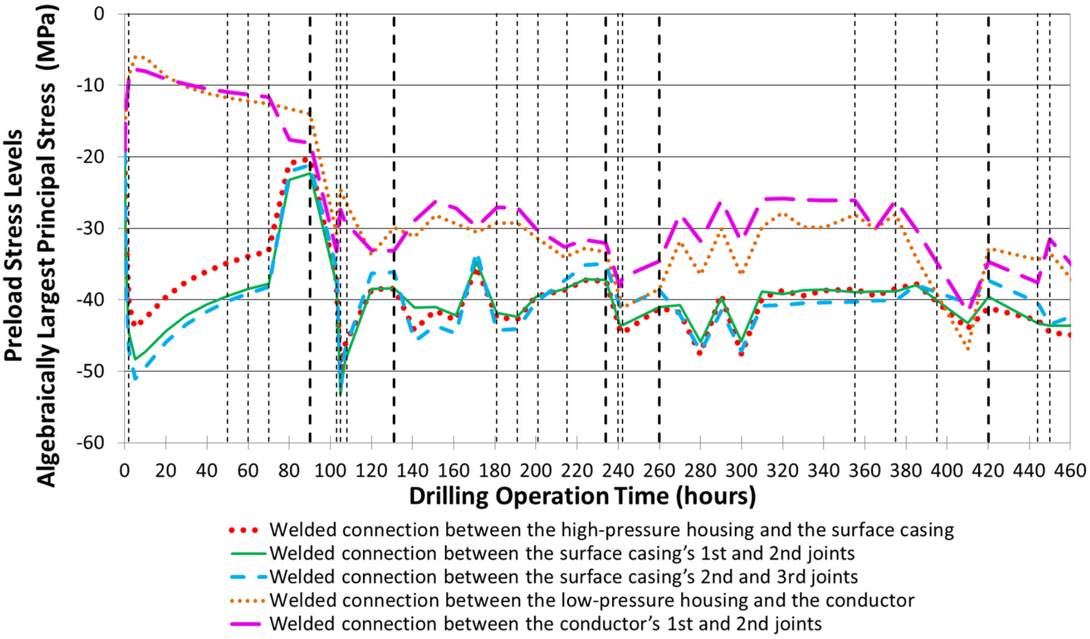

Figure 6.5 – Preload-stress levels calculated for the weld-fatigue hot spots (compression is negative).

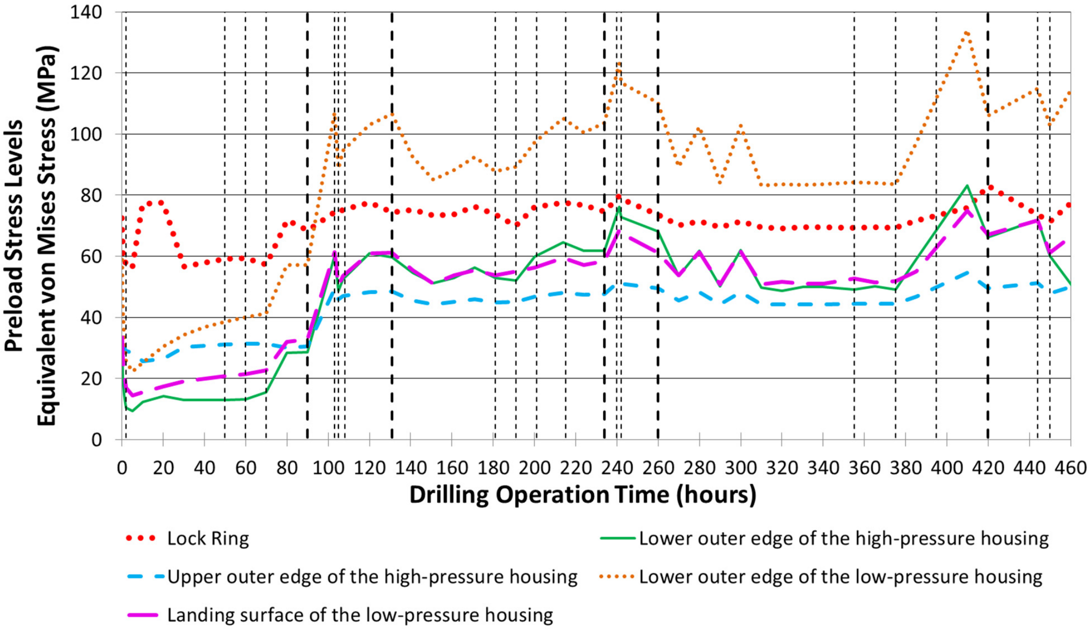

Figure 6.6 – Preload-stress levels calculated for the base-metal- fatigue hot spots.

Figure 6.6 presents the preload von Mises stress levels calculated for the base-metal-fatigue hot spots. The results of analysis within the same operational phase of the well indicate that the preload-stress levels calculated for most of these hot spots are influenced to a lesser extent by the temperature of the well.

The response of the upper outer edge of the high-pressure housing appears to be the least affected by temperature, which may indicate that despite its proximity to the other hot spots (see Figure 6.2) it's located away from region of the high-pressure housing affected by temperature.

The preload-stress levels calculated for the lock ring are significantly affected by temperature at the start of the drilling operations. The calculated variation for the von Mises stress is larger than 20 MPa during the first 30 hours of the simulated drilling operation. However, this fluctuation nearly stops afterwards. This may indicate that according to the mechanical model of the wellhead, the effect of temperature on the calculated stresses of for a hot spot may decrease.

Conversely, the preload-stress levels calculated for the lower edge of the low-pressure housing may considerably fluctuate because of the temperature of the well. Because of its locations, this hot spot could be considered as a continuation of the conductor string, therefore it could be expected to be affected in similar fashion to the conductor welds. The hot spot is located at a corner of the low-pressure housing, which amplifies the stress levels.

6.3.2 Load-to-Stress Curves

Figure 6.7 presents the load-to-stress curves of the welded connection between the high-pressure housing and the surface casing, created for the multiple temperature distributions predicted during the first operational phase of the drilling operation. The load-to-stress curve given by the analysis without temperature is also presented. The curves corresponding to the remaining operational phases can be found in Annex C.

In Figure 6.7, the different temperature distributions are indicated by the points in time for which they were calculated, within the first 90 hours of the drilling operation. The x-axis presents the bending moment load at wellhead datum generated by the riser connection. The y-axis presents the corresponding maximum cyclic stress levels at the compression side of the surface casing weld.

For both wellhead configurations in Figure 6.7, the structural calculations corresponding to the initial hours of operation yield larger cyclic stresses for most of the applied bending moment range than the stresses yielded by the analysis without temperature (time equals zero). This trend is reversed after 20 hours of operation for wellhead A, and 10 hours of operation for wellhead B. Cyclic stresses yielded by the analyses with temperature became smaller in magnitude than the cyclic stresses yielded by the analysis without temperature.

For wellhead A, under a bending moment load of 900 kNm, the stress at t=5 hours will be 74 MPa, later at t=70 hours the stress under the same bending moment load will decrease to 60 MPa. The cyclic stress estimated by the analysis without temperature, and assumed valid for the whole period, would be 66 MPa. Reduction in cyclic stresses, compared to stresses calculated by FEA without temperature, can be expected to be up to 15 MPa and 10 MPa for wellhead A and wellhead B, respectively.

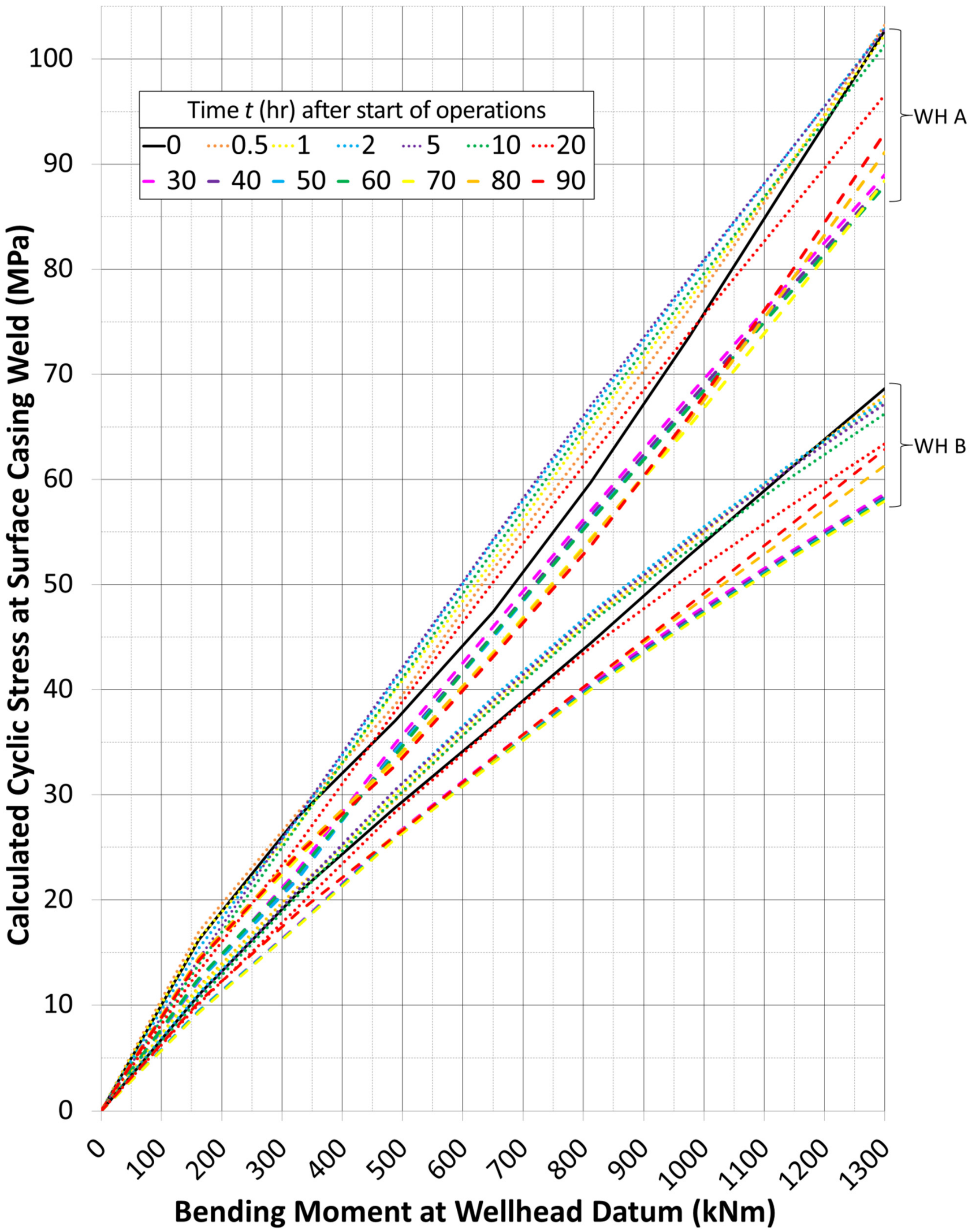

Figure 6.7 – Load-to-stress curves generated for the welded connection between the high-pressure housing and the surface casing. Period [0-90 hr]. The curve *t*=0 hr represents the analysis without temperature of the mechanical configuration assumed by the wellhead during the period.

Figure 6.7, along with the figures in section C.3, shows that incorporating the temperature distribution of the well, which is related to the history of operations performed in the well, to the structural calculation of the wellhead modifies the relation between applied load in the wellhead and resulting cyclic stresses in a fatigue hot spot.

The conventional wellhead fatigue assessment assumes the fatigue-damage rates to remain constant during a given operational phase. But, because the temperature in the well has been shown to influence the cyclic stresses in the wellhead, this assumption is no longer valid.

6.3.3 Estimates of Accumulated Fatigue Damage

Fatigue damage assessments of the wellhead system during the drilling and workover operations, and the investigation of the impact of the temperature distribution on the estimated damage, were performed using the load-to-stress curves, along with the results of the global response analysis for the two riser models.

The results obtained from the drilling case study are shown in section 6.3.3.1, while the results for the workover operation are presented in section 6.3.3.2. In the section 6.3.3.1, only the results for the surface casing/high-pressure housing welded connection are presented. The results for the remaining hot spots in Figure 6.1 can be found in Annex C.

6.3.3.1 Drilling Operation

In Figure 6.8, the fatigue-damage rates and the accumulated fatigue-damage estimates for the welded connection between the high-pressure housing and the surface casing are presented. S-N curve F (Figure 5.11) was used for estimating the fatigue-damage rates.

In the plots, blue colored curves indicate the accumulated fatigue damage, in percentage of the fatigue design life, throughout the well operation. The dashed line represents the results according to the conventional procedure, without temperature, while the dotted line represents the results according to the proposed procedure, with temperature incorporated into the analysis.

Moreover, the orange colored curves indicate the fatigue-damage rates, in percentage of design-fatigue life spent per hour, throughout the well operation. The dashed-dotted line represents the fatigue-damage rate as calculated according to the conventional procedure, once for each of the phases of the simulated operation.

The continuous line shows the fatigue-damage rates calculated at relevant moments, each of the triangular markers, as the actions performed in the well went on. The moments were chosen to cover both the gradual shifts in temperature during long procedures, and the drastic shifts when the procedure performed changed. The short-dashed, vertical, black lines delimit the procedures carried out inside the well, which are presented in Table 6.1.

It can be seen in the figure that the conventional fatigue-damage rate curves display six plateau values, corresponding to the different load configurations the wellhead experiences during the phases of the drilling operation. Thus, the fatigue-damage rate remains constant as long as the wellhead configuration does not change. Wellhead A exhibited the highest values for fatigue-damage rates calculated without temperature.

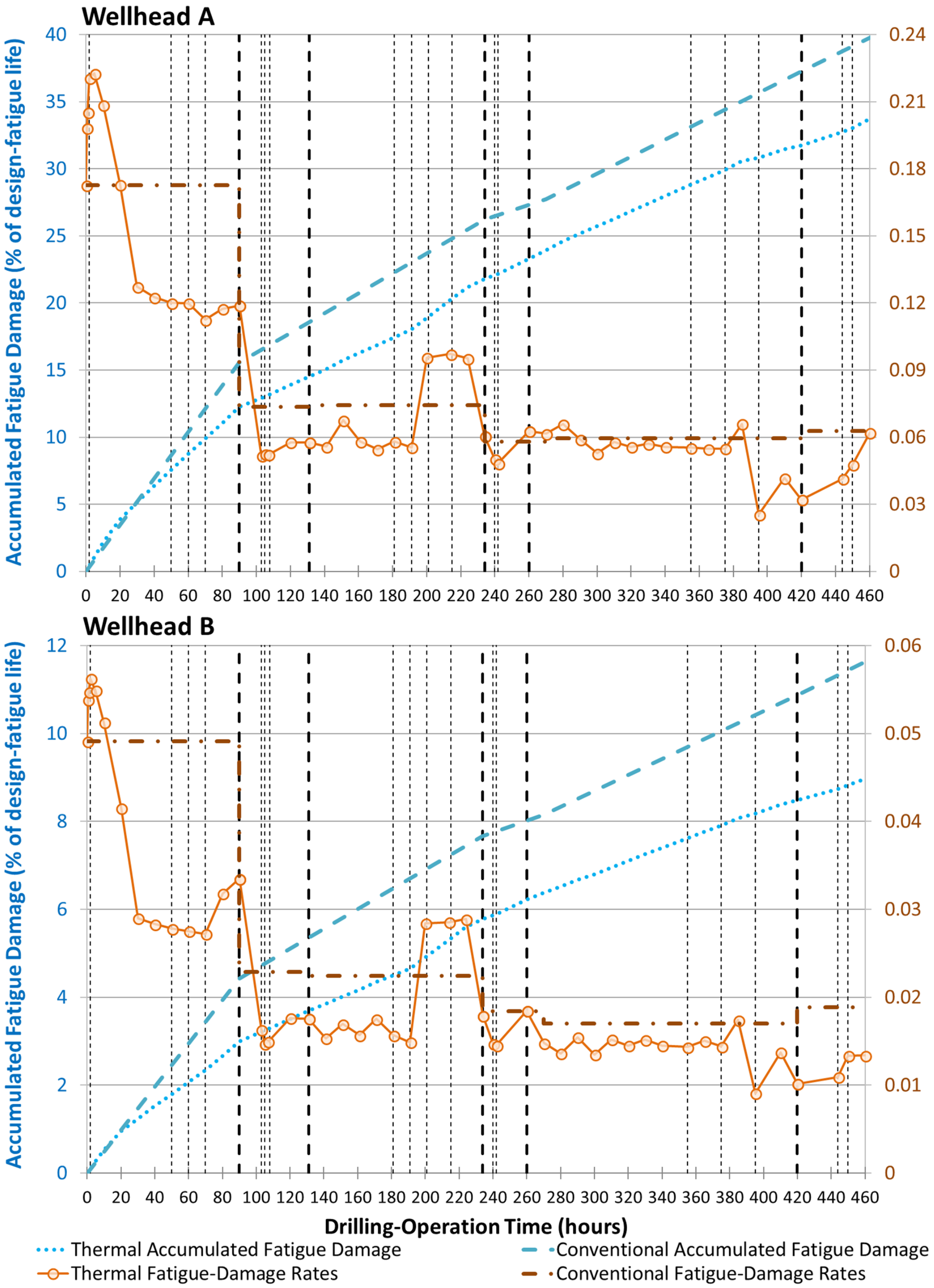

Figure 6.8 – Accumulated fatigue-damage estimates for the welded connection between the high-pressure housing and the surface casing during drilling. Wellheads A and B. DFF=10. S-N curve F.

Alternatively, the fatigue-damage rates calculated taking the temperature into account have shown significantly variations through time, even when the wellhead configuration remains the same. Fatigue-damage rates for both wellhead models seem to follow the same trends, increasing and decreasing around the same points in time.

Changes on fatigue-damage rates are dependent on the well operation being carried out and the related temperature distribution. At the start of the simulated operations the well is circulated, afterwards drilling goes on until the 50 hours mark. Then, the well is circulated for 10 hours.

During the next 30 hours there is no circulation, as the drillstring is being retrieved and the next casing string is being run into the well afterwards. It can be seen that the damage rates first increase as the well is being heated up, to then start decreasing and almost achieve a constant value. Shifting operations changes the way temperature in the well develops and leads to the fatigue-damage rates to increase.

During the 260-354 hours period the responses obtained for the two wellheads significantly diverge: while wellhead B presents near plateau values for the fatigue-damage rates, wellhead A presents a valley in the same period.

From the 375 hours mark to the end of the simulated operations the well is not being circulated, but the drillstring is being tripped in and out of the well during this period. The fatigue-damage rate is seen to fluctuate, and it reaches a peak when the string is halfway in the well, either on its way up or down as it exposes different sections of the well to lower or higher temperatures.

Without circulation the tendency of the temperature distributions of the components in the system is to reach equilibrium as they move toward the undisturbed formation temperature. A tripping operation, as it has been modelled in the study, adds new considerations that can influence the temperature calculation, and consequently the fatigue-damage rate:

- At a given depth in the system, it can either remove or add a component (the drillstring) to the heat exchange process.
- The temperature of the drillstring as it is being maneuvered can be significantly larger or lower than that of its surroundings. This may potentially alter the tendency of temperatures, for a section of the well, from getting closer to those of the undisturbed formation.

The results have mostly shown a decrease in fatigue-damage rates when the well temperature is considered. Moreover, results indicate that temperature has a greater impact on the fatigue-damage rates for wellhead configurations with shallower TOC.

Concerning the accumulated fatigue damage, it can be noticed that the conventional approach for wellhead fatigue assessment has shown to, for these wellhead configurations and load scenarios, overestimate the accumulated fatigue damage, when compared to the estimates given by the corresponding analyses with the effects of well-temperature distribution incorporated.

Table 6.4 summarizes the results of the fatigue assessment conducted for the 10 selected fatigue hot spots. In general, in this study, the estimates from analyses with temperature predicted lower accumulated fatigue damage for all hot spots, when compared with the results of the corresponding analysis without temperature.

Table 6.4 – Drilling fatigue damage assessment summary. DFF=10. 1st tier S-N curves.

ACCUMULATED FATIGUE DAMAGE (% of design-fatigue life)						
			Wellhead A TOC=ML-2m		**Wellhead B TOC=ML-10m**	
	Fatigue Hot Spot	*S-N curve*	*Temperature effects*		*Temperature effects*	
			With	*Without*	*With*	*Without*
1	Welded connection between the high-pressure housing and the surface casing	F	33.7	39.8	8.97	11.6
2	Welded connection between the surface casing's 1st and 2nd joints	F3	6.82	8.61	8.48	11.6
3	Welded connection between the surface casing's 2nd and 3rd joints	F3	0.07	0.09	0.05	0.08
4	Welded connection between the low-pressure housing and the conductor	F3	0.35	0.43	0.84	1.12
5	Welded connection between the conductor's 1st and 2nd joints	F3	4.18	4.46	4.33	4.58
6	Lock Ring	BM4	0.43	0.47	1.42	1.45
7	Lower outer edge of the high-pressure housing	BM4	0.33	0.46	0.36	0.52
8	Upper outer edge of the high-pressure housing	BM4	1.28	1.59	1.31	1.64
9	Lower outer edge of the low-pressure housing	BM4	0.03	0.04	0.02	0.04
10	Landing surface of the low-pressure housing	BM4	7.26	8.20	11.4	12.7

However, it should not be generalized from this study that the conventional wellhead-fatigue analysis methodology overestimates the accumulated damage. The integration of well temperature into the fatigue assessment makes the fatigue estimate dependent on the history of operations performed in the well. Because of the different events that may comprise any given drilling operation, and the corresponding well-temperature distributions, the overall impact of temperature in the accumulated fatigue damage of a wellhead system should be determined on a case-by-case basis.

What may be stated as a general conclusion is that the cyclic stresses experienced by most fatigue hot spots, and the corresponding fatigue-damage rates, will not be constant during a given mechanical configuration of the wellhead, as assumed by the conventional wellhead fatigue assessment methodology. Therefore, there is the need for multiple structural calculations to accurately describe the stress response in the wellhead system.

Among the hot spots with estimated accumulated fatigue damage higher than 1%, the TOC had minimum impact on the fatigue damage estimates of *hot spot 5* (notation given by Table 6.4); the computed difference in the estimates between wellhead models was not greater than 0.25% of design-fatigue life. For the remaining hot spots, the underlined values in Table 6.4 give emphasis to the wellhead model for which the highest accumulated fatigue damage was predicted.

Of the weld hot spots, *hot spot 1* in wellhead A had the highest accumulated fatigue-damage estimates. The results from the analyses with and without temperature were at least 30 percentage points higher than the second highest damaged weld hot spot. For the other weld hot spots with estimated accumulated fatigue damage higher than 1%, with or without temperature, the highest accumulated fatigue damage was predicted to take place in wellhead B. For wellhead B, *hot spots 1* and *2* are tied as the weld with most accumulated fatigue damage.

Within the base metal hot spots, wellhead B presented the worst estimates for accumulated fatigue damage and *hot spot 10* had the highest estimates, up to 10 times higher than the second highest. *Hot spot 9*, despite being subjected to large preload-stress levels, was subjected to low cyclic stresses, which resulted in low accumulated fatigue damage.

Table 6.5 brings attention to the effect the S-N curve chosen to represent the behavior of a fatigue hot spots has on the corresponding estimated accumulated fatigue damage.

The table presents the fatigue damage estimates of each fatigue hot spot as calculated by the three S-N curves (Figure 5.11) immediately below the curve used to compute the results in section 6.3.3.1. The results in Table 6.5 indicate that the difference between the estimates given by the analyses with and without temperature became more significant as the fatigue strength deteriorated.

In the case of fatigue *hot spot 1*, when using the S-N curve F1 the fatigue damage estimate increased to 96.1% for the conventional fatigue assessment of wellhead A, while the analysis with temperature estimated 81.6% of damage, a difference of 14.5 percentage points, compared to the 6.10 percentage points difference computed when using the S-N curve F.

If S-N curve F3 had been selected for fatigue *hot spot 1*, then wellhead A would fail to comply with a design fatigue factor of 10. Both assessments, with and without temperature, would predicts more than 100% accumulated damage for this wellhead. The accumulated fatigue damage by the analysis with temperature would be 31.9 percentage points smaller than the fatigue damage estimated by the conventional analysis without temperature. Finally, if S-N curve G had been selected, both wellheads A and B would fail to comply with a DFF of 10.

Hot spot 2, the welded connection between the first and the second joint in the surface casing, also is predicted to experience significant fatigue damage with considerable difference between the estimates by the analyses with and without temperature. In percentage points, the difference can reach up to 17 and 30 for wellheads A and B, respectively.

In the case of fatigue *hot spot 5*, the welded connection between the first and the second joint in the conductor string, Table 6.5 also emphasizes how little the fatigue estimates for this hot spot are affected by either the temperature or the TOC; the largest difference in accumulated fatigue damage computed was 2.9 percentage points.

Hot spots 6 through *10* are base material points in either the high-pressure housing or the low-pressure housing. Therefore, only the base metal S-N curves in Figure 5.11 are applicable. The material of the housings should be strong enough to be represented by the curve BM4 because, as it can be seen in Table 6.5, weaker material would lead to *hot spot 10* failing or nearly failing to comply with the DFF.

The base material fatigue hot spots follow the same trend of most of the welded connection fatigue hot spots: the S-N curves of weaker material accentuate the difference in estimated fatigue damage by analyses with and without temperature.

Table 6.5 – Effect of 2nd, 3rd and 4th tier S-N curve on fatigue damage assessment. DFF=10.

ACCUMULATED FATIGUE DAMAGE (% of design-fatigue life)						
			Wellhead A TOC=ML-2m		**Wellhead B TOC=ML-10m**	
Fatigue Hot Spot		*S-N Curve*	*Temperature Effects*		*Temperature Effects*	
			With	*Without*	*With*	*Without*
1	Welded connection between the high-pressure housing and the surface casing	F1	81.6	96.1	25.8	32.4
		F3	184	216	66.0	81.0
		G	387	451	150	181
2	Welded connection between the surface casing's 1st and 2nd joints	G	20.2	24.8	23.8	31.1
		W1	49.9	58.8	56.2	71.2
		W2	113	130	125	155
3	Welded connection between the surface casing's 2nd and 3rd joints	G	0.22	0.29	0.16	0.26
		W1	0.66	0.85	0.49	0.77
		W2	1.90	2.40	1.40	2.20
4	Welded connection between the low-pressure housing and the conductor	G	1.11	1.36	2.69	3.58
		W1	3.28	4.01	7.91	10.5
		W2	9.80	12.0	22.4	29.3
5	Welded connection between the conductor's 1st and 2nd joints	G	10.8	11.4	11.0	11.6
		W1	24.1	25.4	24.5	25.9
		W2	52.1	54.8	52.8	55.7
6	Lock Ring	BM3	0.74	0.82	2.44	2.50
		BM2	1.37	1.51	4.51	4.62
		BM1	18.8	20.7	61.9	63.5
7	Lower outer edge of the high-pressure housing	BM3	0.56	0.79	0.62	0.89
		BM2	1.03	1.46	1.14	1.65
		BM1	14.2	20.1	15.7	22.6
8	Upper outer edge of the high-pressure housing	BM3	2.20	2.74	2.26	2.82
		BM2	4.05	5.05	4.16	5.19
		BM1	55.7	69.4	57.2	71.4
9	Lower outer edge of the low-pressure housing	BM3	0.06	0.07	0.04	0.06
		BM2	0.11	0.12	0.07	0.11
		BM1	1.48	1.70	0.97	1.56
10	Landing surface of the low-pressure housing	BM3	86.2	97.3	135	151
		BM2	159	180	250	279
		BM1	317	358	499	557

6.3.3.2 Workover Operation

During any of the operations that might be necessary to carry out in the well after drilling has been completed, the mechanical configuration of the wellhead will be similar to the last configuration assumed during drilling, although the subsea stack (BOP, Xmas tree, EDP, etc.) might be considerably different.

Each of these operations consumes an amount of the remaining fatigue life, until a point might be reached after which it would no longer be safe to access the well.

This section will show how the well-temperature distribution can impact the remaining service life of the wellhead, and how this translates in allowable riser connection days. Because, it would be impractical to try to simulate all the possible operations that could take place after drilling, a workover operation is representing the impact of post-drilling operations, and how many times the fatigue capacity of the wellhead would enable this operation to be performed.

The simulated workover operation is the replacement of the production tubing, with estimated duration of 50 hours. It starts by circulating the well to kill it, replacing the original fluid with a heavier fluid. After that circulation stops, the old tubing is retrieved and a new one is installed.

Despite presenting the highest accumulated fatigue damage at the end of the drilling operation, neither *hot spot 1* in wellhead A nor *hot spot 10* in wellhead B can be assumed to be the limiting factor of the respective wellhead's fatigue life. As the graphs in sections 6.3.3.1 and C.3 below show, there are other fatigue hot spots that undergo higher fatigue-damage rates at the later stages of the drilling operation. The accumulated fatigue damage estimated for *hot spots 1* and *10* because of repeated workover operations could be exceeded by the damage calculated in *hot spots 2*, *4*, *5*, *6* or *8*, since all fatigue hot spots experience fatigue damage at different rates.

Figure 6.9 presents the fatigue-damage rates and accumulated fatigue damage during the simulated workover operation for the welded connections hot spots (*1* through *5*). Figure 6.10 presents the accumulated fatigue damage during the simulated workover operation for the base metal hot spots (*6* through *10*).

Considering the estimates for wellhead A, *hot spot 1* does undergo the most fatigue damage during this workover operation. The corresponding results for wellhead B indicate that *hot spot 2* undergoes the most fatigue damage for this wellhead model. The lock ring (*hot spot 6*) in both wellheads undergoes significantly lower fatigue damage during the workover, while the remaining fatigue hot spots undergo fatigue-damage rates at the same order of magnitude to those calculated for the final mechanical configuration of the wellhead in the drilling operation.

The plots in Figure 6.9 reveal that for the welded connection fatigue hot spots in wellhead B, temperature had a smaller impact on the fatigue estimates when compared to the results of the analyses for wellhead A; the estimates obtained by the analyses with temperature are close to those obtained by the conventional analyses without temperature. In comparison, the TOC level did not seem to influence the impact temperature had on the response predicted for the base-metal-fatigue hot spots, Figure 6.10.

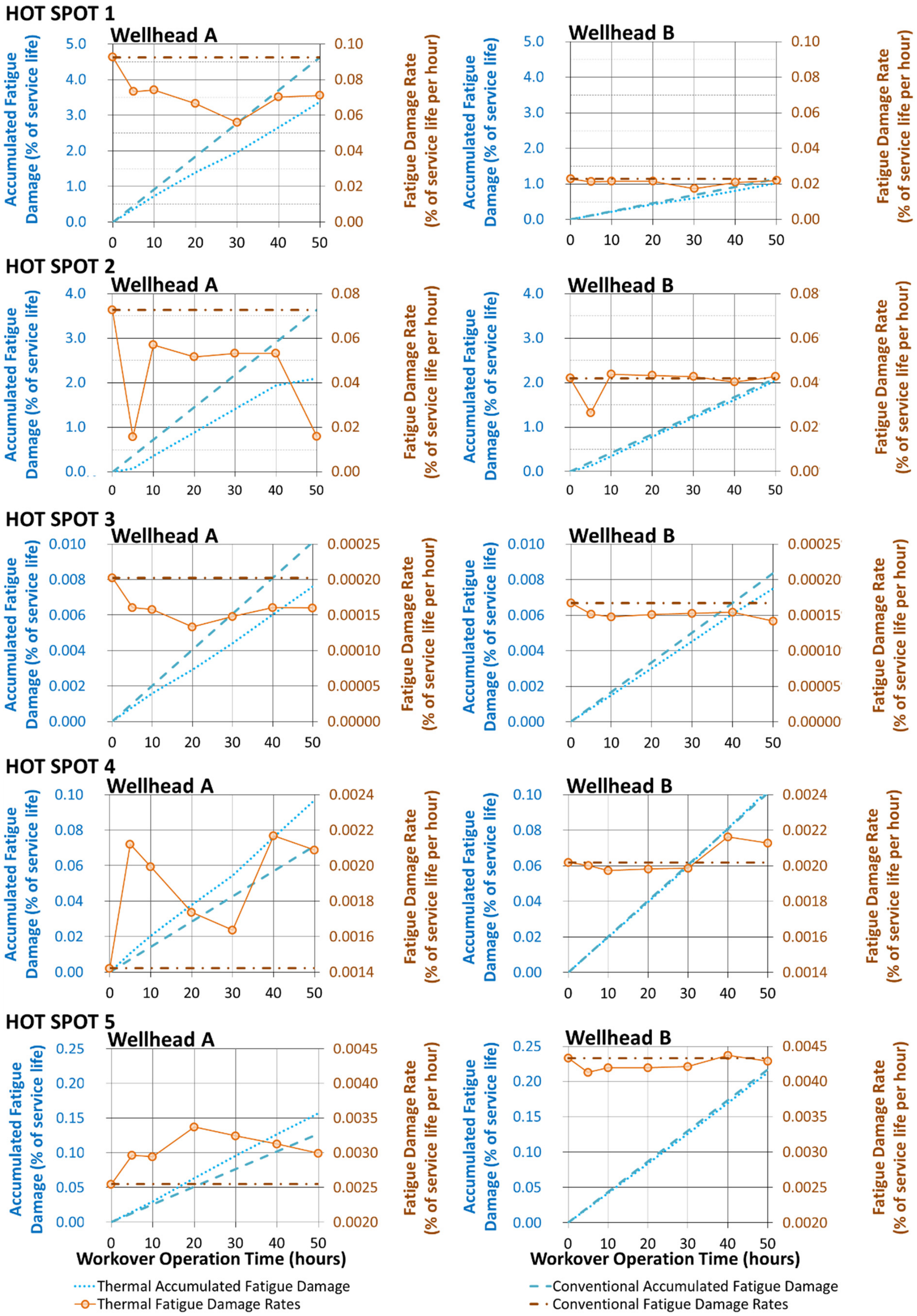

Figure 6.9 – Calculated fatigue damage for the welded-connection-fatigue hot spots for wellheads A and B during the workover. DFF=10. 1st tier S-N curves.

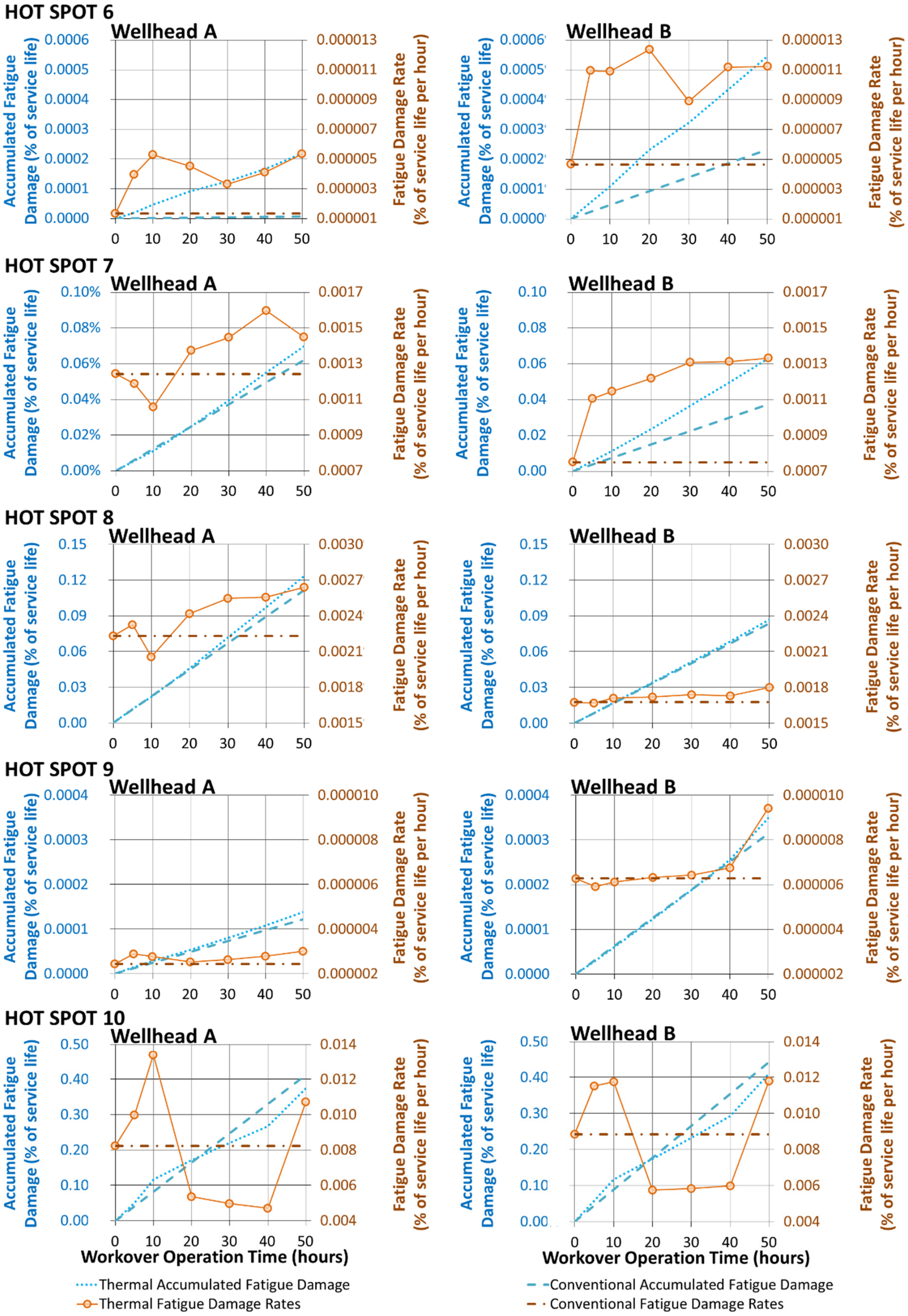

Figure 6.10 – Calculated fatigue damage for the base-metal hot spots for wellheads A and B during the workover. DFF=10. 1st tier S-N curves.

Table 6.6 and Table 6.7 summarize the fatigue assessment conducted for the workover operation. They present for each hot spot the accumulated fatigue damage per workover operation, and the maximum number workover operations that may be performed before fatigue capacity is completely spent. Results are shown for the first and the second-tier S-N curves, respectively.

Considering wellhead A in Table 6.6, the conventional analysis without temperature predicted that the accumulated fatigue damage on *hot spot 1* would limit the workover operation to 13 repetitions, totaling 27 riser connection days. The estimates given by the analyses with temperature limit the workover operations to 19 repetitions, totaling 39 riser connection days, therefore 12 additional riser connection days, or a 44% increase.

Here it is helpful to emphasize the fact that allowable riser connection time increased not due to a less conservative methodology, but because of a more-accurate representation of the wellhead response during well operations, which incorporated into the analysis an important aspect of well operations: the transient temperature distribution of the well.

For wellhead B, both the analyses with and without temperature pointed to fatigue damage in *hot spot 2* as the critical hot spot. The maximum number of workovers estimated by the analyses with and without temperature was 44 and 42, or 91 and 87 days of riser connection time, respectively. *I.e.* an increase of 2% in allowable riser connection time.

Table 6.6 – Workover fatigue damage assessment summary. DFF=10. 1st tier S-N curves.

		CONSUMED FATIGUE CAPACITY (% of design-fatigue life/operation)				**MAXIMUM NUMBER OF WORKOVER OPERATIONS**			
		Wellhead A TOC=ML-2m		**Wellhead B TOC=ML-10m**		**Wellhead A TOC=ML-2m**		**Wellhead B TOC=ML-10m**	
Fatigue Hot Spot	*S-N Curve*	*Temperature effects With*	*Temperature effects Without*	*Temperature effects With*	*Temperature effects Without*	*Temperature effects With*	*Temperature effects Without*	*Temperature effects With*	*Temperature effects Without*
1	F	3.4	4.6	1.0	1.1	19	13	88	77
2	F3	2.1	3.6	2.0	2.1	44	25	44	42
3	F3	7.6 E-3	1.0 E-2	7.5 E-3	8.4 E-3	1.3 E4	9.8 E3	1.3 E4	1.2 E4
4	F3	9.7 E-2	7.1 E-2	1.0 E-1	1.0 E-1	1028	1400	967	979
5	F3	1.6 E-1	1.3 E-1	2.1 E-1	2.2 E-1	610	750	451	440
6	BM4	2.2 E-4	6.6 E-5	5.5 E-4	2.3 E-4	4.6 E5	1.5 E6	1.8 E5	4.2 E5
7	BM4	7.0 E-2	6.2 E-2	6.3 E-2	3.7 E-2	1.4 E3	1.6 E3	1.6 E3	2.7 E3
8	BM4	1.2 E-1	1.1 E-1	8.7 E-2	8.4 E-2	799	882	1137	1173
9	BM4	1.4 E-4	1.2 E-4	3.5 E-4	3.1 E-4	7.3 E5	8.2 E5	2.9 E5	3.2 E5
10	BM4	3.7 E-1	4.1 E-1	4.1 E-1	4.4 E-1	277	250	243	222

The second-tier S-N curves in Table 6.7 yield fewer allowable workover operations. For wellhead A, the analysis without temperature predicted that the fatigue capacity on *hot spot 1* would be depleted during the first workover operation, since more than 90% of the fatigue capacity would have been already been spent (Table 6.5). The estimates by the analyses with temperature limit the workover operations to 2 repetitions, totaling 4 riser connection days before the DFF is met.

There would be no workovers for wellhead B, since *hot spot 10* would have failed, see Table 6.5. But, if *hot spot 2* remained the critical hot spot, the maximum number of workovers estimated by the analyses with and without temperature would be 14 and 12, or 29 and 25 days of riser connection time, respectively. *I.e.* an increase of 17% in allowable riser connection time.

Table 6.7 – Workover fatigue damage assessment summary. DFF=10. 2nd tier S-N curves.

		CONSUMED FATIGUE CAPACITY (% of design-fatigue life/operation)				**MAXIMUM NUMBER OF WORKOVER OPERATIONS**			
		Wellhead A TOC=ML-2m		**Wellhead B TOC=ML-10m**		**Wellhead A TOC=ML-2m**		**Wellhead B TOC=ML-10m**	
Fatigue Hot Spot	*S-N Curve*	*Temperature effects*		*Temperature effects*		*Temperature effects*		*Temperature effects*	
		With	*Without*	*With*	*Without*	*With*	*Without*	*With*	*Without*
1	F1	7.9	10.9	2.8	3.2	2	0	26	21
2	G	5.2	8.8	5.2	5.4	15	8	14	12
3	G	2.4E-02	3.2E-02	2.4E-02	2.7E-02	4.1E03	3.1E03	4.2E03	3.7E03
4	G	3.1E-01	2.3E-01	3.3E-01	3.2E-01	3.2E02	4.4E02	3.0E02	3.0E02
5	G	4.9E-01	4.0E-01	6.5E-01	6.7E-01	1.8E02	2.2E02	1.4E02	1.3E02
6	BM3	2.6E-03	7.9E-04	6.5E-03	2.8E-03	3.8E04	1.3E05	1.5E04	3.5E04
7	BM3	8.3E-01	7.4E-01	7.5E-01	4.4E-01	1.2E02	1.3E02	1.3E02	2.2E02
8	BM3	1.5	1.3	1.0	1.0	66	73	94	97
9	BM3	1.6E-03	1.4E-03	4.1E-03	3.7E-03	6.1E04	6.9E04	2.4E04	2.7E04
10	BM3	4.4	4.9	-	-	3	0	-	-

6.3.4 Discussion

The well at the start of the simulated drilling operation is at a transient state. But, since operational parameters are kept constant for a long period of time, it is shifting towards a steady state (*i.e.* temperature will stabilize). The calculated preload-stress levels presented in section 6.3.1indicate that the hot spots most susceptible to the effects of temperature may be subjected to higher stress levels during the start of the transient temperature state, and not at steady state. This has implications with regards to defining what will be the maximum loads that weak points in the wellhead are subject to during well operations.

The non-linear behavior of the wellhead displayed in Figure 6.7 shows that under different bending moment loads, the cyclic stress due to temperature may be higher or lower than the stress calculated by the conventional method. The comparison of the calculated load-to-stress curves made in the figure may suggest that the overall impact that a temperature distribution has on fatigue estimates should be weighted by the expected load time series acting on the wellhead.

The results in section 6.3.3 indicate that, together with the TOC and the S-N curve used, the effects induced by the temperature distribution of the well may force the wellhead fatigue assessment to shift its focus, as a hot spot previously considered at a low risk of failing might become the critical hot spot in the wellhead.

Chapter 7

Thermal Effects on Wellhead Structural Response

The analytical models presented in Paper III have provided an insight into the physical aspects for how the cyclic stresses on wellhead fatigue hot spots may be influenced by the well temperature. Paper III has also proposed how the thermal strain of tubular components could be used for predicting the fatigue-damage rate under different temperature scenarios. Chapter 7 applies these findings to the wellhead fatigue assessment presented in Chapter 6.

7.1 Induced Thermal Effects on Load Sharing

Valka and Fowler (1985) investigated the behavior of a particular wellhead system and described how load sharing between the surface casing and the conductor developed in a non-linear fashion, as the applied bending-moment load increased, and the wellhead model deformed.

The wellhead in this study has a few modifications in its design that can improve the load sharing between the two wellhead housings. In addition to the shoulder on the low-pressure housing, on which the high-pressure housing is landed, Figure 6.1 shows centralizing fins and a lock ring to connect the two housings.

At any case, when analyzing the effects of temperature, it becomes necessary to investigate the interaction of the housings and the lock ring at their contact points during bending. The first finding is presented in Figure 7.1. This figure shows, at two different temperature scenarios on the tension side of the wellhead system, the resulting position of the lock ring and the housings, for an applied bending moment equal to 1150 kNm.

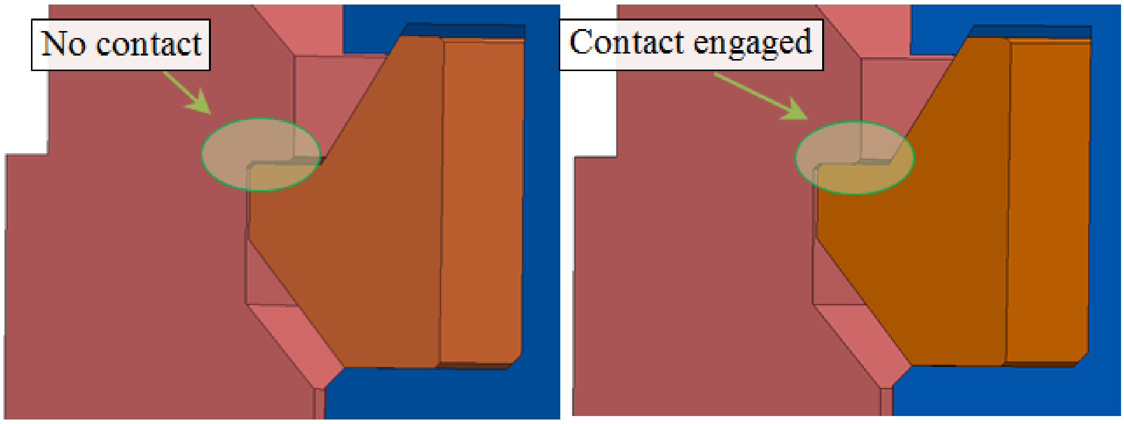

Figure 7.1 – Casing-housings and lock-ring position for an applied bending moment = 1150 kNm. Left: FEA without temperature. Right: FEA with temperature profiles from *t*=70 hr.

The FEA performed without temperature indicates no contact between the lock ring and the low-pressure housing at the highlighted area. In contrast, the temperature distribution incorporated into the FEA led to contact between those components.

Further evidence of that the temperature distribution can alter the load distribution within the wellhead system is presented in Figure 7.2. The graphs present the average value of the forces acting on the surface of the low-pressure housing on which the high-pressure housing is landed, for wellhead B at three different temperature scenarios: With no temperature, the temperature distribution corresponding to 0.5 hours after start of the drilling operation, and the temperature distribution corresponding to 70 hours after start of the drilling operation.

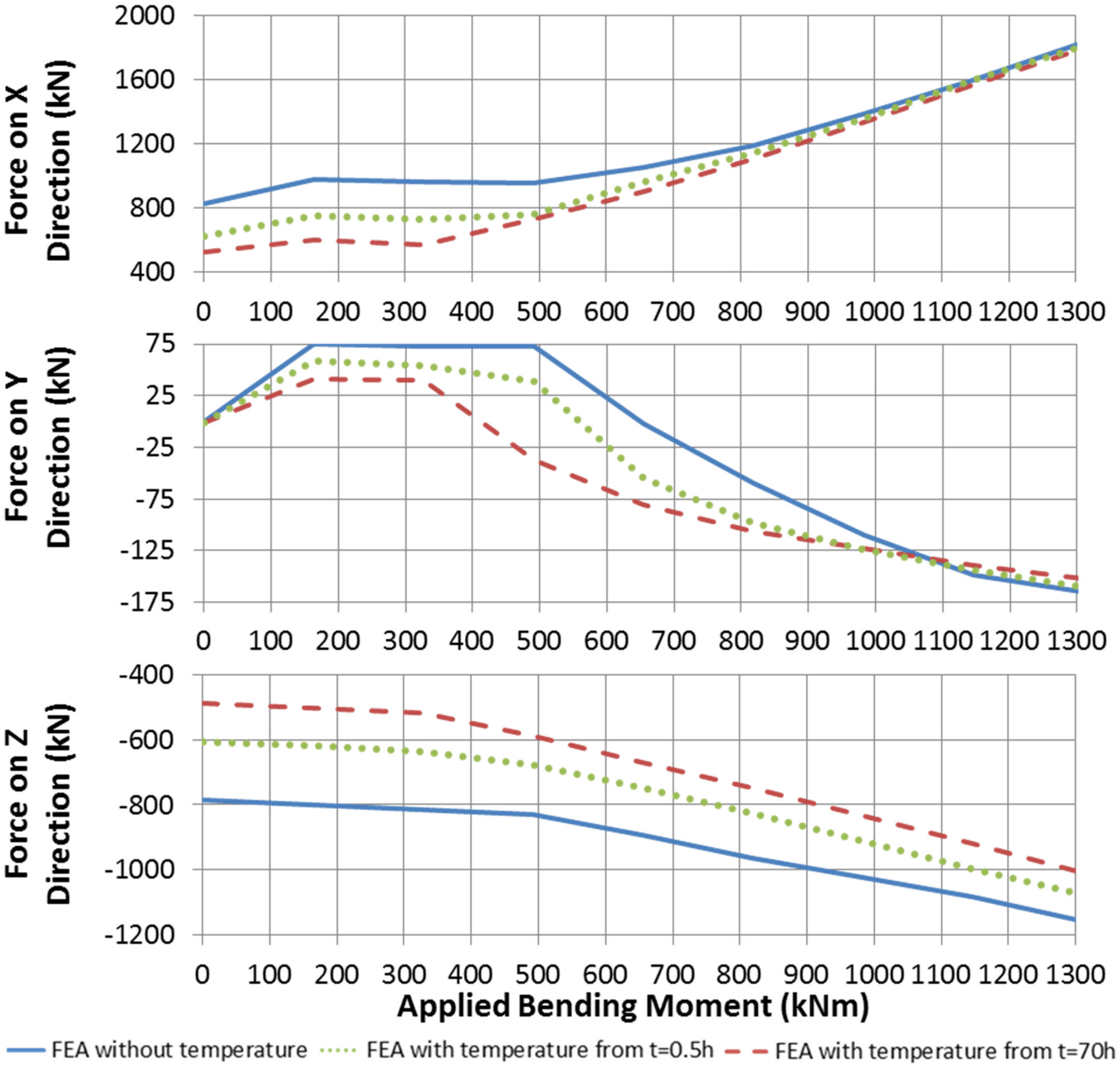

Figure 7.2 – Average value of reaction forces on the low-pressure housing-landing surface for wellhead B, under three different temperature distributions. Reference axes found in Figure 6.1.

If the effect of the incorporated temperature distribution was limited to a superposition of a compressive or tensile stress acting on the wellhead components, then the three curves in each of the graphs in Figure 7.2 should have similar shapes, with the position of the curves generated by the FEA with temperature being shifted to either above or below the curve generated by the FEA without temperature.

The fact that, for different temperature conditions at the same applied bending moment load, the forces acting on this contact surface increase or decrease at different rates indicating that the load sharing between the wellhead housings is influenced by the thermally induced interactions of the wellhead components.

Finally, Figure 7.3 presents the mean value of the vertical force (compression is negative) acting on (A) the surface casing/high-pressure housing welded connection and (B) the conductor/low-pressure housing welded connection. Focusing on the results given by the FEA without temperature (blue curves), it may be seen that the average force value remains constant until the 500 kNm applied bending moment mark is reached, and load sharing between the housing takes place. However, the maximum variation computed by the analyses is not higher than 30 kN.

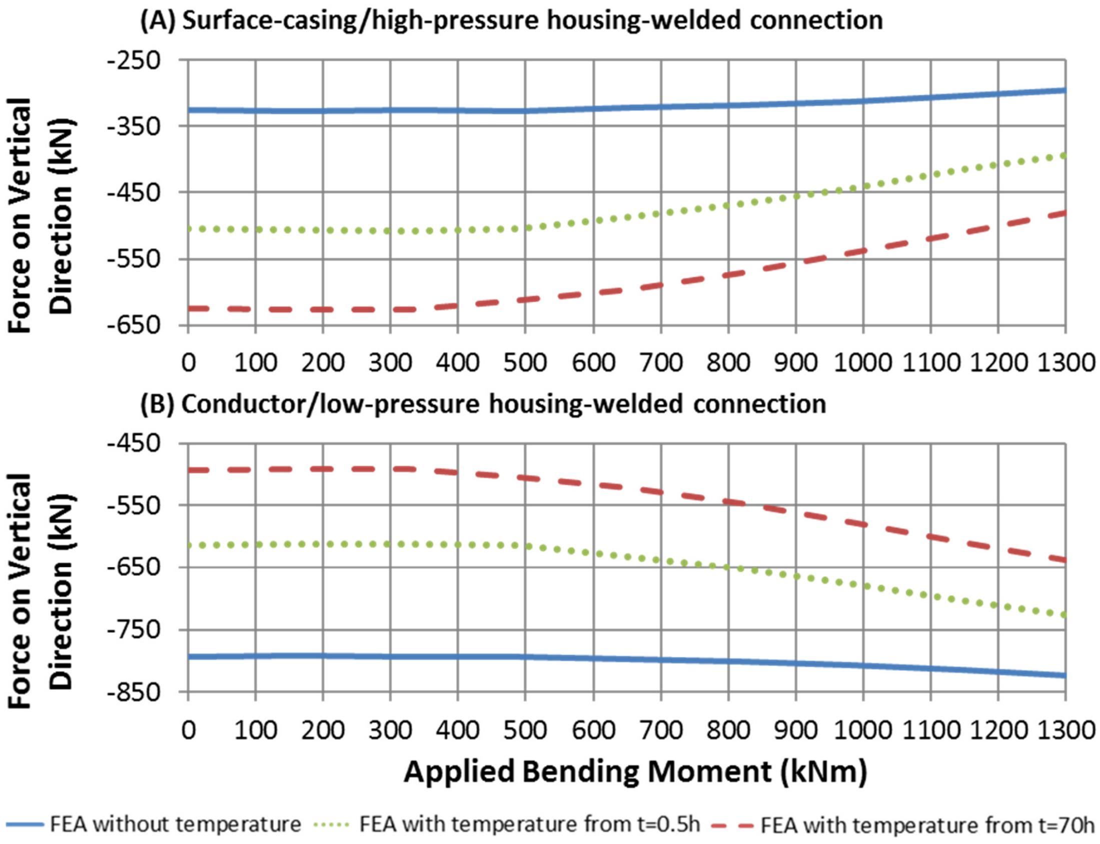

Figure 7.3 – Average value of vertical force on welded connections of wellhead B, under three different temperature distributions. Reference axes found in Figure 6.1.

For the FEA with temperature, not only can the load sharing start to occur at a smaller bending moment load, but within the applied bending moment range the calculated variation on mean force value can be up to 150 kN.

Thus, it may be concluded that each predicted temperature distribution of the well introduces a new set of forces acting on the components of the wellhead. For each incremental step of applied bending moment load, these new forces rearrange the way the load applied at the wellhead datum is shared among the members of wellhead, and consequently alter the magnitude of the load that arrives at the surface casing weld and the resulting cyclic stress.

7.2 Thermally Induced Displacement of Well Components

The impact of temperature can be noticed by the vertical displacement that the wellhead is subjected to. Figure 7.4 presents the wellhead displacement during the first 20 hours of operation. Displacements were relatively calculated from the initial position of the wellhead, when temperature differentials are zero, and which only accounts for the weight of the components of the system and the riser-tension force applied.

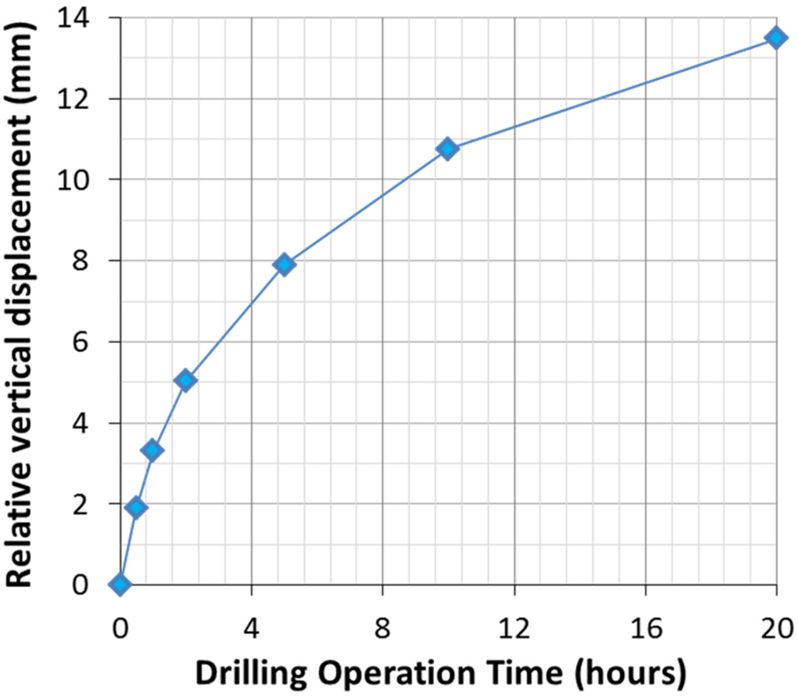

Figure 7.4 – Thermally induced relative vertical displacement computed for wellhead B.

After comparing the wellhead displacement shown in Figure 7.4 with the fatigue damage estimates in sections 6.3.3.1 and C.3, Figure 7.4 does not seem to yield an evident correlation between the wellhead vertical displacement and the expected fatigue-damage rate, given that the relative vertical displacement monotonically increases while the fatigue-damage rate fluctuates. Consequently, it becomes necessary to look at the individual contribution of each of the well's components to the wellhead response.

During the drilling operation the total displacement of the wellhead is influenced by the structural interactions among the surface casing, the conductor casing, and their respective cement sheaths. Each of those casing strings has different dimensions, physical properties, and is subjected to a different temperature profile. It is reasonable to assume that the stress levels on the wellhead are bound to vary as long as the temperature profiles of the well components fluctuate.

Figure 7.5 presents the temperature deviation along the surface casing and conductor at different moments during drilling operations, and it provides a first insight on the overall response of the members of the well.

The surface casing temperature initially ramps up much faster than the temperature of the conductor. However, as the temperature variation in the surface casing is approached by the temperature variation in the other components, the thermally induced interactions between casing strings and wellhead housings led to lower cyclic stress levels (sections 6.3.2 and C.2), and consequently lower fatigue-damage rates (sections 6.3.3 and C.3).

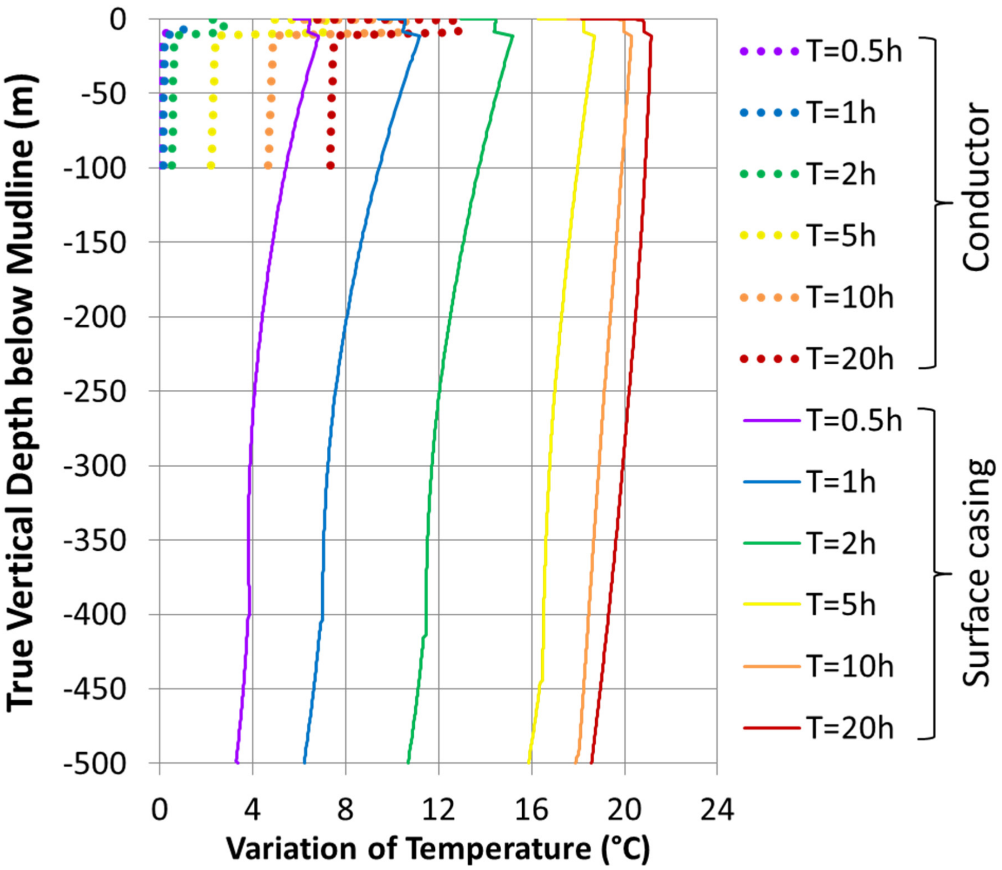

Figure 7.5 – Temperature variation along surface casing and conductor at different moments during drilling (wellhead B).

7.3 Trend Analysis of the Load-to-Stress Curves

It has been shown that the cyclic stresses on the wellhead fatigue hot spots can be influenced by the temperature distribution of the components of the well. The load-to-stress curves calculated for each time step, combined with the calculated dynamic response of the riser and the appropriate S-N curve, yield the fatigue-damage rate for the corresponding temperature distribution in the well.

There are multiple members in a well, of which the temperature varies along their lengths. Consequently, reducing the transient temperature distribution of the well to a single value of variation of temperature becomes impractical. Therefore, it has been proposed here to calculate the axial thermal strain of the tubulars in the well to compare fatigue-damage rates predicted for diverse temperature distributions and identify any trends.

A casing string has been assumed rigidly bonded to its cement sheath. Each member of the casing/cement pair has a different free thermal expansion, but both members of the pair achieve the same variation of length.

According to Hearn (1997) it can be stated that (i) the extension of one member plus the compression of the other equals the difference in free expansions, and (ii) the tensile force applied to one member is equal in magnitude to the compressive force applied to the other.

Based on these two statements, the following system of equations can be used to calculate the thermal expansion of the casing/cement-sheath pair.

$$\frac{\sigma_{casing} \cdot L}{E_{casing}} + \frac{\sigma_{cement} \cdot L}{E_{cement}} = \alpha_{cement} \cdot \Delta T_{cement} - \alpha_{casing} \cdot \Delta T_{casing} \qquad \textbf{Equation 7.1}$$

$$\sigma_{casing} \cdot A_{casing} = \sigma_{cement} \cdot A_{cement} \qquad \textbf{Equation 7.2}$$

where L is the original length, A is the cross-sectional area, and the remaining variables follow the same notation presented in section 2.5.

The temperature in the well varies with depth. Casing and cement can be divided into smaller elements, the thermal expansion of which is calculated using Equation 7.1 and Equation 7.2. The individual expansions of the elements are summed up to yield the overall thermal expansion and thermal strain of the casing/cement-sheath pair.

Therefore, it has been calculated the axial-thermal strain of the surface casing/cement-sheath pair, hereafter referred to as pair (2), and the axial-thermal strain of the conductor/cement-sheath pair, hereafter referred to as pair (1). The calculated strain of one pair is assumed not to be affected by the other. This quantity is hereafter referred to as the unrestrained axial thermal strain.

Given the mechanical interactions between pairs (1) and (2), the expected vertical growth of the wellhead system will be a value in between each pair's unrestrained axial-thermal expansion. However, the unrestrained axial-thermal strain for each pair can be used to predict the tendencies of the casing strings to expand at a given time, and their overall impact on the fatigue-damage rates.

This approach enables a quick comparison between different temperature conditions, and to determine which of those conditions would lead to higher fatigue-damage rates. The disadvantage of this approach is to make the reported results of the analysis less general, as they become suitable only to a restrictive combination of wellhead model, riser model, offshore location, and S-N curves.

However, because of the non-linear stress response that a hot spot might have, as presented in section 5.3.1, it becomes necessary to make this kind of post-analysis specific to the overall system instead of just the wellhead to simplify the interpretation of the results.

The fatigue assessment (section 6.3.3) indicated *hot spots 1*, *2* and *10* as the most critical for the fatigue capacity of the wellhead during drilling and at later stages of the life cycle of the well.

Focus is then given in the following sections to the fatigue response predicted for *hot spots 1*, *2* and *10* during the first mechanical configuration of the wellhead. Results obtained for the remaining mechanical configurations will be discussed in section 7.5, and the generated plots can be found in Annex C, section C.4.

The thermal-strain ratio, denoted by R_{exp}, will represent the ratio between the unrestrained axial-thermal strain of pair (2) and the unrestrained axial-thermal strain of pair (1).

$$R_{exp} = \frac{\varepsilon_{casing/cement\ pair\ (2)}}{\varepsilon_{casing/cement\ pair\ (1)}}$$

Equation 7.3

7.3.1 Welded Connection between High-Pressure Housing and Surface Casing

Figure 7.6 presents for wellheads A and B the normalized estimated fatigue-damage rates predicted for *hot spot 1*, plotted against R_{exp}. These results were obtained from the analyses performed for the period 0-90 hours. *I.e.* the first mechanical configuration assumed by the wellhead models, during which only the surface casing and the conductor are in place (Table 6.3).

The blue circles represent the normalized damage rates given by the analyses with temperature. The analysis without temperature yielded the red dashed line, which is the baseline for damage rate comparison. Figure 7.6 shows that for R_{exp} equal to 1 the damage rate estimated by the analysis with temperature is equal to the fatigue-damage rate estimated by the analysis without temperature.

For R_{exp} smaller than 2.26, the damage rates estimated by the analyses with temperature are smaller than the fatigue-damage rate estimated by the analysis without temperature. The minimum fatigue-damage rate was computed for a value of R_{exp} close to 1.5; down to 65% and 55% of the damage rate predicted by the analysis without temperature for wellheads A and B, respectively.

For R_{exp} greater than 2.26, which correspond to the structural calculations performed for t=0.5, 1, 2, 5 and 10 hours, the damage rates estimated by the analyses with temperature are greater than the damage rate estimated by the analysis without temperature; up to 30 and 15% higher than the damage rate predicted by the analysis without temperature for wellheads A and B, respectively.

From Figure 7.6 it may be noticed that the fatigue damage of the surface casing/high-pressure weld hot spot estimated during the drilling operation would significantly decrease if the temperature distribution in the well were to be kept at such state that R_{exp} is approximately 1.5.

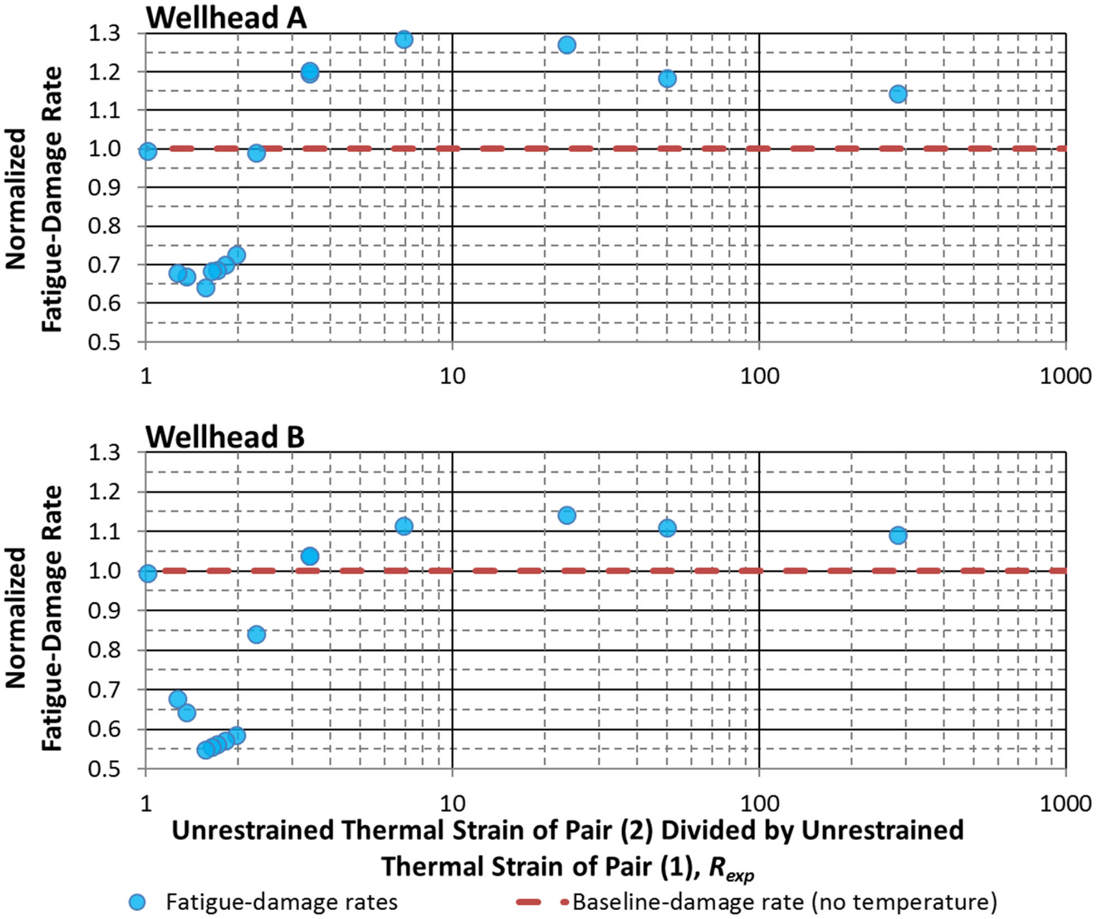

Figure 7.6 – Fatigue-damage rates plotted against R_{exp}. *Hot spot 1*. 1st mechanical configuration assumed by the wellhead model during drilling. DFF=10. S-N curve F.

7.3.2 Welded Connection between the Surface Casing's First and Second Joints

Figure 7.7 presents the normalized damage rates predicted for *hot spot 2*, plotted against R_{exp}, for the structural analyses performed for wellheads A and B during the first mechanical configuration assumed by the wellhead models during the drilling operation.

The results shown enable to predict that for a wide range of well-temperature distributions, the fatigue-damage rates at *hot spot 2* will be smaller than the damage rate predicted by the analysis without temperature.

Wellhead A may experience a reduction down to approximately 30% of the baseline value, when R_{exp} approaches 2; while wellhead B may experience a reduction to approximately 40% of the baseline damage rate value.

The trend detected for *hot spot 2* is similar to the trend detected for *hot spot 1* (Figure 7.6). However, unlike what has been observed for the *hot spot 1*, the normalized damage rates for *hot spot 2* never surpass the baseline value given by the analysis without temperature.

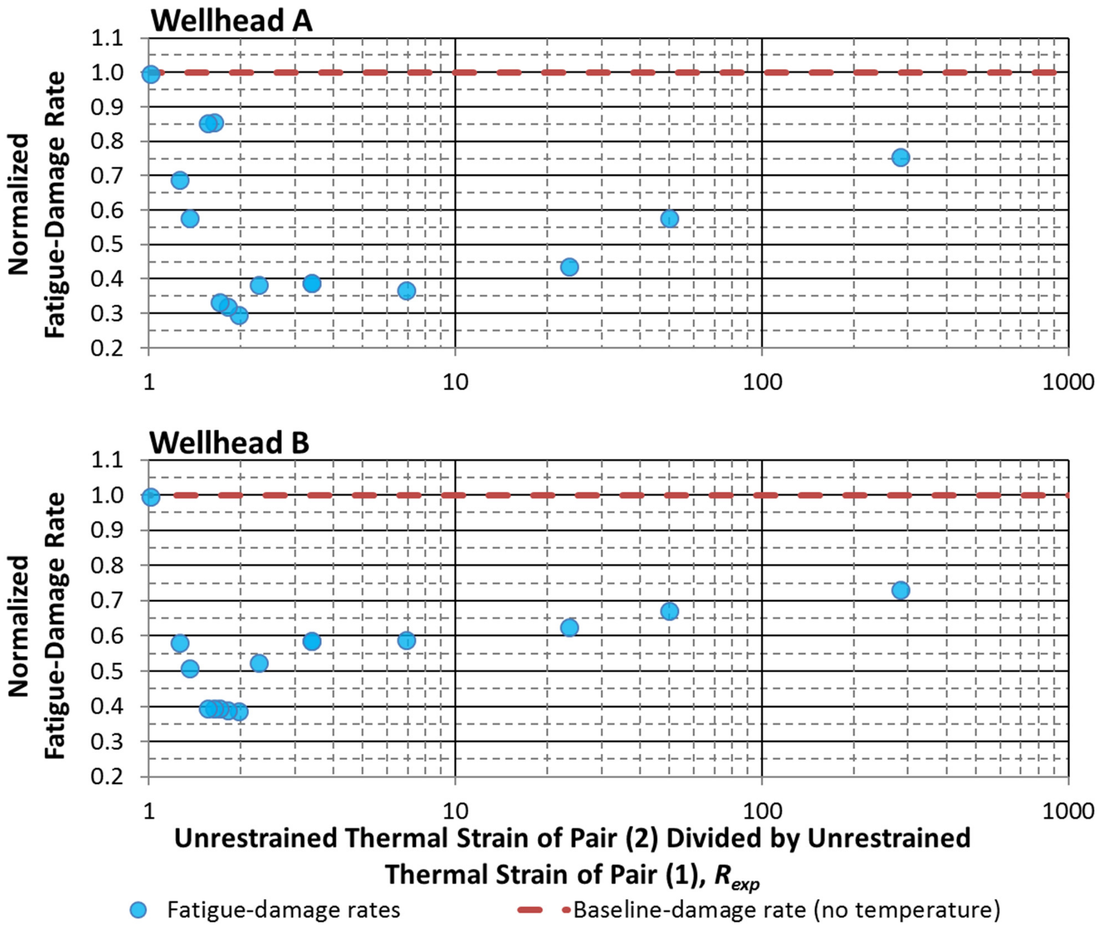

Figure 7.7 – Fatigue-damage rates plotted against R_{exp}. *Hot spot 2*. 1st mechanical configuration assumed by the wellhead model during drilling. DFF=10. S-N curve F3.

7.3.3 Landing Surface on the Low-Pressure Housing

Figure 7.8 presents the normalized fatigue-damage rates predicted for *hot spot 10*, plotted against R_{exp}, for the structural analyses performed for wellheads A and B during the first mechanical configuration assumed by the wellhead models during the drilling operation.

For R_{exp} values approaching 1.2, both wellheads may undergo normalized fatigue-damage rates higher than the respective baseline values. Normalized damage rates predicted for wellhead B remain close to 1 within the [1.4, 10] R_{exp} range.

Within the same range, normalized damage rates predicted for wellhead A undergo a significant reduction; down to half of the respective baseline value. However, both wellheads reach approximately the same normalized damage rate when R_{exp} approaches 300.

When comparing Figure 7.8 to Figure 7.6 and Figure 7.7, it might be indicated that *hot spot 10* has the opposite response of *hot spots 1* and *2*. For *hot spot 10*, damage rates decrease when R_{exp} shifts towards higher values, while the damage rates computed for *hot spots 1* and *2* increase.

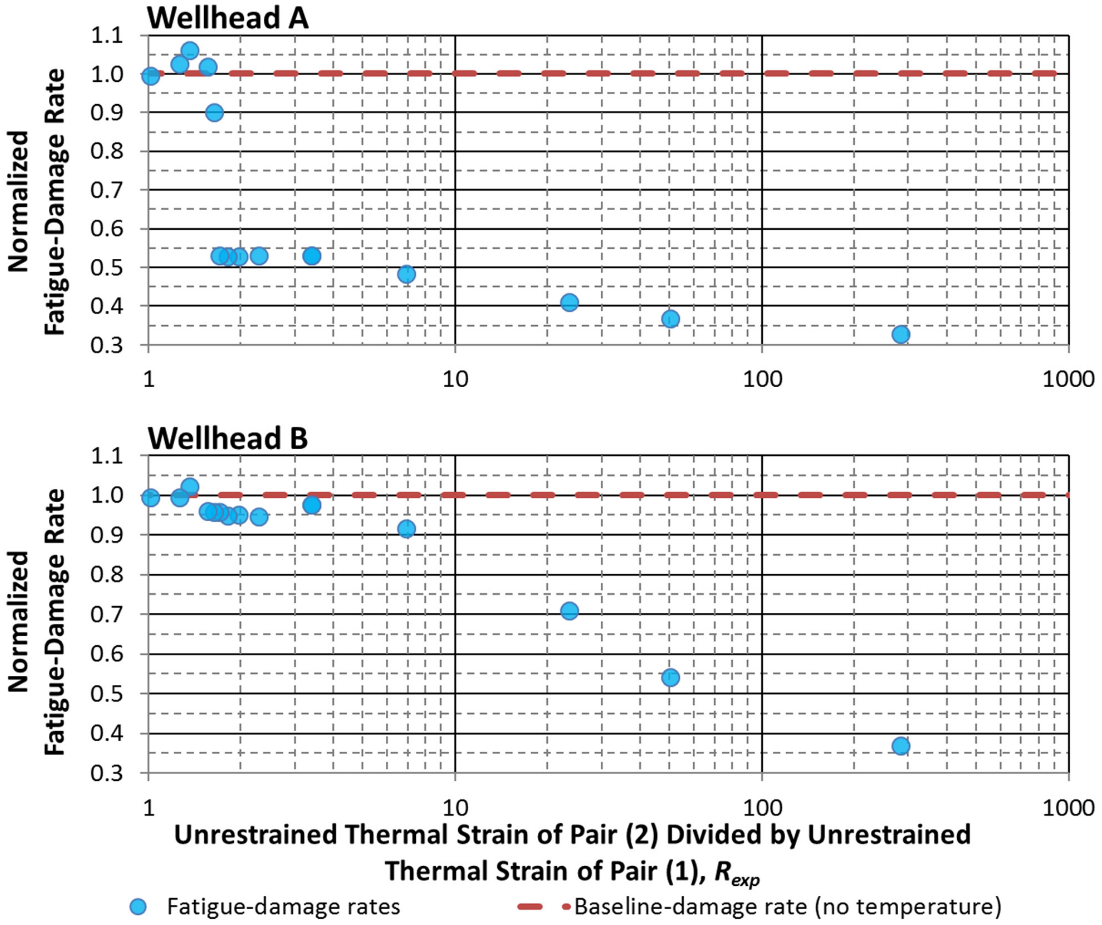

Figure 7.8 – Fatigue-damage rates plotted against R_{exp}. *Hot spot 10*. 1st mechanical configuration assumed by the wellhead model during drilling. DFF=10. S-N curve BM4.

Hot spot 10 is located in the low-pressure housing, while the *hot spots 1* and *2* are subject to the loading that follow through the high-pressure housing. According to the load sharing argument presented in section 7.1, it would be expected for *hot spot 10* to be subject to lower cyclic stresses when *hot spots 1* and *2* are subject to higher cyclic stresses, and vice-versa.

The previous comment may also apply when comparing the fatigue-damage rates obtained for the third (Figure C.22, Figure C.28 and Figure C.34) and fifth (Figure C.24, Figure C.30 and Figure C.36) configuration of the wellhead. Not enough structural calculations were carried for the remaining configurations to enable this comparison.

7.4 Trend Analysis of Preload-stress levels

The approach with the variable R_{exp} has also been applied to the calculated preload-stress levels. Figure 7.9 and Figure 7.10 present the normalized preload-stress levels obtained during the first mechanical configuration assumed by the wellhead during drilling. The results obtained for the remaining configurations are found in section C.5.

Because bending moment has not been included, the results displayed are less likely to have been influenced by non-linearities present in the wellhead system. The weld hot spots (Figure 7.9) seem to follow each a clear trend, which is not the same as the ones detected and discussed for the cyclic stresses.

The calculated preload-stress levels on the welds located on the surface casing increase because of the induced temperature, and the highest increase was calculated for R_{exp} approaching 7. The calculated preload-stress levels on the welds located on the conductor decrease because of temperature and achieve their bottom value also for R_{exp} approaching 7.

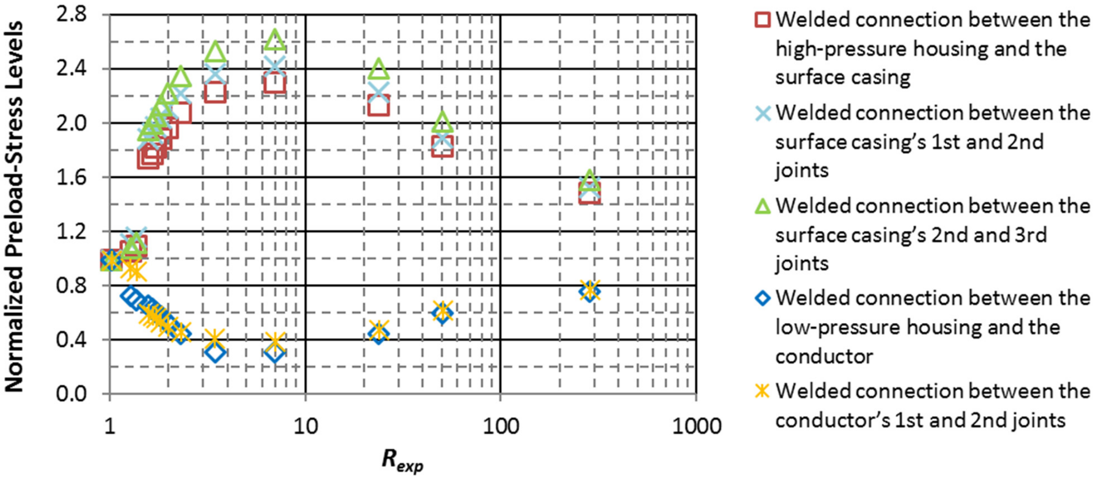

Figure 7.9 – Normalized preload-stress levels plotted against R_{exp}. Welded connection hot spots. 1st mechanical configuration assumed by the wellhead model during drilling.

The results of the analyses in Figure 7.10 may indicate that for values of R_{exp} in between 1 and 4, some of the base metal hot spots do not follow a clear trend. The values obtained for the lock ring and the lower outer edge of the high-pressure housing within that range of R_{exp} are to some degree in conflict. The other hot spots follow each a more definite trend.

The analysis indicates that some of base metal the hot spots may experience a reduction in the preload-stress levels for also for R_{exp} approaching 7. For the lock ring, the reduction in stress vas was obtained for R_{exp} close to 2. For the upper outer edge of the high-pressure housing the biggest reduction in the preload-stress levels was obtained for values of R_{exp} between 3 and 4.

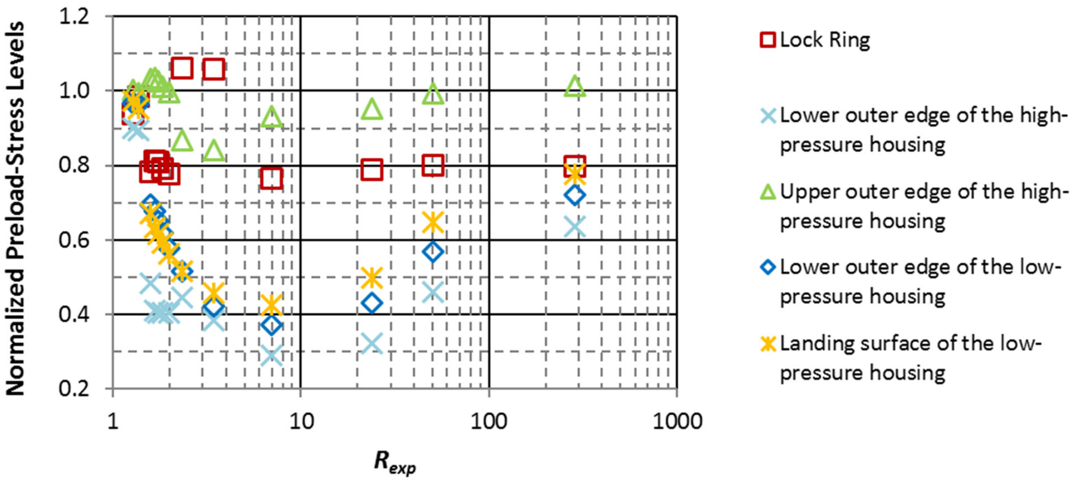

Figure 7.10 – Normalized preload-stress levels plotted against R_{exp}. Base metal hot spots. 1st mechanical configuration assumed by the wellhead model during drilling.

7.5 Discussion

This research has shown that the well-temperature distribution can influence the fatigue-damage rates of the wellhead hot spots in different ways (sections 6.3.3 and C.3). Therefore, it recommends that well temperature be incorporated into the wellhead fatigue assessment, so the estimates obtained may originate from a more-accurate modeling of the response of the system.

Following that recommendation, the next step would be to investigate if the well temperature could be used to minimize wellhead fatigue. Sections 7.3.1, 7.3.2 and 7.3.3 have presented the predicted response for the three most critical hot spots in the particular wellhead models tested.

The approach used, with the proposed R_{exp} variable, had as goals to correlate the induced thermal expansion of the tubular components of the well with the cyclic stresses predicted at the hot spots, and to expand the results obtained from an already known set of temperature distributions to other, not previously analyzed, temperature distributions that generate the same R_{exp}.

The results pertaining to the sections mentioned above, along with the results obtained for some of the mechanical configurations of the wellhead which are presented in section C.4, indicate that the proposed approach might be suitable for extrapolating the response of a fatigue hot spot to not previously experienced temperature scenarios. Although, the fatigue-damage rate predicted for a hot spot might be found within a range of values, instead of a specific value.

Figure C.24 shows the results for the 5th mechanical configurations of the wellhead. For wellhead B, there are data points clustered within the [1.4, 1.5] R_{exp} range. The results in Figure C.24 do not enable to specify the exact value of the normalized fatigue-damage rate for a new temperature scenario within this R_{exp} range; only that it would be between 0.8 and 0.9.

7.6 Active Control of Well Temperature to Mitigate Wellhead Fatigue

The proposed approach may indicate under which R_{exp} ranges the wellhead would be subject to the lowest and the highest damage rates. Thus, based on the real-time temperature measurements of the drilling fluid together with a thermal model of the well (Sevillano et al. 2017), the drilling engineer could have the actual value of R_{exp} calculated. Based on this data, adjustments could be made to operations, steering them towards the R_{exp} range which yields minimal fatigue-damage rate.

The safe execution of well operations, however, takes precedence over control of the development of well temperature. As the results presented in sections 6.3.3.1 and C.3 reveal, stopping and restarting the circulation in the well may sharply increase fatigue-damage rates, but it cannot be avoided when, for instance, it is necessary to change the drill bit.

Nevertheless, there are alternatives for managing well temperature that do not necessarily increase the overall duration of well operations. Controlling the temperature of the fluid that enters the drillstring, by heating it up during specific periods of time, might be a non-intrusive measure that could keep fatigue-damage rates low. The additional heat transferred to the conductor, and ensuing increase of its temperature distribution, prior to a period of non-circulation may restrain R_{exp} from rising sharply when circulation restarts.

Conversely, the auxiliary lines along the riser could be used to pump fluid down to the BOP. This fluid would be cooled down by the sea water, and as it mixes with the upwards annulus fluid, it could be expected that it would cool down the downwards fluid in the drillstring. Maintaining fluid circulation during tripping operations might also help managing the well-temperature distribution.

Figure 7.11 summarizes how the variable R_{exp} could be used within a real time operational context, and how it would integrate the results of the fatigue modelling with the monitoring of operational parameters. Figure 7.12 and Figure 7.13 present examples of charts that may be available for a drilling engineer to manage R_{exp}.

The charts present the ranges of R_{exp} that yield the least amount of fatigue damage in *hot spots 1*, *2* and *10* for wellheads A and B, respectively, throughout the different mechanical configurations assumed during operations (Table 6.3).

Except for the first mechanical configuration of the wellhead during drilling, the optimal ranges of R_{exp} predicted for the hot spots in both wellheads are the same. Most noticeable difference was computed for fatigue *hot spot 10*. The damage rates at this hot spot benefit from a large value of R_{exp}, but the optimal range predicted for wellhead B [50, 300] is considerably shorter than the range predicted for wellhead A [1.7, 300].

Figure 6.8 showed that the largest fatigue-damage rates were experienced by *hot spot 1* during the first and third mechanical configurations. Figure C.12 shows that the same is valid for *hot spot 2* in wellhead B, while in wellhead A the highest damage rates are concentrated during the third mechanical configuration. Conversely, Figure C.20 shows that *hot spot 10* experiences considerably lower damage rates during the first mechanical configuration of the wellhead.

If these hot spots experienced similar levels of fatigue-damage rate, then their distinct responses would require a different hot spot to be the focus of fatigue damage mitigation during each of the mechanical configurations of the wellhead. The results of this study, however, point that for wellhead A, *hot spot 1* is the critical component for future operations. For wellhead B, the critical component is *hot spot 2*.

Table 7.1 presents the accumulated fatigue damage on wellheads A and B during the drilling operation if it was possible to manage the well temperature distribution to minimize fatigue damage.

In case of uncertainty about the effective TOC level, it might be necessary to minimize the accumulated fatigue in both hot spot 1 and 2, instead of prioritizing one of them. A simple way of achieving the optimal combined fatigue damage is by testing values of Rexp and selecting the values that yield the lowest combined fatigue damage. Table 7.1 also presents the estimates obtained when the effective TOC is uncertain.

It may be established that the accumulated damage in wellhead A could decrease 8.9 percentage points if it was the critical hot spot, or it could decrease 3.7 percentage points if the effective TOC was uncertain. Correspondingly, the accumulated damage in wellhead B could decrease between 1.9 and 1.5 percentage points.

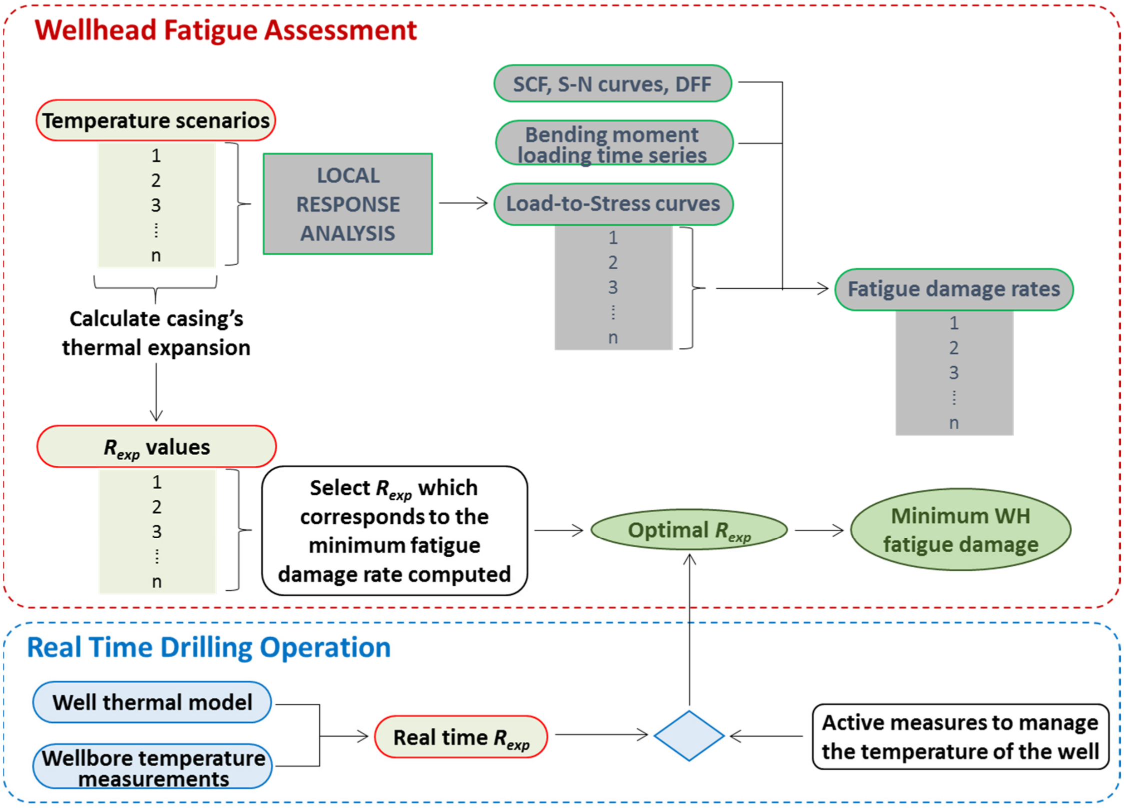

Figure 7.11 – Fatigue-modelling results integrated with real time operations.

Table 7.1 – Minimized accumulated fatigue damage summary. DFF=10. 1st tier S-N curves.

ACCUMULATED FATIGUE DAMAGE (% OF DESIGN-FATIGUE LIFE)			
Wellhead / Hot spot	**Without temperature control**	**Minimized on critical hot spot**	**Minimized on both hot spots due to uncertain TOC level**
A / 1	33.7	24.9	30.1
B / 2	8.97	7.06	7.45

Table 7.2 is analogous to Table 7.1, but it presents the accumulated fatigue-damage estimates based on the second tier S-N curves. *Hot spot 1* becomes the critical hot spot for both wellheads. Therefore, the optimal range of R_{exp} for *hot spot 1* can be selected, independently of TOC level. The reduction in fatigue damage for wellhead A was 19.5 percentage points. The reduction estimated for wellhead B was 12 percentage points.

Table 7.2 – Minimized accumulated fatigue damage summary. DFF=10. 2nd tier S-N curves.

ACCUMULATED FATIGUE DAMAGE (% OF DESIGN-FATIGUE LIFE)		
Wellhead / Hot spot	**Without temperature control**	**Minimized on critical hot spot**
A / 1	81.6	62.1
B / 1	32.4	20.4

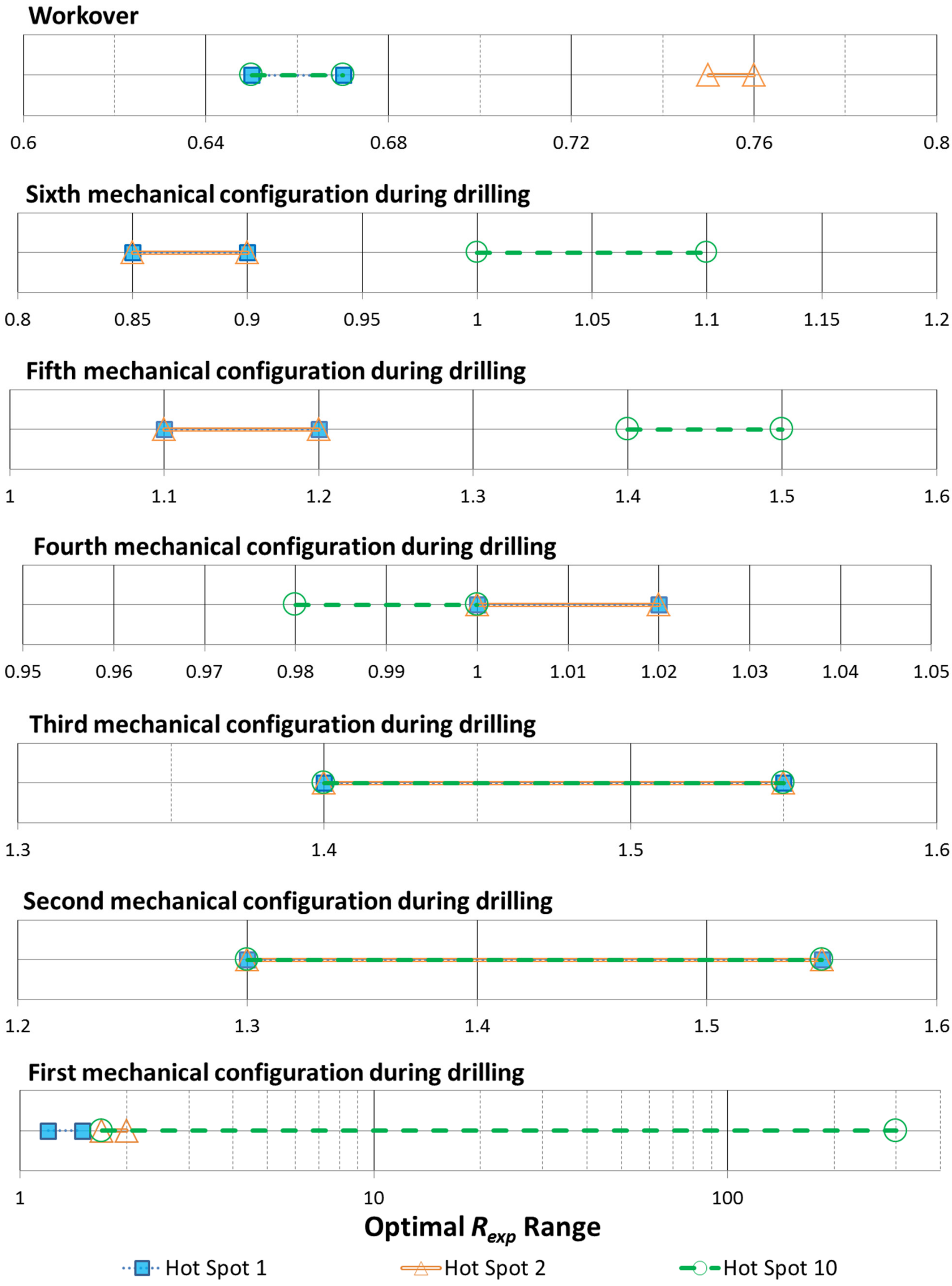

Figure 7.12 – Ranges of R_{exp} that yield the least amount of fatigue damage throughout the different mechanical configurations assumed by the wellhead A. *Hot spots 1*, *2* and *10*.

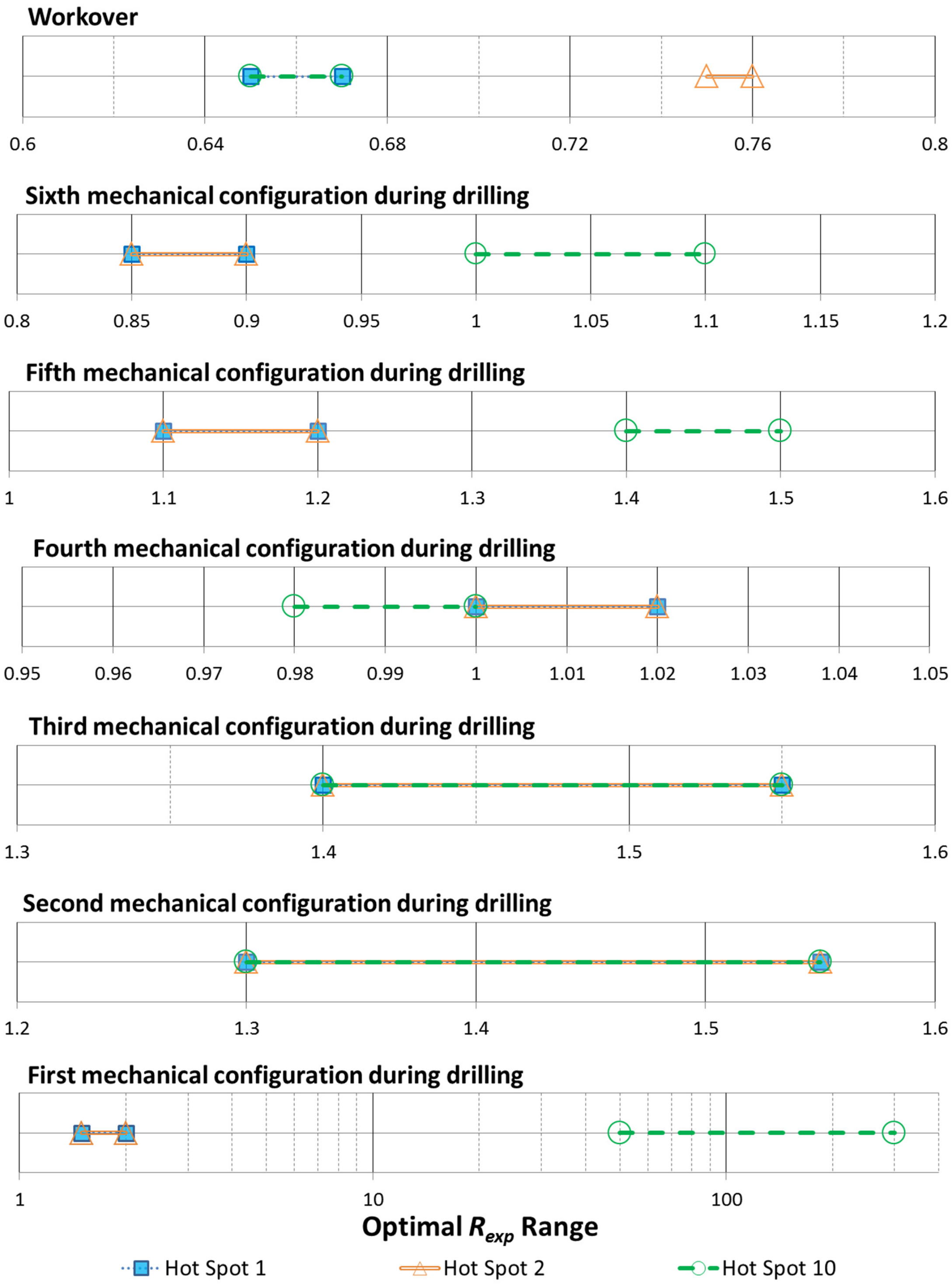

Figure 7.13 – Ranges of R_{exp} that yield the least amount of fatigue damage throughout the different mechanical configurations assumed by the wellhead B. *Hot spots 1*, *2* and *10*.

Chapter 8

Alternative Mitigating Method for Wellhead Fatigue

Repairing or replacing an existing subsea wellhead is not practical, as it is a permanent structural component of the well. Therefore, the importance of improving the methodology used for assessing fatigue damage; a more-accurate estimate of the fatigue damage might prolong the service lifetime of the wellhead without being required to perform any improvements on the equipment.

This doctoral work proposed an approach for incorporating well temperature into the fatigue assessment. Section 1.2 mentions other approaches that aimed to improve the fatigue assessment by focusing on the measurement and modelling of the environmental loads transferred from the riser to the wellhead. Nevertheless, there might come to a point during the life of a well on which the fatigue capacity of the wellhead is nearly completely depleted, without the possibility of further interventions being carried out, and thus imposing the abandonment of the well.

Structural reinforcement of the BOP stack, however, is an alternative to an early well abandonment. Successful reinforcement methods reduce dynamic stresses transferred to critical fatigue components, minimizing damage rates during re-entry operations, by decreasing the bending moment that is transferred from the riser to the wellhead.

This chapter presents one said approach that aims to reduce the bending moment load by employing a BOP tethering system. Said system and others with similar objective (Rørgård et al. 2017) could also be implemented from the start of the drilling operations, thus greatly reducing fatigue damage on the wellhead.

8.1 BOP Tethering System

A BOP tethering system can be briefly described as an assembly of anchors disposed around the subsea wellhead, which are connected to the BOP by cables. Figure 8.1 presents a sketch of a BOP tethering system with three or four anchors.

In the figure, drop anchors are shown providing the anchoring points, but suction piles or concrete blocks could also perform this task (2H offshore 2017). Individual tensioning systems can be used to control the tension load on each mooring line, maintaining it within a certain range, thus limiting the deflection of the BOP and consequently the bending imposed on the wellhead.

BOP tethers are a novel approach. An internal document of the Department of Geoscience and Petroleum of the Norwegian University of Science and Technology from 2009 presents the approach (Sangesland 2009). A master thesis from the same department provides a detailed description of the approach's configurations and materials (Lien 2010).

More recently, the company Trendsetter Vulcan Offshore has submitted patents applications of similar concepts (Kebadze et al. 2014), and it has shown promising results in a workshop organized by the Norwegian Geotechnical Institute in collaboration with Texas A&M at College Station and University of Texas at Austin (Mittendorf 2016).

Within the context of the wellhead fatigue assessment methodology presented in this thesis, evaluating the merits of a BOP tethering system to mitigate wellhead fatigue would require both local and global response analyses.

In the local response analysis, the cables at constant tension connected to the BOP add new forces acting on the subsea stack, which can influence the stresses on the fatigue hot spots on the wellhead system. In the global response analysis, the anchor and cables arrangement create a different bottom condition for the riser model.

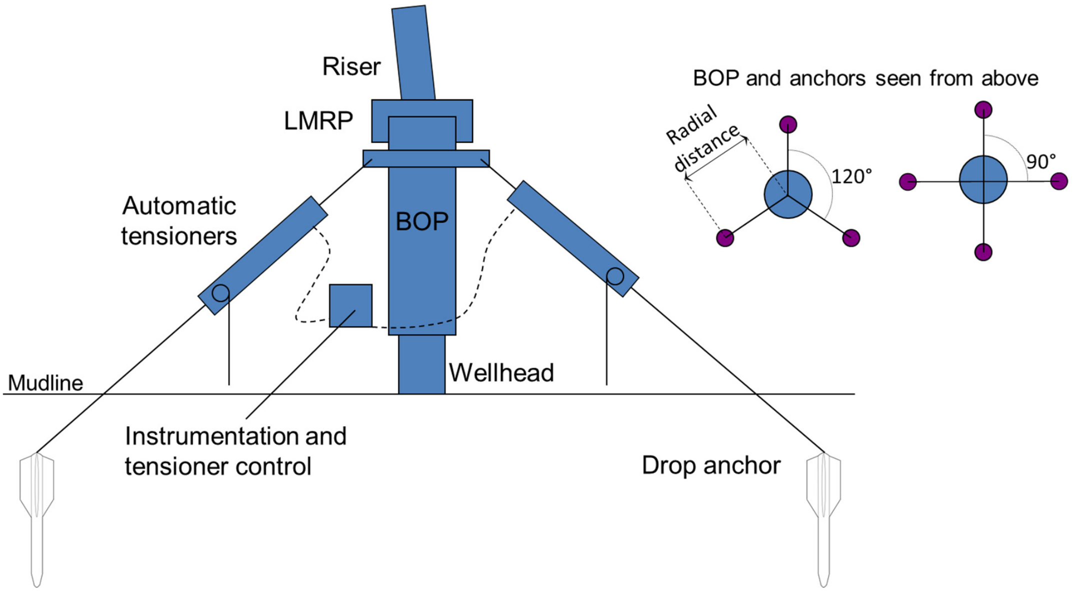

Figure 8.1 – Sketch of a BOP-tethering system.

8.2 Case Study

Lien (2010) has demonstrated the effectiveness of a BOP tethering system under static loading conditions, based on the induced inclination of the riser at its connection point to the BOP.

The case study performed within this thesis has investigated the global response of a riser, subsea stack and wellhead model obtained for different BOP tethering systems. The parameters studied were the material of the tethers and the positioning of the anchoring points.

The tension on the tethers was set at one of the calculation stages of the static response analysis of the riser model, based on the stiffness of the tether material and the induced deformation, as presented by Figure 8.2, but it was not modified during operations.

The geometric length of the tether, in Figure 8.2 corresponds to the distance between the connection point on the BOP and the top of the anchor. The tether is deformed from the stress-free length until it reaches the anchor position. Pre-tension on the tether was set to 25% of the maximum load it can withstand. There is no documentation available on the installation of this equipment, so it was opted to keep pre-tension at a low level.

Loading was applied to the wellhead system due to multiple sea sates, in a similar fashion to what has been described in Chapter 3 of this thesis. For fatigue calculation purposes, it was assumed that the load-to-stress curves obtained for the wellhead systems in Chapter 6 remained valid.

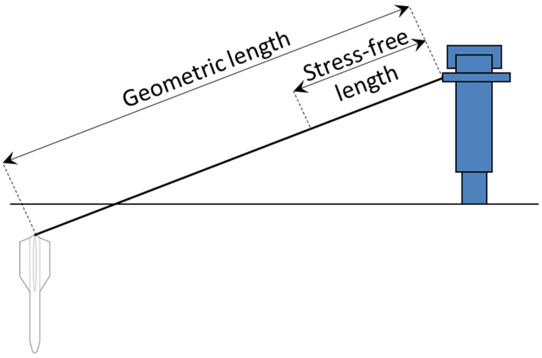

Figure 8.2 – Sketch of the induced deformation on the BOP tethers.

8.2.1 Tethering System Characteristics

8.2.1.1 Drop Anchors

The total length of the modelled drop anchors was 15 meters. The top of the anchors was located two meters below the sea bottom level. Prior to computing the wellhead response towards wave induced loads, the anchor was assumed to maintain the vertical position. The anchoring points were set surrounding the wellhead, either 120° apart from each other in the case of three anchors, or 90° in the case of four anchors. The tested values for the radial distance were 10, 15 and 20 meters.

Figure 8.3 presents the finite-element modelling employed for the drop anchor. The interaction with the surrounding soil layers was modelled using non-linear, translational springs acting in the horizontal plane. The anchor rotates around a pivot node at an intermediary position, determined by a prior anchor-soil interaction analysis.

8.2.1.2 Tethering Lines

The impact the physical characteristics of the tethering lines had on the resulting load at the wellhead was evaluated by testing five different materials. Radial distance of tethers was set to 10 m. Table 8.1 presents the properties of the different ropes used to model the tethering system. The axial stiffness of the ropes is presented by Figure 8.4.

Table 8.1 – Properties of ropes used for tethering the BOP. (Bexco 2018).

Rope Type	Diameter (mm)	Weight (kg/100m)	Break load (kN)
1	120	893	3047
2	128	1020	3430
3	136	1150	3905
4	144	1280	4380
5	152	1425	4855

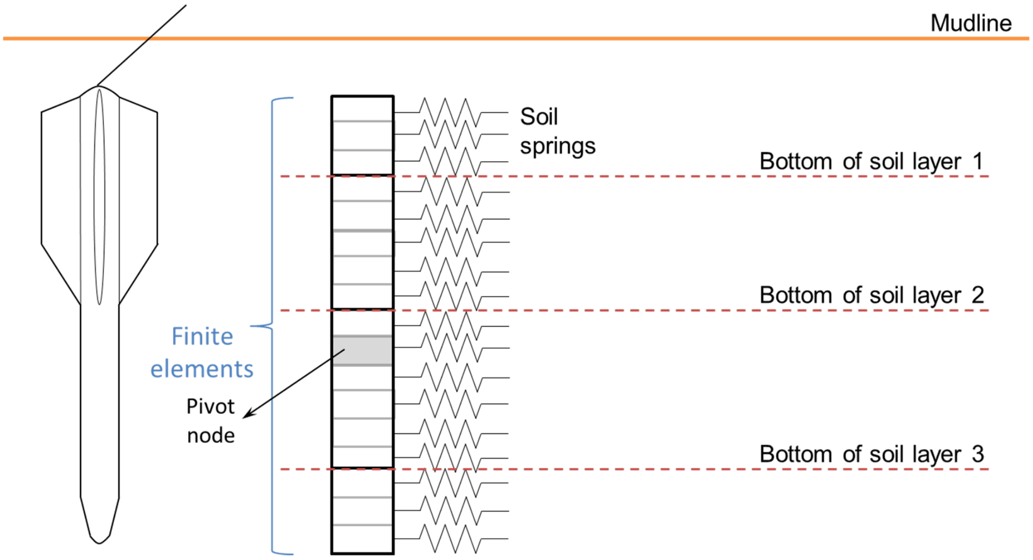

Figure 8.3 – Drop anchor finite-element modelling

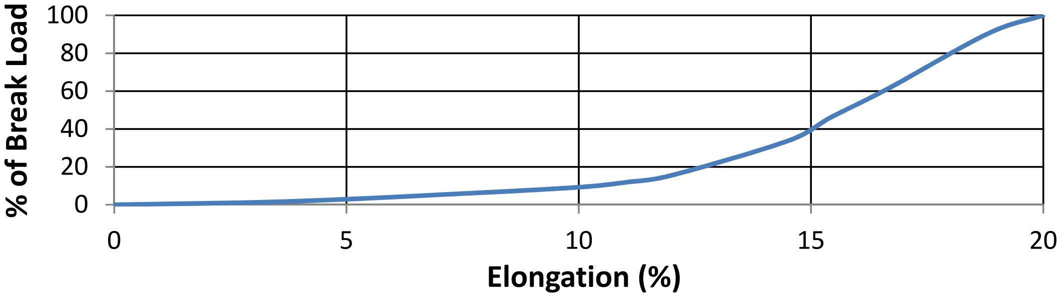

Figure 8.4 – Sketch of the induced deformation on the BOP tethers. (Bexco 2018).

8.3 Results

8.3.1 Physical Characteristics of Tethers

The five ropes types presented in Table 8.1 were tested. Figure 8.5 presents the bending moment time history corresponding to the largest reduction in the estimated load at the wellhead datum, calculated for the tethering system with rope type 5. In the figure, the loading range at the wellhead, as generated by the multiple sea states presented in Table 3.3, decreased from approximately [-1500, 1500] kNm to [-1000, 1000] because of the BOP tethering system.

Table 8.2 summarizes the results obtained in terms of the accumulated fatigue damage during the drilling operation and during a workover operation. The selected wellheads and their respective hot spots are the welded connection between the high-pressure housing and the surface casing in wellhead A, and the welded connection between the first and second joints of the surface casing in wellhead B (hot spots and wellheads description found in Chapter 5).

Table 8.2 shows that the BOP tethering system with rope type 5 may reduce the accumulated damage in wellhead A, at the end of either the drilling operation or the workover operation, to almost one fourth of the damage estimated for the non-tethered subsea system. If the tethering system were implemented after the drilling operation, the maximum riser connection days would increase from 27 days to 92 days.

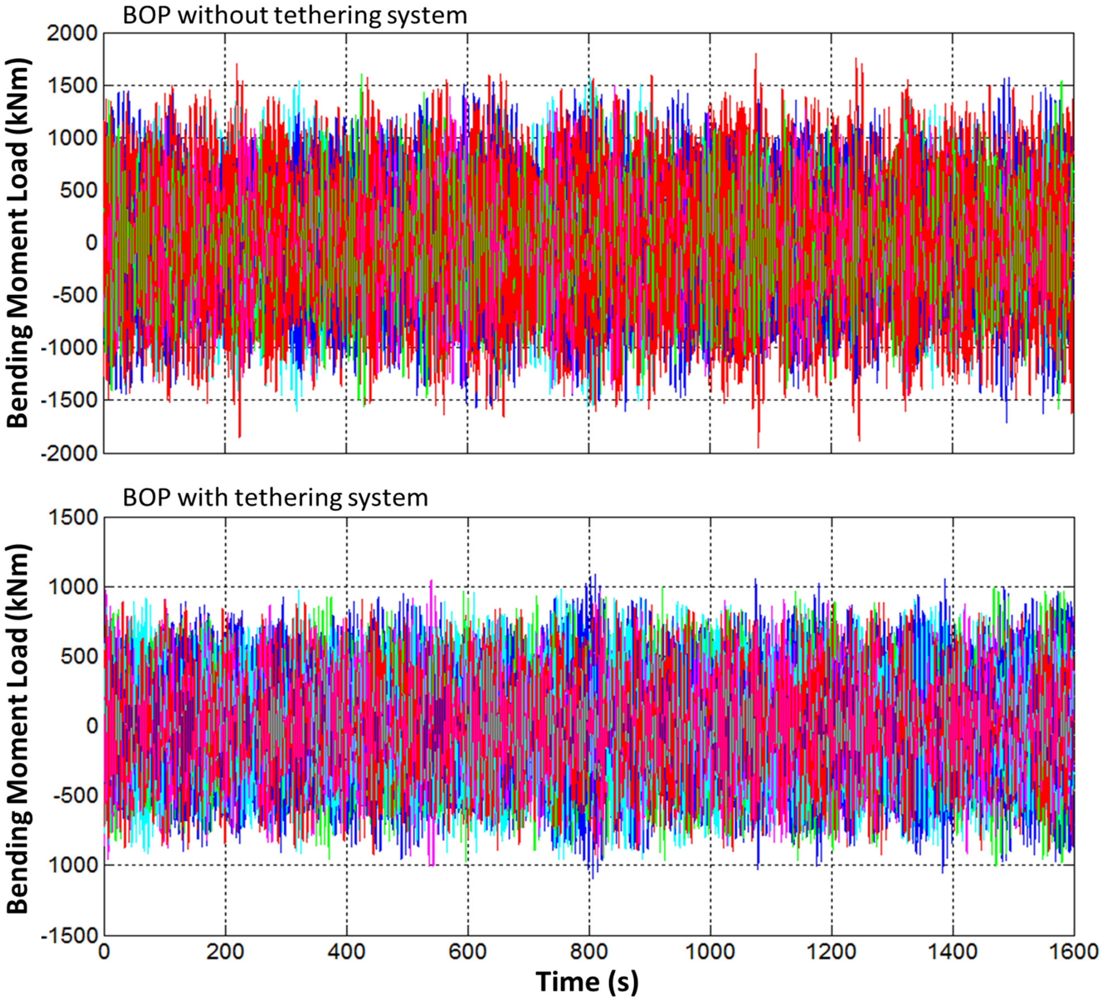

Figure 8.5 – Bending moment loading at WH datum. BOP systems with and without tethers.

For wellhead B the estimated accumulated fatigue damage could become as low as approximately 20% of the original estimates. Considering the tethering system is implemented after the drilling operation for the workover operation the maximum riser connection days could increase from 181 days to 401 days.

Table 8.2 – Accumulated damage at wellhead fatigue hot spots during drilling for BOP tethering systems with different rope types. Conventional analysis without temperature.

Accumulated fatigue damage (% of design-fatigue life). DFF=10. 1st tier S-N curves				
	Wellhead A – Hot Spot 1		**Wellhead B – Hot Spot 2**	
Rope Type	**Drilling**	**Workover**	**Drilling**	**Workover**
No rope	39.8	4.60	11.6	2.10
1	21.9	2.53	5.27	1.01
2	19.1	2.22	4.43	0.86
3	16.1	1.88	3.55	0.70
4	13.6	1.59	2.84	0.57
5	11.5	1.34	2.27	0.46

8.3.2 Location of Tethers

The influence of the location of the tethers was investigated by testing the BOP tethering system with rope type 5 with radial distances equal to 15 m and 20 m. Table 8.3 presents the results obtained for the cases simulated. It can be seen that an increase in the radial distance of the tethers to 20 m led to 3.4 percentage points higher accumulated damage for *hot spot 1* in wellhead A at the end of the drilling operation.

Table 8.3 – Accumulated damage at wellhead fatigue hot spots during drilling for BOP tethering systems with different radial distances. Conventional analysis without temperature.

Accumulated fatigue damage (% of design-fatigue life). DFF=10. 1^{st} tier S-N curves				
Radial Distance (m)	**Wellhead A – Hot Spot 1**		**Wellhead B – Hot Spot 2**	
	Drilling	**Workover**	**Drilling**	**Workover**
20	14.9	1.74	3.16	0.63
15	12.8	1.49	2.58	0.52
10	11.5	1.34	2.27	0.46

Space constraints around the wellhead site can prevent the adoption of the optimum radial distance for the tethers, but the results in Table 8.3 show that the gains in fatigue life of the wellhead can still be considerable when compared to the accumulated damage without a tethering system, as presented by Table 8.2.

8.3.3 Number of Tethers

The configuration of the tethering system in the analysis of the previous sections had three tethers. The influence of the additional tethers was investigated by testing a BOP tethering arrangement with four and five tethers.

Table 8.4 presents the results obtained. For the cases run, employing four tethers instead of three reduced the accumulated fatigue damage at the end of the drilling operation to 6.53% and 1.07% for wellheads A and B, respectively. Employing five tethers further reduced the calculated accumulated fatigue damage to 3.78% and 0.53%.

Table 8.4 – Accumulated damage at wellhead fatigue hot spots during drilling for BOP tethering systems with different number of tethers. Conventional analysis without temperature.

Accumulated fatigue damage (% of design-fatigue life). DFF=10. 1st tier S-N curves

Number of Tethers	Wellhead A – Hot Spot 1		Wellhead B – Hot Spot 2	
	Drilling	Workover	Drilling	Workover
5	3.78	0.44	0.53	0.11
4	6.53	0.76	1.07	0.22
3	11.5	1.34	2.27	0.46

Analogous to the previous discussion on radial distance, the number of tethers that could be employed is also subject to the space constrains around the wellhead. Moreover, the installation and material cost of additional anchors and tethers must also be accounted for when deciding which tethering system design best suits the required fatigue capacity by the operations planned throughout the life of the well.

8.4 Summary

The results of the study conducted have shown that tethering the BOP system during drilling or reentry operations has the potential to decrease the accumulated fatigue damage in the wellhead and should be regarded as an alternative for mitigating wellhead fatigue. The gains in production because of the increased operational life of the well have the potential to surpass the costs inherent to installing the tethering system.

From the configurations tested for the subsea system modelled in the study, the tethering system with 5 tethers connected to anchors 10 meters away from the wellhead yielded the greatest reduction in wellhead fatigue damage. The other configurations also provided considerable gain in fatigue life, indicating that even if installation restrictions prevent the optimum design to be used this approach could still be advantageous.

The study focused solely on how the tethers influenced the bending moment on the wellhead. Future work should focus on how the stresses in the wellhead fatigue hot spots, as given by the structural calculations in the local response analysis would be impacted by the tethering system.

Chapter 9

Conclusions

The main focus of the work conducted in this PhD thesis has been the mitigation of wellhead fatigue. The incorporation of temperature into the analytical models employed by wellhead fatigue assessment methodologies has been proposed to increase the scope of the current methodologies and to yield more-accurate estimates of accumulated fatigue damage.

The conventional analysis procedure was adapted to accommodate for well temperature as an additional input parameter. In addition to the need for obtaining the temperature distribution of the well at different times during any given operation, it has been deemed necessary to carry out several structural analyses of the wellhead model to fully cover the transient effect of temperature.

The results obtained by studying the effects of temperature on the response of the analytical models of the wellhead system enabled drawing the following concluding remarks:

- When added to the structural calculation of the wellhead model, the temperature distribution of the well modifies the relation between the load applied in the wellhead and the resulting cyclic stresses in a fatigue hot spot, so called the load-to-stress curves.
- Temperature led most wellhead configurations and hot spots to experience lower cyclic stresses throughout operations, resulting in lower accumulated fatigue damage. The fatigue estimates of the most susceptible hot spots to temperature were 10 to 20% lower than what a conventional analysis would indicate
- Thermal stresses generated by induced/restrained deformation are added to the mean stress acting on a fatigue hot spot. Therefore, thermal stresses cannot directly explain the changes in magnitude calculated for the cyclic stresses.
- Each predicted well-temperature distribution introduces a new set of forces that acts upon the components of the wellhead. Consequently, the way the riser dynamic loading is shared among the components of the wellhead will vary. Hence the changes in magnitude of cyclic stresses.
- The conventional wellhead fatigue assessment assumes fatigue-damage rates to remain constant during a given operational phase. But, because the temperature in the well has been shown to influence the cyclic stresses in the wellhead, this assumption is not valid.
- The depth to TOC of the surface casing may influence the effect temperature has on the stress response of fatigue hot spots. The estimated fatigue damage for the wellhead configurations with TOC closer to the mudline may be influenced to a greater extent by temperature than its counterparts with TOC located farther down.
- The calculated thermal strain of the tubular components in the well was used to establish a direct relation between temperature distributions and fatigue-damage rates. This

approach may be used to predict damage rates under well-temperature distributions not previously experienced, and to identify the interval of thermal scenarios that yields the most favorable loading conditions for a given fatigue hot spot.

- Incorporating temperature into the analyses increases the computational costs. However, the contribution of the proposed approach can be translated into safer planned field operations and extended service lifetime of the wellhead.
- The overall impact of temperature on fatigue damage estimates is dependent on the mechanical configuration of the wellhead and on the history of operations performed in the well. Thus, it should be assessed on a case-by-case basis.

The experience gained conducting the global response analyses in this study also enabled to expand the scope of the approach used to mitigate wellhead fatigue.

In the case that the wellhead fatigue capacity has been considerably spent, but there is the need for a reentry operation, a BOP tethering system may be used to reduce the loading at the wellhead system. The results of simulations for different design options have shown the potential of this approach to increase the service life of a wellhead, potentially doubling it.

9.1 Recommendations for Future Works

The results of the thesis have shown that the temperature of the well can influence the stress response of wellhead fatigue hot spots.

A more-detailed and systematic future investigation of the temperature induced interactions of the wellhead components could lead to charts that better correlate the thermal expansion of casing strings with the stresses at the fatigue hot spots, and thus eliminating the need for a local response analysis for each new temperature distribution in the well.

Together with real time monitoring of environmental loading conditions and a comprehensive thermal model of the well, said charts could be used to estimate the fatigue damage in the wellhead as operations are being carried out.

This thesis has suggested non-intrusive methods that could be used during well operations to manage the well temperature. Another future line of research could investigate the feasibility of lowering wellhead fatigue by taking advantage of eventual windows of opportunity within drilling or reentry operations, and actively controlling the well temperature.

This thesis has briefly discussed SRA, despite presenting a deterministic analysis. The impact that temperature might have on wellhead response, the uncertainty associated to temperature calculation, and the benefits of SRA warrant future investigation of these combined approaches.

Moving forward with the BOP tethering system as an alternative to mitigating wellhead fatigue, more-extensive analysis could be performed to model the anchor-soil response for different anchoring alternatives, as how it impacts the response of the wellhead. Laboratory scaled-down experiments could also give validation to simulation results.

References

2H offshore. 2017. http://2hoffshore.com/blog/re-entering-old-wells-deal-fatigue/ (accessed 2 January 2018).

Aasen, J.A., Aadnøy, B. 2004. Multistring Analysis of Well Growth. Presented at the IADC/SPE Asia Pacific Drilling Technology Conference and Exhibition, Kuala Lumpur, Malaysia, 13-15 September. SPE-88024-MS. https://dx.doi.org/10.2118/88024-MS.

API RP 2RD, Design of Risers for Floating Production Systems (FPSs) and Tension-Leg Platforms (TLPs). 2006. Washington, DC: API.

ANSYS. 2016. http://www.ansys.com/About-ANSYS/news-center/08-11-15-ANSYS-16-2-Releases-The-Latest-Advances-In-Systems-Engineering-Technology (accessed 29.12.2016).

Anzai, H., Endo, T. 1979. On-site Indication of Fatigue Damage under Complex Loading. *International Journal of Fatigue* **1** (1): 49-57. Elsevier-0142-1123. https://dx.doi.org/10.1016/0142-1123(79)90044-6.

Bergman, T. L., Lavine, A. S., Incropera, F. P., Dewitt, D. P. *Fundamentals of Heat and Mass Transfer*, seventh edition. New York, NY: John Wiley and Sons.

Bexco, 2018. http://www.bexco.be/data/RGS%20U12.022.003.03%20Spm%20DB%2012.pdf (accessed 8.1.2018).

Boehm, C. F. 1986. Severe Environment 18¾-in., 15,000-psi Wellhead. Presented at the Offshore Technology Conference, Houston, Texas, 5-8 May. OTC-5152-MS. https://dx.doi.org/10.4043/5152-MS.

Bourgoyne, A. T., Jr., Millheim, K. K., Chenevert, M. E., Young Jr., F. S. 1986. *Applied Drilling Engineering, SPE Textbook Series Vol. 2*. Society of Petroleum Engineers.

BP Incident Investigation Team. 2010. Deepwater Horizon Accident Investigation Report. [Online], http://www.bp.com/content/dam/bp/pdf/sustainability/issue-reports/Deepwater_Horizon_Accident_Investigation_Report.pdf (accessed 22 August 2017).

Britton, J. S., Henderson, G. 1988. Improving Wellhead Performance with Programmed Cement Shortfall. *SPE Drilling Engineering* **3** (4): 381-384. SPE-166117-PA. https://dx.doi.org/10.2118/16617-PA.

Buchmiller, D., Hørte, T., Grytøyr, G., Haug, L. T. 2012a. Establishing an Industry Best Practice on Subsea Wellhead Fatigue Assessment. Presented at the IADC/SPE Drilling Conference and Exhibition, San Diego, California, 6-8 March, 2012. IADC/SPE-151198-MS. https://dx.doi.org/10.2118/151198-MS.

Buchmiller, D., Rengård, O., Haug, L. T., Hørte, T. 2012b. Advancements in Structural Well Integrity Design and Operation. Presented at the Offshore Technology Conference, Houston, Texas, 30 April-3 May. OTC-23278-MS. https://dx.doi.org/10.4043/23278-MS.

Çengel, Y. A., Boles, M. A. 1989. *Thermodynamics: An engineering approach*, International Edition. New York, NY: McGraw Hill, Inc.

Chakrabarti, S. K. 2005. *Handbook of Offshore Engineering*, first edition. Amsterdam, the Netherlands: Elsevier Inc.

DNGLV-RP-C203, Fatigue Design of Offshore Steel Structures. 2016. Høvik, Norway: Det Norske Veritas GL AS.

DNVGL-RP-0142, Wellhead Fatigue Analysis, first edition. 2015. Høvik, Norway: Det Norske

Veritas GL AS.

Dykes, C. E. Hopper, H. P., Jones, R. G. 1989. Development and Implementation of a Universal Subsea Wellhead System. Presented at the SPE/IADC Drilling Conference, 28 February-3 March, New Orleans, Louisiana. SPE-18699-MS. https://dx.doi.org/10.2118/18699-MS.

Edwardson, M. J., Girner, H. M., Parkison, H. R., Williams, C. D., Matthews, C. S. 1962. Calculation of Formation Temperature Disturbances Caused by Mud Circulation. *Journal of Petroleum Technology* **14** (04):416-426. SPE-124-PA. https://dx.doi.org/10.2118/124-PA.

Evans, J. T., MacGrail, J. 2011. An Evaluation of the Fatigue Performance of Subsea Wellhead Systems and Recommendations for Fatigue Enhancements. Presented at the Offshore Technology Conference, Houston, Texas, 2-5 May. OTC-21400-MS. https://dx.doi.org/10.4043/21400-MS.

Farris, R. F. 1941. A Practical Evaluation of Cements for Oil Wells. Presented at the Drilling and Production Practice, 1 January, New York, NY. API-41-283.

Forrest, P. G. 1962. *Fatigue of Metals*. London, UK: Pergamon Press.

Fricke, W. 2005. Effects of Residual Stresses on the Fatigue Behavior of Welded Steel Structures. *Materialwissenschaft und Werkstofftechnik* **36** (11): 642-649. https://dx.doi.10.1002/mawe.200500933.

Gale, W. F., Totemeier, T. C. 2004. *Smithells Metal Reference Book*, eighth edition. Amsterdam, the Netherlands: Elsevier Inc.

Grytøyr, G., Steinkjer, O. 2012. Uncertainty of Long Term Fatigue Load of Subsea Well Heads. Proc., ASME 31st International Conference on Ocean, Offshore and Artic Engineering, Rio de Janeiro, Brazil, 1-6 July. OMAE2012-83686. https://dx.doi.org/10.1115/OMAE2012-83686.

Grytøyr, G., Reinås, L., Eilertsen, L. E., Russo, M. 2016. Full Scale Measurements of Cyclic Bending Moments on Subsea Wellheads on the Norwegian Continental Shelf. Presented at the SPE International Conference and Exhibition on Health, Safety, Security, Environment, and Social Responsibility, Stavanger, Norway, 11-13 April. SPE-179444-MS. https://dx.doi.org/10.2118/179444-MS.

Halliburton. 2018. WELLCAT ™ Casing Design, https://www.landmark.solutions/WELLCAT (accessed 12.02.2018).

Healy, B., Feng, L., Jaiswal, V., Sharma, P. 2017. Fatigue Analysis of a Rigid Locked Wellhead. Proc., ISOPE 27th International Ocean and Polar Engineering Conference, San Francisco, California, 25-30 June. ISOPE-I-17-557.

Hearn, E. J. 1997. *Mechanics of materials 1: An Introduction to the Mechanics of Elastic and Plastic Deformation of Solids and Structural Materials*, third edition. Oxford, United Kingdom: Butterworh-Heinemann.

Hokstad, P., Håbrekke, S., Johnsen, R., Sangesland, S. 2010. Ageing and Life Extension for Offshore Facilities in General and for Specific Systems. [Online], http://www.ptil.no/getfile.php/1311458/PDF/Ageing%20and%20Life%20Extension%20Report%202%20final%20%28Sintef%202010%29.pdf (accessed 23 August 2017).

Holmes, C. S., Swift, S. C. 1970. Calculation of Circulating Mud Temperatures. *Journal of Petroleum Technology* **22** (6):670-674. SPE-2318-PA. https://dx.doi.org/10.2118/2318-PA.

Hopper, C. T. 1983. Vortex Induced Oscillations of Long Marine Drilling Risers. Proc., 2nd Deep Offshore Technology Conference, Valletta, Malta, 17-19 October.

Howell, H, Rimmer, A., Ward, P. 2015. Subsea Well Life Extension Fatigue Challenges. Presented at the SPE Bergen One Day Seminar, Bergen, Norway, 22 April. SPE-173848-MS. https://dx.doi.org/10.2118/173848-MS.

Hørte, T., Reinås, L., Mathisen, J. 2012. Wellhead Fatigue Analysis Method: Benefits of a Structural Reliability Analysis Approach. Proc., ASME 31st International Conference on Ocean, Offshore and Artic Engineering, Rio de Janeiro, Brazil, 1-6 July. OMAE2012-83141. https://dx.doi.org.10.1115/OMAE2012-83141.

Hørte, T., Russo, M., Macke, M., Reinås, L. 2013. Benefit of Measurements and Structural Reliability Analysis for Wellhead Fatigue. Proc. ASME 32nd Conference on Ocean, Offshore and Artic Engineering, Nantes, France, 9-14 July. OMAE2013-10932. https://dx.doi:10.1115/OMAE2013-10932.

ISO 13624, Petroleum and natural gas industries – Drilling and production equipment – Part 2: Deepwater drilling riser methodologies, operations, and integrity technical report. 2009. Geneva, Switzerland: ISO.

Jaiswal, V., Feng, L., Saraswat, R., Healy, B., Hørte, T. 2016. Fatigue Analysis of Non-rigid Locked Wellhead. Proc., ISOPE 26th International Ocean and Polar Engineering Conference, Rhodes, Greece, 26 Jule-1 July. ISOPE-I-16-524.

Jaiswal, V. Healy, B. Latest Developments in Fatigue Analysis of Wellhead Systems. *Dnvgl.us*, October 2016, https://www.dnvgl.us/Downloads/TW16-Latest-Developments_tcm14-80212.pdf (accessed 9 September 2017).

Journée, J. M. J., Massie, W. W. 2001. *Offshore Hydrodynamics*, first edition. [Online], http://www.shipmotions.nl/DUT/LectureNotes/index.html (accessed 22 August 2017).

Kebadze, E. B., Henderson, J. D., Maher, J. V., Lugo, M., Cox, B. 2014. Systems and Methods for Tethering Subsea Blowout Preventers to Enhance the Strength and Fatigue Resistance of Subsea Wellheads and Primary Conductors. US Patent No. 2014/0374115 A1.

Kebadze, E. B., Killbourn, S., Henderson, J., Chomczuk, G. et al. 2017. Wellhead Monitoring – Measured Fatigue Damage Validation. Proc., ASME 36th International Conference on Ocean, Offshore and Artic Engineering, Trondheim, Norway, 25-30 June. OMAE2017-61081. https://dx.10.1115/OMAE2017-61081.

Keller, H. H., Couch, E. J. 1968. Well Cooling by Down-Hole Circulation of Water. *Society of Petroleum Engineers Journal* **8** (4):405-412. SPE-2134-PA. https://dx.doi.org/10.2118/2134-PA.

Keller, H. H., Couch, E. J., Berry, P. M. 1973. Temperature Distribution in Circulating Mud Columns. *SPE Journal* **13** (1): 23-30. SPE-3605-PA. https://dx.doi.org/10.2118/3605-PA.

King, G. W. 1990. Drilling Engineering for Subsea Development Wells. *Journal of Petroleum Technology* **42** (9): 1176-1183. SPE-18687-PA. https://dx.doi.org/10.2118/18687-PA.

King, G. W., Burton, K., Hodgson, T. A Coupled Analysis Approach to the Assessment of Marine Drilling Systems. SPE Drilling & Completion Journal 8 (2):131-137. SPE-20932-PA. https://dx.doi.org/10.2118/20932-PA.

Kuzmichev, S., Garcia, J. R., Aronsen, K. H., Grytøyr, G. et al. 2017. Fatigue Capacity of Wellhead Housings. Proc., ASME 36th International Conference on Ocean, Offshore and Artic Engineering, Trondheim, Norway, 25-30 June. OMAE2017-61421. https://dx.doi.org/10.1115/OMAE2017-61421.

Kårstad, E., Aadnøy, B. S. 1999. Optimization of mud temperature and fluid models in offshore applications. Presented at the SPE Offshore Europe Oil and Gas Exhibition and Conference, Aberdeen, United Kingdom, 7-10 September. SPE-56939-MS. https://dx.doi.org/10.2118/56939-MS.

Lake, W. L. 2006. *Petroleum Engineering Handbook*. Society of Petroleum Engineers.

Leggatt, R. H. 2007. Residual Stresses in Welded Structures. *International Journal of Pressure Vessels and Piping* **85** (3): 144-151. https://doi.org/10.1016/j.ijpvp.2007.10.004.

Liang, Q. J. 2012. Casing Thermal Stress and Wellhead Growth Behavior Analysis. Presented at the SPE Asia Pacific Oil and Gas Conference and Exhibition, Perth, Australia, 2-24 October. SP-157977-MS. https://dx.doi.org/10.2118/157977-MS.

Lien, A. K. D. 2010. *Analysis of Methods for Reducing Subsea Wellhead Fatigue*. Master Thesis. Norwegian University of Science and Technology, Trondheim, Norway.

Marshal, D. W., Bentsen, R. G. 1982. A Computer Model to Determine the Temperature Distribution in a Wellbore. *Journal of Canadian Petroleum Technology* **21** (1): 63-75. PETSOC-82-01-05. https://dx.doi.org/10.2118/82-01-05.

Milberger, L.J., Yu, A., Hosie, S., Hines, F. 1991, Structural Requirements for the Effective Transfer of Environmental Loadings in a Subsea Wellhead System. Presented at the Offshore Technology Conference, Houston, Texas, 6-9 May. OTC-6706-MS. https://dx.doi.org/10.4043/6706-MS.

Ministry of Petroleum and Energy. 2010. *Økt utvinning på norsk kontinentalsokkel*. [Online], https://www.regjeringen.no/globalassets/upload/oed/pdf_filer/oktutvinning.pdf (accessed 22 August 2017).

Nelson, E. B., Guillot, D. 2006. *Well Cementing*, second edition. Amsterdam, the Netherlands: Elsevier Inc.

Mittendorf, K. 2016. Mitigation and Control of Wellhead Fatigue, https://www.ngi.no/eng/News/NGI-News/Workshop-Geotechnical-aid-to-Well-Integrity (accessed 2 January 2018).

Nilsen, S. H., Russo, M., Grytøyr, G. 2017. Comprehensive Instrumentation of Two Offshore Rigs for Wellhead Fatigue Monitoring. Proc., ASME 36th International Conference on Ocean, Offshore and Artic Engineering, Trondheim, Norway, 25-30 June. OMAE2017-61291. https://dx.doi.org/10.1115/OMAE2017-61291.

NORSOK D-010, Well integrity in drilling and well operations, fourth edition. 2013. Stavanger, Norway: Norwegian Oil Industry Association (OLF)/ Federation of Norwegian Manufacturing Industries (TBL).

NORSOK N-004, Design of steel structures, second edition, 2004. Stavanger, Norway: Norwegian Oil Industry Association (OLF)/ Federation of Norwegian Manufacturing Industries (TBL).

Oster, C. A., Scheffler, W. A. 1982. Temperature Profiles and Aquifer Mass Transfer in a Circulating Well. *ASME Journal of Heat Transfer* **104** (1):173-179. https://dx.doi:10.1115/1.3245046.

Petrolwiki. 2015. Subsea wellhead systems (26 June 2015 revision), http://petrowiki.org/Subsea_wellhead_systems (accessed 22 August 2017).

Poletto, F., Miranda, F. 2004. *Seismic While Drilling - Fundamentals of Drill-Bit Seismic for Exploration*, first edition. Amsterdam, the Netherlands: Elsevier Inc.

Ramey Jr., H. J. Wellbore Heat Transmission. *Journal of Petroleum Technology* **14** (04):427-435. SPE-96-PA. https://dx.doi.org/10.2118/96-PA.

Read, J., Shilling, R. 2016. Legacy BOP technology could be approaching design limitations. *Offshore-mag*, 2 May 2016, http://www.offshore-mag.com/articles/print/volume-76/issue-2/drilling-and-completion/legacy-bop-technology-could-be-approaching-design-limitations.html (accessed 9 September 2017).

Reinås, L. 2012. *Wellhead Fatigue Analysis Surface casing cement boundary conditions for subsea wellhead fatigue analytical models*. PhD Thesis, University of Stavanger, Stavanger, Norway.

Reinås, L., Hørte, T., Sæther, M., Grytoyr, G. 2011. Wellhead Fatigue Analysis Method. Proc., ASME 30th International Conference on Ocean, Offshore and Arctic Engineering, Rotterdam, the

Netherlands, 19-24 June. OMAE2011-50026. https://dx.doi.org/doi:10.1115/OMAE2011-50026.

Reinås, L., Russo, M., Grytøyr, G. 2012a. Wellhead Fatigue Analysis Method: The Effect of Variation of Lower Boundary Conditions in Global Riser Load Analysis. Proc., ASME 31st International Conference on Ocean, Offshore and Arctic Engineering, Rio de Janeiro, Brazil, 1-6 July. OMAE2012-83314. http://dx.doi.org/10.1115/OMAE2012-83314.

Reinås, L., Sæther, M., Svensson, J. 2012b. Wellhead Fatigue Analysis Method: A New Boundary Condition Modelling of Lateral Cement Support in Local Wellhead Models. Proc., ASME 31st International Conference on Ocean, Offshore and Arctic Engineering, Rio de Janeiro, Brazil, 1-6 July. OMAE2012-83049. http://dx.doi.org/10.1115/OMAE2012-83049.

Russo, M., Zakeri, A., Kuzmichev, S., Grytøyr, G. et al. 2016. Integrity Assessment of Offshore Subsea Wells: Evaluation of Wellhead Finite Element Model Against Monitoring Data Using Different Soil Models. *ASME Journal of Offshore Mechanics and Arctic Engineering* **138** (6): 061301-061301-11. OMAE-15-1115. http://dx.doi.org/10.1115/1.4034099.

Rørgård, O., Sønåsen, K. O., Ellefsen, Ø. 2017. Introducing Reactive Flex-Joint: 10-15 Times Prolonged Wellhead Life. Presented at the Offshore Technology Conference, Houston, Texas, 1-4 May. OTC-27584-MS. http://dx.doi.org/10.4043/27584-MS.

Sangesland, S. 2009. *Possible methods for reducing loads on subsea wellheads*. Internal document. Norwegian University of Science and Technology, Trondheim, Norway.

Schlumberger. 2018. Drillbench Dynamic Drilling Simulation Software, https://www.software.slb.com/products/drillbench (accessed 12.02.2018).

Sevillano, L. C., De Andrade, J., Stanko, M., Sangesland, S. 2016a. Thermal Effects on Subsea Wellhead Fatigue during Workover Operations. Presented at the International SPE Bergen One Day Seminar, Bergen, Norway, 20 April. SPE-180065-MS. https://dx.doi.org/10.2118/180065-MS.

Sevillano, L. C., De Andrade, J., Stanko, M., Sangesland, S. 2016b. Subsea Wellhead Fatigue Analysis with Focus on Thermal Conditions. Proc. ASME 35th International Conference on Ocean Offshore and Arctic Engineering, Busan, South Korea, 19-24 June. OMAE2016-54088. https://dx.doi.org/doi:10.1115/OMAE2016-54088.

Sevillano, L. C., De Andrade, J., Sangesland, S. 2017. Estimation of Undisturbed Geothermal Gradient in Wells from Measured Drilling Data – A Numerical Approach. Proc., ASME 36th International Conference on Ocean, Offshore and Artic Engineering, Trondheim, Norway, 25-30 June. OMAE2017-62205. https://dx.doi.org/10.1115/OMAE2017-62205.

Shigley, J. E. and Mischke, C. R. 1989. *Mechanical Engineering Design*, fifth edition. New York, NY: McGraw Hill, Inc.

Sines, G. 1955. *Failure of Materials Under Combined Repeated Stresses with Superimposed Static Stresses*. Technical Note, NACA-TN-3495.

Singeetham, S. P. 1989. An Optimized Design of a Typical Subsea Drilling System for Fatigue Applications. Proc. ASME 8th International Conference on Offshore Mechanics and Arctic Engineering, The Hague, the Netherlands, March 19-23.

SINTEF. 2016. Riflex Riser System Analysis Program, https://www.sintef.no/globalassets/upload/marintek/pdf-filer/factsheets/riflex.pdf (accessed 29.12.2016).

Sparks, C. P. 2007. *Fundamentals of Marine Riser Mechanics: Basic Principles and Simplified Analyses*, first edition. Tulsa, Oklahoma: PennWell Corporation.

Stephens, R. I., Fatemi, A., Stephens, R. R., Fuchs H. O. 2001. *Metal Fatigue in Engineering*, second edition. New York, NY: John Wiley and Sons.

Steinkjer, O., Sødahl, N., Grytøyr, G. 2010. Methodology for Time Domain Fatigue Life Assessment of Risers and Umbilicals, Proc. ASME 29th International Conference on Ocean Offshore and Arctic Engineering, Shanghai, China, 6-11 June. OMAE2010-20119. https://dx.doi.org/10.1115/OMAE2010-20119.

Thorogood, J. L., Train, A. S., Adams, A. J. 1998. Deep Water Riser System Design and Management. Presented at the IADC/SPE Drilling Conference, Dallas, Texas, 3-6 March. SPE-39295-MS. https://dx.doi.org/10.2118/39295-MS.

Valka, W. A., Fowler, J. R. 1985. The Design and Analysis of a TLP Subsea Wellhead. Presented at the Offshore Technology Conference, Houston, Texas, 6-9 May. OTC-4983-MS. https://dx.doi.org/10.4043/4983-MS.

Vignes, B., Aadnøy, B. 2010. Well Integrity Issues Offshore Norway. *SPE Production & Operations Journal* **25** (2) 145-150. SPE-112535-PA. https://dx.doi.org/10.2118/112535-PA.

Vignes, B., Andreassen, J., and Tonning, S.A. 2006. Well Integrity Challenges on the Norwegian Shelf. Presented at the PSA's Well Safety Seminar, 4 May. Petroleum Safety Authority Norway (PSA).

Walker, K. M., Agarwal, P., McNeill, S., Bhalla, K. et al. 2017. Comparison of Riser and Well System Response Predictions to Full-Scale Measurements in Shallow Water Harsh Environment Karen. Proc., ASME 36th International Conference on Ocean, Offshore and Artic Engineering, Trondheim, Norway, 25-30 June, OMAE2017-61300. https://dx.doi.org/10.1115/OMAE2017-61300.

Wooley, G. R. 1980. Computing Downhole Temperatures in Circulation, Injection, and Production Wells. Journal of Petroleum Technology 32 (9): 1509-1522. SPE-8441-PA. https://dx.doi.org/10.2118/8441-PA.

Annex A – Wellhead Beam-Proxy Model

A.1 Summary

The Wellhead Fatigue Analysis Technical Report based on the finding of the JIP on structural well integrity presented the method using for deriving a stiffness model representative of the global dynamic behavior of the wellhead from the local response analysis. This beam and non-linear spring wellhead proxy model is used as the lower boundary of the riser system in the global dynamic analyses. Because the technical report is no longer available to the general public, said method is outlined here.

A.2 Method Outline

Figure 3.7 is reproduced here as Figure A.1 to illustrate the method. The beam is partially buried into the soil. The lower extremity is fixed, while at the ML level it is connected to a non-linear spring. The properties and interactions of the components of the wellhead are converted into a simplified beam system, the properties of which must be determined. To accomplish that two local response analyses are run:

- Analysis A: Pure shear force loading applied at the top of the BOP.
- Analysis B: Pure bending moment loading applied at the top of the BOP.

The beam properties are obtained based on the displacement, *d*, and rotation, *α*, calculated at the wellhead datum. Following that the non-linear stiffness of the spring is calculated.

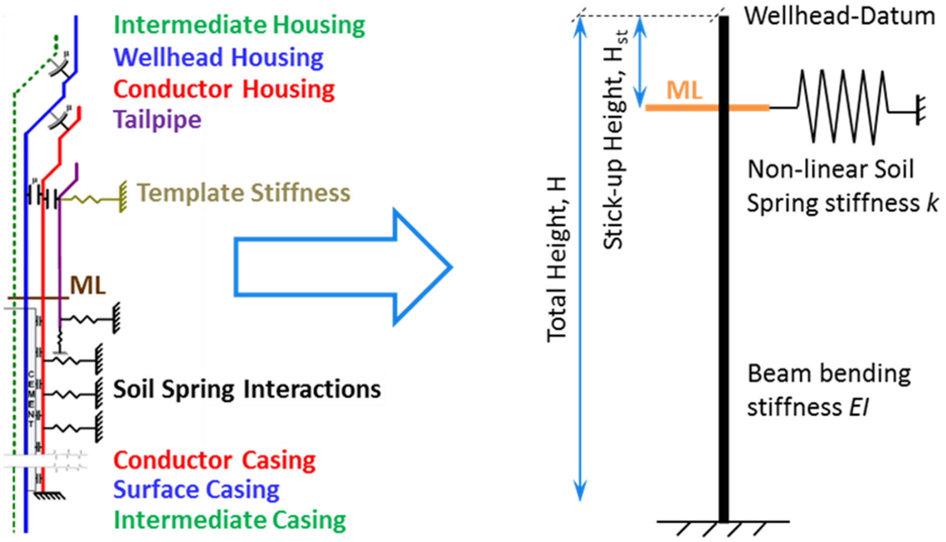

a) Wellhead system modelled in the structural local analysis

b) Wellhead beam proxy model used in the riser global analysis

Figure A.1 – Wellhead beam-proxy model created from local analysis (Reinås et al. 2011). ©American Society of Mechanical Engineers.

A.3 Determining Beam Properties

The beam system properties are determined combining the deflections and rotations of two simpler cases, presented by Figure A.1. From Analysis A for a value of shear force, F_a, applied at the top of the BOP the resulting bending moment at the wellhead datum, M_a, d_a and α_a are extracted. The sum of the displacements d_1 and d_2 must equal the displacement d_a, while the angles α_1 and α_2 add up to α_a.

$$d_a = d_1 + d_2 \qquad \textbf{Equation A.1}$$

$$\alpha_a = \alpha_1 + \alpha_2 \qquad \textbf{Equation A.2}$$

Assuming small angles:

$$\alpha_2 = {}^{d_2}/_{H} \qquad \textbf{Equation A.3}$$

This enables obtaining two equations for d_2:

$$d_2 = d_\alpha - d_1(H, H_{st}, EI, F_a, M_a) \qquad \textbf{Equation A.4}$$

$$d_2 = \alpha_\alpha - \alpha_1(H, H_{st}, EI, F_a, M_a) \qquad \textbf{Equation A.5}$$

where d_1 and d_2 are determined analytically, based on the system's properties and applied loading. It is possible then to isolate EI as it is shown in Equation A.6.

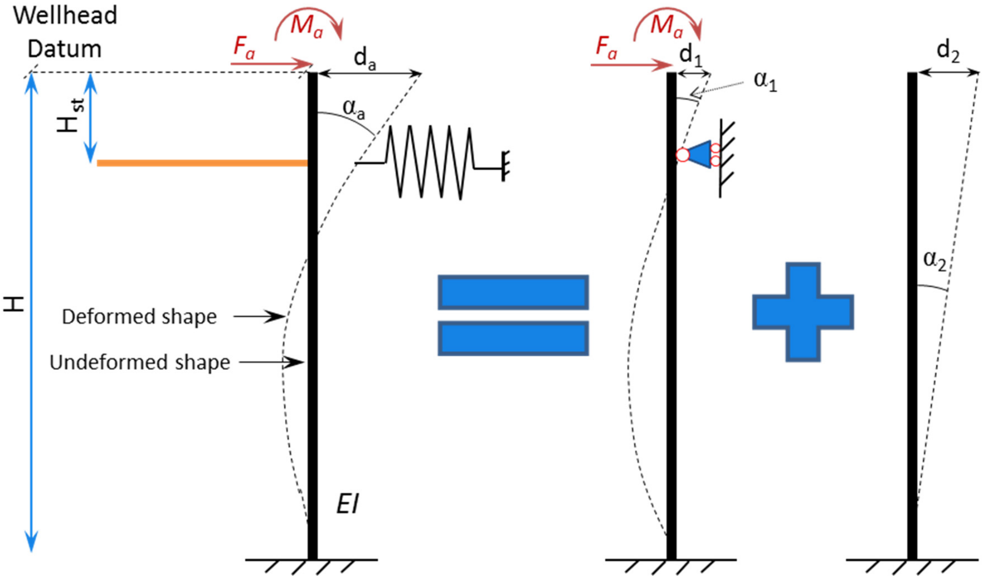

Figure A.2 – Deformation of wellhead model as a sum of simpler cases.

In analysis B, the bending moment M_b is applied at the top of the BOP, and the resulting bending moment at the wellhead datum, M_b, d_b and α_b are extracted. Those values are employed in Equation A.7, where the total height H variable has been isolated.

$$\mathrm{EI} = -\frac{2 \cdot \mathrm{F}_a \cdot H^2 \cdot H_{st} + 2 \cdot M_a \cdot H^2 - F_a \cdot H \cdot H_{st}^2 + 2 \cdot M_a \cdot H_{st}^2}{6 \cdot d_a - 6 \cdot H \cdot \alpha_a} \qquad \textbf{Equation A.6}$$

$$\mathrm{H} = -\frac{3}{M_b} \cdot \left[\frac{H \cdot M_b - 3 \cdot EI \cdot \alpha_b}{6} \pm \frac{\sqrt{(EI)^2 \cdot \alpha_b^2 - \frac{2 \cdot EI \cdot H_{st} \cdot M_b \cdot \alpha_b}{3} - \frac{4 \cdot d_b \cdot EI \cdot M_b}{3} + \frac{H_{st}^2 \cdot M_b^2}{3}}}{2} \right] \qquad \textbf{Equation A.7}$$

Because there are three unknowns variables (H, H_{st} and EI) for the two equations above it is recommended to assume a value of H_{st}, as well as using a numerical solving method. In the case that two values of H satisfy the system of equations the most realistic value should be selected.

A.4 Determining Spring Properties

Because the beam is free to rotate at its bottom the characteristics of the horizontal spring are independent of the bending stiffness, *EI*. The reaction forces, *R*, on the spring end are calculated as a function of the shear forces applied in Analysis A according to the Equation A.8 below:

$$\mathrm{R}(F) = \frac{\mathrm{F} \cdot H + M(F)}{H - H_{st}} \qquad \textbf{Equation A.8}$$

where *M(F)* is the resulting bending moment at the wellhead datum because of the applied shear force *F*.

The displacements, d_s, on the spring end are given by:

$$\mathrm{d}_s(F) = \alpha_{2a}(\mathrm{F}) \cdot (H - H_{st}) \qquad \textbf{Equation A.9}$$

where $\alpha_{2a}(F)$ is given by:

$$\alpha_{2a}(F) = \alpha_a - \frac{\mathrm{F} \cdot H_{st} \cdot [2 \cdot (H - H_{st}) + H_{st}]}{6 \cdot EI} - \frac{M(F) \cdot (H - H_{st})}{3 \cdot EI} - \frac{M(F) \cdot H_{st}}{EI} \qquad \textbf{Equation A.10}$$

The spring stiffness, *K*, is given by:

$$\mathrm{K}(F) = \frac{\mathrm{R}(F)}{\mathrm{d}_s(F)} \qquad \textbf{Equation A.11}$$

Annex B – Well Thermal Model

B.1 Summary

The doctoral work investigated the effects on wellhead fatigue that might arise from the temperature variations that occur during the different operations that can be carried out on a well when there is connection to a floating rig through a riser (*e.g.* circulation, tripping, drilling, cementing, etc.).

To investigate these thermal effects, a computer code was developed in *Matlab* that calculates the transient temperature distribution of the different components that are part of the well, subsea stack, and riser system. This annex will present the methodology on which the computer code is based and the results that can be obtained from it.

B.2 Methodology

The methodology is based on the works dealing on wellbore temperature distribution published by Keller and Couch (1968), Keller et al. (1973), and Marshall and Bentsen (1982). It assumes the following:

- Heat transfer within the drilling fluid is by axial convection, conduction may be neglected except when the fluid is immobile;
- The radial temperature gradient within the drilling fluid may be neglected;
- Heat generation by viscous dissipation within the fluid may be neglected.

Take the drilling well schematic shown in Figure B.1, and consider the region emphasized by the dashed rectangle. Moving radially outwards from the center there can be seen:

1. Drillstring drilling fluid.
2. Drillstring wall.
3. Annulus drilling fluid.
4. 13-⅜-in. casing wall.
5. 13-⅜-in. casing annulus.
6. Surface casing wall.
7. Surface casing annulus.
8. Conductor wall.
9. Conductor cement.
10. Rock formation.

Figure B.1 also presents the well's components cross-sections and the notation used to differentiate the temperature and radii of the various components.

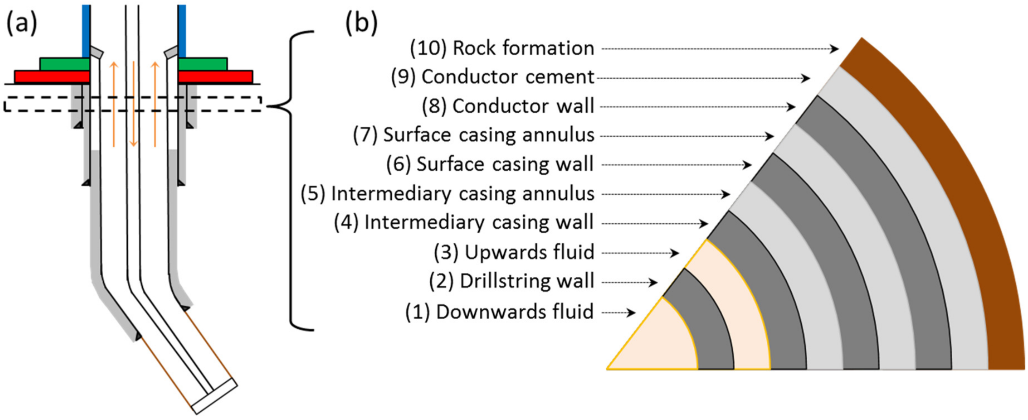

Figure B.1 – A: Well schematics. B: Components of the well system at a given depth.

B.2.1 Energy Balance in the Flowing Fluid Inside the Drillstring

The energy balance for the downwards flowing fluid is shown in Figure B.2 and Equation B.1. The orange arrows represent the fluid entering/leaving the control volume, while the red arrow represents the heat that leaves/enters the control volume.

In Figure B.2 the parameter *w* is the mass flow rate, *H* is the enthalpy, *V* is the flow speed, *z* is the measured depth, *g* is the acceleration of gravity, *α* is the angle with the horizontal, $Q_{1\text{-}2}$ is the heat flux exchanged radially between the fluid and the drillstring, Q_{pl_ds} is the heat gained per unit of length generated mostly by the flow's pressure losses inside the drillstring, *m* is the mass of the control volume and *E* is the energy within the control volume.

$$w\left(H+\frac{1}{2}V^2+zgsin\alpha\right)_z - w\left(H+\frac{1}{2}V^2+zgsin\alpha\right)_{z+\Delta z} - Q + Q_{pl\_ds}\Delta z = \frac{\Delta(mE)_{CV}}{\Delta t}$$ **Equation B.1**

The energy of the fluid entering the control volume must equal the summation of the energy of the fluid leaving the control volume, the energy being exchanged radially, and the energy accumulated within the control volume.

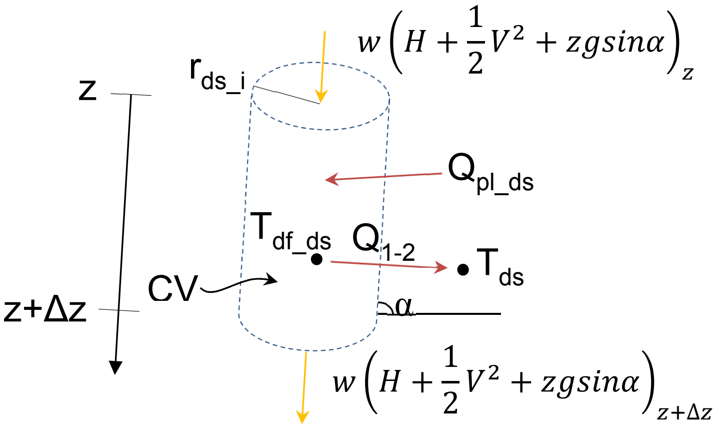

Figure B.2 – Control volume of the flowing fluid inside the drillstring used for energy balance.

The radially exchanged heat, *Q*, can be written as shown in Figure B.2, where h_{ds_i} is the coefficient for forced convection in the drillstring's inner surface, A_{ds_i} is control volume lateral area, T_{df_ds} is the temperature of the drilling fluid inside the drillstring, and T_{ds} is the temperature of the drillstring along the cross-section.

$$Q = h_{ds\_i}A_{ds\_i}\left(T_{df} - T_{ds}\right) = h_{ds\_i}2\pi r_{ds\_i}\Delta z\left(T_{df\_ds} - T_{ds}\right)$$ **Equation B.2**

The mass, *m*, of the control volume is constant and can be expressed by its volume and the drilling fluid's specific mass, ρ_{df}. Also, the variation of energy inside the control volume can be expressed by its temperature variation and the drilling fluid's heat capacity, C_{p_df}.

$$\frac{\Delta(mE)_{CV}}{\Delta t} = \frac{mC_{p\_df}\Delta(T)_{CV}}{\Delta t} = \rho_{df}\pi r_{ds\_i}^2\Delta z C_{p\_df}\frac{\Delta T}{\Delta t}$$ **Equation B.3**

Substituting Equation B.2 and Equation B.3 into Equation B.1, rearranging the equation's terms, neglecting the change in flow speed, and writing mass flow, *w*, as the product of the fluids specific mass and its flow rate, *q*, yields:

$$\rho_{df}q\Delta H + \Delta z w g sin\alpha + h_{ds\_i}2\pi r_{ds\_i}\Delta z\left(T_{df\_ds} - T_{ds}\right) = Q_{pl\_ds}\Delta z - \rho_{df}\pi r_{ds\_i}^2\Delta z C_{p\_df}\frac{\Delta T}{\Delta t}$$ **Equation B.4**

The enthalpy change of the drilling fluid can be expressed by its temperature variation and heat capacity. Dividing by Δz and taking the limits $\Delta z \rightarrow 0$, and $\Delta t \rightarrow 0$ yields:

$$\rho_{df}qC_{p\_df}\frac{\partial T}{\partial z} + w g sin\alpha + h_{ds\_i}2\pi r_{ds\_i}\left(T_{df\_ds} - T_{ds}\right) = Q_{pl\_ds} - \rho_{df}\pi r_{ds\_i}^2 C_{p\_df}\frac{\partial T}{\partial t}$$ **Equation B.5**

B.2.2 Energy Balance in the Drillstring Wall

Figure B.3 shows the energy balance for the drillstring wall. Here the orange arrows represent the fluid flows that are in contact with the control volume, while the red arrows represent the heat that crosses the boundaries of the control volume.

The axial heat exchange by conduction between two points immediately above and below the control volume is given by Equation B.6.

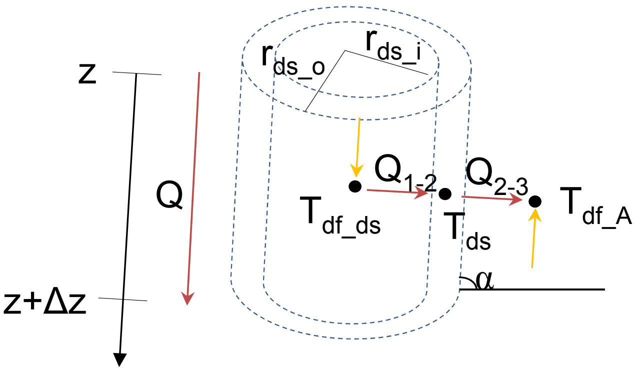

Figure B.3 – Control volume of the drillstring wall used for energy balance.

$$Q = k_{ds}A_{ds}\frac{\left(T_{ds\_z} - T_{ds\_z+\Delta z}\right)}{\Delta z} = k_{ds}\pi\left(r_{ds\_o}^2 - r_{ds\_i}^2\right)\frac{\left(T_{ds\_z} - T_{ds\_z+\Delta z}\right)}{\Delta z}$$

Equation B.6

Where k is the thermal conductivity of the drillstring material and A_{ds} is the cross-sectional area of the drillstring. The inner area of the drillstring, as well as its outer area will exchange heat with the flowing fluids in similar fashion as previously presented by Equation B2. Combining all effects in Equation B7 yields:

$$k_{ds}\pi\left(r_{ds\_o}^2 - r_{ds\_i}^2\right)\frac{\left(T_{ds\_z} - T_{ds\_(z+\Delta z)}\right)}{\Delta z} + h_{ds\_i}2r_{ds\_i}\Delta z\left(T_{df\_ds} - T_{ds}\right)$$
$$+h_{ds\_o}2\pi r_{ds\_o}\Delta z\left(T_{ds} - T_{df\_A}\right) = \rho_{ds}\Delta z\pi\left(r_{ds\_o}^2 - r_{ds\_i}^2\right)C_{p\_ds}\frac{\Delta T}{\Delta t}$$

Equation B.7

Rearranging the terms in the equation and taking the limits Δz and Δt to zero yields:

$$k_{ds}\frac{\partial^2 T}{\partial z^2} + \frac{h_{ds\_i}2r_{ds\_i}}{\left(r_{ds\_o}^2 - r_{ds\_i}^2\right)}\left(T_{df\_ds} - T_{ds}\right) + \frac{h_{ds\_o}2r_{ds\_o}}{\left(r_{ds\_o}^2 - r_{ds\_i}^2\right)}\left(T_{ds} - T_{df\_A}\right) = \rho_{ds}C_{p\_ds}\frac{\partial T}{\partial t}$$

Equation B.8

B.2.3 Energy Balance in the Flowing Annulus

The energy balance in the flowing annulus is shown by Figure B.4 and Equation B.9. It is similar to the energy balance of the fluid in the drillstring, except that the fluid flows in the opposite direction, and there are two wall interfaces through which heat is exchanged radially.

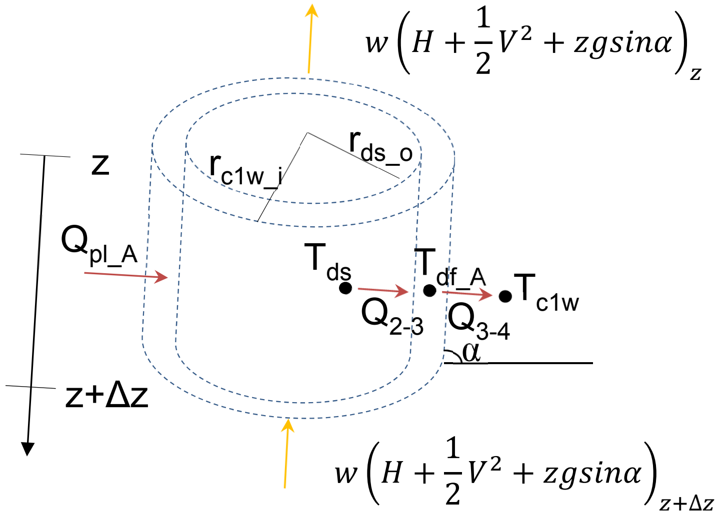

Figure B.4 – Control volume of the flowing fluid in the annulus used for energy balance.

$$\rho_{df}qC_{p\_df}\frac{\partial T}{\partial z} + wgsin\alpha + h_{ds\_o}2\pi r_{ds\_o}\left(T_{ds} - T_{df\_A}\right) + h_{c1w\_i}2\pi r_{c1w\_i}\left(T_{df\_A} - T_{c1w}\right)$$
$$= \rho_{df}\pi\left(r_{c1w\_i}^2 - r_{ds\_o}^2\right)C_{p\_df}\frac{\partial T}{\partial t} - Q_{pl\_A}$$

Equation B.9

B.2.4 Energy Balance in the Casing Wall

Heat transfer at the lateral external surface of the casing wall happens by conduction. Figure B.5 shows the notation used. The heat, *Q*, transferred between casing wall and casing annulus is formulated in the set of Equations B.10. The subscript *m* denotes the mean of inner and outer radii.

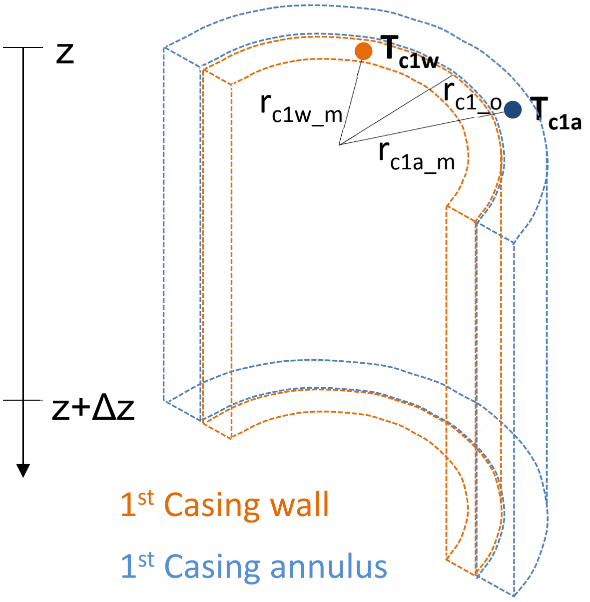

Figure B.5 – Control volume of casing wall and annulus used to model conduction heat transfer.

$$Q = \frac{T_{c1w} - T_{c1a}}{R_{c1w} - R_{c1a}}$$ **Equation B.10-a**

$$R_{c1w} = \frac{r_{c1w\_o} - r_{c1w\_m}}{k_{c1w} A_{lm\_c1w}}$$ **Equation B.10-b**

$$r_{c1w\_m} = \frac{r_{c1w\_o} + r_{c1w\_i}}{2}$$ **Equation B.10-c**

$$A_{lm\_c1w} = \frac{\left(r_{c1w\_o} - r_{c1w\_m}\right)2\pi\Delta z}{ln\left(r_{c1w\_o}/r_{c1w\_m}\right)}$$ **Equation B.10-d**

$$R_{c1a} = \frac{r_{c1a\_m} - r_{c1w\_o}}{k_{c1a} A_{lm\_c1a}}$$ **Equation B.10-e**

$$r_{ca1\_m} = \frac{r_{c1a\_o} + r_{c1a\_i}}{2}$$ **Equation B.10-f**

$$A_{lm\_c1a} = \frac{\left(r_{c1a\_m} - r_{c1w\_o}\right)2\pi\Delta z}{ln\left(r_{c1a\_m}/r_{c1w\_o}\right)}$$ **Equation B.10-g**

$$Q = \frac{(T_{c1w} - T_{c1a})2\pi\Delta z}{1}\frac{k_{c1w}k_{c1a}}{k_{c1a} ln\left(r_{c1w\_o}/r_{c1w\_m}\right) + k_{c1w} ln\left(r_{c1a\_m}/r_{c1w\_o}\right)}$$ **Equation B.10-h**

Equation B.11 shows all the heat transfer mechanisms acting on the casing string wall.

$$k_{c1w}\frac{\partial^2 T}{\partial z^2}+\frac{h_{c1i}2r_{c1i}}{\left(r_{c1i}^2-r_{ds_o}^2\right)}\left(T_{df_A}-T_{c1w}\right)+\frac{2\left(T_{c1w}-T_{c1a}\right)}{\left(r_{c1i}^2-r_{ds_o}^2\right)}\times \frac{k_{c1w}k_{c1a}}{k_{c1a}ln\left(\frac{r_{c1w\_o}}{r_{c1w\_m}}\right)+k_{c1w}ln\left(\frac{r_{c1a\_m}}{r_{c1w\_o}}\right)}=\rho_{c1w}C_{p\_c1w}\frac{\partial T}{\partial t} \qquad \textbf{Equation B.11}$$

B.2.5 Energy Balance in the Casing Annulus and Subsequent Layers

For the casing annulus and the subsequent layers heat transfer on the control volume occurs by conduction and assumes the general form shown in Equation B.12, which uses the notation from Keller et al. (1973), and where the subscript *j,* identifies the current component (strings, annuli, rock formation) in the well system according to the notation previously presented in the text and in Figure B.2, *(i+1)* identifies the following component in the well system, and (*i-1)* identifies the previous component in the well system.

$$k_j\frac{\partial^2 T}{\partial z^2}+\frac{\left(T_j-T_{j+1}\right)}{r_{j\_o}\Delta r_j}\frac{k_jk_{j+1}}{k_{j+1}ln\left(\frac{r_{j\_o}}{r_{j\_m}}\right)+k_jln\left(\frac{r_{(j+1)\_m}}{r_{j\_o}}\right)}+\frac{\left(T_{j-1}-T_j\right)}{r_{j\_o}\Delta r_j}\frac{k_{j-1}k_j}{k_jln\left(\frac{r_{(j-1)\_o}}{r_{(j-1)\_m}}\right)+k_{j-1}ln\left(\frac{r_{j\_m}}{r_{(j-1)\_o}}\right)}=\rho_jC_{p\_j}\frac{\partial T}{\partial t} \qquad \textbf{Equation B.12}$$

B.2.6 Energy Balance in the Riser

Heat exchange on the riser joints covered by buoyancy modules will be analogous as the case presented for the casing string wall. Bare riser joints are exposed to sea water and subjected to heat exchange by natural convection and forced convection. The respective coefficients can be summed up and calculated according to the formulations presented by Bergman et al. (2011).

$$k_{rw}\frac{\partial^2 T}{\partial z^2}+\frac{h_{rw\_i}2r_{rw\_i}}{\left(r_{rw\_i}^2-r_{ds\_o}^2\right)}\left(T_{rw}-T_{df\_A}\right)+\frac{h_{rw\_o}2r_{rw\_o}}{\left(r_{rw\_o}^2-r_{rw\_i}^2\right)}\left(T_{rw}-T_{sea}\right)=\rho_{rw}C_{p\_rw}\frac{\partial T}{\partial t} \qquad \textbf{Equation B.13}$$

B.2.7 Partial Differential Terms

According to Keller and Bentsen (1982), the terms in the previous equations which are first order partial derivatives can be represented by two-point forward and backward difference approximations, while the second order derivatives can be represented by three-point centered difference approximations.

Thus, discretization of the well system, as shown in Figure 4.3 reproduced here as Figure B.6, enables Equation B.5 to assume, for a given node, the form:

$$\rho_{df} q C_{p\_df} \frac{\left(T_{1,j-1}^{n+1} - T_{1,j}^{n+1}\right)}{\Delta z_j} + h_{ds\_i} 2\pi r_{ds\_i}\left(T_{1,j}^{n+1} - T_{2,j}^{n+1}\right) = -\rho_{df}\pi r_{ds\_i}^2 C_{p\_df}\frac{\left(T_{1,j}^{n+1} - T_{1,j}^{n}\right)}{\Delta t} - wgsin\alpha$$

Equation B.14

Where *j* refers to the node's vertical position in the system, and *n+1* refers to the instant in time for which temperature is being calculated for.

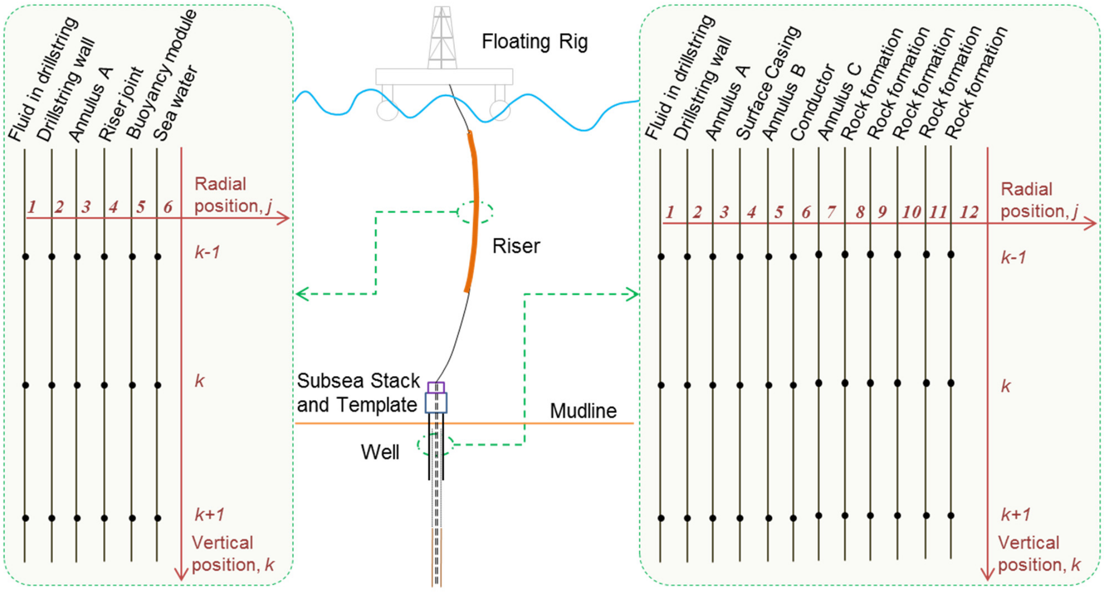

Figure B.6 – Schematic representation of well system's mesh.

Rearranging the terms on Equation B.14 according to the unknown temperature yields:

$$T_{1,j-1}^{n+1}\frac{\rho_{df} q C_{p\_df}}{\Delta z_j} - T_{2,j}^{n+1}\cdot h_{ds\_i} 2\pi r_{ds\_i} + T_{1,j}^{n+1}\left(\frac{\rho_{df}\pi r_{ds\_i}^2 C_{p\_df}}{\Delta t} + h_{ds\_i} 2\pi r_{ds\_i} - \frac{\rho_{df} q C_{p\_df}}{\Delta z_j}\right) = \rho_{df}\pi r_{ds\_i}^2 C_{p\_df}\frac{T_{1,j}^{n}}{\Delta t} - wgsin\alpha$$

Equation B.15

This can be written as a vector multiplication:

$$\begin{bmatrix} \frac{\rho_{df} q C_{p\_df}}{\Delta z_j} & 1 & \left(\frac{\rho_{df}\pi r_{ds\_i}^2 C_{p\_df}}{\Delta t} + h_{ds\_i} 2\pi r_{ds\_i} - \frac{\rho_{df} q C_{p\_df}}{\Delta z_j}\right) & 1 & -h_{ds\_i} 2\pi r_{ds\_i} \end{bmatrix} \begin{bmatrix} T_{1,j-1}^{n+1} \\ 0 \\ T_{1,j}^{n+1} \\ 0 \\ T_{2,j}^{n+1} \end{bmatrix} = \left[\rho_{df}\pi r_{ds\_i}^2 C_{p\_df}\frac{T_{1,j}^{n}}{\Delta t} - wgsin\alpha\right]$$

Equation B.16

Applying this procedure to Equation B.8, and employing the notation shown in Figure 4.3, gives:

$$\frac{k_{ds}}{\Delta z_j}\left[\frac{\left(T_{2,j+1}^{n+1}-T_{2,j}^{n+1}\right)}{\Delta z_{j+0.5}}-\frac{\left(T_{2,j}^{n+1}-T_{2,j-1}^{n+1}\right)}{\Delta z_{j-0.5}}\right]+\frac{h_{ds\_i}2r_{ds\_i}}{\left(r_{ds\_o}^2-r_{ds\_i}^2\right)}\left(T_{1,j}^{n+1}-T_{2,j}^{n+1}\right)-\frac{h_{ds\_o}2r_{ds\_o}}{\left(r_{ds\_o}^2-r_{ds\_i}^2\right)}\left(T_{2,j}^{n+1}-T_{3,j}^{n+1}\right)=\rho_{ds}C_{p\_ds}\frac{\left(T_{2,j}^{n+1}-T_{2,j}^{n}\right)}{\Delta t}$$

Equation B.17

$$T_{2,j}^{n+1}\left[-\frac{k_{ds}}{\Delta z_j\Delta z_{j+0.5}}-\frac{k_{ds}}{\Delta z_j\Delta z_{j-0.5}}-\frac{h_{ds\_i}2r_{ds\_i}}{\left(r_{ds_o}^2-r_{ds_i}^2\right)}-\frac{h_{ds\_o}2r_{ds\_o}}{\left(r_{ds_o}^2-r_{ds_i}^2\right)}-\frac{\rho_{ds}C_{p\_ds}}{\Delta t}\right]+T_{2,j+1}^{n+1}\frac{k_{ds}}{\Delta z_j\Delta z_{j+0.5}}+T_{2,j-1}^{n+1}\frac{k_{ds}}{\Delta z_j\Delta z_{j-0.5}}$$

$$+T_{1,j}^{n+1}\frac{h_{ds\_i}2r_{ds\_i}}{\left(r_{ds\_o}^2-r_{ds\_i}^2\right)}+T_{3,j}^{n+1}\frac{h_{ds\_o}2r_{ds\_o}}{\left(r_{ds\_o}^2-r_{ds\_i}^2\right)}=-T_{2,j}^{n}\frac{\rho_{ds}C_{p\_ds}}{\Delta t}$$

Equation B.18

$$\left[\frac{h_{ds\_i}2r_{ds\_i}}{\left(r_{ds\_o}^2-r_{ds\_i}^2\right)}\quad\frac{k_{ds}}{\Delta z_j\Delta z_{j-0.5}}\quad\left[-\frac{k_{ds}}{\Delta z_j\Delta z_{j+0.5}}-\frac{k_{ds}}{\Delta z_j\Delta z_{j-0.5}}-\frac{h_{ds\_i}2r_{ds\_i}}{\left(r_{ds\_o}^2-r_{ds\_i}^2\right)}-\frac{h_{ds\_o}2r_{ds\_o}}{\left(r_{ds\_o}^2-r_{ds\_i}^2\right)}-\frac{\rho_{ds}C_{p\_ds}}{\Delta t}\right]\right.$$

$$\left.\dashrightarrow\frac{k_{ds}}{\Delta z_j\Delta z_{j+0.5}}\quad\frac{h_{ds\_o}2r_{ds\_o}}{\left(r_{ds\_o}^2-r_{ds\_i}^2\right)}\right]\begin{bmatrix}T_{1,j}^{n+1}\\T_{2,j-1}^{n+1}\\T_{2,j}^{n+1}\\T_{2,j+1}^{n+1}\\T_{3,j}^{n+1}\end{bmatrix}=\left[-T_{2,j}^{n}\frac{\rho_{ds}C_{p\_ds}}{\Delta t}\right]$$

Equation B.19

For the fluid in the annulus, it yields:

$$\rho_{df} q C_{p\_df} \frac{\left(T_{3,j+1}^{n+1} - T_{3,j}^{n+1}\right)}{\Delta z_j} + h_{ds\_o} 2\pi r_{ds\_o}\left(T_{2,j}^{n+1} - T_{3,j}^{n+1}\right) - h_{c1w\_i} 2\pi r_{c1w\_i}\left(T_{3,j}^{n+1} - T_{4,j}^{n+1}\right) = \rho_{df}\pi\left(r_{c1w\_i}^2 - r_{ds\_o}^2\right) C_{p\_df} \frac{\left(T_{3,j}^{n+1} - T_{3,j}^{n}\right)}{\Delta t} - wgsin\alpha$$

Equation B.20

$$T_{3,j}^{n+1}\left[-\frac{\rho_{df} q C_{p\_df}}{\Delta z_j} - h_{ds\_o} 2\pi r_{ds\_o} - h_{c1w\_i} 2\pi r_{c1w\_i} - \frac{\rho_{df}\pi\left(r_{c1w\_i}^2 - r_{ds\_o}^2\right) C_{p\_df}}{\Delta t}\right] + T_{3,j+1}^{n+1} \frac{\rho_{df} q C_{p\_df}}{\Delta z_j} + T_{2,j}^{n+1} h_e 2\pi r_e + T_{4,j}^{n+1} h_{c1w\_i} 2\pi r_{c1w\_i} = -T_{3,j}^{n} \frac{\rho_{df}\pi\left(r_{c1w\_i}^2 - r_{ds\_o}^2\right) C_{p\_df}}{\Delta t} - wgsin\alpha$$

Equation B.21

$$\begin{bmatrix} h_{ds\_o} 2\pi r_{ds\_o} & 1 & \left[-\frac{\rho_{df} q C_{p\_df}}{\Delta z_j} - h_{ds\_o} 2\pi r_{ds\_o} - h_{c1w\_i} 2\pi r_{c1w\_i} - \frac{\rho_{df}\pi\left(r_{c1w\_i}^2 - r_{ds\_o}^2\right) C_{p\_df}}{\Delta t}\right] & \frac{\rho_{df} q C_{p\_df}}{\Delta z_j} & h_{c1w\_i} 2\pi r_{c1w\_i} \end{bmatrix} \begin{bmatrix} T_{2,j}^{n+1} \\ 0 \\ T_{3,j}^{n+1} \\ T_{3,j+1}^{n+1} \\ T_{4,j}^{n+1} \end{bmatrix} = \left[-T_{3,j}^{n} \frac{\rho_{df}\pi\left(r_{c1w\_i}^2 - r_{ds\_o}^2\right) C_{p\_df}}{\Delta t} - wgsin\alpha\right]$$

Equation B.22

For the casing wall:

$$\frac{k_{c1w}}{\Delta z_j}\left[\frac{\left(T_{4,j+1}^{n+1}-T_{4,j}^{n+1}\right)}{\Delta z_{j+0.5}}-\frac{\left(T_{4,j}^{n+1}-T_{4,j-1}^{n+1}\right)}{\Delta z_{j-0.5}}\right]+\frac{h_{c1w\_i}2r_{c1w\_i}}{\left(r_{c1w\_i}^2-r_{ds\_o}^2\right)}\left(T_{3,j}^{n+1}-T_{4,j}^{n+1}\right)-\frac{\frac{2k_{c1w}k_{c1a}}{\left(r_{c1w\_i}^2-r_{ds\_o}^2\right)}}{k_{c1a}ln\left(\frac{r_{c1w\_o}}{r_{c1w\_m}}\right)+k_{c1w}ln\left(\frac{r_{c1a\_m}}{r_{c1w\_o}}\right)}\left(T_{4,j}^{n+1}-T_{5,j}^{n+1}\right)$$

$$=\rho_{c1w}C_{p\_c1w}\frac{\left(T_{4,j}^{n+1}-T_{4,j}^{n}\right)}{\Delta t}$$

Equation B.23

$$T_{4,j}^{n+1}\left[-\frac{k_{c1w}}{\Delta z_j\Delta z_{j+0.5}}-\frac{k_{c1w}}{\Delta z_j\Delta z_{j-0.5}}-\frac{h_{c1w\_i}2r_{c1w\_i}}{\left(r_{c1w\_i}^2-r_{ds\_o}^2\right)}-\frac{\frac{2k_{c1w}k_{c1a}}{\left(r_{c1w\_i}^2-r_{ds\_o}^2\right)}}{k_{c1a}ln\left(\frac{r_{c1w\_o}}{r_{c1w\_m}}\right)+k_{c1w}ln\left(\frac{r_{c1a\_m}}{r_{c1w\_o}}\right)}-\frac{\rho_{cw}C_{p\_c1w}}{\Delta t}\right]+T_{4,j+1}^{n+1}\frac{k_{c1w}}{\Delta z_j\Delta z_{j+0.5}}$$

$$+T_{4,j-1}^{n+1}\frac{k_{c1w}}{\Delta z_j\Delta z_{j-0.5}}+T_{3,j}^{n+1}\frac{h_{c1w\_i}2r_{c1w\_i}}{\left(r_{c1w\_i}^2-r_{ds\_o}^2\right)}+T_{5,j}^{n+1}\frac{\frac{2k_{c1w}k_{c1a}}{\left(r_{c1w\_i}^2-r_{ds\_o}^2\right)}}{k_{c1a}ln\left(\frac{r_{c1w\_o}}{r_{c1w\_m}}\right)+k_{c1w}ln\left(\frac{r_{c1a\_m}}{r_{c1w\_o}}\right)}=-T_{4,j}^{n}\frac{\rho_{c1w}C_{p\_c1w}}{\Delta t}$$

Equation B.24

$$\left[\frac{h_{c1w\_i}2r_{c1w\_i}}{\left(r_{c1w\_i}^2-r_{ds\_o}^2\right)}\quad\frac{k_{c1w}}{\Delta z_j\Delta z_{j-0.5}}\quad-\frac{k_{c1w}}{\Delta z_j\Delta z_{j+0.5}}-\frac{k_{c1w}}{\Delta z_j\Delta z_{j-0.5}}-\frac{h_{c1w\_i}2r_{c1w\_i}}{\left(r_{c1w\_i}^2-r_{ds\_o}^2\right)}-\frac{\frac{2k_{c1w}k_{c1a}}{\left(r_{c1w\_i}^2-r_{ds\_o}^2\right)}}{k_{c1a}ln\left(\frac{r_{c1w\_o}}{r_{c1w\_m}}\right)+k_{c1w}ln\left(\frac{r_{c1a\_m}}{r_{c1w\_o}}\right)}-\frac{\rho_{c1w}C_{p\_c1w}}{\Delta t}\right.$$

$$\dashrightarrow\left.\frac{k_{c1w}}{\Delta z_j\Delta z_{j+0.5}}\quad\frac{\frac{2k_{c1w}k_{c1a}}{\left(r_{c1w\_i}^2-r_{ds\_o}^2\right)}}{k_{c1a}ln\left(\frac{r_{c1w\_o}}{r_{c1w\_m}}\right)+k_{c1w}ln\left(\frac{r_{c1a\_m}}{r_{c1w\_o}}\right)}\right]\begin{bmatrix}T_{3,j}^{n+1}\\T_{4,j-1}^{n+1}\\T_{4,j}^{n+1}\\T_{4,j+1}^{n+1}\\T_{5,j}^{n+1}\end{bmatrix}=\left[-T_{4,j}^{n}\frac{\rho_{c1w}C_{p\_c1w}}{\Delta t}\right]$$

Equation B.25

For the subsequent components:

$$
\left[\frac{\frac{2k_{i-1}k_i}{r_{i\_o}\Delta r_i}}{k_i ln\left(\frac{r_{(i-1)\_o}}{r_{(i-1)\_m}}\right)+k_{i-1}ln\left(\frac{r_{i\_m}}{r_{(i-1)\_o}}\right)} \quad \frac{k_i}{\Delta z_j \Delta z_{j-0.5}}\right.
$$

$$
-\frac{k_i}{\Delta z_j \Delta z_{j+0.5}} - \frac{k_i}{\Delta z_j \Delta z_{j-0.5}} - \frac{\frac{2k_{i-1}k_i}{r_{i\_o}\Delta r_i}}{k_i ln\left(\frac{r_{(i-1)\_o}}{r_{(i-1)\_m}}\right) + k_{i-1} ln\left(\frac{r_{i\_m}}{r_{(i-1)\_o}}\right)} - \frac{\frac{2k_i k_{i+1}}{r_{i\_o}\Delta r_i}}{k_{i+1} ln\left(\frac{r_{i\_o}}{r_{i\_m}}\right) + k_i ln\left(\frac{r_{(i+1)\_m}}{r_{i\_o}}\right)} - \frac{\rho_i C_{\mathrm{p\_i}}}{\Delta t}
$$

Equation B.26

$$
\left.\frac{k_i}{\Delta z_j \Delta z_{j+0.5}} \quad \frac{\frac{2k_i k_{i+1}}{r_{i\_o}\Delta r_i}}{k_{i+1} ln\left(\frac{r_i}{r_{i\_m}}\right) + k_i ln\left(\frac{r_{(i+1)\_m}}{r_i}\right)}\right] \begin{bmatrix} T_{i-1,j}^{n+1} \\ T_{i,j-1}^{n+1} \\ T_{i,j}^{n+1} \\ T_{i,j+1}^{n+1} \\ T_{i+1,j}^{n+1} \end{bmatrix} = \left[-T_{i,j}^{n} \frac{\rho_i C_{p_i}}{\Delta t}\right]
$$

Grouping the several vector multiplications leads to a matrix equation of the form:

$$\begin{bmatrix} \ddots & \vdots & \vdots & & & & \\ \cdots & a_{J_{MAX}(i-1)+j-2,J_{MAX}(i-1)+j-2} & a_{J_{MAX}(i-1)+j-2,J_{MAX}(i-1)+j-1} & a_{J_{MAX}(i-1)+j-2,J_{MAX}(i-1)+j} & & & \\ \cdots & a_{J_{MAX}(i-1)+j-1,J_{MAX}(i-1)+j-2} & a_{J_{MAX}(i-1)+j-1,J_{MAX}(i-1)+j-1} & a_{J_{MAX}(i-1)+j-1,J_{MAX}(i-1)+j} & a_{J_{MAX}(i-1)+j-1,J_{MAX}(i-1)+j+1} & & \\ & a_{J_{MAX}(i-1)+j,J_{MAX}(i-1)+j-2} & a_{J_{MAX}(i-1)+j,J_{MAX}(i-1)+j-1} & a_{J_{MAX}(i-1)+j,J_{MAX}(i-1)+j} & a_{J_{MAX}(i-1)+j,J_{MAX}(i-1)+j+1} & a_{J_{MAX}(i-1)+j,J_{MAX}(i-1)+j+2} & \\ & & a_{J_{MAX}(i-1)+j+1,J_{MAX}(i-1)+j-1} & a_{J_{MAX}(i-1)+j+1,J_{MAX}(i-1)+j} & a_{J_{MAX}(i-1)+j+1,J_{MAX}(i-1)+j+1} & a_{J_{MAX}(i-1)+j+1,J_{MAX}(i-1)+j+2} & \cdots \\ & & & a_{J_{MAX}(i-1)+j+2,J_{MAX}(i-1)+j} & a_{J_{MAX}(i-1)+j+2,J_{MAX}(i-1)+j+1} & a_{J_{MAX}(i-1)+j+2,J_{MAX}(i-1)+j+2} & \cdots \\ & & & & \vdots & \vdots & \ddots \end{bmatrix}$$

$$\dashrightarrow \begin{bmatrix} \vdots \\ T^{n+1}_{J_{MAX}(i-1)+j-2} \\ T^{n+1}_{J_{MAX}(i-1)+j-1} \\ T^{n+1}_{J_{MAX}(i-1)+j} \\ T^{n+1}_{J_{MAX}(i-1)+j+1} \\ T^{n+1}_{J_{MAX}(i-1)+j+2} \\ \vdots \end{bmatrix} = \begin{bmatrix} \vdots \\ b_{J_{MAX}(i-1)+j-2} \\ b_{J_{MAX}(i-1)+j-1} \\ b_{J_{MAX}(i-1)+j} \\ b_{J_{MAX}(i-1)+j+1} \\ b_{J_{MAX}(i-1)+j+2} \\ \vdots \end{bmatrix}$$

Equation B.27

The size of the matrix in Equation B.27 is $(J_{MAX}*I_{MAX})^2$, where J_{MAX} is the maximum number of elements in the vertical direction, and I_{MAX} the maximum number of elements in the radial direction. The *a* coefficients are calculated according to which component in the well they refer to and the corresponding formulation of heat transfer. The same applies for the *b* coefficients. The temperature vector is calculated then by inverting the coefficient matrix.

B.2.8 Energy Source Terms

In addition to temperature differential, the heat transferred through a control volume in the drillstring/annulus fluid could come from the sources below:

- The heat from the generated rock cuttings;
- The viscous energy generated from pressure losses inside the drillstring, in the drill bit and in the annulus
- The mechanical work input by the rotary table, divided among drillstring and drill bit.

B.2.8.1 ***Rock cuttings***

The conservation of mass in the well system would require accounting for the added rock cuttings into the annulus fluid during drilling. But since the amount of drill cutting added may be considered insignificant compared to the mass flow rate of the circulation mud fluid annulus (Kårstad & Aadnøy, 1999), the annulus flow rate can be the same as the mass flow rate inside the drillstring.

B.2.8.2 ***Pressure Losses***

The pressure losses that generate the viscous energy added to the system can be calculated based on the flow characteristics and the geometry of the flow path: drillstring, drill bit, or annulus. The code presented in the paper used the formulations presented by Marshall and Bentsen (1982), and adapted below into Equations B28 through B33, to carry out the necessary pressure losses calculations.

First flow regime is determined comparing the power-law Reynolds Number, *Re*, Equation B.28, with a flow transition criterion, Re_c, such as the one proposed by Hanks (1963), Equation B.29.

$$Re = \frac{D^n V^{2-n} \rho}{8^{n-1} K \left(\frac{3n+1}{4n}\right)^n}$$ **Equation B.28**

$$Re_c = \frac{6464n}{(1+3n)^2 \left(\frac{1}{2+n}\right)^{2+n/1+n}}$$ **Equation B.29**

The Fanning friction factor, f_{ds}, inside the drillstring was calculated based on the empirical Torrance formulation (Torrance, 1963) for the turbulent flow of power-law fluids in rough pipes:

$$\frac{1}{\sqrt{f_{ds}}} = \frac{4.07}{n} \frac{\log r_{ds\_i} \times 10^3}{\epsilon} + 6 - \frac{2.65}{n}$$ **Equation B.30**

where *n* is the power-law fluid behavior index, ε is the roughness of the pipe.

And the pressure drop inside the drillstring, ΔP_{ds}, is obtained by:

$$\Delta P_{ds} = \frac{2 f_{ds} V^2 L}{D_{ds\_i} g_c} \qquad \textbf{Equation B.31}$$

where V is the flow velocity, L is the length of the drillstring, and g_c is a conversion factor.

The Bernoulli equation for flow thorough an orifice is used to derive the pressure losses in the drill bit, ΔP_{db}:

$$\Delta P_{db} = \frac{\rho_{df}}{2g}\left(\frac{q}{0.95 \times A_n}\right)^2 \qquad \textbf{Equation B.32}$$

where A_n is the nozzle area. Since A_n is much smaller than the drillstring cross-sectional area it enables the orifice coefficient to be assumed equal to the discharge coefficient of 0.95.

The formulation for the pressures losses in the annulus, ΔP_A, is presented in Equation B.33, which used the Fredrickson and Bird (1985) parallel plate approximation:

$$\Delta P_A = \frac{2KL}{(r_{cs\_i} - r_{ds\_o}) g_c}\left[\frac{2(n+1)q}{n\pi(r_{cs\_i} + r_{ds\_o})(r_{cs\_i} - r_{ds\_o})^2}\right]^n \qquad \textbf{Equation B.33}$$

B.2.8.3 *Mechanical Energy*

The mechanical energy provided to the system comes from the surface equipment that provides the torque necessary to rotate the drillstring. The total surface torque is the sum of the frictional torque, generated from rotational friction between drillstring and casing/formation, the dynamic torque, generated from the viscous force between drillstring and drilling fluid, and the drill bit torque.

The drill bit torque can be measured during drilling, and the total power at the drill bit can be estimated (Poletto and Miranda 2004) from the torque on bit (TOB), weight on bit (WOB), the rotations per minute (RPM) at the drill bit, and the rate of penetration (ROP), as seen in Equation B.34:

$$P_{drill\ bit} = \frac{2\pi TOB \times RPM}{60} + \frac{WOB \times ROP}{3600} \qquad \textbf{Equation B.34}$$

Not all the mechanical energy will be converted into thermal energy, as some of it is used to cut the rock, and this amount is dependent on the lithology and the bit model. To simplify the analysis, the latest version of the code considered that 50% of the mechanical energy calculated at the bit turned into thermal energy.

The frictional torque is a function of the friction factor, side forces, axial load, and well profile. The calculated torque at a given element in the drillstring will vary according to its weight and inclination. Figure B.7 shows a sketch of the drillstring for torque calculation purposes. The angle α with the horizontal and the angle θ, developed as the pipe climb up the side of the wellbore as it rotates, determine the value of the normal force N (Equations B35 and B36).

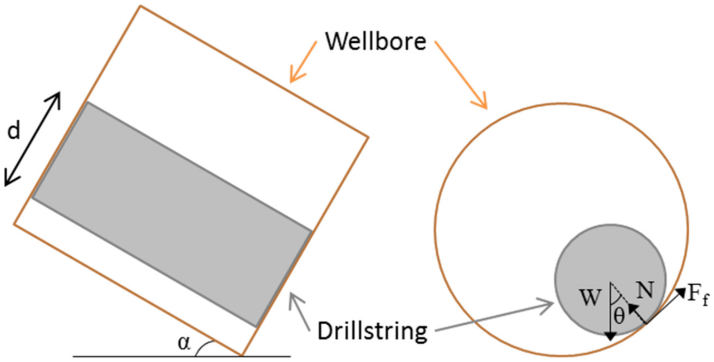

Figure B.7 – Sketch of a drillstring element for torque calculation purposes. Left: longitudinal view. Right: cross-section view.

$$\sum F_{Tangent\ direction} = 0 \rightarrow F_f - W \sin\alpha \sin\theta \rightarrow \mu N = W \sin\alpha \sin\theta$$ **Equation B.35**

$$\sum F_{Tangent\ direction} = 0 \rightarrow N - W \sin\alpha \cos\theta \rightarrow N = W \sin\alpha \cos\theta$$ **Equation B.36**

Where W is the weight of the drillstring element and μ is the friction coefficient. Solving the two previous equations enables the angle θ to be determined.

$$\frac{\mu N}{N} = \frac{W \sin\alpha \sin\theta}{W \sin\alpha \cos\theta} \rightarrow \mu = \tan\theta \rightarrow \theta = \tan^{-1}\mu$$ **Equation B.37**

The torque, T, at the element then is calculated as

$$T = F_f \frac{d}{2} = \mu N \frac{d}{2} = \mu W \sin\alpha \sin\theta \frac{d}{2}$$ **Equation B.38**

And the element's mechanical energy, E_{mec}, turned thermal energy, E_{the}, is shown in Equation B.39, where ω is the angular velocity of the drillstring.

$$E_{the} = E_{mec} = T\omega$$ **Equation B.39**

Since surface torque is one of the provided inputs to the simulation, the dynamic torque is simply calculated by subtracting the bit torque and the total frictional torque from the surface torque. As a simplification it is assumed that the dynamic torque is uniformly distributed along the drillstring.

B.2.8.4 *Summary*

The total thermal energy added to the fluid in the annulus, Q_A, will be the sum of the energy converted from the work to rotate the drillstring and the energy originated from the pressure losses.

For the fluid inside the drillstring the thermal energy added, Q_{ds}, comes solely from fluid friction losses, except for the node at the bottom of the well, where there is the additional energy from the work done by the drill bit, and the pressure losses through the bit.

B.3 Validation

The validation of the routine was accomplished by comparing similar cases simulated in commercial programs. *Drillbench* (Schlumberger 2018) version 6.1 and *WELLCAT*^{TM} (Halliburton 2018) version 2003.11.0.0 were available for that purpose.

The simulated operation was a simplified drilling operation. Starting from a measured depth (MD) of 800 m, of which 327 m were of water column, the well was continuously drilled at a constant rate of penetration until the target MD of 2300 m was reached. Casing strings installed in place were the conductor (shoe at 365 m MD) and the surface casing (shoe at 800 m MD). Initial temperature of the well was set to be the undisturbed formation temperature.

Figure B.8, Figure B.9 and Figure B.10 present snapshots of the temperature distributions of the circulating drilling fluid, calculated by both commercial programs. It can be observed from the figures that the results given by the two programs differ considerably. Most noticeable is the fact that the calculations by *Drillbench* indicate a colder temperature at the bottom of the annulus fluid column than the temperature for the fluid inside the drillstring at the same depth.

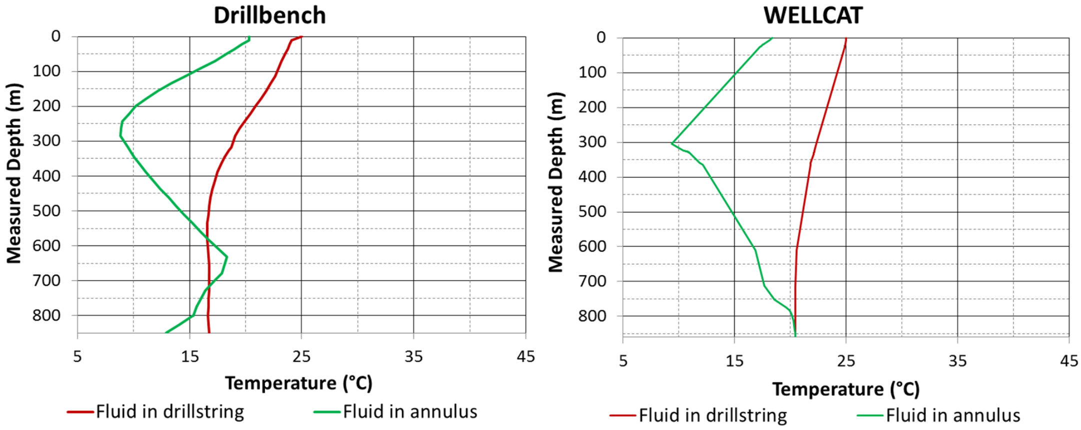

Figure B.8 – Comparison of calculated temperatures after 6 hr of drilling operation. Left: *Drillbench*. Right: *WELLCAT*.

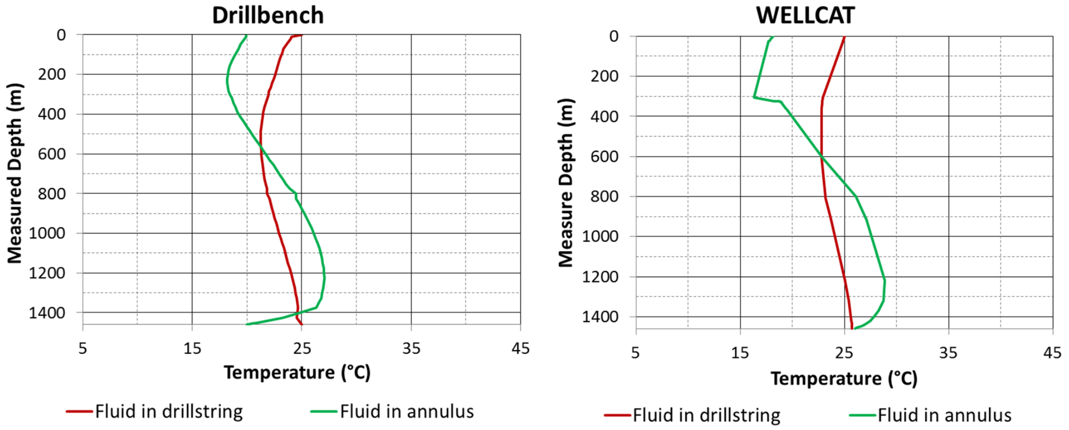

Figure B.9 – Comparison of calculated temperatures after 11 hr of drilling operation. Left: *Drillbench*. Right: *WELLCAT*.

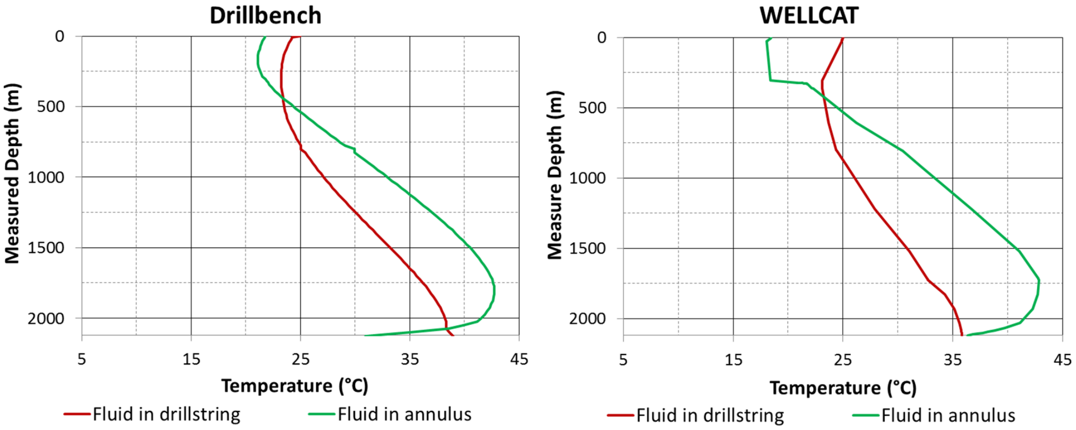

Figure B.10 – Comparison of calculated temperatures after 22 hr of drilling operation. Left: *Drillbench*. Right: *WELLCAT*.

Because of the disparity of the results, though the exact same operation was modelled, only one of the programs could be employed for validation purposes.

The same temperature value for the fluids in the annulus and in the drillstring at the drill bit level is one of the boundary conditions stipulated by Marshal and Bentsen (1982), and one of the boundary conditions adopted for the *Matlab* routine.

Therefore, *Drillbench* could not be used to validate the routine since this program clearly adopts different premises in its modelling of the wellbore temperature.

B.2.9.1 *Comparison of Matlab Routine and WELLCAT*

The same well and operation were designed in the *WELLCAT* program, to evaluate the results obtained by the *Matlab* routine. Comparisons of the temperature distribution pertaining to surface casing, conductor and their respective cement sheaths are shown below.

Figure B.11 shows the temperature distribution of the surface casing as it was calculated by the *Matlab* routine throughout the drilling operation. The time step used by the routine was of one hour, but here are shown the curves obtained every six hours, between 6 and 84 hours of operation, and then at the instant when the target depth was reached. The temperature of surface casing continually increases, but at a decreasing rate, as the operation goes on. Maximo reached temperature is of 27° C at the bottom of the casing string and approximately 16° C near its top.

Figure B.12 shows the temperature distribution of the surface casing as it was calculated by *Wellcat*. The curves shown are the end results of successive runs considering firstly 6 hours of operation, then 12, and so on. It can be seen that after 132 hours of operation the casing string reaches a higher temperature, but temperatures at the mudline level are lower.

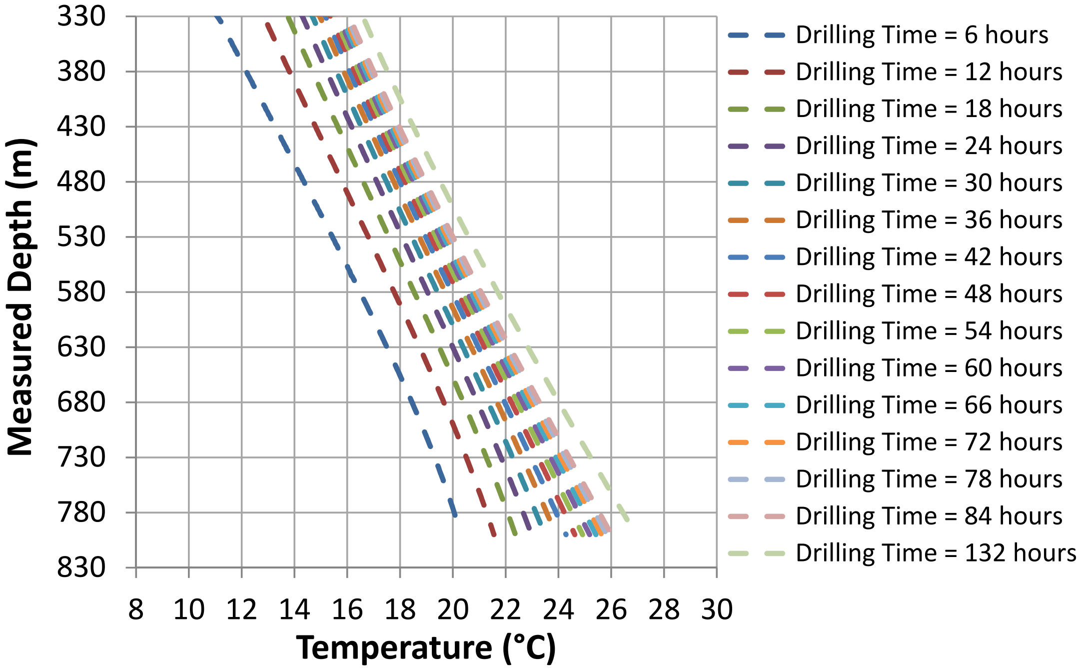

Figure B.11 – Surface casing temperature profiles obtained by *Matlab* code.

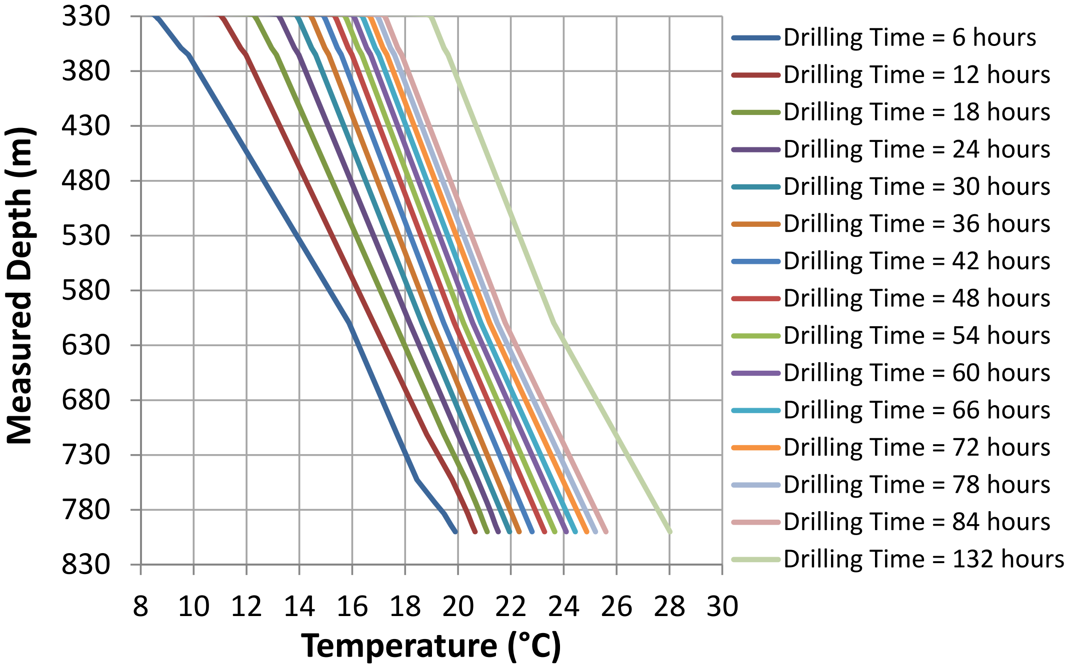

Figure B.12 – Surface casing temperature profiles obtained by *Wellcat.*

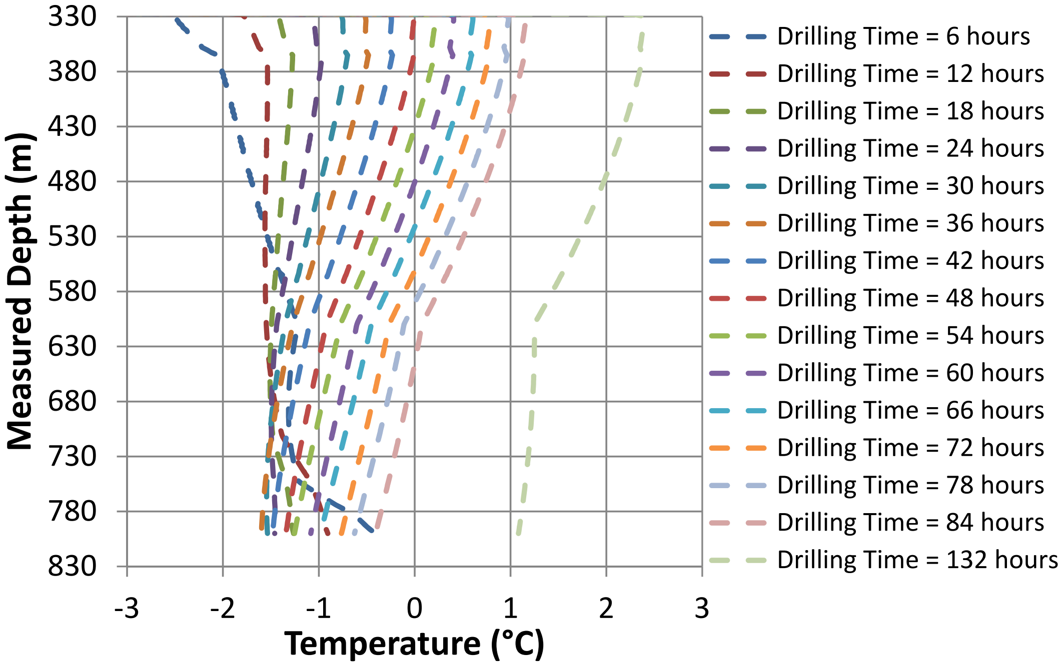

Figure B.13 – Surface casing temperature profiles obtained by *Matlab* code subtracted by the corresponding profiles yielded by *Wellcat.*

Figure B.13 shows the curves obtained when subtracting the temperature profiles obtained by *Wellcat* from those profiles obtained by the *Matlab* code. During most of the simulated drilling operation the *Matlab* code overestimates the temperature between 1 to 2 degrees. Eventually, though, this trend is reversed and *Wellcat'*s temperature becomes 1 or 2 degrees higher.

Overall the difference between the two was ± 2° C. Except at the mudline level, where the temperature difference reached 10 degrees. This is most likely due to the way the subsea stack is modelled by each program, and the corresponding assumed boundary conditions.

Figure B.14 shows the temperature profiles obtained for the surface-casing cement by the *Matlab* code. The calculated temperature is a few degrees smaller than the surface casing temperature. Although the cement sheath in the model does not go all the way up to the mudline, there are no recognizable sudden changes in temperature at the TOC level.

Figure B.15 shows the temperature profiles obtained for the surface-casing cement by *Wellcat*. Here it is possible to easily identify the cement/mud interface around the measured depth of 365 m.

Figure B.16 compares the results obtained by the two programs. For most of the curves the calculated difference remains in the [-1, 1] interval. Though for the 132 hours profile, the difference between the two approaches reached 2° C. At the mudline level the *Matlab* code overestimated the temperature around 5° C.

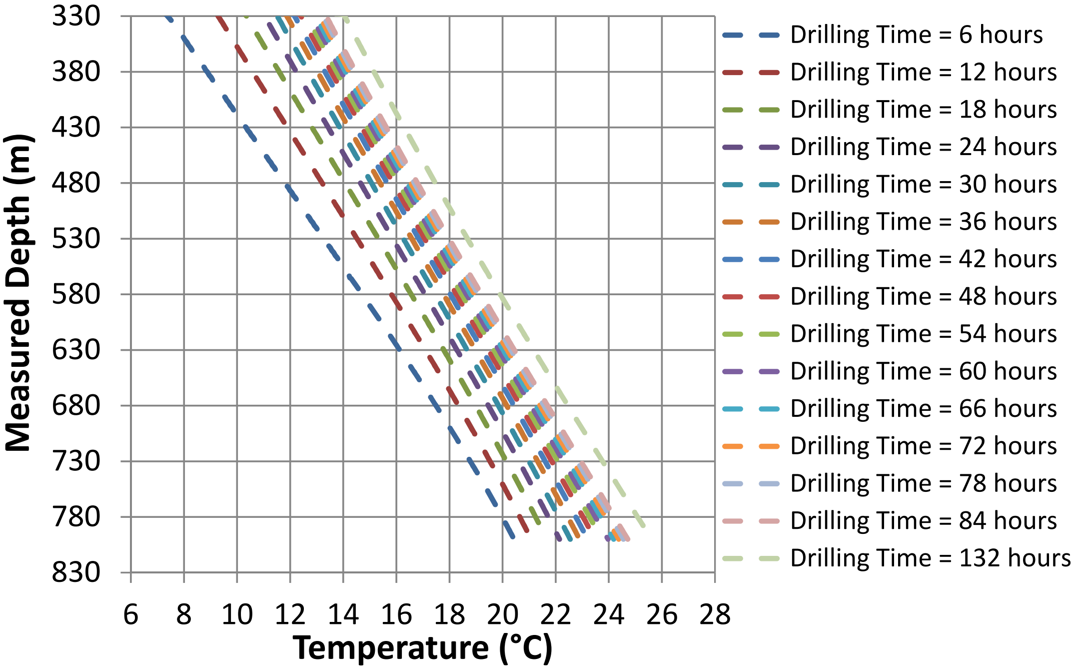

Figure B.14 – Surface-casing cement temperature profiles obtained by *Matlab* code.

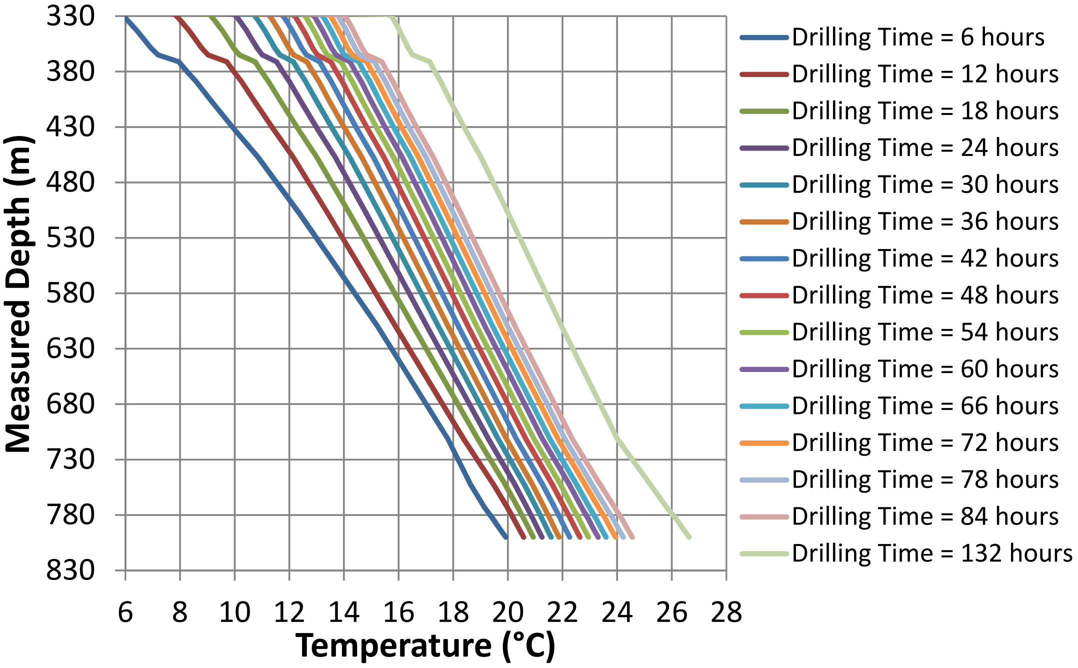

Figure B.15 – Surface-casing cement temperature profiles obtained by *Wellcat.*

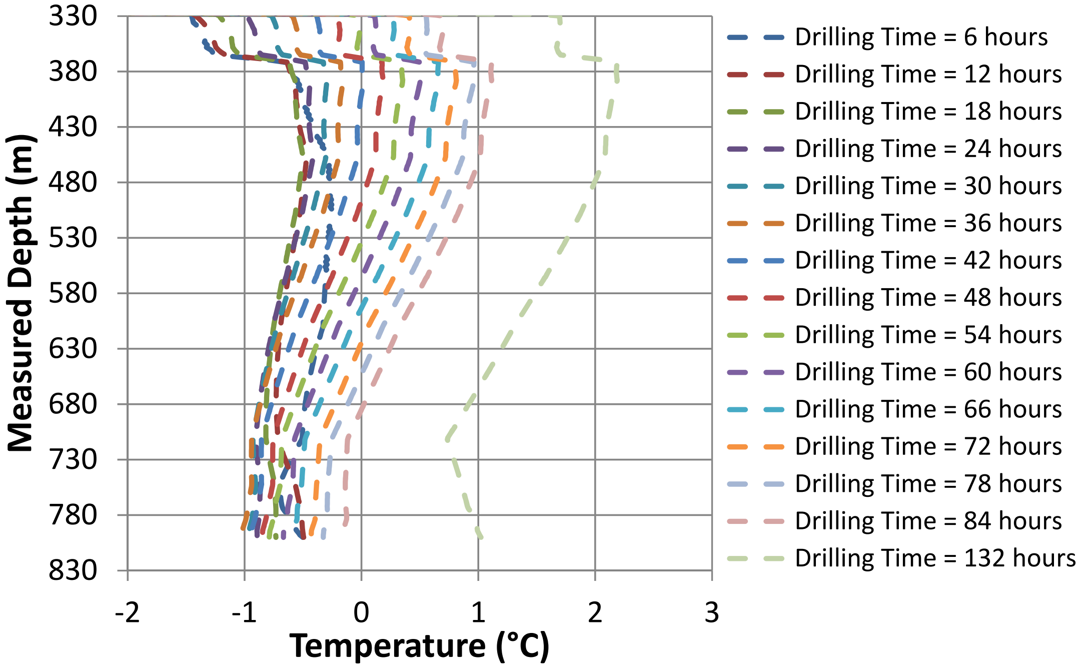

Figure B.16 – Surface-casing cement temperature profiles obtained by Matlab code subtracted by the corresponding profiles yielded by Wellcat.

Figure B.17 shows the conductor temperature profiles obtained by the *Matlab* code, while Figure B.18 shows the conductor temperature profiles obtained by *Wellcat*. The conductor's bottom measured depth is 365 m. At its top the temperature remains close to the 4-5° C value. Discounting the temperature at the top, it can be seen that as the drilling operation continues the difference in temperature throughout its length is relatively small.

Figure B.19 shows that difference between the two models' results remains constant throughout the conductor's length at a given moment, but it continually shifts along the interval [-0.5, 1.5] during the simulated drilling operation.

Figure B.20 and Figure B.21 show the temperature profiles for the conductor cement as calculated by the *Matlab* code and *Wellcat*, respectively. The curves given by the latter are not as inclined as the ones given by the former. Also, the temperature at the top of the cement is close to 4° C for both models. This was expected from the Matlab code, since, contrary to the other components, the top surface of the conductor cement is directly exposed to the sea water temperature.

Figure B.22 compares the results from both programs for the conductor cement temperature and shows that the *Matlab* code underestimated the conductor cement's temperature during the whole operation. The largest difference in temperature, approximately 3.1° C, was obtained for this component at 132 hours of operation.

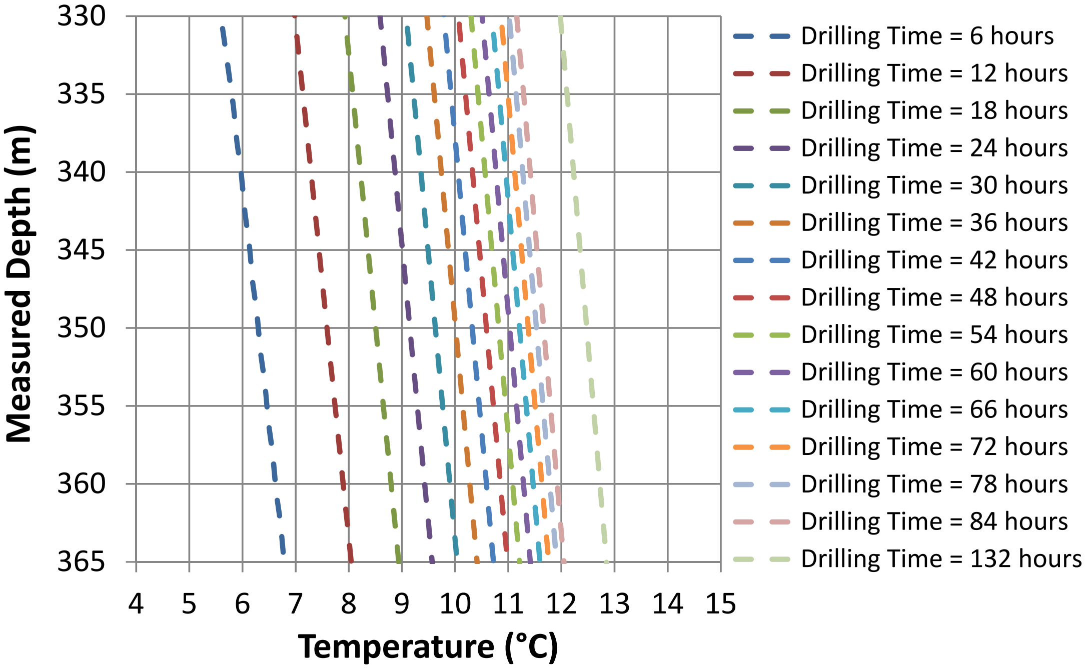

Figure B.17 – Conductor temperature profiles obtained by *Matlab* code.

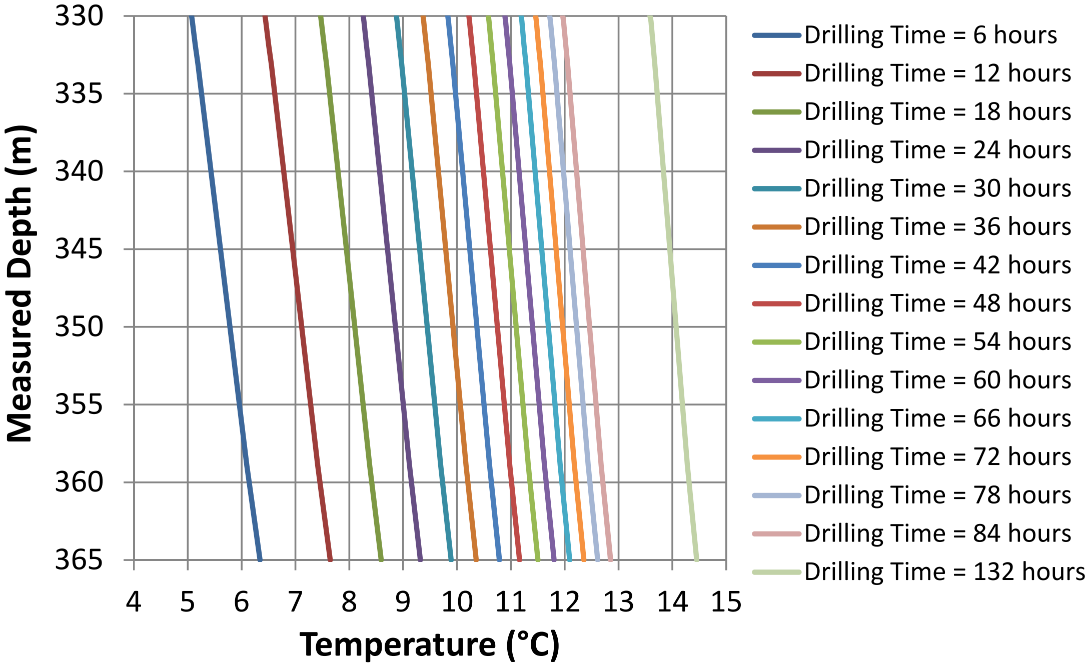

Figure B.18 – Conductor temperature profiles obtained by *Wellcat.*

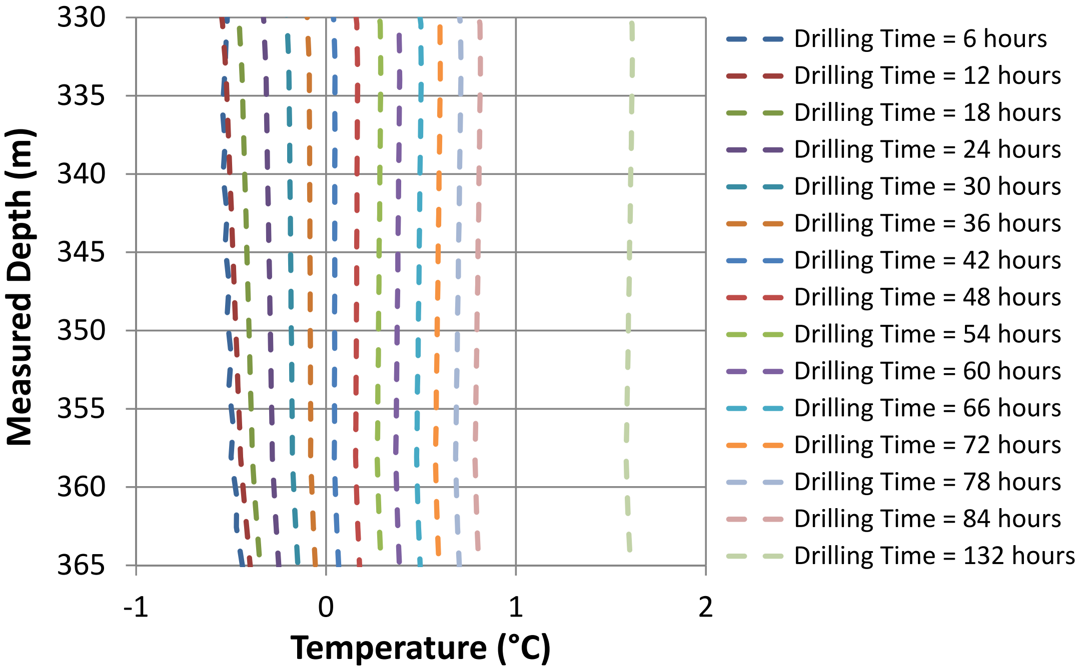

Figure B.19 – Conductor temperature profiles obtained by Matlab code subtracted by the corresponding profiles yielded by Wellcat.

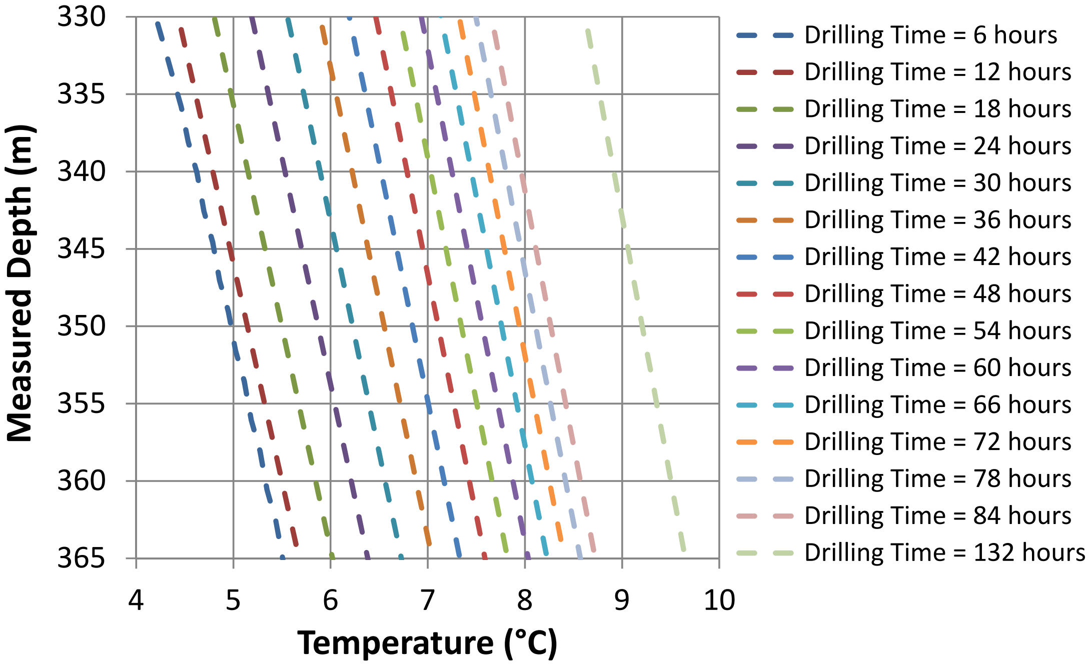

Figure B.20 – Conductor cement temperature profiles obtained by *Matlab* code.

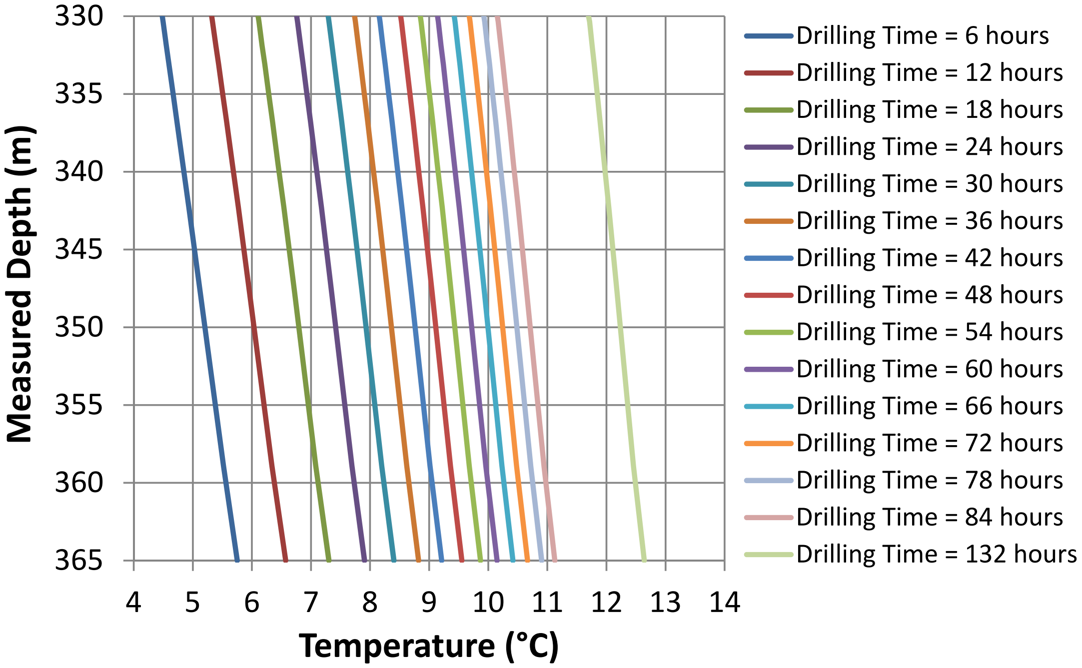

Figure B.21 – Conductor cement temperature profiles obtained by *Wellcat.*

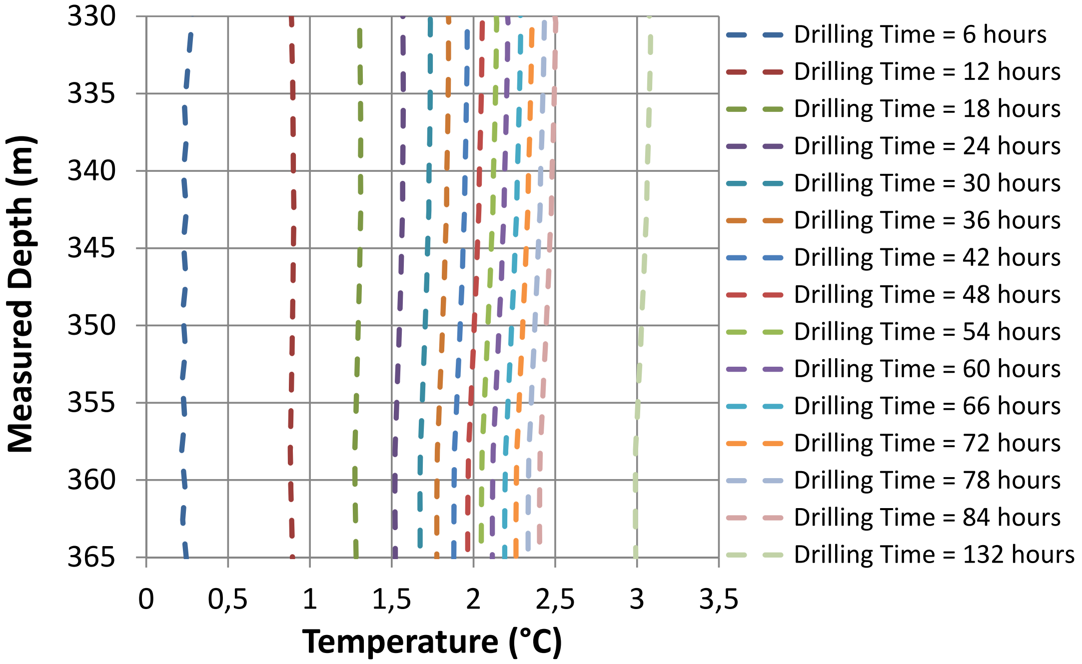

Figure B.22 – Conductor cement temperature profiles obtained by Matlab code subtracted by the corresponding profiles yielded by Wellcat.

B.2.9.2 *Summary*

The *Matlab* code calculates the temperature of the fluids in the wellbore, the drillstring, the casing strings, the casing annuli, the riser string, the subsea stack, and the surrounding rock formation during several operations that can been carried out in the well.

The system is represented by a mesh grid of nodes, and the routine employs equations that come from the energy balance in the different components to describe how the nodes interact with each other. The end result is a matrix equation that calculates the nodes' temperature according to the assumed initial and boundary conditions.

When comparing the routine's results with that of a commercial program, it has been seen that the longer the simulated operation is, the larger the difference in temperature between them is. However, in average the two approaches' results differ in ± 2° C.

Given the user friendliness of the *Matlab* code, and the possibility to readily adapt it to the user's needs, it has been a powerful tool used under this doctoral work.

Annex C – Additional Plots

C.1 Bending Moment Cycles Count – Section 5.3.3

Figure C.1 presents the comparison for the wellhead model with TOC=ML-5m. Similarly to the figures presented in section 5.3.3, the cycle counts for the models with and without temperature coincide within the high cycle/lower load range. However, the dissimilarities begin around the 1000 kNm mark.

The cumulative cycle density comparison in Figure C.2 shows that for both temperature conditions more than 90% of the identified bending moment cycles are lower than 700 kNm. There is a disagreement between the two curves within the 500-700 kNm range, but otherwise the cumulative densities are identical.

Figure C.3 presents the comparison for the wellhead model with TOC=ML-10m. The trend for high cycle/lower load repeats itself, and it is keep right until the 1300 kNm mark. It can be observed in Figure C.4 that the two cumulative cycles densities are practically identical, and more than 90% of the identified bending moment cycles are lower than 700 kNm.

Figure C.5 presents the comparison for the wellhead model with TOC=ML-25m. A clear distinction between the cycles count for the two temperature conditions can be noticed starting around the 700 kNm mark.

The cumulative cycles density comparison in Figure C.6 shows that for the riser model with the bottom boundary condition without temperature more than 90% of the identified bending moment cycles are lower than 720 kNm, while for the other wellhead model the corresponding bending moment value is 740 kNm. A slight disagreement between the two curves can be observed for the 600-800 kNm range, but otherwise the cumulative densities are identical.

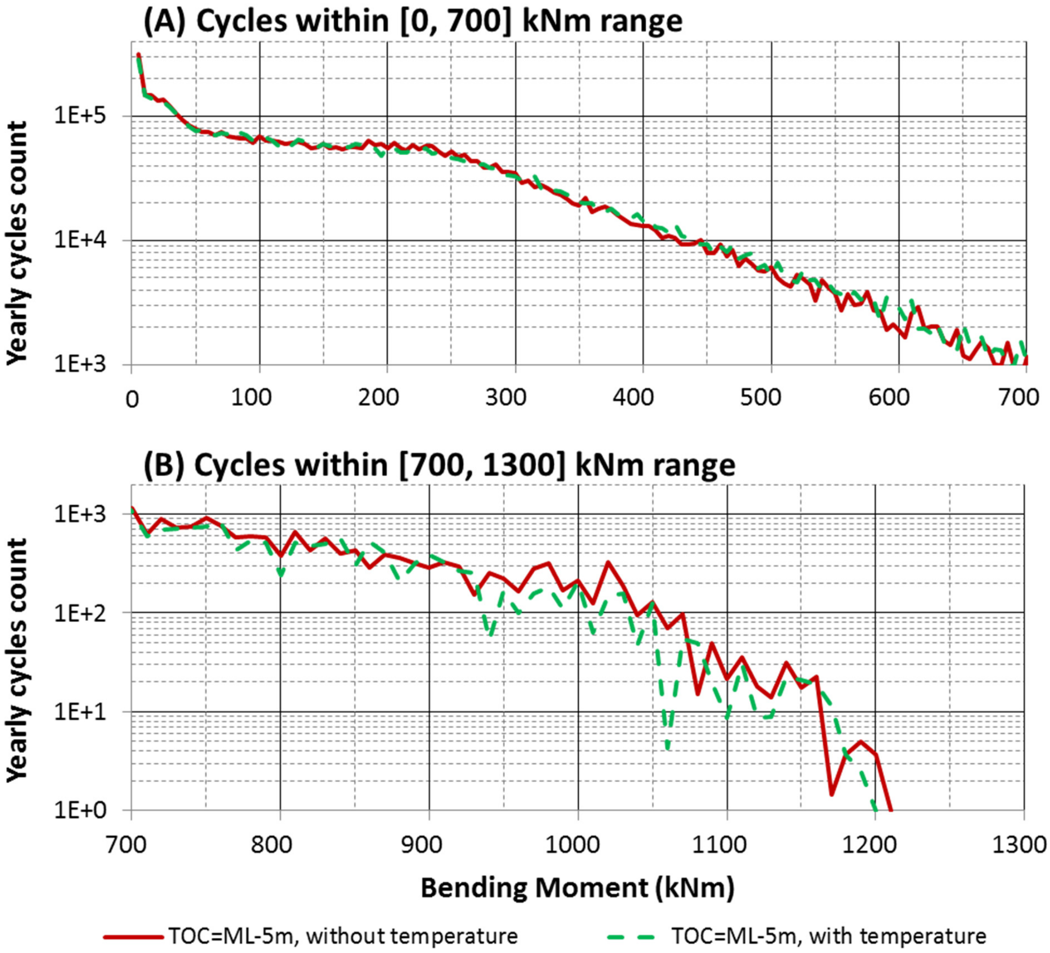

Figure C.1 – Comparison of long-term bending moment histograms. Global riser dynamic analyses with and without temperature. TOC=ML-5m.

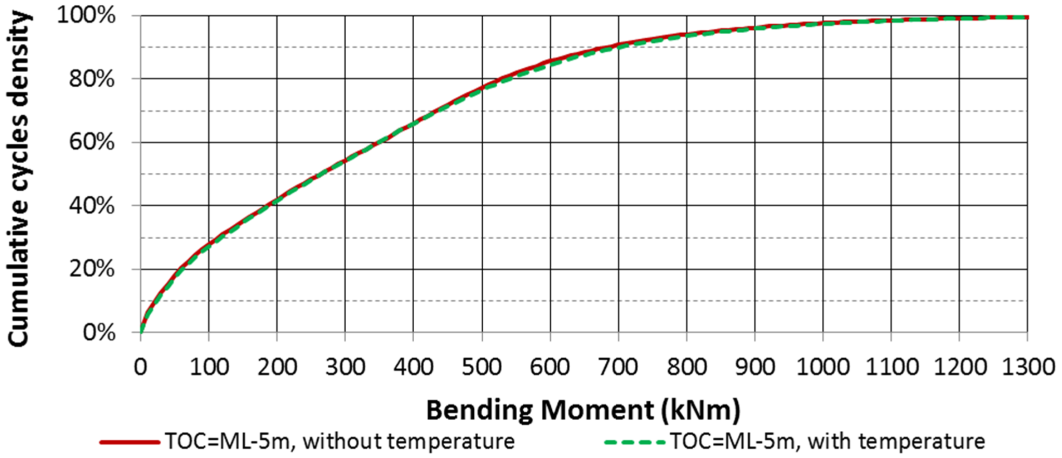

Figure C.2 – Cumulative cycle density comparison of long-term histograms presenting the indirect impact of the temperature distribution of the well. TOC=ML-5m.

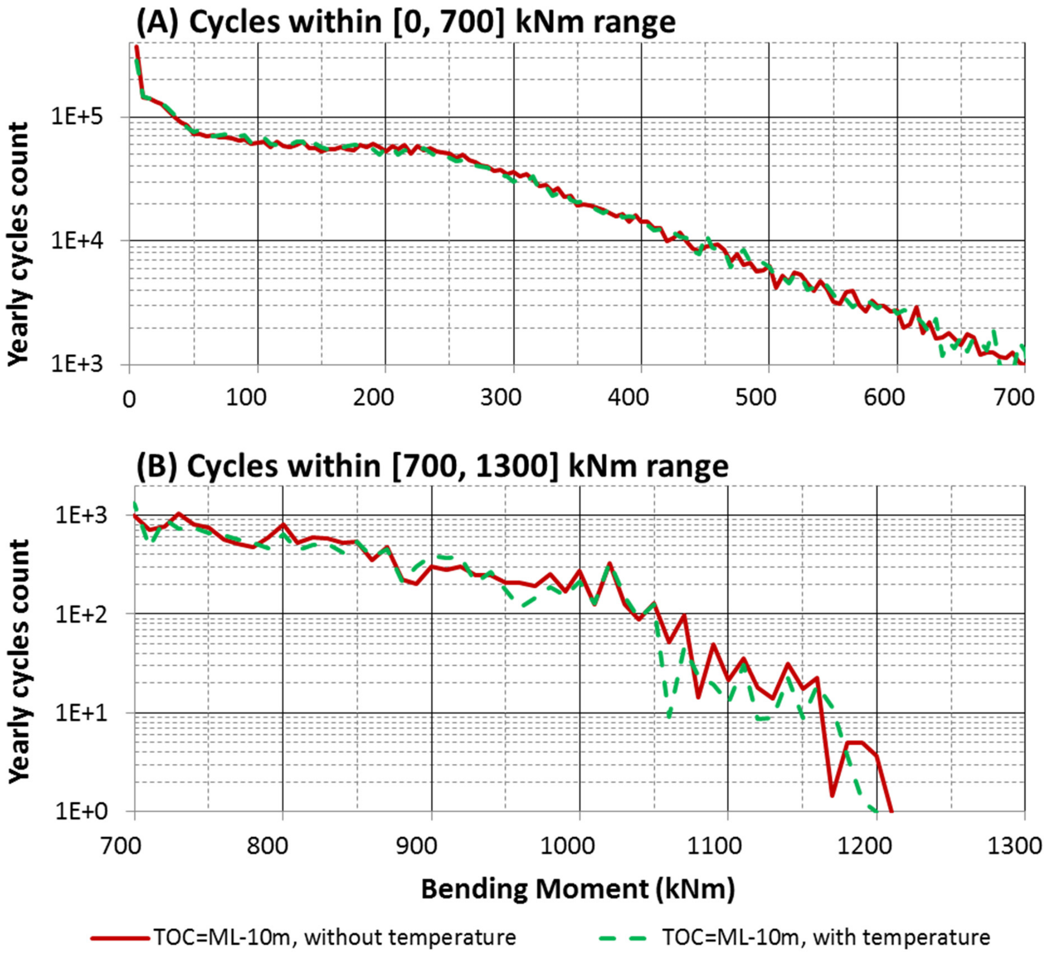

Figure C.3 – Comparison of long-term bending moment histograms. Global riser dynamic analyses with and without temperature. TOC=ML-10m.

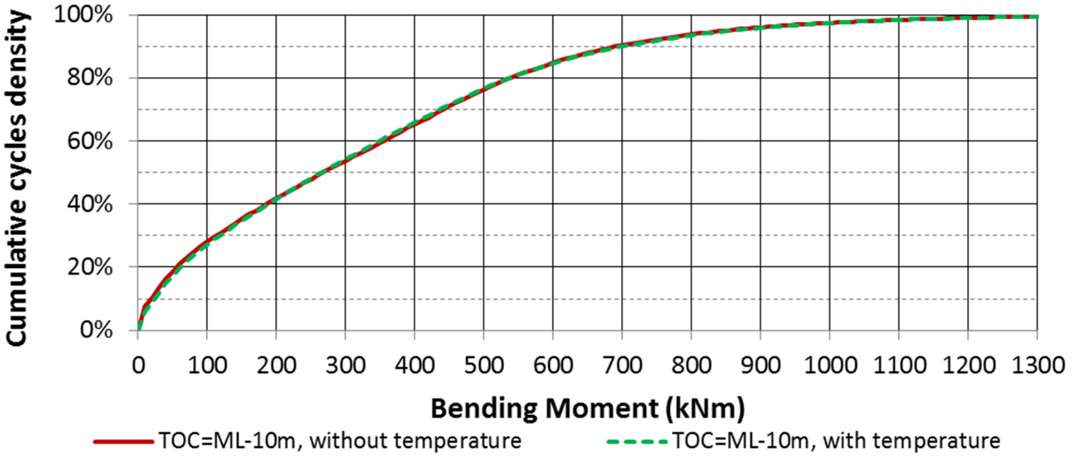

Figure C.4 – Cumulative cycle density comparison of long-term histograms presenting the indirect impact of the temperature distribution of the well. TOC=ML-10m.

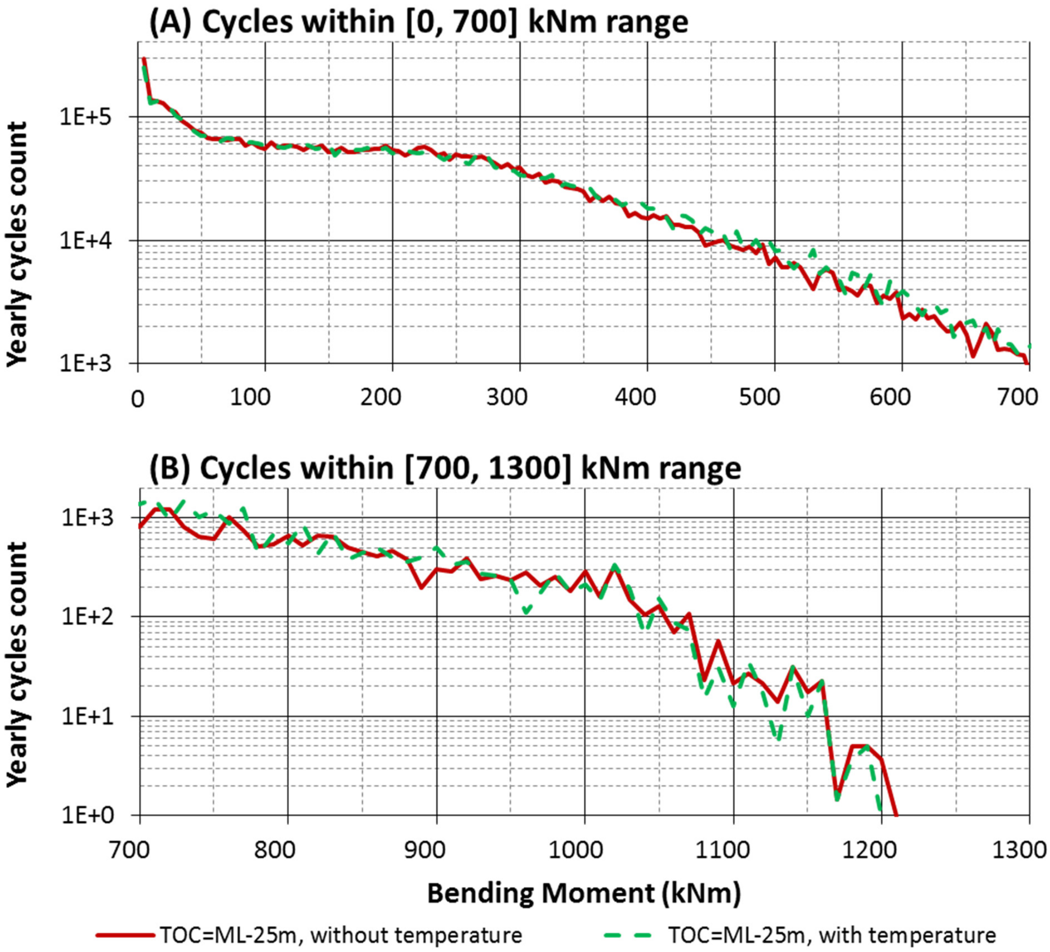

Figure C.5 – Comparison of long-term bending moment histograms. Global riser dynamic analyses with and without temperature. TOC=ML-25m.

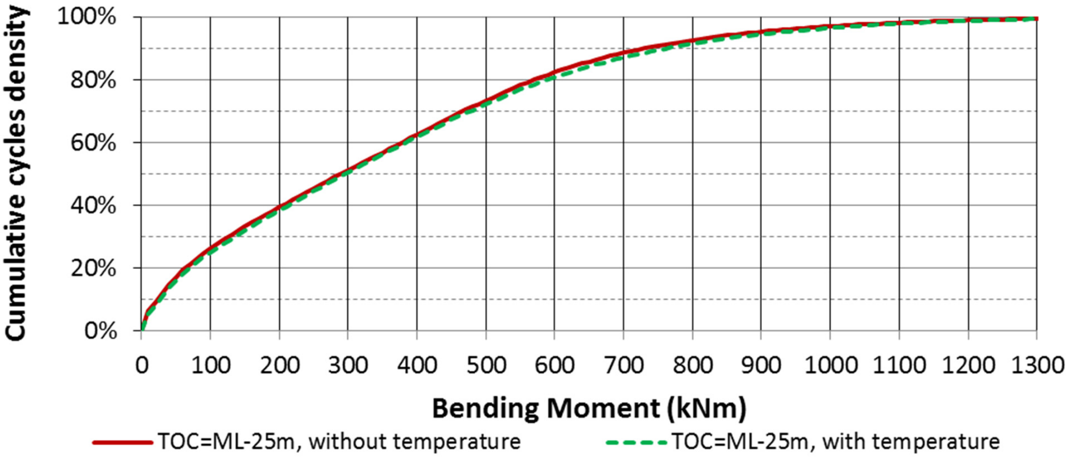

Figure C.6 – Cumulative cycle density comparison of long-term histograms presenting the indirect impact of the temperature distribution of the well. TOC=ML-25m.

C.2 Load-to-Stress Curves – Section 6.3.2

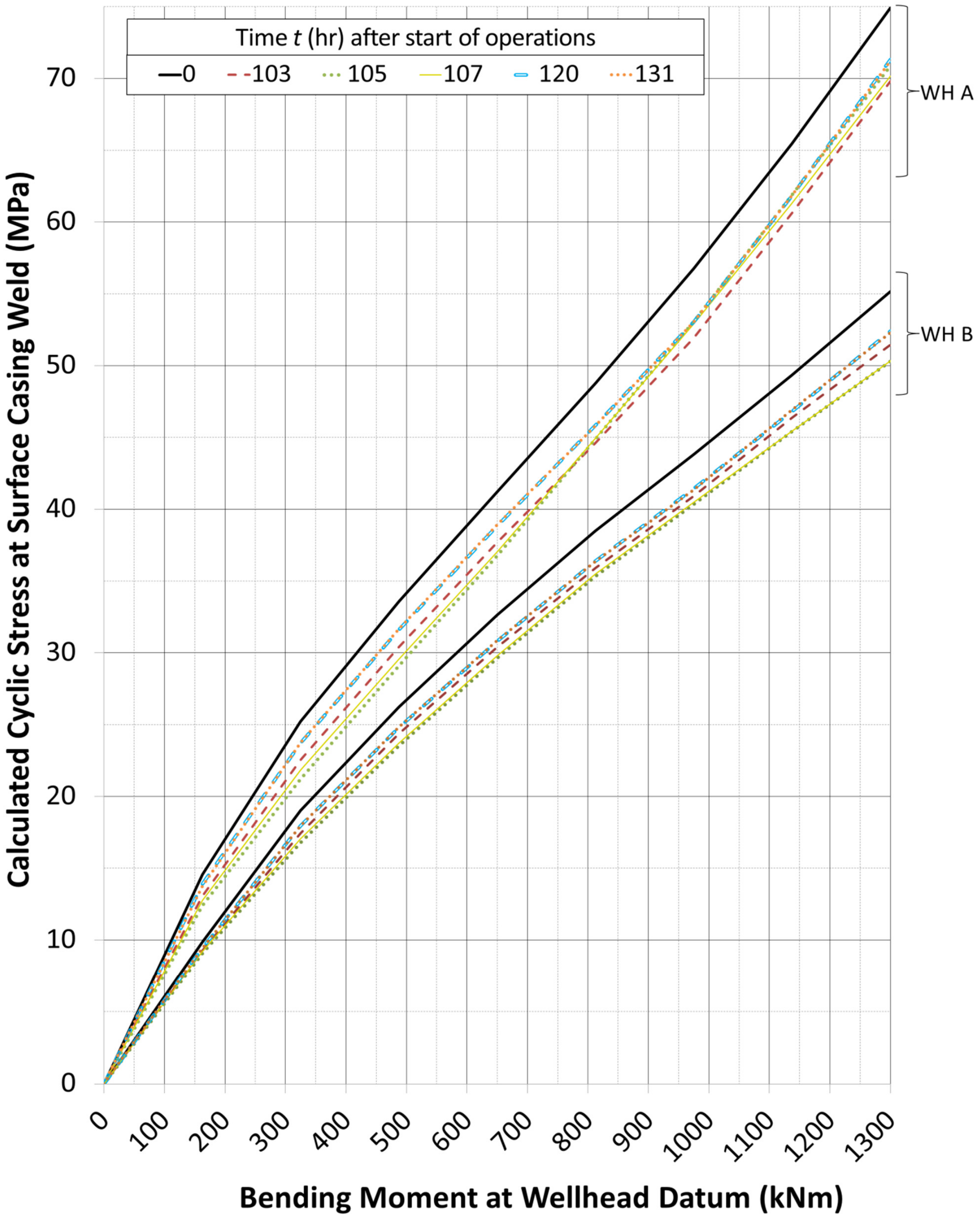

Figure C.7 – Load-to-stress curves generated for the welded connection between the high-pressure housing and the surface casing. Period [90,131 hr]. Results for *t*=0 hr represents the analysis without temperature of the mechanical configuration assumed by the wellhead during the period.

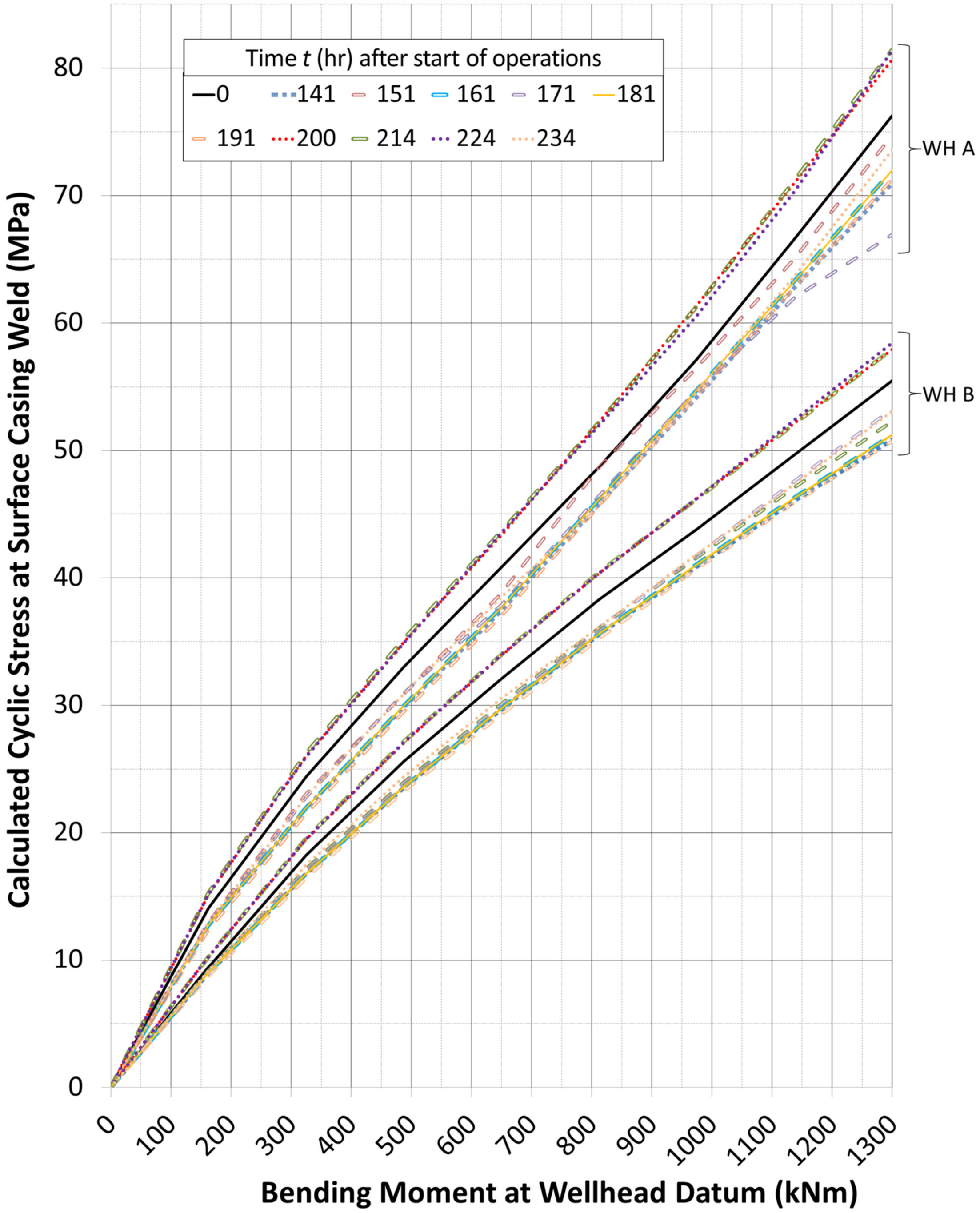

Figure C.8 –Load-to-stress curves generated for the welded connection between the high-pressure housing and the surface casing. Period [131, 234 hr]. Results for *t*=0 hr represents the analysis without temperature of the mechanical configuration assumed by the wellhead during the period.

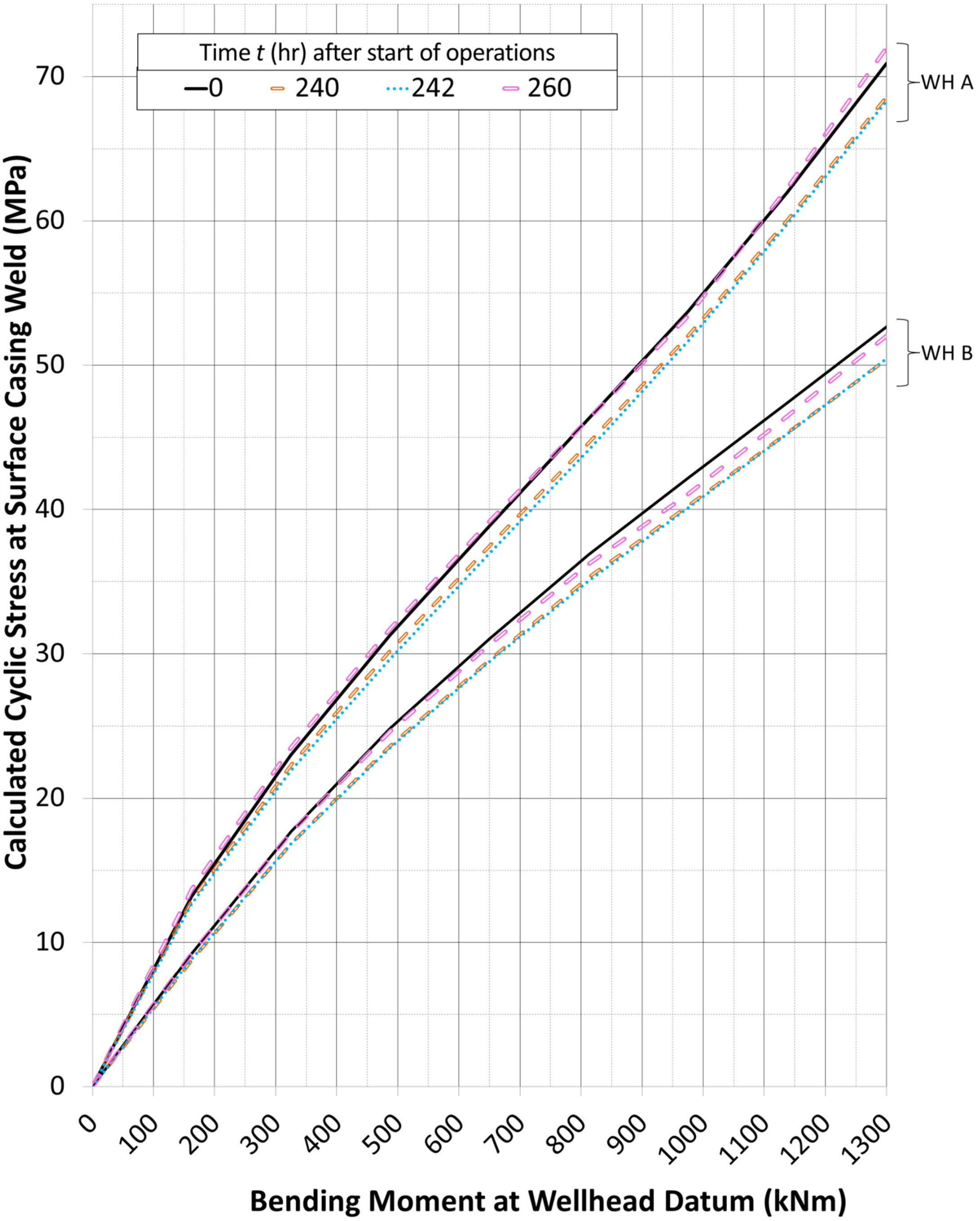

Figure C.9 – Load-to-stress curves generated for the welded connection between the high-pressure housing and the surface casing. Period [234, 260 hr]. Structural analysis without temperature of the mechanical configuration assumed by the wellhead is denoted by the curve *t*=0 hr.

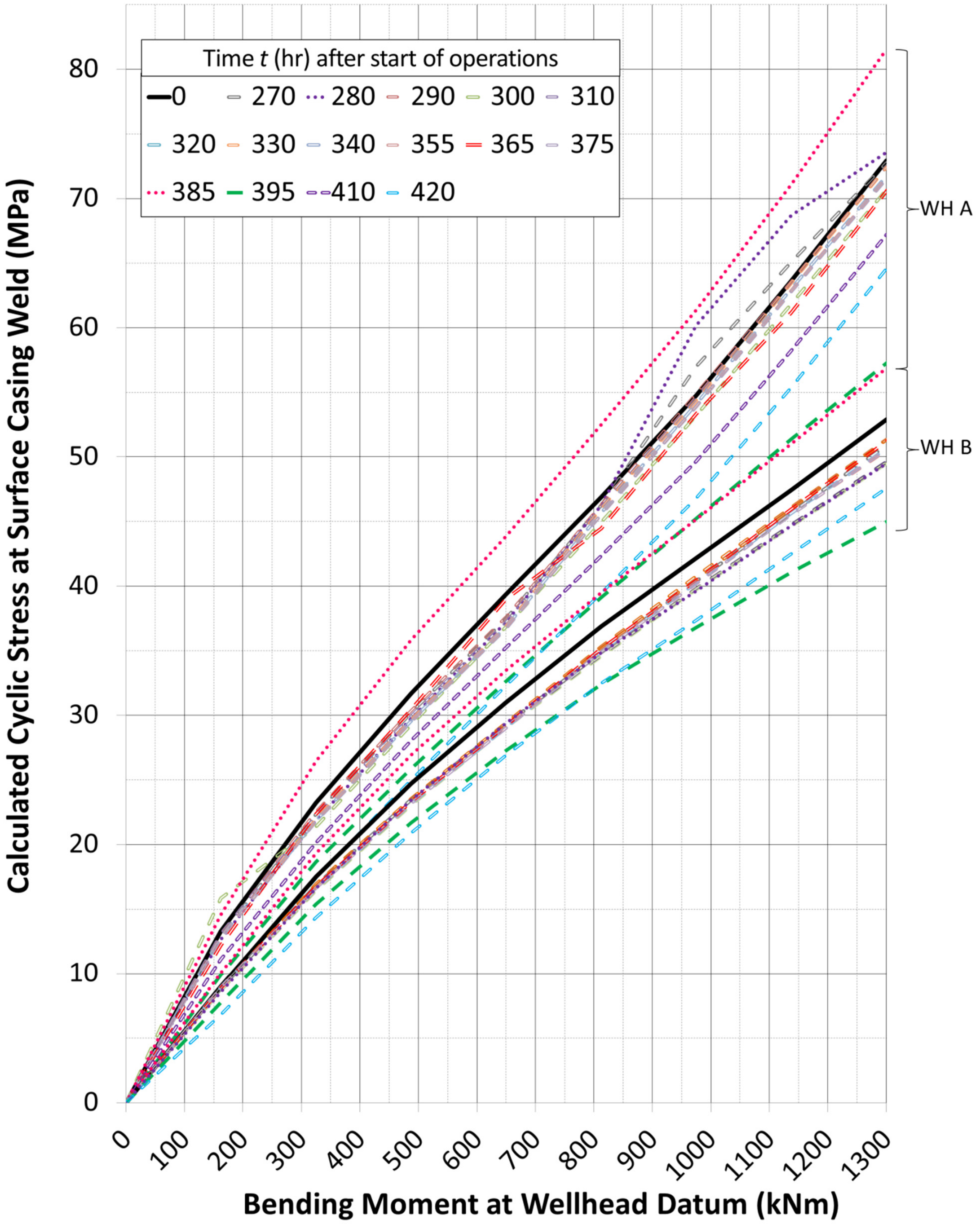

Figure C.10 – Load-to-stress curves generated for the welded connection between the high-pressure housing and the surface casing. Period [260, 420 hr]. Structural analysis without temperature of the mechanical configuration assumed by the wellhead is denoted by the curve *t*=0 hr.

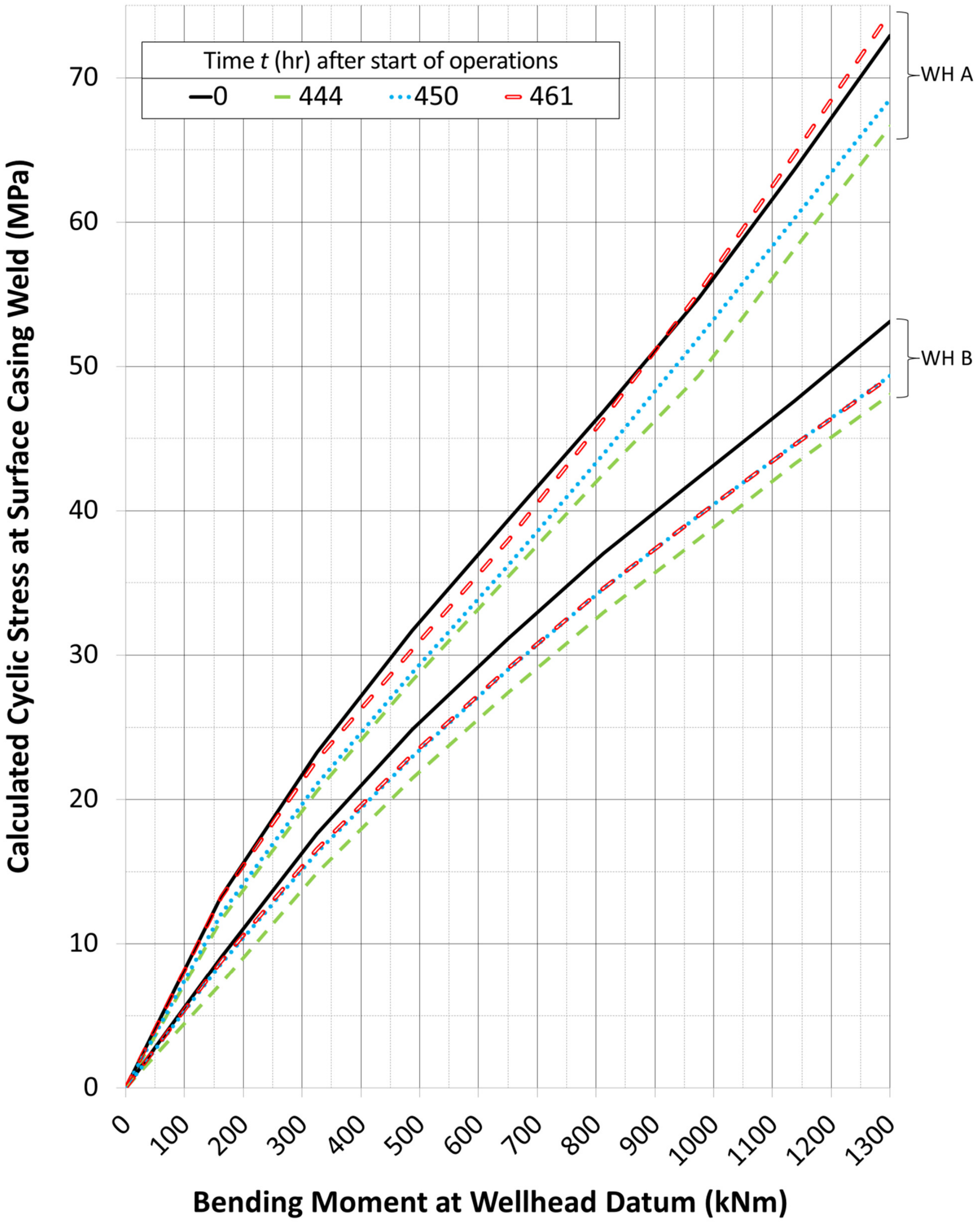

Figure C.11 – Load-to-stress curves generated for the welded connection between the high-pressure housing and the surface casing. Period [420, 462 hr]. Structural analysis without temperature of the mechanical configuration assumed by the wellhead is denoted by the curve *t*=0 hr.

C.3 Estimates of Accumulated Fatigue Damage – Section 6.3.3.1

C.3.1 Welded Connection Between the Surface Casing's First and Second Joints

Figure C.12 presents the accumulated fatigue-damage estimates for the welded connection between the first and second joints in the surface casing string. S-N curve F3 (Figure 5.17) was used for estimating the fatigue damage.

In contrast with the results obtained for *hot spot 1*, the fatigue-damage rates estimated by the analyses with temperature during the first mechanical configuration of the wellhead were either the least damaging (wellhead A) or at the same level of the damage rates estimated for the remaining of the operation (wellhead B), for this hot spot's life.

The fatigue-damage rates for both wellhead models reach their lowest values between the 5 and 50-hour marks.

At the 60-hour mark the well is no longer being drilled, but the drilling fluid is still being circulated. Since drilling ahead has stopped the well system is not increasing, and this fact changes how the heat within the system is being distributed, compared to the previous period, as there are no more thermally undisturbed rock formations being uncovered.

Overall, there is an increase in cyclic stresses on the welded connection between the first and second joints in the surface casing string, reflected on the apparent increase in fatigue-damage rates.

The next drastic change in fatigue-damage rates takes place at the 201 hours mark, when the fluid in the well has not been circulated for a while, and the drillstring is being retrieved. During this period the fatigue-damage rates estimated for both wellhead models reach their peak value.

Fatigue-damage rates reach a local minimum at the 280 hours mark, during drilling ahead, but soon reach a stable value. Later, at the 420 hours mark during the retrieval and deploying of strings in the well, the fatigue-damage rates reach another local minimum value.

Regarding the impact of the TOC, the trend in accumulated fatigue damage is reversed for this fatigue hot spot. The hot spot in wellhead B has the highest accumulated fatigue-damage estimates, 8.48% and 11.64% for the analyses with and without temperature, respectively. Corresponding estimates for wellhead A were 6.82% and 8.61%.

C.3.2 Welded Connection Between the Surface Casing's Second and Third Joints

Figure C.13 presents the accumulated fatigue-damage estimates for the welded connection between the second and third joints in the surface casing string. S-N curve F3 (Figure 5.11) was used for estimating the fatigue damage.

Like the previous fatigue hot spot, the fatigue damage estimates were not highly impacted by the TOC, as both wellhead models presented similar values for accumulated fatigue damage, between 0.05% and 0.09% of the design life.

Comparing the response of the two wellhead models, the fatigue-damage rate estimates followed the same trends during the simulated drilling operation, apart from the rates calculated during the 260-420 hours period. For most of this period, the damage rates obtained for wellhead A remained constant, while the corresponding rates obtained for wellhead B fluctuated.

C.3.3 Welded Connection Between the Low-Pressure Housing and the Conductor

Figure C.14 presents the accumulated fatigue-damage estimates for the welded connection between the low-pressure housing and the conductor. S-N curve F3 (Figure 5.11) was used for estimating the fatigue damage.

For this hot spot, estimates for accumulated fatigue damage were higher for wellhead B: 0.84% and 1.12% for the analyses with and without temperature, respectively. The corresponding estimates for wellhead A were 0.35% and 0.43%.

For both wellheads the estimated fatigue-damage rates reached considerably low values during the 20-70 hours period. However, at the 80 hours mark, when the 13⅜-in. casing is being run, the damage rates increase considerably.

For the remainder of wellhead A's simulated operations, damage rates remain between 0.0006% and 0.0009% of design-fatigue life per hour. For wellhead B, fatigue damages rates remain between 0.0018% and 0.0025%.

Wellhead A experiences a peak value in fatigue-damage rates at the 410 hours mark, during the running of the 7-in. liner. Wellhead B experiences a peak value in fatigue-damage rates at the 395 hours mark, during the retrieving of the drillstring.

C.3.4 Welded Connection Between the Conductor's First and Second Joints

Figure C.15 presents the accumulated fatigue-damage estimates for the welded connection between the first and second joints in the conductor string. S-N curve F3 (Figure 5.11) was used for estimating the fatigue damage.

For both wellheads models, fatigue-damage rates experience their maximum value during the first mechanical configuration assumed by the wellhead. However, damage rates given by the analyses with temperature considerably decrease after 20 hours of operation and remain lower than the rates predicted by the conventional fatigue analyses until the 200 hours mark is reached, when retrieving the drillstring and running the 9⅝-in. casing, fatigue-damage rates on this fatigue hot spot reach a peak value.

Following that, the fatigue-damage rates given by the analyses with temperature remain at a relatively constant value for most of the drilling operation, slightly above the damage rates given by the conventional analyses. The TOC level had a small impact on the final accumulated fatigue damage: for wellhead A the estimates were 4.18% and 4.46 with and without temperature, respectively. The corresponding estimates obtained for wellhead B were 4.33% and 4.58%.

C.3.5 Lock Ring

Figure C.16 presents the accumulated fatigue-damage estimates for the lock ring. S-N curve BM4 (Figure 5.11) was used for estimating the fatigue damage. Final accumulated fatigue-damage estimates are lower than 1.5% for wellhead B, and lower than 0.5% for wellhead A.

Except for the period that encompasses the first mechanical configuration of the wellhead, fatigue-damage rates estimated by the analyses with temperature remain close to damage rates estimated by the conventional analyses.

However, during the first mechanical configuration of the wellhead, analyses with temperature for wellhead A presents lower damages rates than those obtained for wellhead B, when compared to the corresponding damage rates given by the structural calculation without temperature.

C.3.6 Lower Edge in the High-Pressure Housing

Figure C.17 presents the accumulated fatigue-damage estimates for the identified lower edge in the high-pressure housing. S-N curve BM4 (Figure 5.11) was used for estimating the fatigue damage.

The TOC level has a small impact on the estimated fatigue damage of this hot spot. For wellhead A estimates were 0.33% and 0.46% of the design life, obtained by the analyses with and without temperature respectively. Corresponding estimates for wellhead B were 0.36% and 0.52%.

The analyses without temperature yielded the highest fatigue-damage rates for the mechanical configuration during which the 9⅝-in. casing is suspended from the wellhead. The analyses with temperature yielded the highest fatigue damage at the 410 hours mark, after the 9⅝-in. casing has been cemented, and during the running of the 7-in. liner.

Like analyses with and without temperature, the lowest fatigue-damage rates were obtained for the first mechanical configuration assumed by the wellhead.

C.3.7 Upper Edge in the High-Pressure Housing

Figure C.18 presents the accumulated fatigue-damage estimates for the identified upper edge in the high-pressure housing. S-N curve BM4 (Figure 5.11) was used for estimating the fatigue damage.

Accumulated fatigue damage estimated for this fatigue hot spot is considerably higher when compared with the previous hot spot, despite both being located quite close to each other.

The TOC level has little impact in accumulated fatigue damage. For wellhead A, estimates were 1.28% and 1.59% of the design life, for the analyses with and without temperature, respectively. Corresponding estimates for wellhead B were 1.31% and 1.64%.

Like the previous fatigue hot spot, the analyses without temperature yielded the highest fatigue-damage rates when the 9⅝-in. casing was suspended from the wellhead, while the analyses with temperature yielded the highest fatigue damage after the 9⅝-in. casing had been cemented, during the running of the 7-in. liner.

The lowest fatigue-damage rates were obtained when the wellhead assumed its first mechanical configuration.

C.3.8 Lower Edge in the Low-Pressure Housing

Figure C.19 presents the accumulated fatigue-damage estimates for the location identified as the lower edge in the low-pressure housing. S-N curve BM4 (Figure 5.11) was used for estimating the fatigue damage. Final accumulated fatigue-damage estimates were considerably low for both wellhead models; lower than 0.05% of design life.

Most noticeable difference in the response of the wellheads is that the thermal fatigue-damage rates of wellhead B remained considerably lower than those given by the conventional analyses, which explains the larger difference between accumulated fatigue-damage estimates for wellhead B with and without temperature, when compared with the difference between the estimates obtained for wellhead.

C.3.9 Landing Surface on Low-Pressure Housing

Figure C.20 presents the accumulated fatigue-damage estimates for the landing surface on the low-pressure housing. S-N curve BM4 (Figure 5.11) was used to estimate the fatigue damage.

Fatigue-damage rates estimated for this hot spot, with and without temperature, reach their lowest value during the first mechanical configuration of the wellhead.

Damage rates estimates for the subsequent mechanical configurations remain at a higher, relatively stable level, just below the damage rates predicted by the corresponding structural calculations without temperature.

Overall, the inclusion of temperature led to significantly lower accumulated fatigue-damage estimates. For wellhead A, estimates were 7.26% and 8.20% for the analyses with and without temperature, respectively. The corresponding estimates for wellhead B were 11.43% and 12.75%.

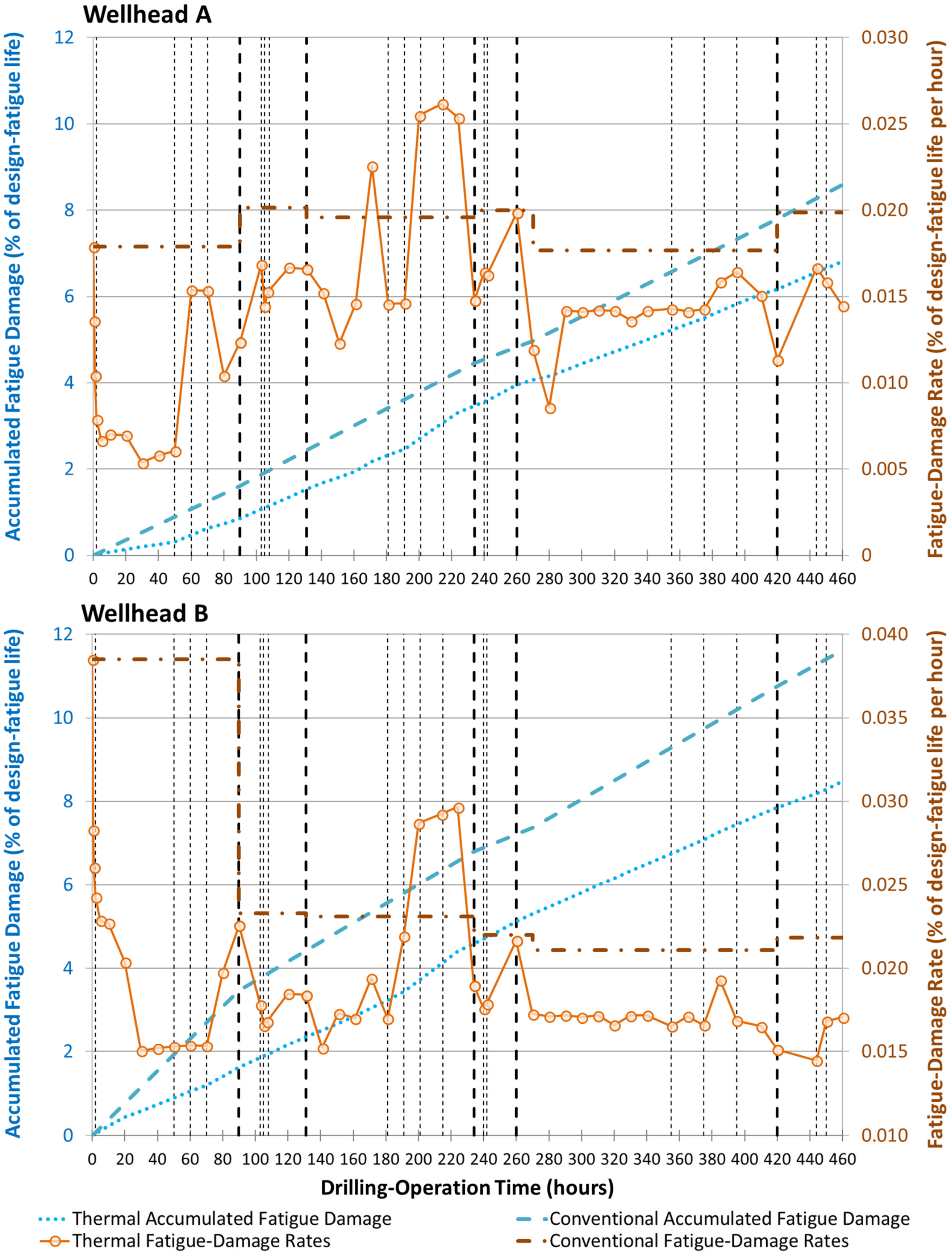

Figure C.12 – Accumulated fatigue-damage estimates for the welded connection between the 1st and 2nd joints in the surface casing during drilling. Wellheads A and B. DFF=10. S-N curve F3.

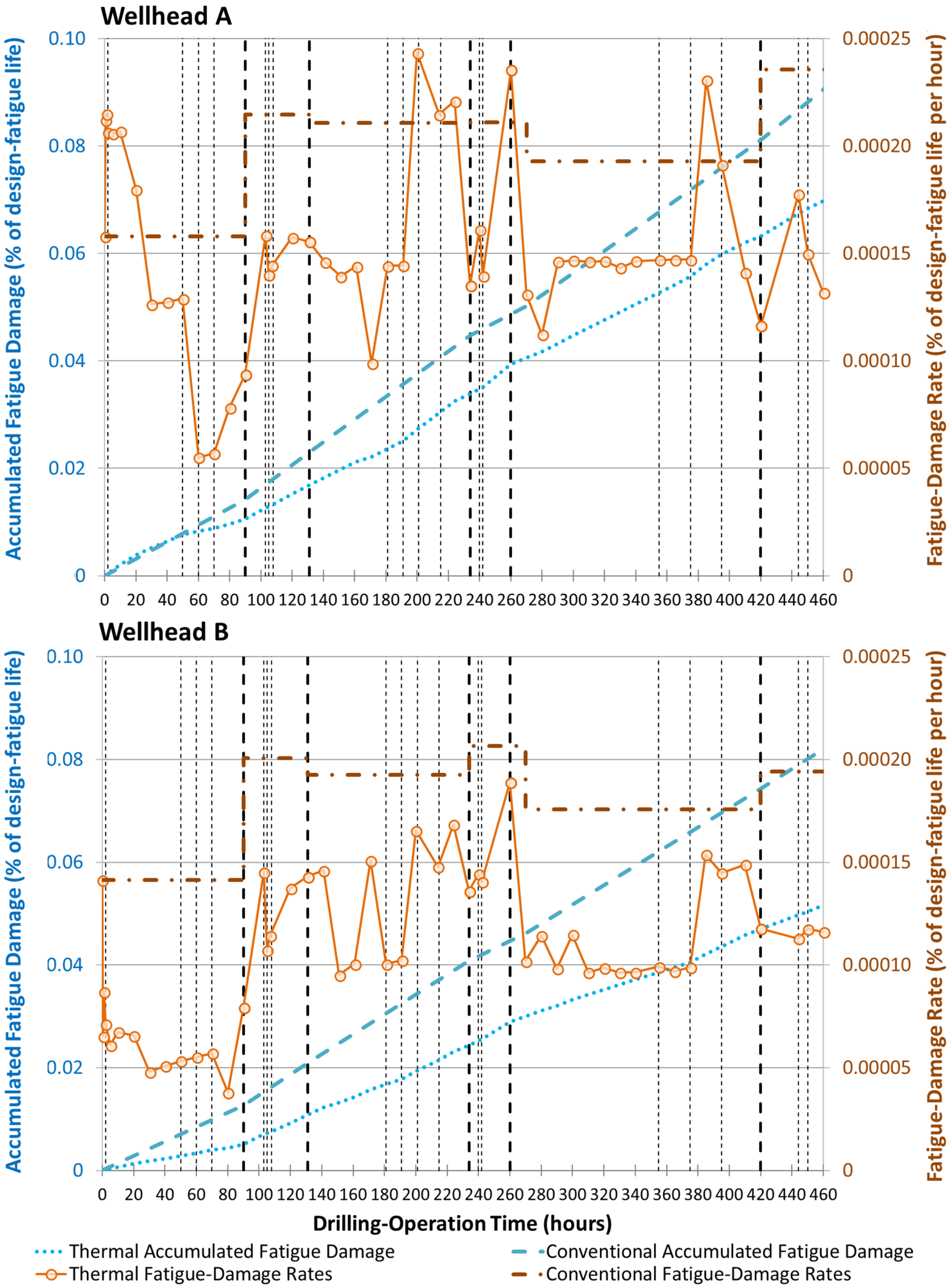

Figure C.13 – Accumulated fatigue-damage estimates for the welded connection between the 2nd and 3rd joints in the surface casing during drilling. Wellheads A and B. DFF=10. S-N curve F3.

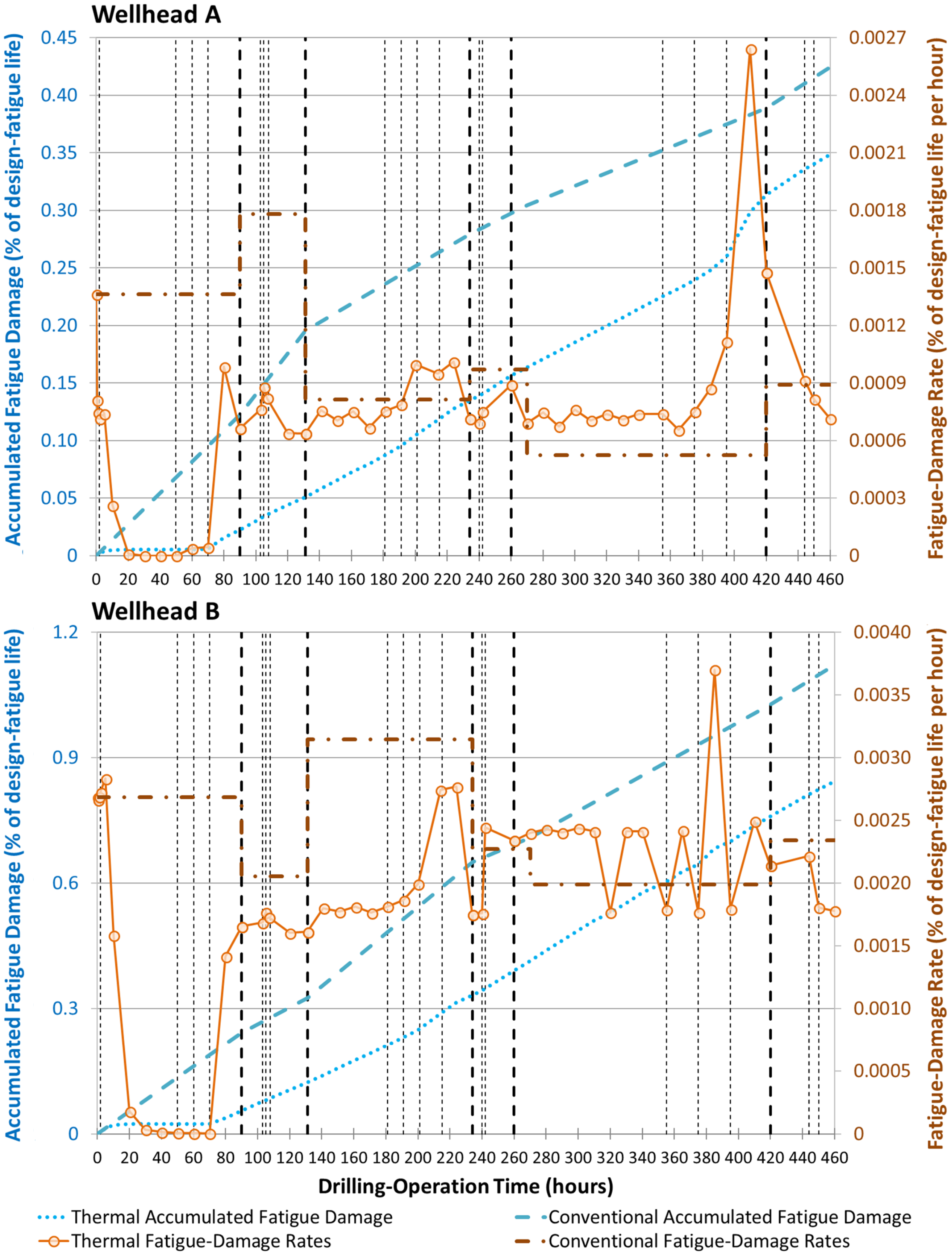

Figure C.14 – Accumulated fatigue-damage estimates for the welded connection between low-pressure housing and conductor during drilling. Wellheads A and B. DFF=10. S-N curve F3.

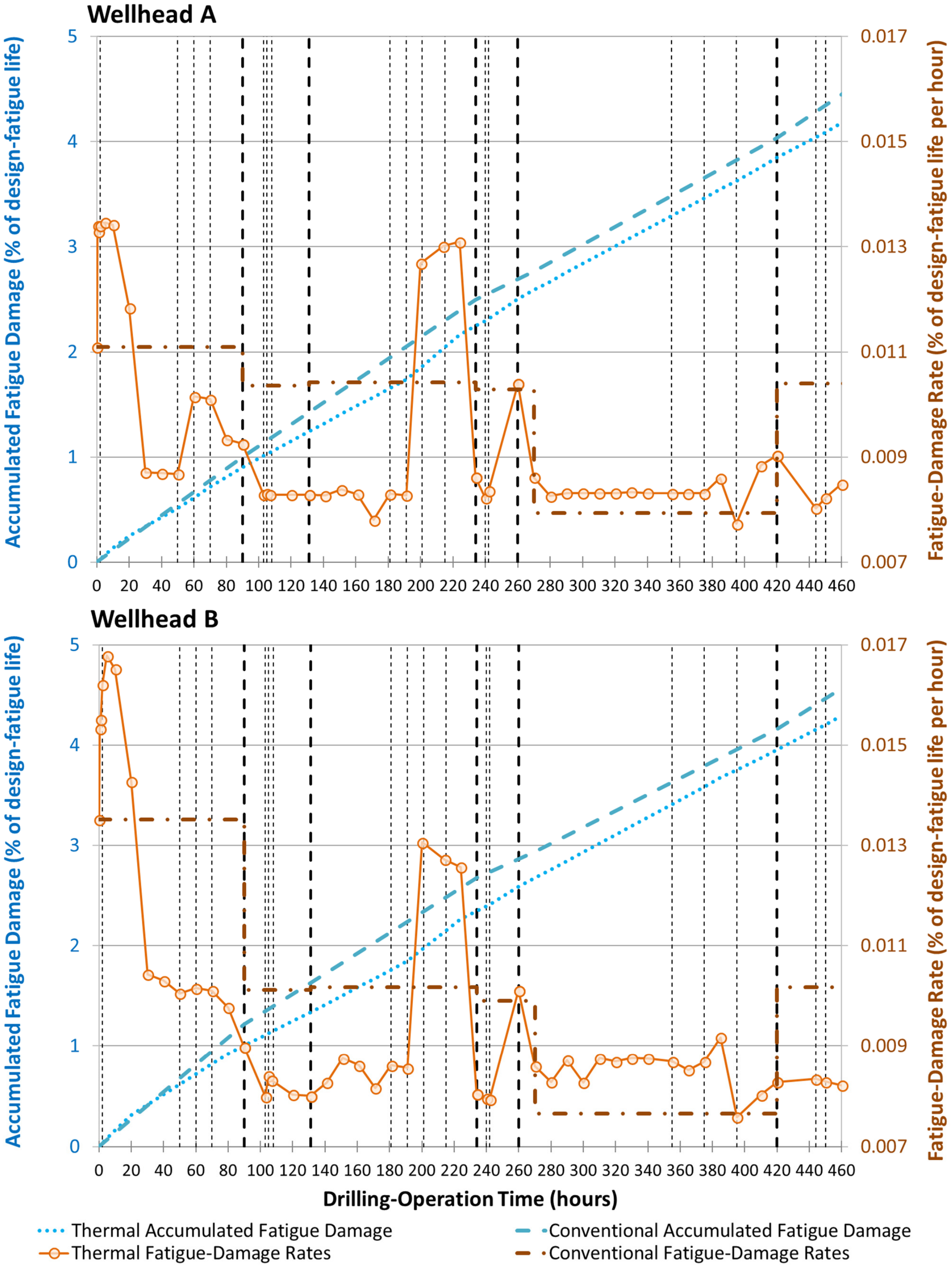

Figure C.15– Accumulated fatigue-damage estimates for the welded connection between the 1st and the 2nd joints in the conductor during drilling. Wellheads A and B. DFF=10. S-N curve F3.

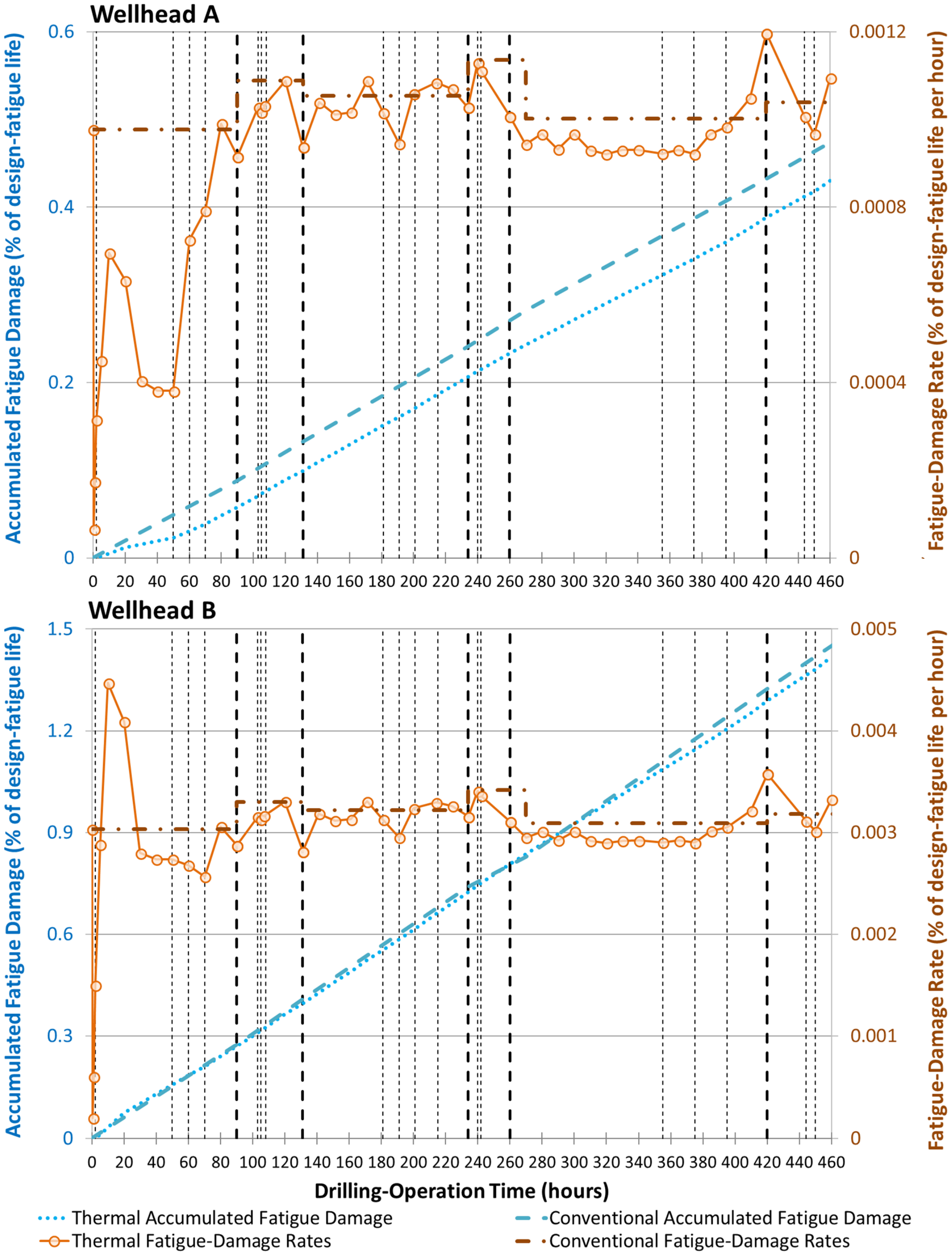

Figure C.16 – Accumulated fatigue-damage estimates for the lock ring during drilling. Wellheads A and B. DFF=10. S-N curve BM4.

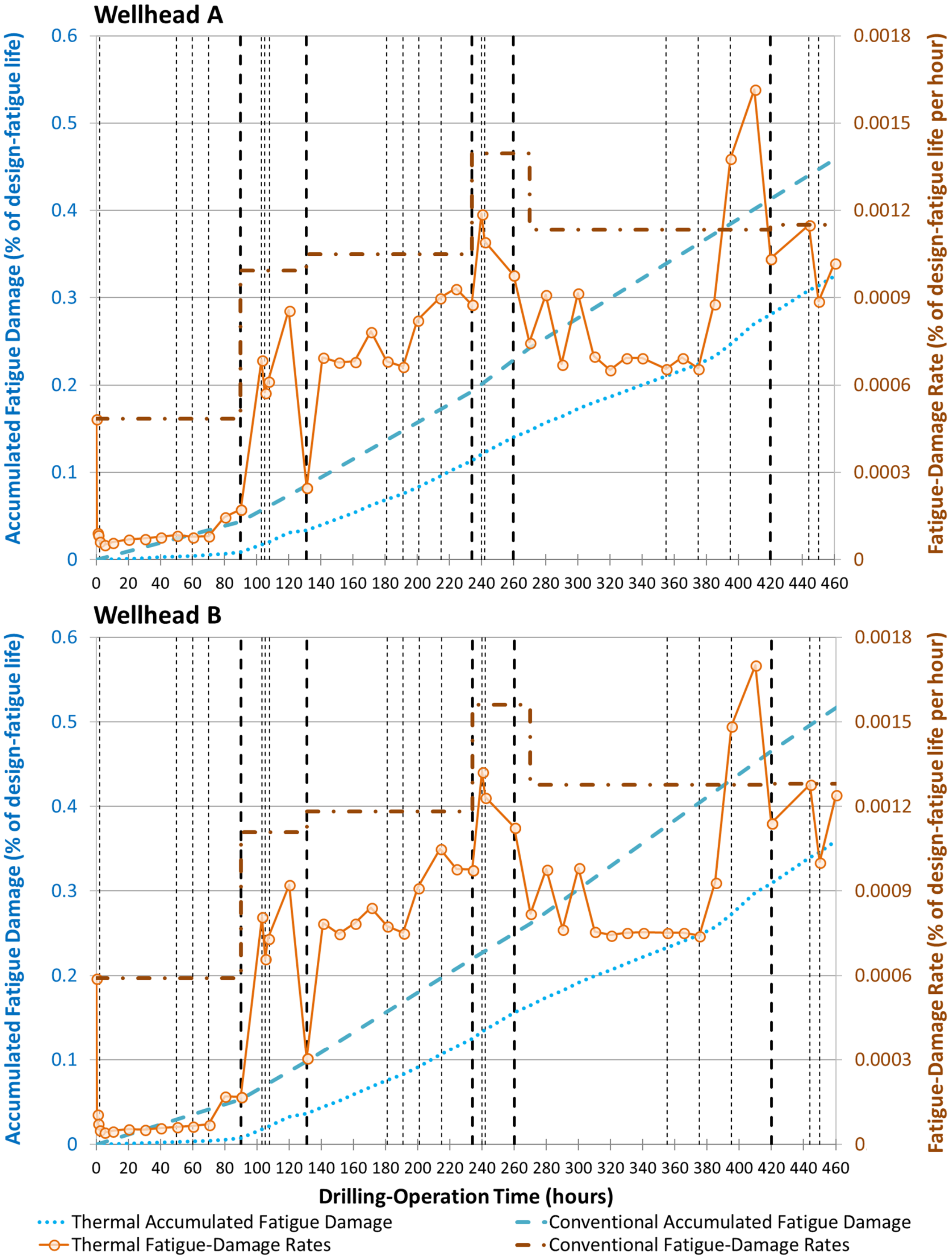

Figure C.17 – Accumulated fatigue-damage estimates for the lower edge on the high-pressure housing during drilling. Wellheads A and B. DFF=10. S-N curve BM4.

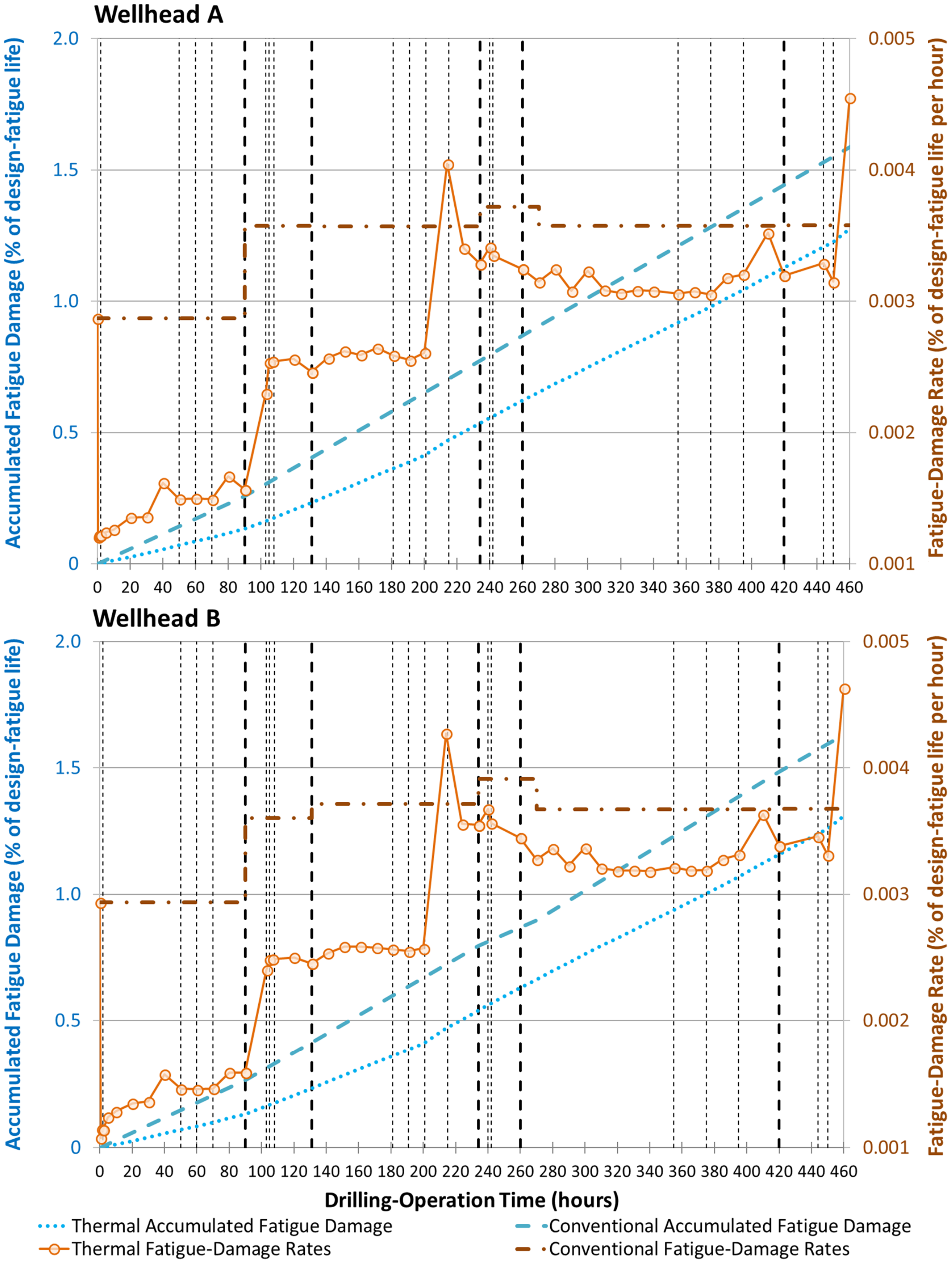

Figure C.18 – Accumulated fatigue-damage estimates for the upper edge on the high-pressure housing during drilling. Wellheads A and B. DFF=10. S-N curve BM4.

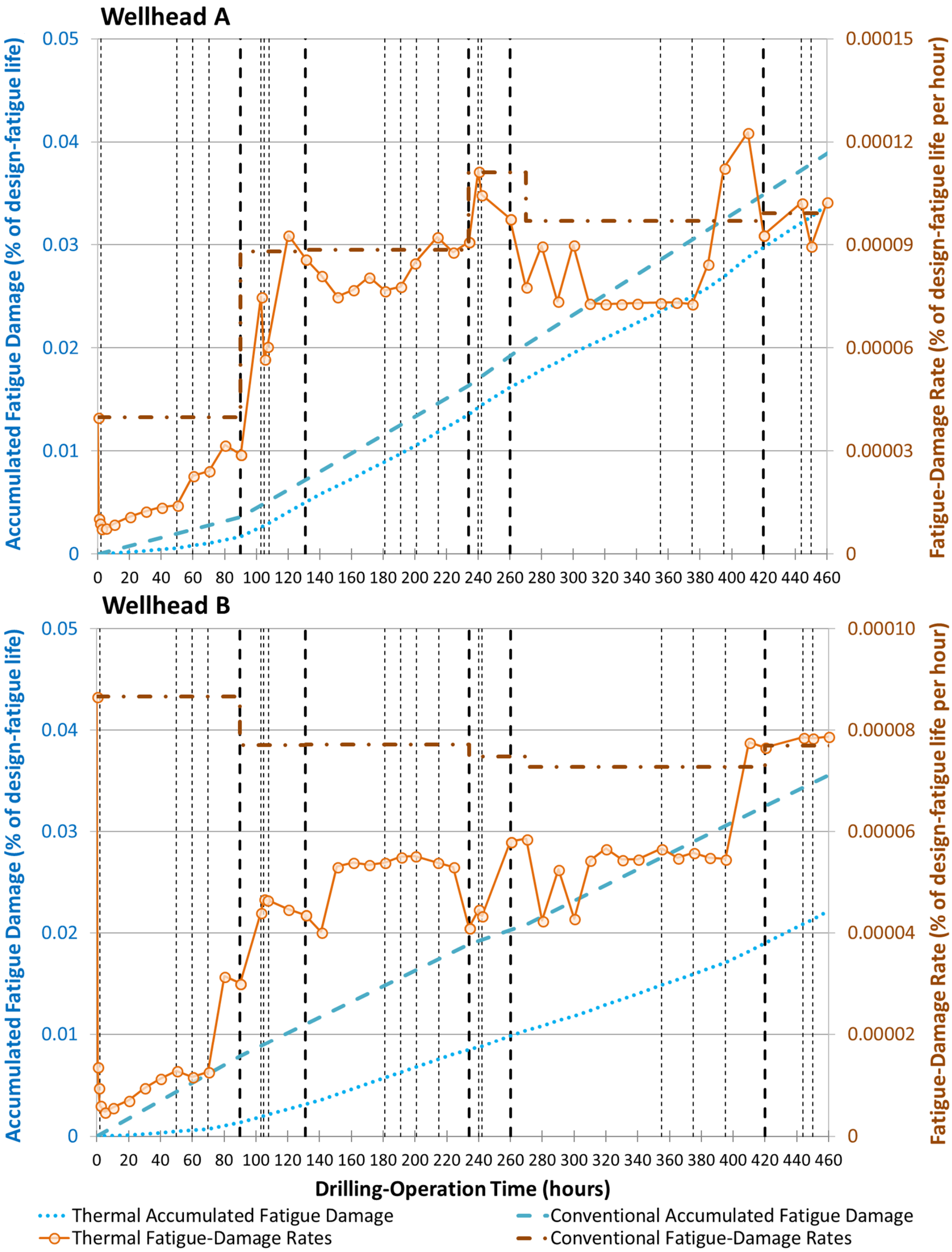

Figure C.19 – Accumulated fatigue-damage estimates for the lower edge on the low-pressure housing during drilling. Wellheads A and B. DFF=10. S-N curve BM4.

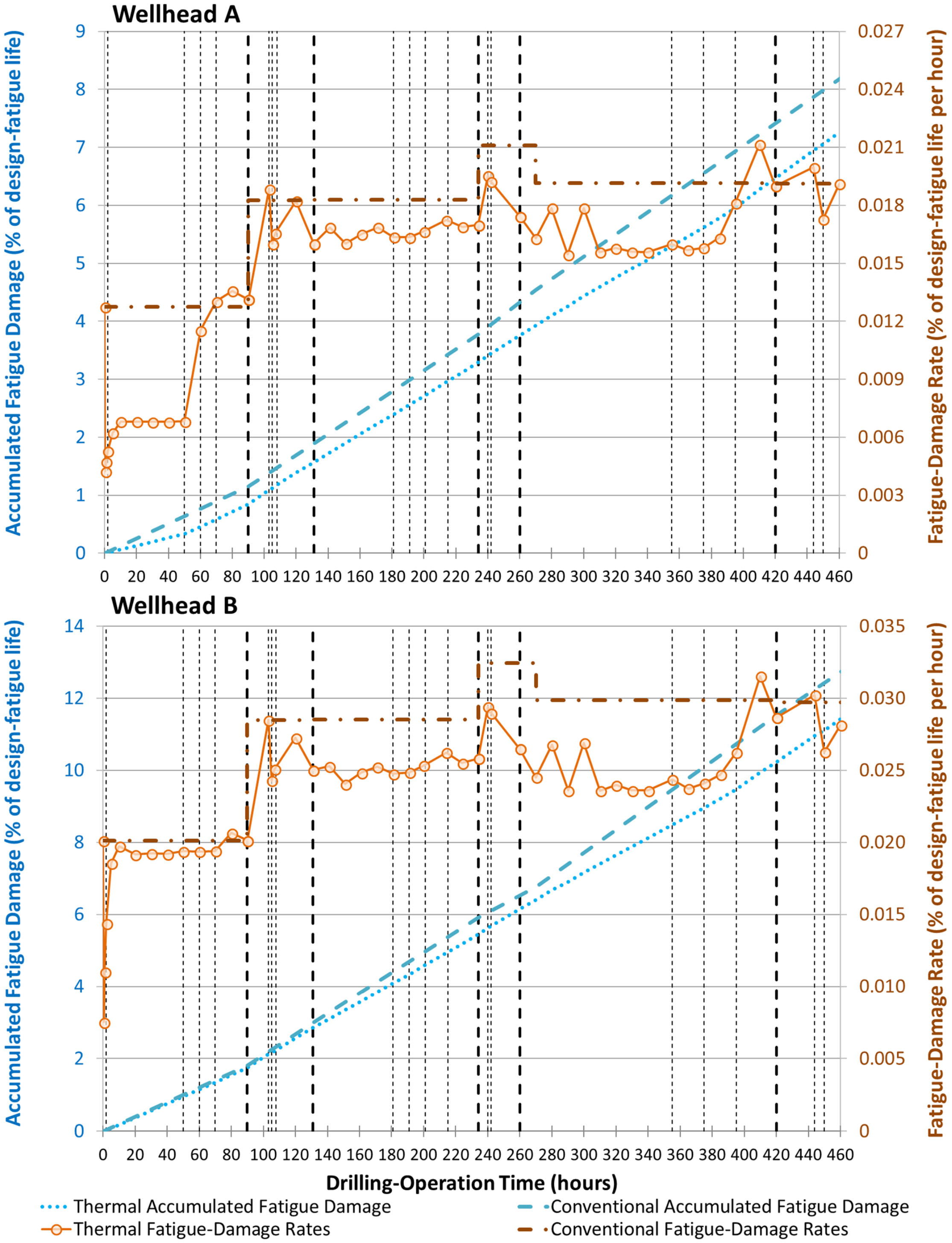

Figure C.20 – Accumulated fatigue-damage estimates for the lower-pressure housing landing surface during drilling. Wellheads A and B. DFF=10. S-N curve BM4.

C.4 Normalized Fatigue-Damage Rates – Sections 7.3.1, 7.3.2 and 7.3.3

C.4.1 Welded Connection between High-Pressure Housing and Surface Casing

Figure C.21 presents the normalized fatigue-damage rates plotted against R_{exp}, for the structural analyses performed for wellheads A and B during the period 90-141 hours (*i.e.* the second mechanical configuration assumed by the wellhead models, during which the 13⅜-in. casing is suspended from the wellhead).

The well operations simulated during this mechanical configuration did not enable to determine for which values of R_{exp}, or under which temperature scenarios, the baseline damage rate might be surpassed. Within the range of values assumed by R_{exp}, [0.75-0.85] and [1.3-1.6], the analyses with temperature predicted lower cyclic stresses, and therefore lower fatigue-damage rates.

For wellhead A, the fatigue-damage rates predicted by the analyses with temperature were between 70 and 80% of the damage predicted by the analysis without temperature. For wellhead B, the fatigue-damage rates predicted by the analyses with temperature were between 65 and 80% of the damage predicted by the analysis without temperature.

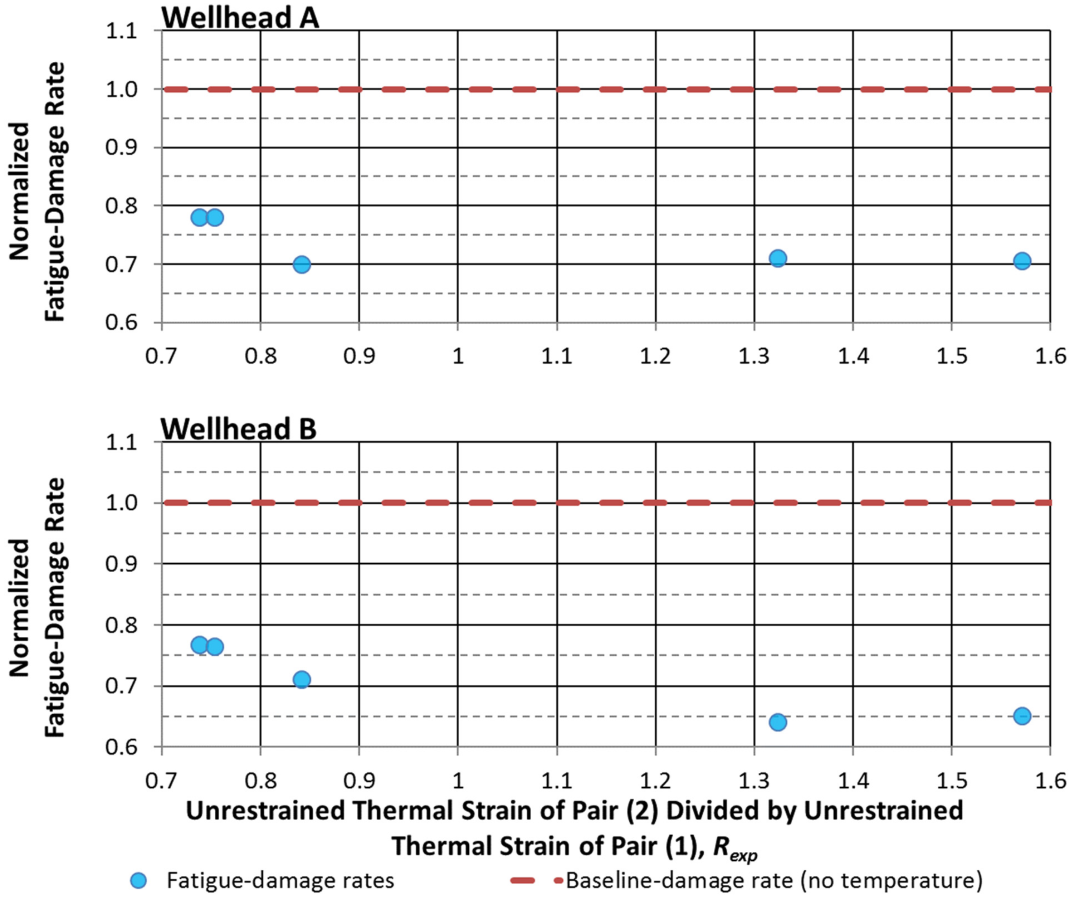

Figure C.21 – Fatigue-damage rates plotted against R_{exp}. *Hot spot 1*. 2nd mechanical configuration assumed by the wellhead model during drilling. DFF=10. S-N curve F.

Figure C.22 presents the normalized fatigue-damage rates plotted against R_{exp}, for the structural analyses performed for wellheads A and B during the period 141-241 hours (*i.e.* the third mechanical configuration assumed by the wellhead models, during which 13⅜-in. casing has been cemented in place).

For R_{exp} approaching 1.02, it has been estimated that the damage rate for both wellheads would be 80% of the baseline value. However, this single result makes it difficult to discern a trend. Conversely, the results for the fatigue-damage rates obtained for R_{exp} between 1.05 and 1.25 indicate that, within that range, the damage rates for both wellheads would between 20 and 30% higher than the baseline value.

For R_{exp} within the range [1.4, 1.55], the behavior predicted for each wellhead differs. For wellhead A the damage rates are predicted to be mostly between 70 and 80% of the baseline value, with an increase to 90% for R_{exp} approaching 1.55.

The results yielded for wellhead B indicate that that fatigue-damage rates predicated by the analyses with temperature would be between 65 and 80% of the baseline value.

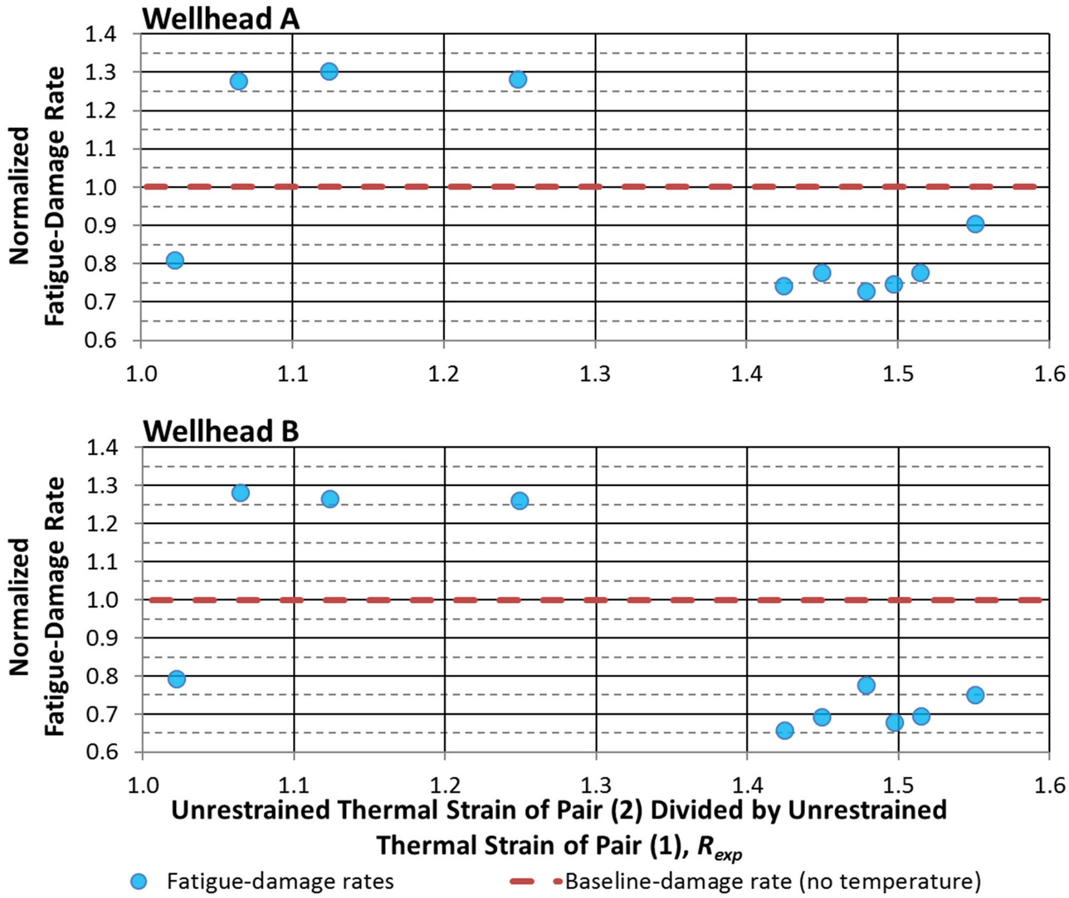

Figure C.22 – Fatigue-damage rates plotted against R_{exp}. *Hot spot 1*. 3rd mechanical configuration assumed by the wellhead model during drilling. DFF=10. S-N curve F.

Figure C.23 presents the normalized damage rates plotted against R_{exp}, for the structural analyses performed for wellheads A and B during the period 241-270 hours (*i.e.* the fourth mechanical configuration assumed by the wellhead models, during which the 9⅝-in. casing is suspended from the wellhead).

The set of calculations carried out for this mechanical configuration, together with the short range of R_{exp}, did not enable to identify any broad trends. But, it can be seen a significant change in behavior when compared the responses of wellheads A and B, since wellhead A may experience fatigue-damage rates higher than the baseline value.

The lowest normalized fatigue-damage rates have been predicted for wellhead B, approximately 79% of the baseline value. For wellhead A, the available results predict that damage rates might be as low as 84% of the baseline value.

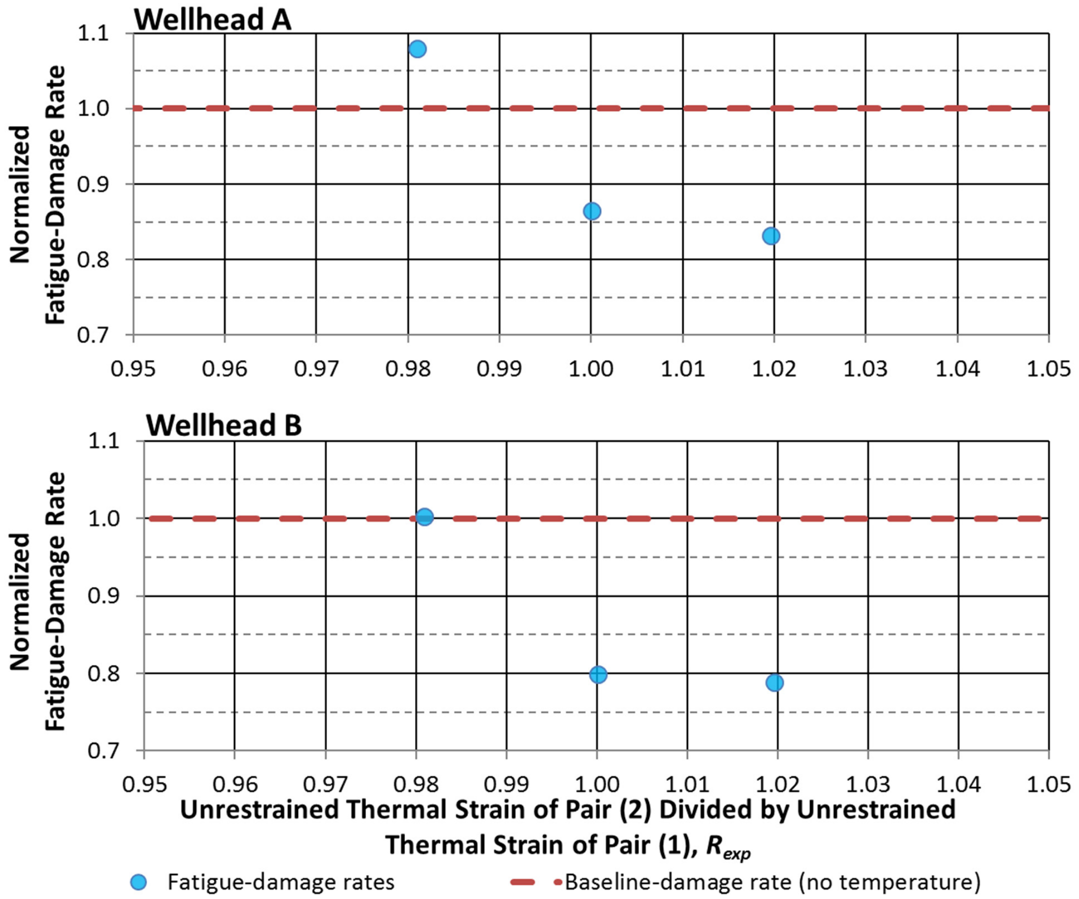

Figure C.23 – Fatigue-damage rates plotted against R_{exp}. *Hot spot 1*. 4th mechanical configuration assumed by the wellhead model during drilling. DFF=10. S-N curve F.

Figure C.24 presents the normalized damage rates plotted against R_{exp}, for the structural analyses performed for wellheads A and B during the period 270-444 hours (*i.e.* the fifth mechanical configuration assumed by the wellhead models, during which the 9⅝-in. casing has been cemented in place).

Four regions may be discerned in Figure C.24. For values of R_{exp} between the range [0.3, 0.4] or approaching 1.15, the predicted fatigue-damage rate is smaller than the corresponding baseline values. Unlike the previous results in previous figures, for this range wellhead B experiences the least reduction in damage rate.

For values of R_{exp} approaching 1.25, the trend reverses. Both wellheads may experience damage rates higher than the respective baseline values. The results gathered around R_{exp}=1.45 indicate that wellhead B may experience damage rates between 79 and 91% of the baseline value.

Within the 1.4-1.5 R_{exp} range, there might be temperature scenarios under which wellhead A may experience fatigue-damage rates up to 10% higher than the baseline value.

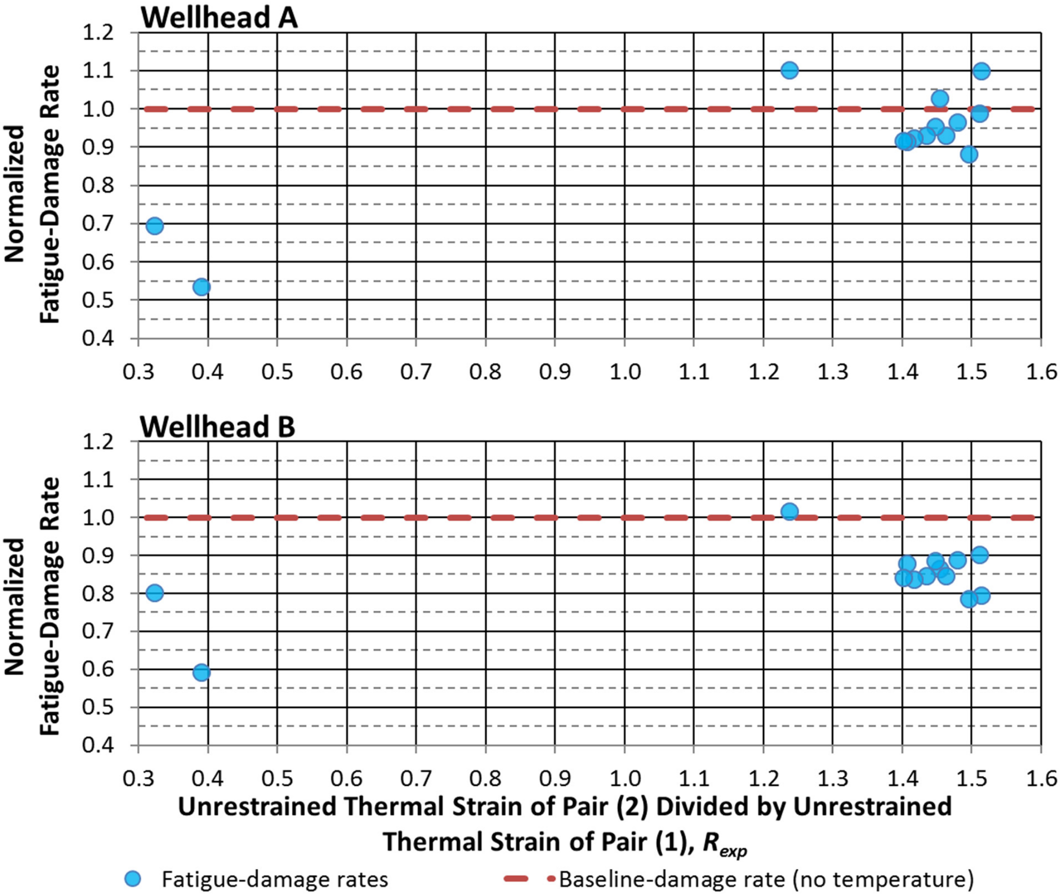

Figure C.24 – Fatigue-damage rates plotted against R_{exp}. *Hot spot 1*. 5th mechanical configuration assumed by the wellhead model during drilling. DFF=10. S-N curve F.

Figure C.25 presents the normalized fatigue-damage rates plotted against R_{exp}, for the structural analyses performed for wellheads A and B during the period 444-460 hours (*i.e.* the sixth mechanical configuration assumed by the wellhead models, during which the 7-in. liner is suspended from the 9⅝-in. casing).

Like Figure C.23, the set of structural results makes it difficult to identify any broad trends in Figure C.25. The results of the analyses with temperature could predict that of the two wellheads, wellhead B may experience the largest reduction in normalized fatigue-damage rate: between 58 and 71% of the baseline value.

Figure C.25 indicate that wellhead A may experience a significant increase in fatigue damage when subject to well-temperature distributions for which R_{exp} approaches 1.

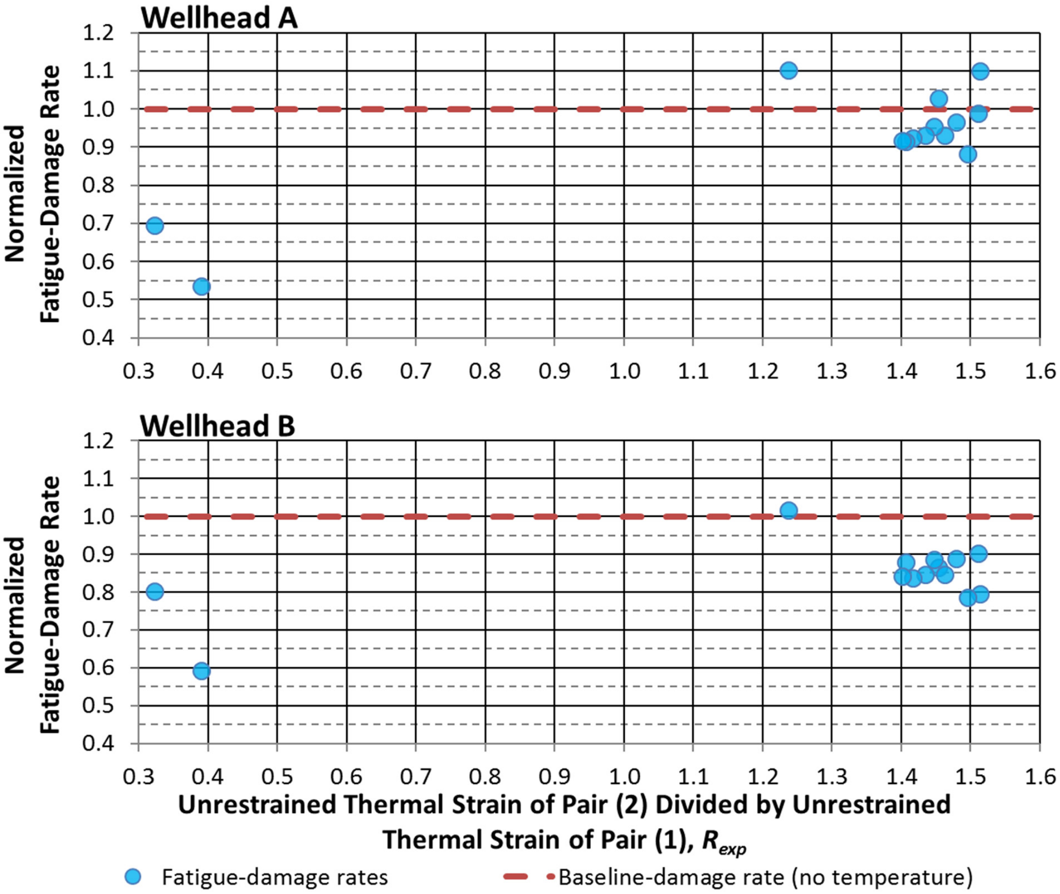

Figure C.25 – Fatigue-damage rates plotted R_{exp}. *Hot spot 1*. 6th mechanical configuration assumed by the wellhead model during drilling. DFF=10. S-N curve F.

Figure C.26 presents the normalized estimated fatigue-damage rates plotted against R_{exp}, for the structural analyses performed for wellheads A and B during the simulated workover operation. For the workover operation the wellhead configuration is like that of the fifth mechanical configuration assumed during drilling. However, the subsea stack and riser model is different (Figure 6.3)

The temperature distributions predicted during the workover operations did not lead to damage rates higher than the baseline value, for either wellhead model.

Under the temperature scenarios predicted, the calculated reduction in normalized fatigue-damage rates is considerably smaller for wellhead B; damage rates remain mostly between 90 and 96% of the baseline value. For wellhead A, normalized damage rates remain mostly between 72 and 80% of the baseline value.

The outlier displayed at R_{exp} approaching 0.66 corresponds to the analyses performed at t=30 hours. Similar response is displayed in Figure 6.9, which shows the fatigue-damage rate at different moments during the drilling operation.

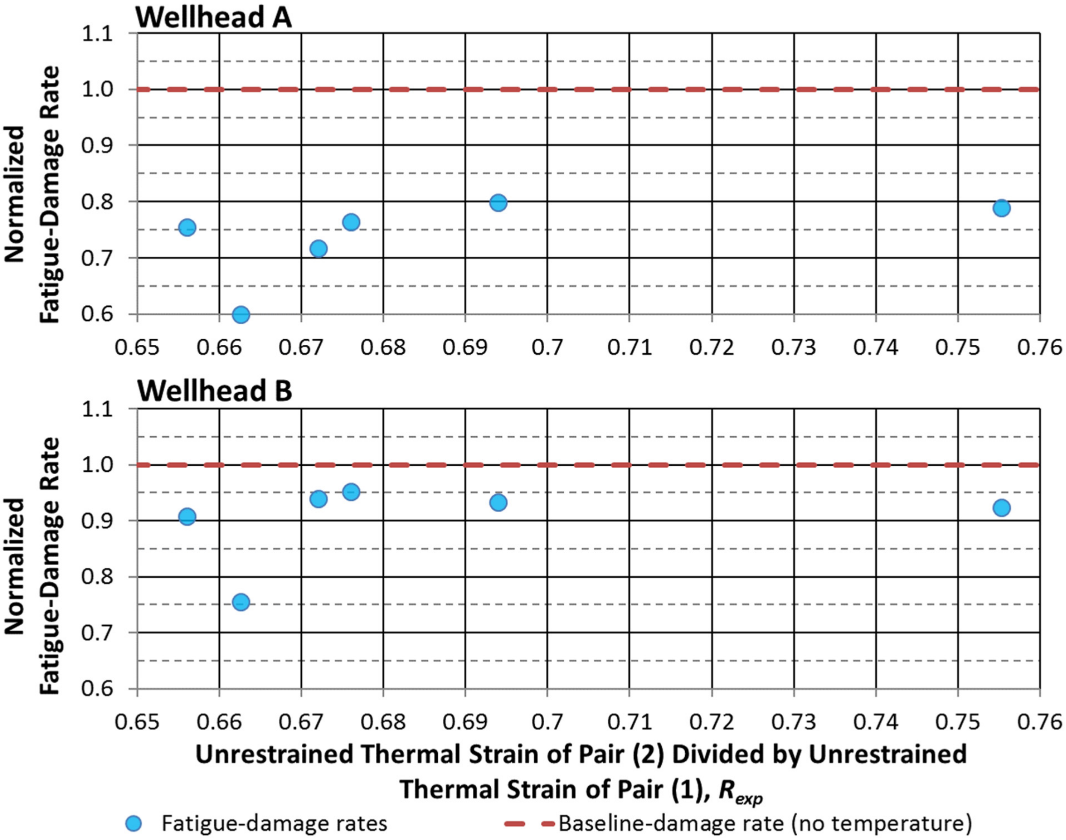

Figure C.26 – Fatigue-damage rates plotted R_{exp}. *Hot spot 1*. Mechanical configuration assumed by the wellhead model during workover. DFF=10. S-N curve F.

C.4.2 Welded Connection between the Surface Casing's First and Second Joints

Figure C.27 presents the normalized damage rates plotted against R_{exp}, for the structural analyses performed for wellheads A and B during the second mechanical configuration assumed by the wellhead models during the drilling operation.

The analyses with temperature have predicted a similar behavior for both wellheads. However, for R_{exp} within the range [0.75-0-85] it could be expected for fatigue-damage rates in wellhead B to undergo a larger reduction in value, approaching 75% of the baseline value, while the damage rates in wellhead A may decrease down to 82% of the respective baseline value.

There is a considerable distance, [0.9-1.3] R_{exp} range, between the clustered results in Figure C.27. This gap restricts the range of well-temperature distributions for which predictions might be made concerning the response of *hot spot 2*.

Though Figure C.27 might indicate so, the non-linear stress response of the wellhead system does not enable to predict that the damage rates of *hot spot 2* will remain at a lower level than the rates predicted by the analyses without temperature, for values of R_{exp} within the [0.9-1.3] range.

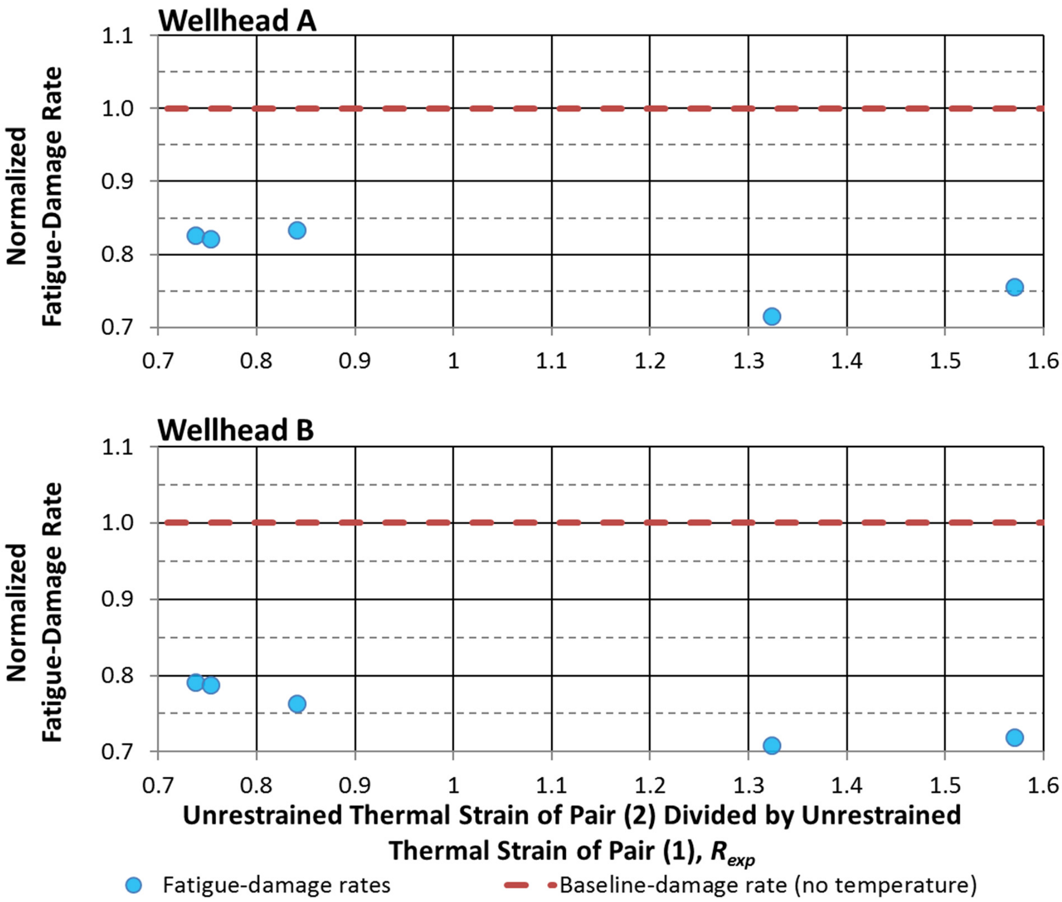

Figure C.27 – Fatigue-damage rates plotted against R_{exp}. *Hot spot 2*. 2nd mechanical configuration assumed by the wellhead model during drilling. DFF=10. S-N curve F3.

Figure C.28 presents the normalized damage rates plotted against R_{exp}, for the structural analyses performed for wellheads A and B during the third mechanical configuration assumed by the wellhead models during the drilling operation.

The response predicted for *hot spot 2* indicate that within the [1.05, 1.25] R_{exp} range, both wellheads may experience normalized fatigue-damage rates up to 35% higher than the respective baseline values.

Within the [1.4, 1.6] R_{exp} range, both wellheads may experience fatigue-damage rates down to approximately 70% of the respective values. However, Figure C.28 indicates that the normalized damage rates may fluctuate within this range. For wellhead A, there is a visible outlier for R_{exp} approaching 1.47, for which the normalized damage rates becomes higher than the baseline value.

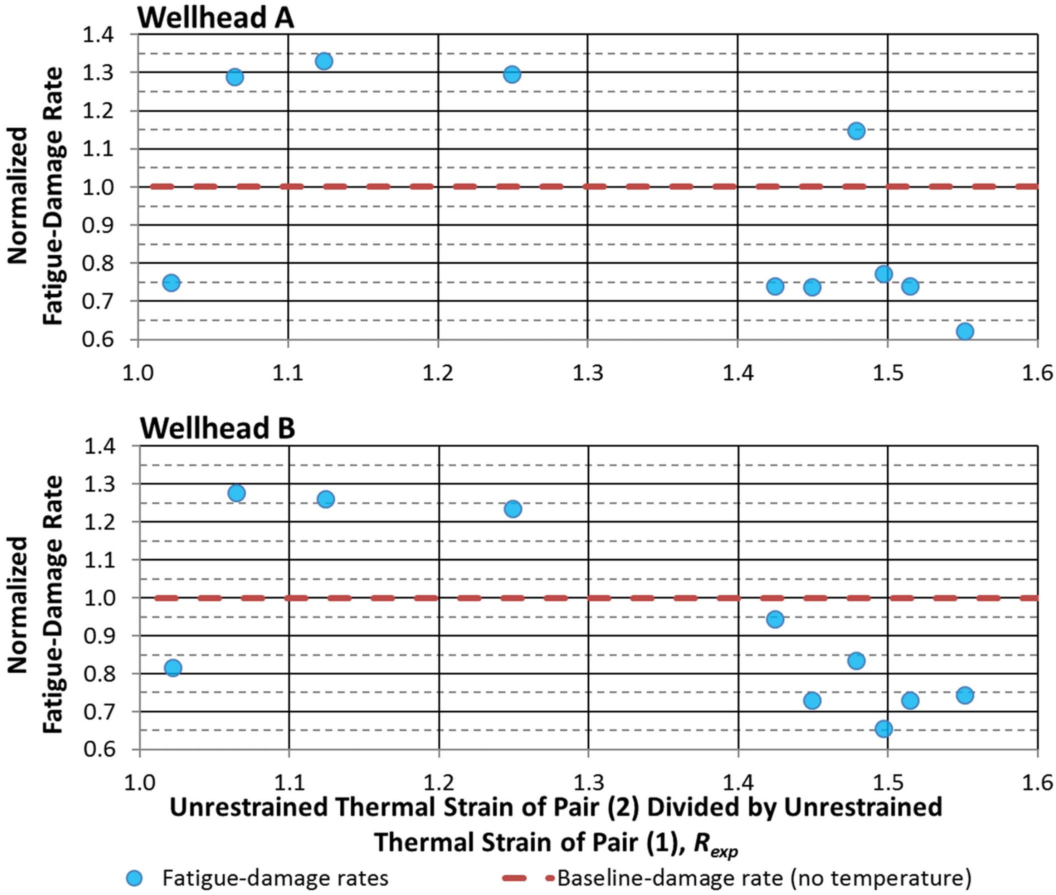

Figure C.28 – Fatigue-damage rates plotted against R_{exp}. *Hot spot 2*. 3rd mechanical configuration assumed by the wellhead model during drilling. DFF=10. S-N curve F3.

Figure C.29 presents the normalized damage rates plotted against R_{exp}, for the structural analyses performed for wellheads A and B during the fourth mechanical configuration assumed by the wellhead models during the drilling operation.

Like Figure C.23, the few calculations carried out for this mechanical configuration, together with the short range of R_{exp}, does not enable to identify any broad trends.

The response predicted by the analyses with temperature for both wellheads is very similar. The normalized fatigue-damage rates may decrease down to 80% of the respective baseline values.

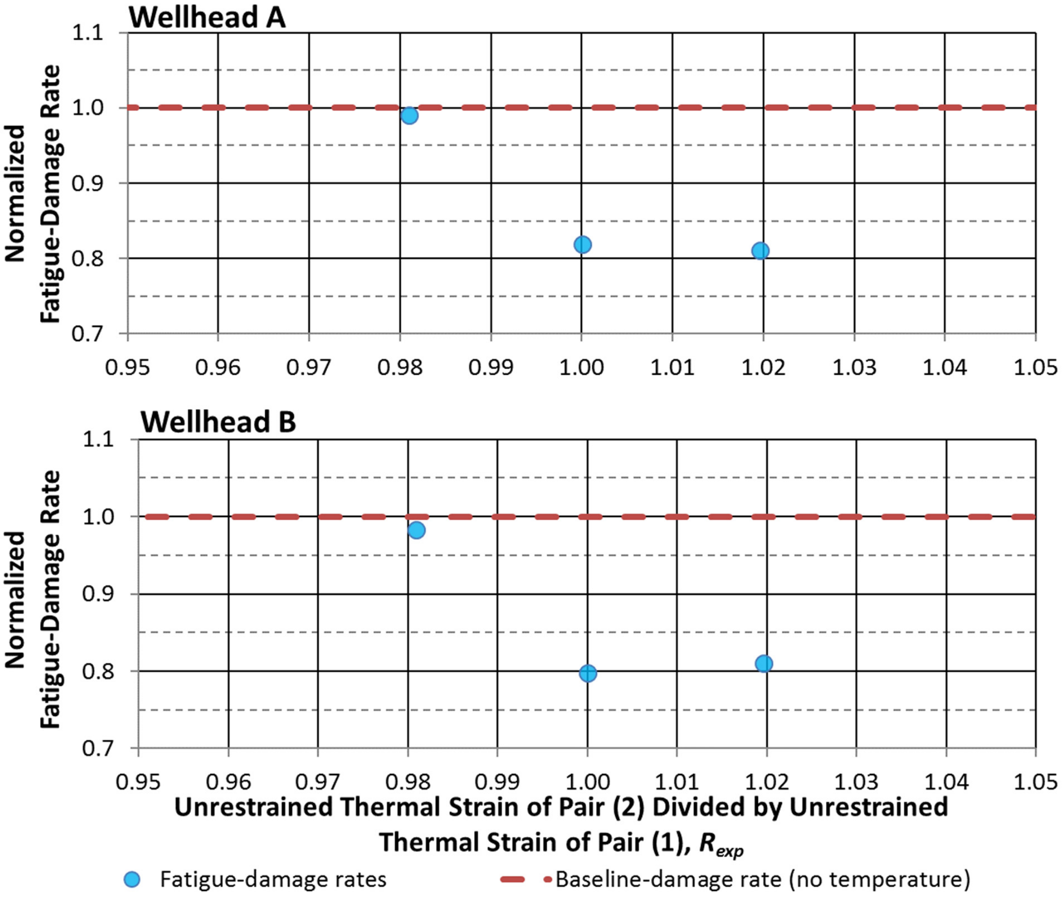

Figure C.29 – Fatigue-damage rates plotted against R_{exp}. *Hot spot 2*. 4th mechanical configuration assumed by the wellhead model during drilling. DFF=10. S-N curve F3.

Figure C.30 presents the normalized fatigue-damage rates plotted against R_{exp}, for the structural analyses performed for wellheads A and B during the fifth mechanical configuration assumed by the wellhead models during the drilling operation.

For both wellheads, the analyses with temperature predicted normalized fatigue-damage rates lower than those predicted by the respective analyses without temperature.

The damage rates predicted for wellhead B remained around 80% of the baseline value. The damage rates predicted for wellhead A show a pair of outliers within the [1.4, 1.5] R_{exp} range, otherwise damage rates also remain around 80% of the respective baseline value.

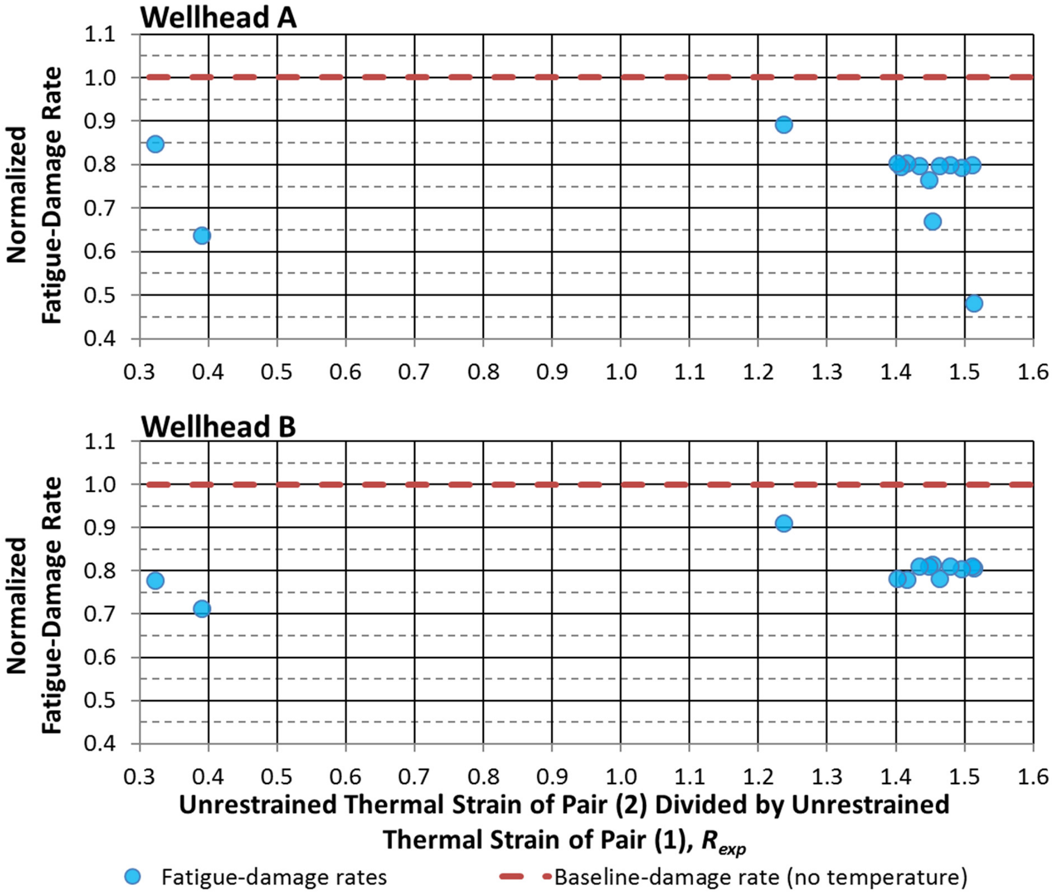

Figure C.30 – Fatigue-damage rates plotted against R_{exp}. *Hot spot 2.* 5th mechanical configuration assumed by the wellhead model during drilling. DFF=10. S-N curve F3.

Figure C.31 presents the normalized fatigue-damage rates plotted against R_{exp}, for the structural analyses performed for wellheads A and B during the sixth mechanical configuration assumed by the wellhead models during the drilling operation.

For both wellheads, the normalized damage rates predicted by the analyses with temperature were lower than those predicted by the corresponding analyses without temperature. Damage rates in wellhead B may become as low as 65% of the baseline value.

Within the same R_{exp} range, but at a different value of R_{exp} and consequently at a different well-temperature distribution, damage rates in wellhead A may become as low as 73% of the respective baseline value.

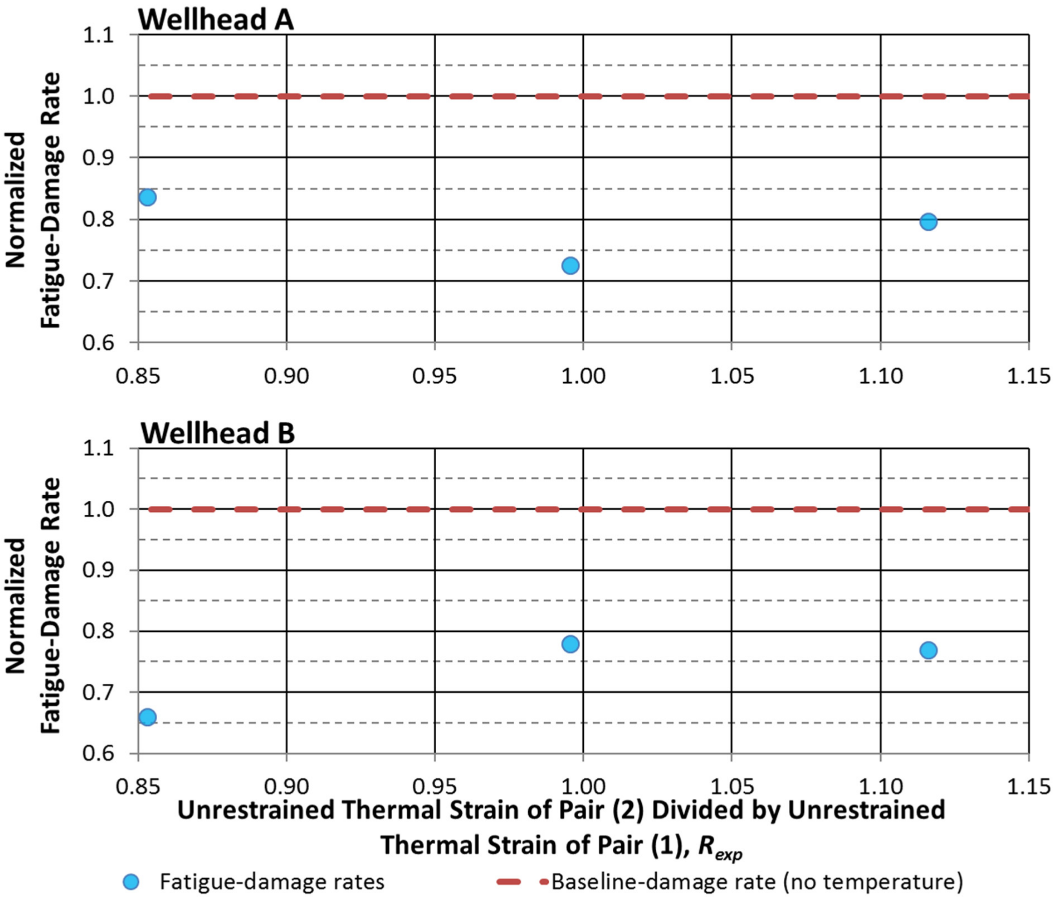

Figure C.31 – Fatigue-damage rates plotted against R_{exp}. *Hot spot 2*. 6th mechanical configuration assumed by the wellhead model during drilling. DFF=10. S-N curve F3.

Figure C.32 presents the normalized fatigue-damage rates plotted against R_{exp}, for the structural analyses performed for wellheads A and B during the workover operation.

Even if the outlier in the graph for wellhead A, which corresponds to the analysis performed at t=50 hours, is taken out of the discussion, it is visible in Figure C.32 that wellhead A may experience considerably lower normalized fatigue-damage rates that wellhead B.

While normalized damage rates in wellhead B may be up to 5% higher than the baseline value, for the corresponding R_{exp} range wellhead A may experience damage rates that are 70% of the respective baseline value.

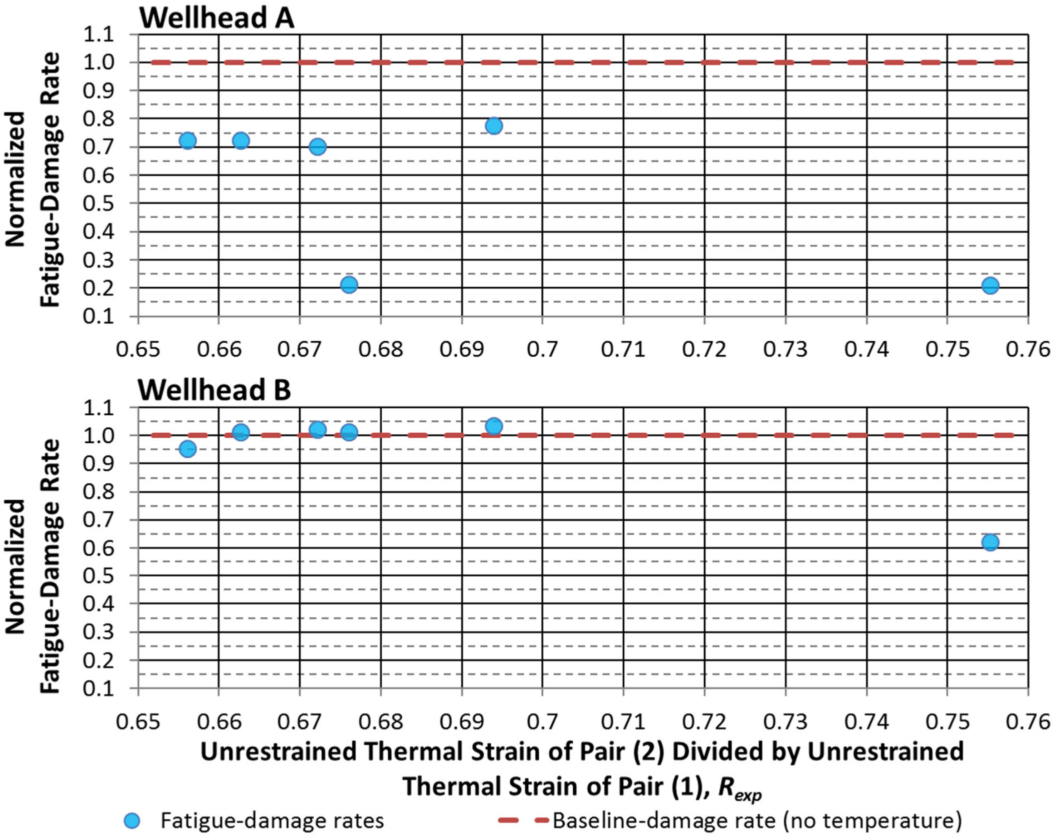

Figure C.32 – Fatigue-damage rates plotted against R_{exp}. *Hot spot 2*. Mechanical configuration assumed by the wellhead model during workover. DFF=10. S-N curve F3.

C.4.3 Landing Surface on the Low-Pressure Housing

Figure C.33 presents the normalized fatigue-damage rates plotted against R_{exp}, for the structural analyses performed for wellheads A and B during the second mechanical configuration assumed by the wellhead models during the drilling operation.

The response predicted for the both wellheads during this mechanical configuration are similar. Normalized damage rates predicted for wellhead B may undergo larger reductions in value, when comparted to the damage rates predicted for wellhead A.

The results presented for both wellhead models in Figure C.33 do not show a clear trend for the fatigue-damage rates estimated for values of R_{exp} below 0.9, but it may be predicted for both wellheads that damage rates will be at the lowest levels within the [1.3, 1.6] R_{exp} range.

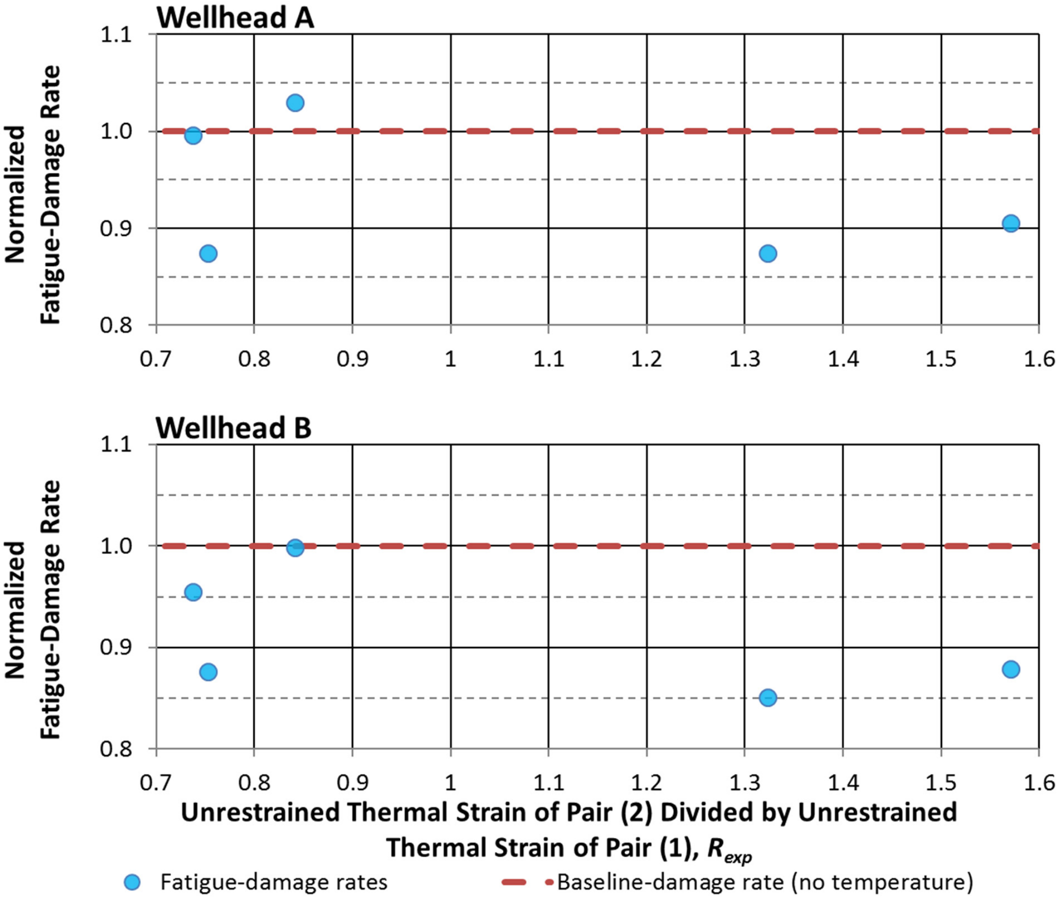

Figure C.33 – Fatigue-damage rates plotted against R_{exp}. *Hot spot 10*. 2nd mechanical configuration assumed by the wellhead model during drilling. DFF=10. S-N curve BM4.

Figure C.34 presents the normalized fatigue-damage rates plotted against R_{exp}, for the structural analyses performed for wellheads A and B during the third mechanical configuration assumed by the wellhead models during the drilling operation.

For both wellhead models, the structural calculations with temperature predicted lower normalized fatigue-damage rates. The damage rates predicted for wellhead A are between 85 and 95% of the baseline value. The damage rates predicted for wellhead B are between 84 and 92% of the respective baseline value.

The predicted trend from the analyses with temperature may indicate that fatigue-damage rates for *hot spot 10*, under this mechanical configuration, reach their lowest value under well-temperature distributions that generate a R_{exp} close 1.6.

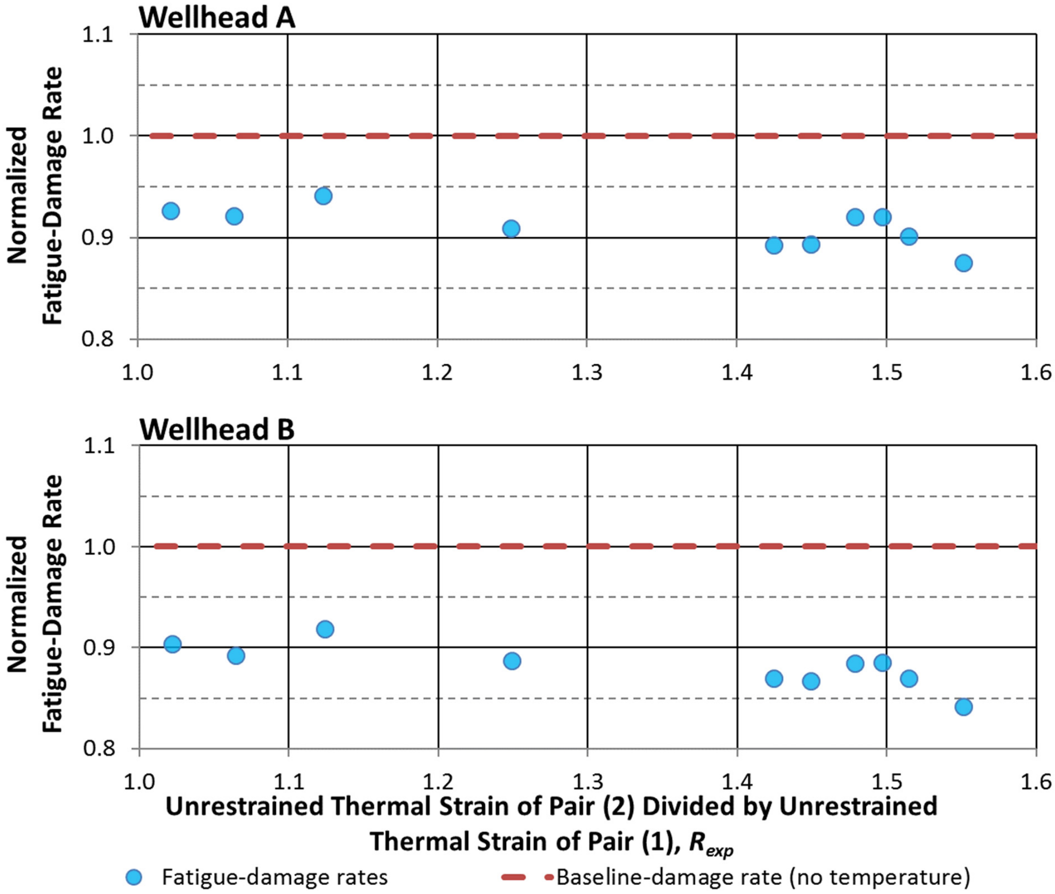

Figure C.34 – Fatigue-damage rates plotted against R_{exp}. *Hot spot 10*. 3rd mechanical configuration assumed by the wellhead model during drilling. DFF=10. S-N curve BM4.

Figure C.35 presents the normalized fatigue-damage rates plotted against R_{exp}, for the structural analyses performed for wellheads A and B during the fourth mechanical configuration assumed by the wellhead models during the drilling operation.

The few analyses and short range of R_{exp} covered by the structural calculations makes it difficult to determine a trend for the response of the wellhead. But, it may be concluded for both wellheads that, under this mechanical configuration, the normalized fatigue-damage rates predicted by the analyses with temperature may be smaller than the damage rate estimated by the respective analyses without temperature.

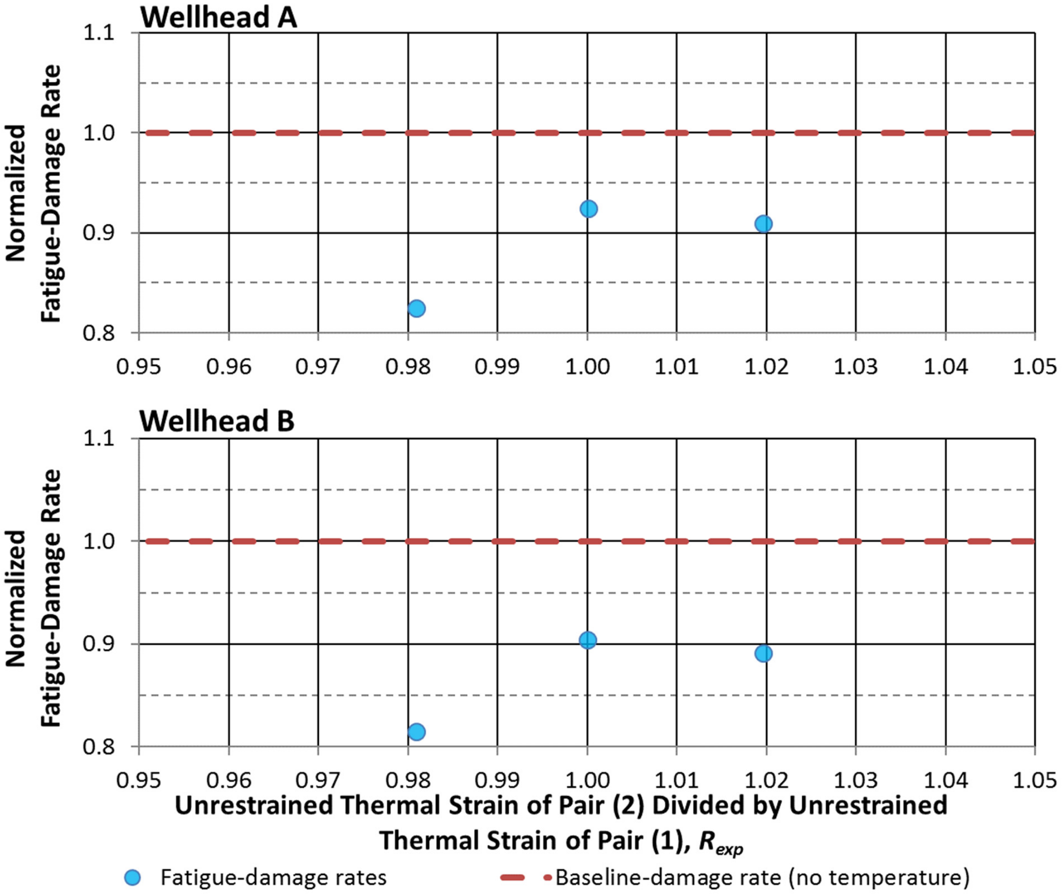

Figure C.35 – Fatigue-damage rates plotted against R_{exp}. *Hot spot 10*. 4th mechanical configuration assumed by the wellhead model during drilling. DFF=10. S-N curve BM4.

Figure C.36 presents the normalized fatigue-damage rates plotted against R_{exp}, for the structural analyses performed for wellheads A and B during the fifth mechanical configuration assumed by the wellhead models during the drilling operation.

The two wellhead models present similar responses. However, the fatigue-damage rates predicted for wellhead B may undergo larger reductions in value. From the structural calculations run, it could be predicted that the lowest fatigue-damage rates would be experienced for value of R_{exp} between 1.4 and 1.5. The highest damage rates have been predicted for the [0.3, 0.4] range R_{exp},

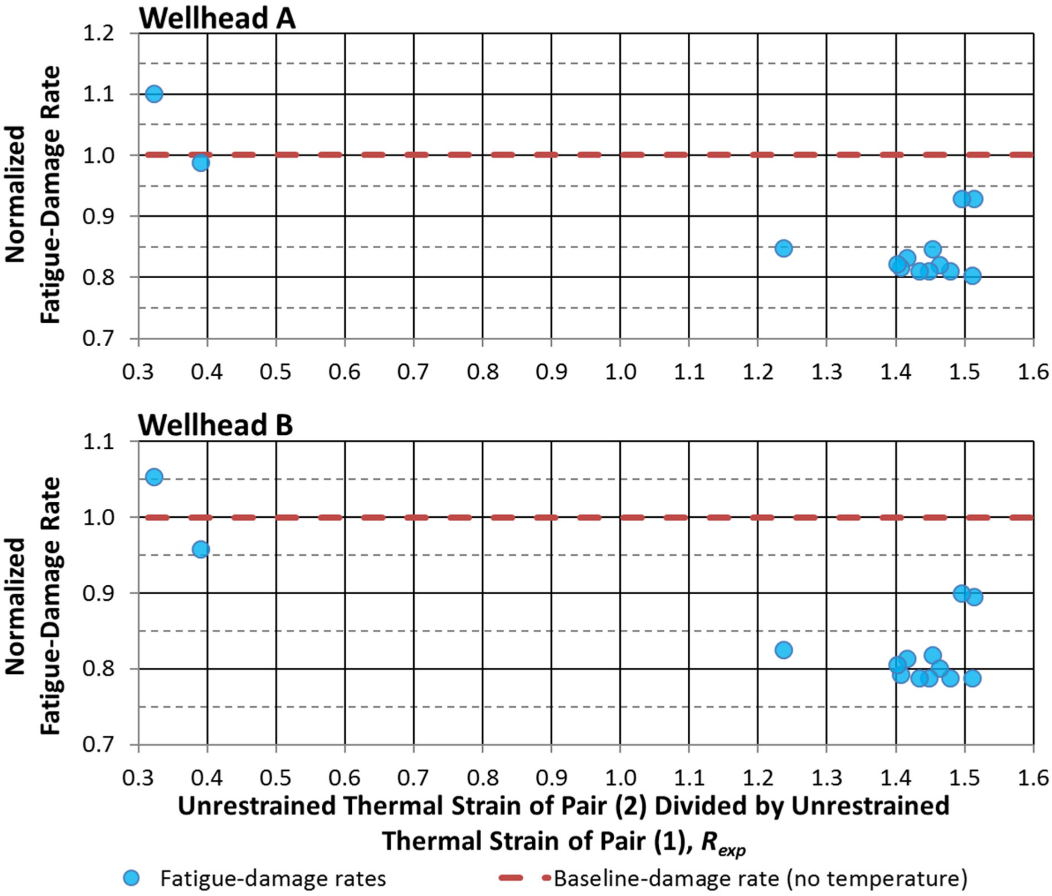

Figure C.36 – Fatigue-damage rates plotted against R_{exp}. *Hot spot 10*. 5th mechanical configuration assumed by the wellhead model during drilling. DFF=10. S-N curve BM4.

Figure C.37 presents the normalized fatigue-damage rates plotted against R_{exp}, for the structural analyses performed for wellheads A and B during the sixth mechanical configuration assumed by the wellhead models during the drilling operation.

Like Figure C.35, the few calculations carried out make it difficult to determine a trend for the response of the wellhead. But since a larger range of R_{exp} has been covered in Figure C.37, from the results shown it might be predicted that both wellheads will undergo the lowest damage rates under well-temperature distributions that yield R_{exp} approaching 1.12.

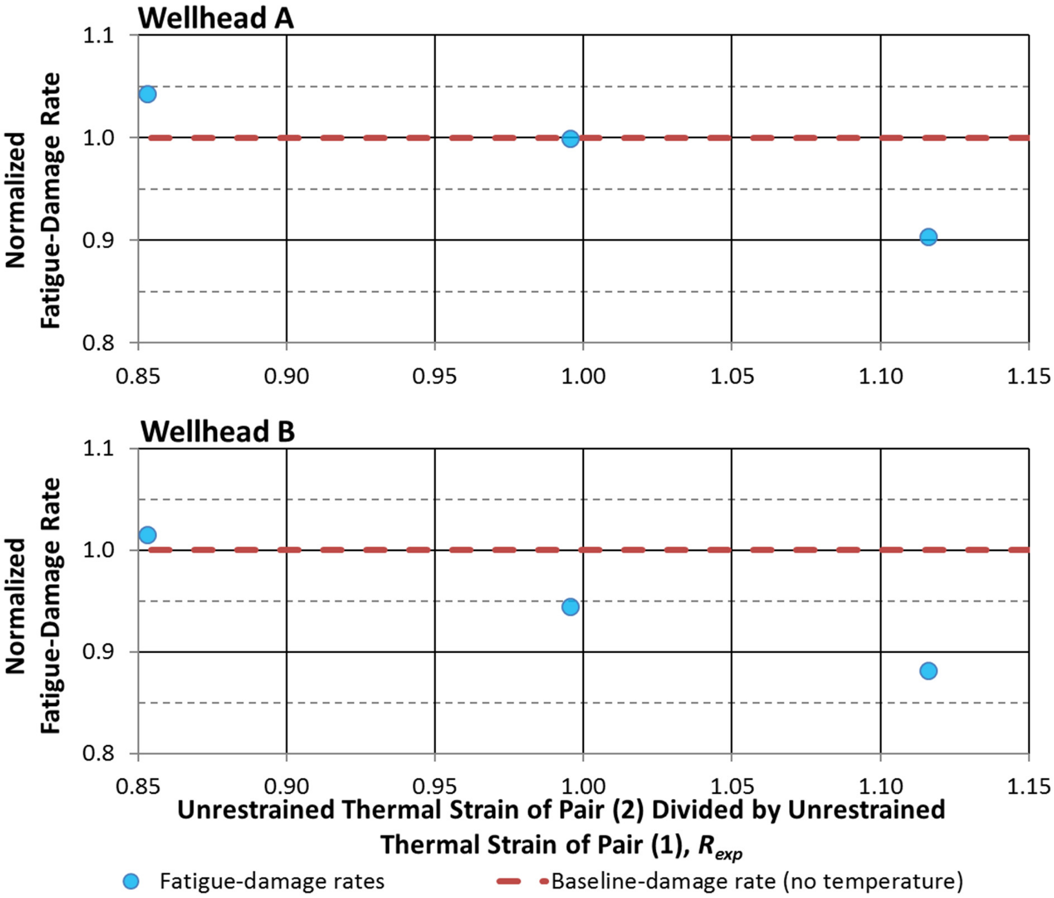

Figure C.37 – Fatigue-damage rates plotted against R_{exp}. *Hot spot 10*. 6th mechanical configuration assumed by the wellhead model during drilling. DFF=10. S-N curve BM4.

Figure C.38 presents the normalized fatigue-damage rates plotted against R_{exp}, for the structural analyses performed for wellheads A and B during the workover operation.

The response predicted for both wellheads enable to delimit two regions, within the R_{exp} range covered. For values of R_{exp} below 0.675, the damage rates in *hot spot 10* may undergo a reduction in value, reaching approximately 60% of the baseline value.

For wellhead B, fatigue-damage rates predicted for R_{exp} above 0.675 may be up to 30% higher than the baseline value. For wellhead A, fatigue-damage rates my increase up to 60% higher than the respective baseline value.

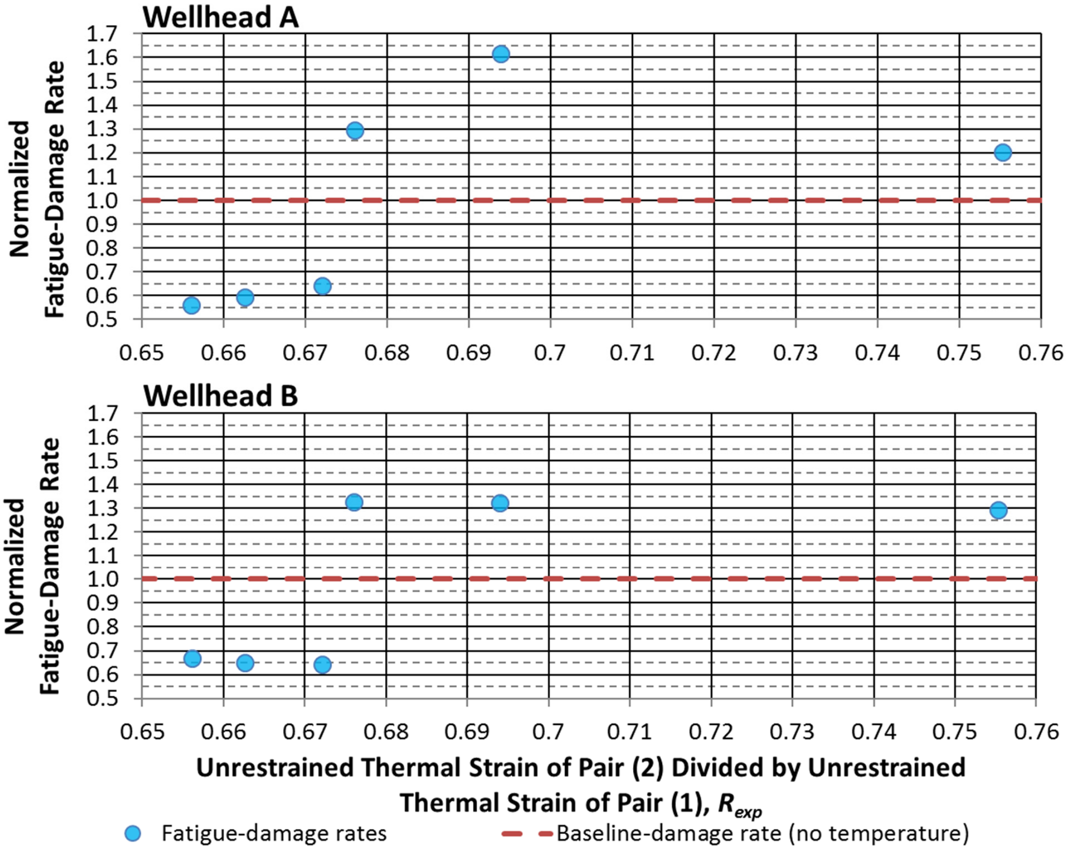

Figure C.38 – Fatigue-damage rates plotted against R_{exp}. *Hot spot 10.* Mechanical configuration assumed by the wellhead model during workover. DFF=10. S-N curve BM4.

C.5 Normalized Preload-Stress Levels – Section 7.4

The normalized preload-stress levels calculated during the remaining of the drilling operations are presented in this section. Like the remarks found in C.4, the few analyses run do not enable to make concluding remarks regarding any trends of the fourth and sixth mechanical configurations.

The results obtained for the weld hot spots during the second mechanical configuration of the wellhead during drilling (Figure C.39) indicate that the highest variation on the preload-stress levels may be predicted for a value of R_{exp} approaching 1.3.

Contrary to what the R_{exp} approach might have initially suggested, the analyses run for R_{exp} smaller than zero did not indicate a decrease in the preload-stress levels of the welded connections in the surface casing. However, the reader must note that a R_{exp} smaller than zero does not necessary imply that the induced thermal deformation of the conductor is larger than the deformation on the surface casing. Therefore, at the cases presented in Figure C.39, the surface casing is still exerting a tension force on the conductor.

The results obtained for both the welds and the base metal hot spots indicate that the preload-stress levels are not majorly influenced by the temperature of the well, when the temperature of scenario of the well may be represented by a value of R_{exp} smaller than 1.

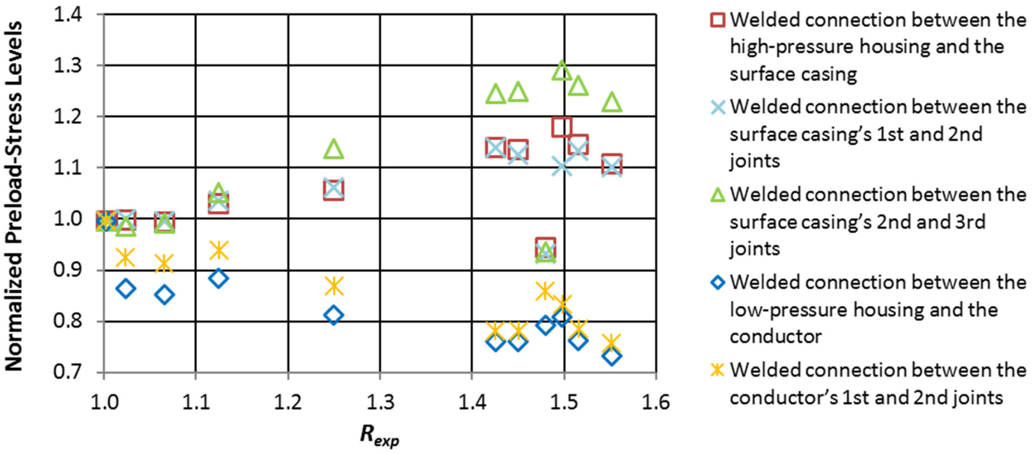

Figure C.39 – Normalized preload-stress levels plotted against R_{exp}. Welded connection hot spots. 2nd mechanical configuration assumed by the wellhead model during drilling.

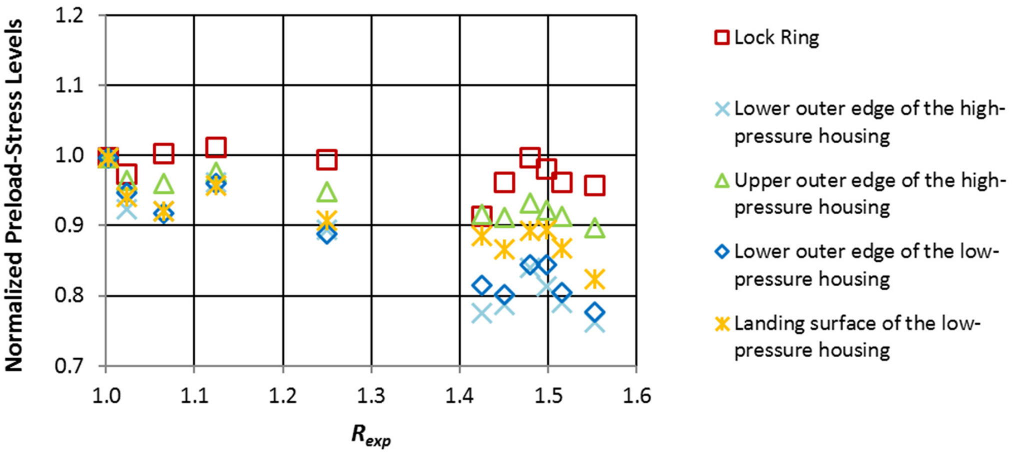

Figure C.40 – Normalized preload-stress levels plotted against R_{exp}. Base metal hot spots. 2nd mechanical configuration assumed by the wellhead model during drilling.

The results from the analyses run for the third mechanical configuration of the wellhead during drilling confirm the remarks previously presented in section 7.4. The largest variations on the preload-stress levels have been calculated for a value of R_{exp} near 1.5. The approach with R_{exp}

may also provide an extra tool for detecting irregularities in the analyses, because there may be an outlier among the results clustered around R_{exp} equal to 1.5, which could warrant an inspection.

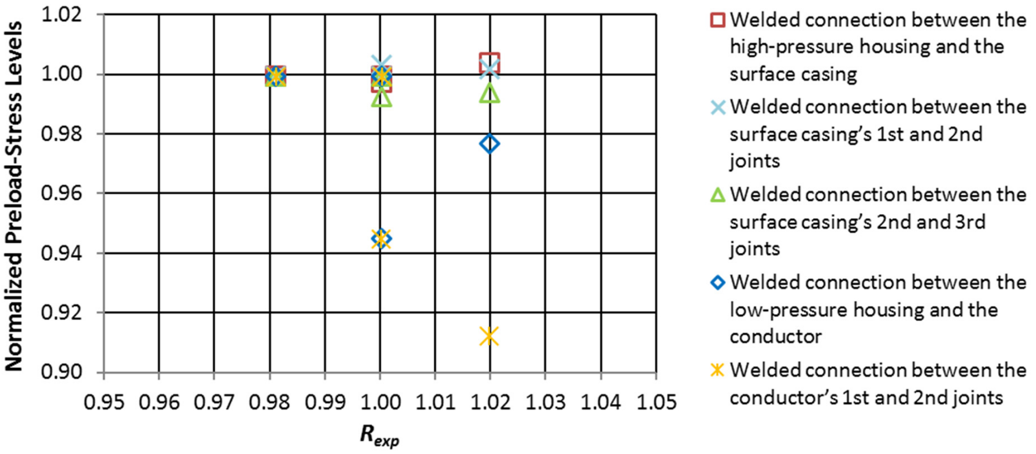

Figure C.41 – Normalized preload-stress levels plotted against R_{exp}. Welded connection hot spots. 3rd mechanical configuration assumed by the wellhead model during drilling.

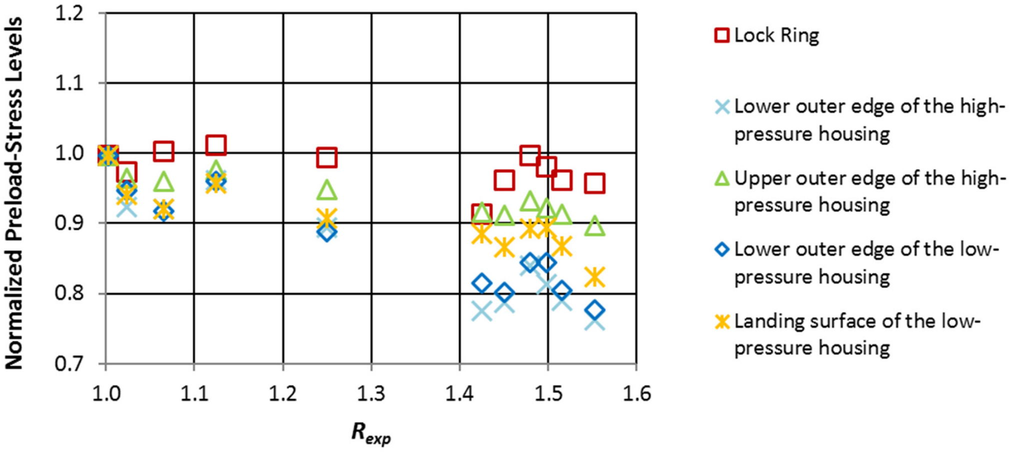

Figure C.42 – Normalized preload-stress levels plotted against R_{exp}. Base metal hot spots. 3rd mechanical configuration assumed by the wellhead model during drilling.

The results of the analyses run for the fifth mechanical configuration of the wellhead assumed during drilling are mostly clustered within the [1.4, 1.5] R_{exp} range, which makes it difficult to detect any trends. However, it may be said that the preload-stress levels on the base metal and the conductor welds might decrease because of the temperature distribution of the well.

Conversely, the preload-stress levels on the surface casing welds seem to be slightly affected by temperature, right up the 1.5 R_{exp} mark, when the calculated preload-stress levels start to steeply increase.

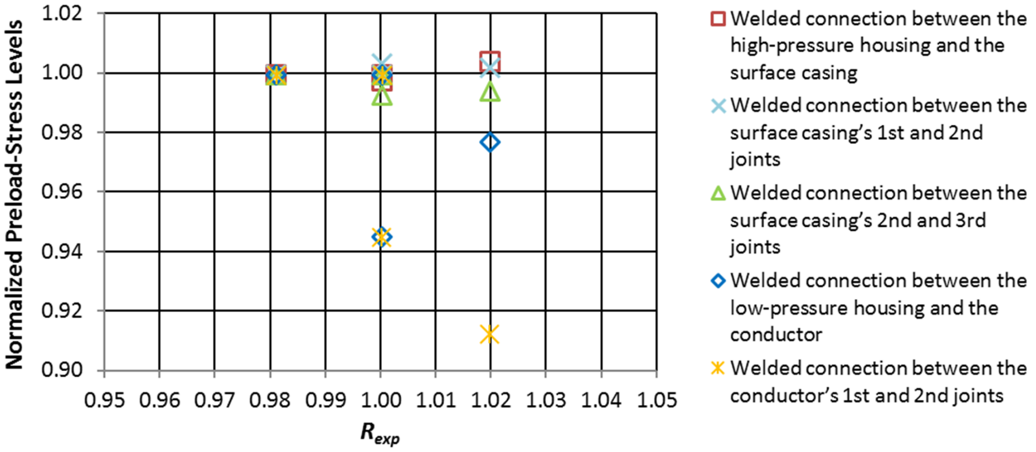

Figure C.43 – Normalized preload-stress levels plotted against R_{exp}. Welded connection hot spots. 4th mechanical configuration assumed by the wellhead model during drilling.

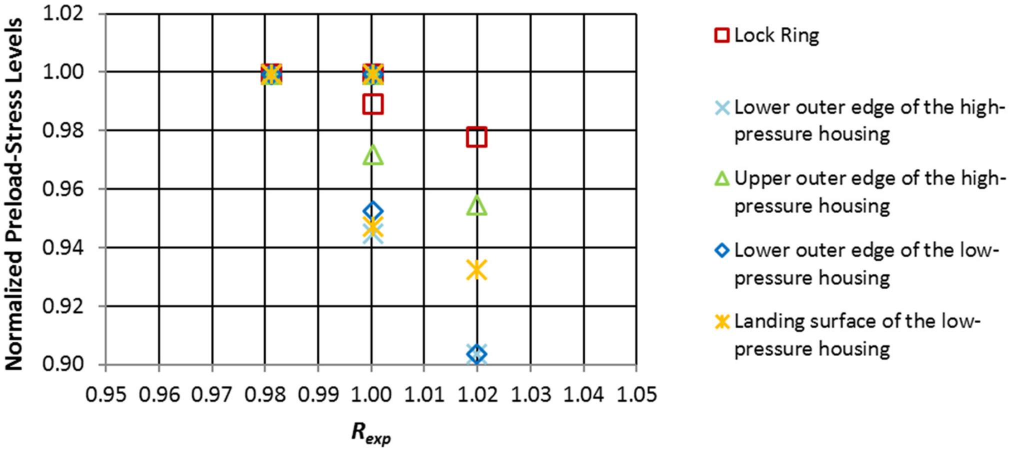

Figure C.44 – Normalized preload-stress levels plotted against R_{exp}. Base metal hot spots. 4th mechanical configuration assumed by the wellhead model during drilling.

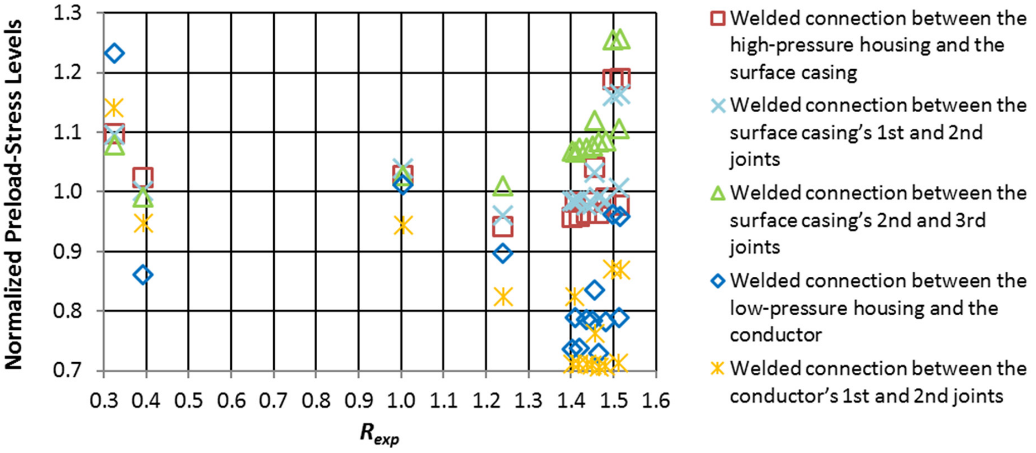

Figure C.45 – Normalized preload-stress levels plotted against R_{exp}. Welded connection hot spots. 5th mechanical configuration assumed by the wellhead model during drilling.

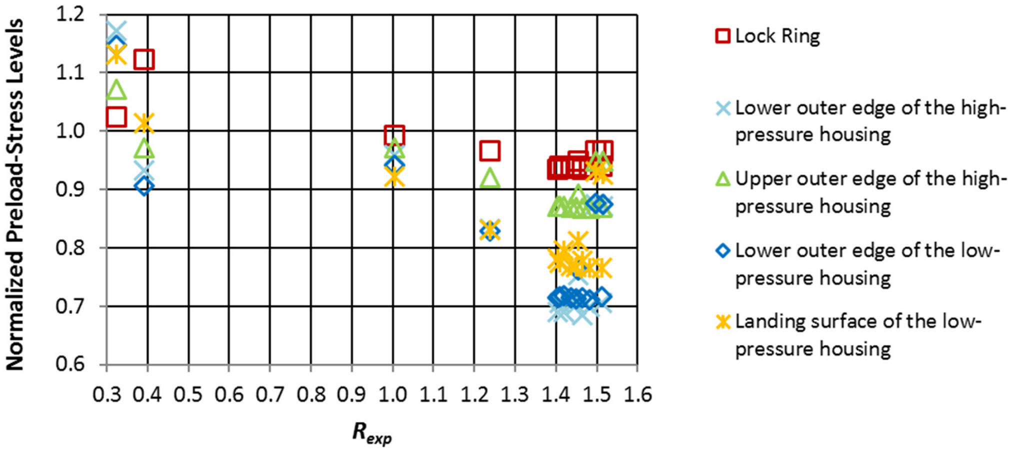

Figure C.46 – Normalized preload-stress levels plotted against R_{exp}. Base metal hot spots. 5th mechanical configuration assumed by the wellhead model during drilling.

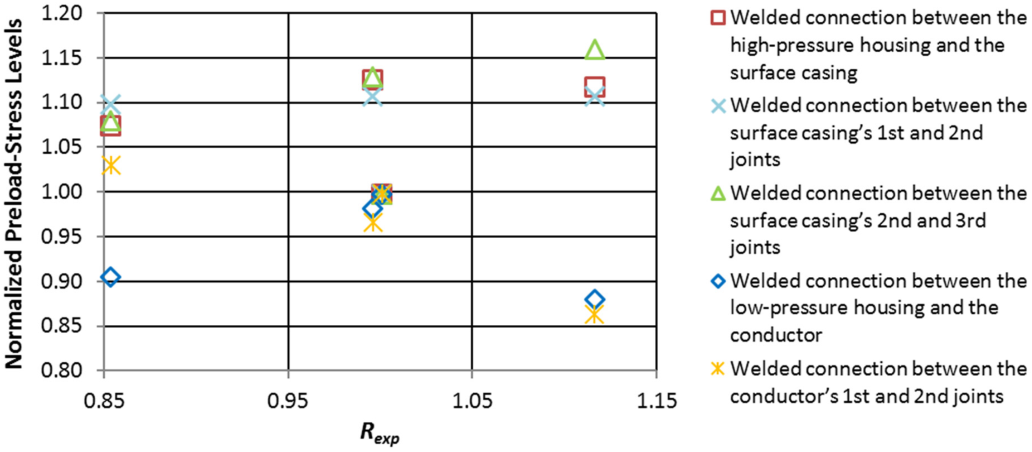

Figure C.47 – Normalized preload-stress levels plotted against R_{exp}. Welded connection hot spots. 6th mechanical configuration assumed by the wellhead model during drilling.

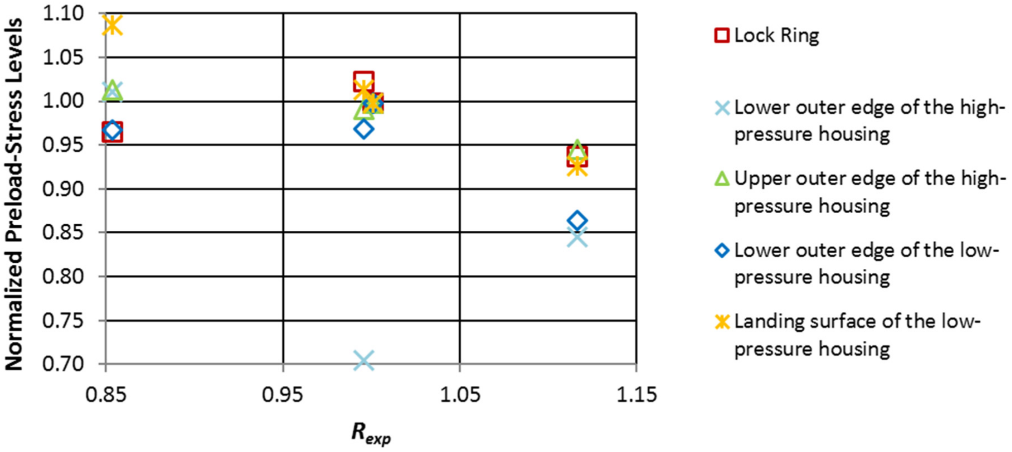

Figure C.48 – Normalized preload-stress levels plotted against R_{exp}. Base metal hot spots. 6th mechanical configuration assumed by the wellhead model during drilling.

Annex D – Paper I

Lucas Cantinelli Sevillano, Jesus de Andrade, Milan Stanko, Sigbjørn Sangesland

Thermal Effects on Subsea Wellhead Fatigue during Workover Operations

Is not included due to copyright

Annex E – Paper II

Lucas Cantinelli Sevillano, Jesus de Andrade, Milan Stanko, Sigbjørn Sangesland

Subsea Wellhead Fatigue Analysis with Focus on Thermal Conditions

Annex F – Paper III

Lucas Cantinelli Sevillano, Jesus de Andrade, Sigbjørn Sangesland

Subsea Wellhead Life Cycle Fatigue Analysis and the Role of Well Temperature

Is not included due to copyright

Annex G – Paper IV

Lucas Cantinelli Sevillano, Jesus de Andrade, Sigbjørn Sangesland

Estimation of Undisturbed Geothermal Gradient in Wells from Measured Drilling Data – A Numerical Approach

Is not included due to copyright